Active Chatter Suppression with Monitoring-Based Process Control for Self-Optimizing Machining Systems

February 2021

Shuntaro Yamato

A Thesis for the Degree of Ph.D. in Engineering

Active Chatter Suppression with Monitoring-Based Process Control for Self-Optimizing Machining Systems

February 2021

Graduate School of Science and Technology
Keio University

Shuntaro Yamato

Table of contents

Nomenclature

Roman symbols

a_e	Radial depth of cut
a_l	Elements of denominator coefficient vector of digital filter ($l \in \mathbb{N}_0$)
a_p	Depth of cut (axial depth of cut in milling process)
a_w	Cutting chord length projected onto the axis perpendicular to feed direction
A_c	Chatter vibration amplitude
A_s	Dynamic cutting area
A_τ	Variation amplitude in delay term
b_c	Cutting width in vibration direction
b_r	Regenerative cutting width in vibration direction
b_w	Cutting chord length projected onto the axis parallel to feed direction
b_l	Elements of numerator coefficient vector of digital filter ($l \in \mathbb{N}_0$)
c	Feed per tooth
C_a	Total damping coefficient in rigid body motion ($= C_m + C_t$)
C_e	Capacitor
$C_m (= D_m/R^2)$	Equivalent value of D_m in translational motion
C_t	Damping coefficient of translational element
d_f	Directional factor
$dF_t, dF_r,$ and dF_a	Minute cutting force in tool tangential, radial, and axial directions, respectively
$dF_x, dF_y,$ and dF_z	Minute cutting forces in Cartesian coordinate system
d_s	Diameter of screw shaft
D	Tool/workpiece diameter
D_m	Viscous friction coefficient of rotational element
$D_r(s)$	Denominator of transfer function for motion equation
E_{act}	Active (mechanical) energy
E_{app}	Apparent (mechanical) energy
E_e	Voltage in electrical circuit
E_s	Young's modulus of screw shaft
E_d	Energy dissipated by inherent damping capacity of machine
E_f	Net inflow of energy in CWS
E_n	Energy produced by negative work of cutting force on CWS
E_p	Energy produced by positive work of cutting force on CWS
f_c	Chatter frequency
f_s	Frequency of (sinusoidal) spindle speed variation
f_s	Swing frequency
f_z	Tooth-passing frequency
F, F_q $(q: x, y, z)$	Cutting force in Cartesian coordinate system
F_c	Resultant cutting force on CWS
F_{dis}	Disturbance force
F_f	Feed force

F_{ls}	Load-side force
F_{sf}	Friction force
$F_t, F_r,$ and F_a	Tangential(principal) force, radial force, and axial force, respectively
g_{LPF}	Cutoff frequency of low-pass filter
G_c	Cascaded compensation digital filter
G_{HPF}	High-pass filter
G_l	General one-dimensional l-th order proper digital filter ($l \in \mathbb{N}_0$)
G_{LPF}	Low-pass filter
h	Index number (e.g., data number and minute disk element number)
h_c	Uncut chip thickness
h_{cu}	Geometric surface roughness (e.g., cusp height).
h_m	Number of modes
i	Imaginary unit
I_a	Motor current
I_e	Current in electrical circuit
j	Index number (e.g., tooth number)
J_e	Error function for parameter identification
$J_l(m_f)$	l-th order Bessel function of the first kind ($l \in \mathbb{Z}$) with modulation index
J_m	Total inertia of motor, coupling, and ball-screw
k	Sample number at present time in the difference equation
k_c	Chatter lobe number
k_r	Ratio of radial to tangential cutting force ($= K_{rc}/K_{tc}$)
K_b	Axial stiffness of bearing
K_{bs}	Summation of K_b and K_s
K_{b1}	Axial stiffness of motor side bearing
K_{b2}	Axial stiffness of anti-motor side bearing
K_m	Torque coefficient of servomotor
K_{nut}	Axial stiffness of nut
K_r	Total stiffness of feed screw system
K_s	Axial stiffness of screw shaft
K_t	Thrust-force coefficient of linear motor
$K_{te}, K_{re},$ and K_{ae}	Edge force coefficient in tangential, radial, and axial directions, respectively
$K_{tc}, K_{rc},$ and K_{ac}	Specific cutting force in tangential(principal), radial, and axial direction, respectively
l	Index for number of orders such as filter, Bessel function, and modulation
ℓ_p	Lead length of ball screw
L_e	Inductor
L_s	Length of ball screw shaft
m_f	Modulation index
m_p	Arbitrary integer in variable pitch cutter principle
M, C, K	(Modal) mass, damping, stiffness, respectively
M_a	Total movable mass in rigid body motion ($= M_m + M_t$)

$M_m(=J_m/R^2)$	Equivalent value of J_m in translational motion
M_t	Movable mass
MEF	Mechanical energy factor
MFT	Moving Fourier transform
MPF	Mechanical power factor
n_m	Number of waves in the vibration mode
N_c	Number of teeth
N_L	Number of minute disk elements (i.e., divisions along axial depth of cut)
N_r	Number of tooth passes
N_w	Number of samples corresponding to the calculation window length
p	Index number (e.g., tool number)
p_r	Intermediate variable representing eigenvalue
P_{act}	Active power
P_{app}	Apparent power
P_c	Complex power
P_{react}	Reactive power
PF	Power factor
q $(q: x, y, z)$	Vibration displacement in X-/Y-/Z- direction
q_c	Dynamic displacement in a certain vibration direction in 3D space
r_a	Acceleration rate
R_a	Surface roughness
R_A	Relative variation amplitude of SSV (i.e., RVA)
R_e	Resistor
R_F	Relative variation frequency of SSV (i.e., RVF)
R_r	Transformation coefficient for rotational to translational motion $(=\ell_p/2\pi)$
RF	Regeneration factor
RV	RV factor $(=R_A \times R_F)$
s	Laplace operator
S	Spindle speed
S_{new}	New spindle speed after update in discrete spindle speed tuning
t	Time
t_b, t_e	Integral time section for calculating net inflow energy: $[t_b, t_e]$
T_a	Delay time for servo amplifier
T_m	Total delay time in numerical differential and signal transmission at motor side
T_s	Sampling period
T_{sf}	Friction torque
T_t	Total delay time by numerical differential and signal transmission at stage side
T_w	Calculation window time length
T_1, T_2, and T_3	Dead time in phase lag compensation for signals of motor current, motor angle, and stage position, respectively, for sensorless cutting force estimation
u	Certain input signal
U, V	Rotating coordinate system UV

x, y, z	Displacement in X-/Y-/Z-axis (x only indicates its physical quantity in Chapter 3)
X, Y, and Z	Cartesian coordinate system XYZ
X_A	Absolute stage position from the motor side bearing
$X_m(= R\Theta_m)$	Equivalent value of Θ_m in translational motion
X_r	Relative displacement ($X_m - X_t$)
X_t	Stage position
v	Velocity
W_{act}	Active mechanical power
W_{app}	Apparent mechanical power
z	z operator

Greek symbols

α	Time-varying directional dynamic milling force coefficient
α_c	Constant for proportional damping
$\alpha_r(= M_t/M_m)$	Inertia ratio
α_0	Time-invariant average directional dynamic milling force coefficient
β and γ	Directional angles of vibration on the plane parallel and perpendicular to the principal force direction, respectively
β_L	Helix angle
δ	Unit step function to judge tooth engagement
Δa_p	Thickness of each minute disk element
ΔC_a	Variation in total damping coefficient
ΔK_m	Variation in torque coefficient
ΔM_a	Variation in total movable mass
ΔS	Difference of spindle speed between two tools
ΔX_t	Amount of movement in stage position
$\Delta\varepsilon_c$	Phase difference between regenerative waves
$\Delta\theta_p$	Optimal pitch angle difference
$\Delta\tau$	Difference between tooth-pass periods of two tools
$\Delta\omega_c$	Maximum frequency shift in the modulated signal
ϵ_e	Sum of squares of the residuals
ε_c	Phase shift between present and previous vibration left on the machined surface
ζ_m	Damping ratio of rotational elements
ζ_r	Modal damping ratio
ζ_t	Damping ratio of translational elements
η	Chip flow angle
θ	Spindle rotating angle
θ_{IE}	Phase difference between current and voltage in AC circuit
θ_p	Pitch angle
θ_{st}, θ_{ex}	Start and exit angles of cutter engagement
θ_{sw}	Swing angle
θ_{vF}	Phase difference between velocity and load force in mechanical system

θ_{xF}	Phase difference between displacement and load force in mechanical system
θ_0	Offset angle in tool swing motion
Θ_{cm}	Angle of counter motor
Θ_m	Motor angle
λ_r	Eigenvalue
μ_f	Constant ratio of the force in chip flow direction to the principal force
μ_c	Overlap factor
ρ	Ratio of the expected and the exact variation amplitude of time delay terms
τ	Time delay between two consecutive cuts (i.e., the regenerative feedback effect)
$\Phi_{qq'}$	Compliance frequency response function (q, q' : direction of displacement response and input force in Cartesian coordinate system, i.e., x, y, z; e.g., Φ_{xx})
ψ_c	Initial vibration phase
ω	Angular frequency
ω_c	Chatter angular frequency
ω_{ext}	Targeted angular frequency for extraction
ω_L	Bandwidth of current loop
ω_r	Resonance/modal angular frequency (e.g., axial resonance in dual-inertia system)
ω_s	Angular frequency of (sinusoidal) spindle speed variation
ω_{sw}	Swing angular frequency
ω_t	Anti-resonance angular frequency at motor side in dual-inertia system

Matrices and vectors

$\boldsymbol{a_l}$	Denominator coefficient vector of digital filter ($l \in \mathbb{N}_0$)
$\boldsymbol{A}, \boldsymbol{b}$	Matrix/vector for procedure in least squares method
$\boldsymbol{A_0}$	Directional matrix of milling process force in parallel milling process
$\mathbf{b_c}$	Cutting width vector
$\boldsymbol{b_l}$	Numerator coefficient vector of digital filter ($l \in \mathbb{N}_0$)
$\boldsymbol{DM_\Delta}$	Delay matrix depending on speed difference in parallel milling process
$\mathbf{e}$	Error vector ($J_e = \sqrt{\mathbf{e}\mathbf{e}^T}$)
$\mathbf{e_q}$	Unit vector in chatter vibration direction
$\boldsymbol{F}$	Force vector
$\boldsymbol{F_c}$	Resultant cutting force vector
$\mathbf{K_c}$	Specific cutting force vector
$\boldsymbol{M}, \boldsymbol{C}$, and $\boldsymbol{K}$	Mass, damping, and stiffness matrices
$\boldsymbol{q_c}$	Chatter vibration vector
$\mathbf{r}$	Reference signal dataset
$\mathbf{r_c}$	Regenerative width vector
$\mathbf{R_G}$	Frequency gain vector of reference signal ($\mathbf{R_G} = \mathrm{Abs}(\mathrm{FFT}[\mathbf{r}])$)
$\boldsymbol{TF}$	Transfer function matrix
$\mathbf{u}$	Input signal dataset
$\mathbf{U_G}$	Frequency gain vector of input signal ($\mathbf{U_G} = \mathrm{Abs}(\mathrm{FFT}[\mathrm{u}])$)
$\boldsymbol{X}$	Displacement/position vector

$\boldsymbol{\lambda}$	Targeted parameter vector for identification
$\boldsymbol{\phi}$	Modal matrix
$\boldsymbol{\varphi}$	Eigenvector

Subscript

d	Value in modal coordinate system
g	Value in rigid body mode
h	Index number (e.g., data number and minute disk element number)
ic	Value for initial condition
j	Index number (e.g., tooth number)
max	Maximum value
min	Minimum value
n	Nominal value
q $(q: x, y, z)$	Direction in Cartesian coordinate of machine
v	Value in vibration mode

Superscripts

$comp$	Value in compensated signal
CUR	Value in current-based estimation
DOB	Value in disturbance observer
$LDOB$	Value in load-side disturbance observer
$MEDOB$	Value in multi-encoder-based disturbance observer
(n)	Index for number of cutting tests
ref	Reference value
res	Response value
RIG	Value in rigid body mode-based disturbance observer
S_{max}	Value at maximum spindle speed
S_{min}	Value at minimum spindle speed
tp	Value for tool p in parallel turning/milling process
VIB	Value in vibration mode-based disturbance observer
w	Value for workpiece
$\bar{}$ (bar)	Average value
$\hat{}$ (hat)	Estimated value
$\tilde{}$ (tilde)	Identification/approximated value

Abbreviations

AC	Alternating current
AE	Acoustic emission
AI	Artificial intelligence
ATO	Angular tool offset
CAD	Computer aided design

CAM	Computer aided manufacturing
CMM	Coordinate measuring machine
CNC	Computerized numerical control
CSS	Constant spindle speed
CSSV	Continuous spindle speed variation (= SSV)
CSI	Chatter stability index
CWE	Cutter-workpiece engagement
CWS	Cutter-workpiece system
DC	Direct current
DFT	Discrete Fourier transform
DOB	Disturbance observer
DoF	Degree of freedom
DSST	Discrete spindle speed tuning
FE	Finite element
FEA	Finite element analysis
FFT	Fast Fourier transform
FM	Frequency modulation
FRF	Frequency response function
HPF	High pass filter
HSS	High-speed steel
IoT	Internet of Things
LDOB	Load-side disturbance observer
LPF	Low pass filter
LSM	Least square method
MA	Moving average
MDoF	Multiple degree of freedom
MEDOB	Multi-encoder-based disturbance observer
MEF	Mechanical energy factor
MEMS	Micro electro mechanical systems
MFT	Moving Fourier transform
MI	Modulation index
ML	Machine learning
MPF	Mechanical power factor
MRR	Material removal rate
NC	Numerical control
PC	Personal computer
PF	Power factor
PLC	Programmable logic controller
PM	Phase modulation
PSD	Power spectrum density
RCD	Rotating cutting force dynamometer
RF	Regeneration factor

RMS	Root mean square
RMSE	Root mean square error
RVA	Relative variation amplitude of SSV
RVF	Relative variation frequency of SSV
SCF	Sensory characteristic feature
SDFT	Sliding discrete Fourier transform
SDM	Speed difference method
SDoF	Single degree of freedom
SLD	Stability lobe diagram
SOMS	Self-optimizing machining systems
SSV	Spindle speed variation (= CSSV)
SSSV	Sinusoidal spindle speed variation
STFT	Short time Fourier transform
TCM	Tool condition monitoring
TF	Transfer function
TMD	Tuned mass damper
TSM	Tool swing motion
TSSV	Triangular spindle speed variation
VHC	Variable helix cutter
VMDOB	Vibration mode-based disturbance observer
VPC	Variable pitch cutter
WT	Wavelet transform
ZOA	Zeroth order approximation
1D	One-dimensional

1. Introduction

1.1. Overview of self-optimizing machining systems

For the final product to exhibit the required functions and costs, the machining accuracy and efficiency of the components must be improved. The shape accuracy of the machined parts depends on the motion accuracy of the machine tools for feeding and positioning the cutting tools and workpiece to the desired location. Generally, the motion accuracy of the machine tools is required to be less than 1/10th of the shape accuracy of a part. If a machining accuracy of 10 μm is required, a machine tool that cuts this part must have a motion accuracy of 1 μm or less. As the superiority or inferiority of the machine tool's performance determines the production capacity and considerably affects the competitiveness of the products, each country positions the machine tool industry as a strategic key industry and makes intensive effort for advanced development [1].

The technology of machine tools has been deepened to attain highly accurate and efficient machining with high-precision and high-speed positioning. In the United States, the world's first numerical control (NC) machine tool was developed at the MIT Servo Mechanism Research Center in 1952 against the backdrop of an early mass consumption society. The advent of NC machine tools enabled the automation of machining, which was impossible to be achieved with analog/manual mechanical control, and then realized a mass production system by improving the machining efficiency and homogenization of machining accuracy. Positioning accuracy and speed of machine tools have been considerably improved through the continuous development of element technologies for feed drive systems, such as trajectory generation and control algorithms, mechanical drives and guides, amplifiers, motors, and sensors [2]. Additionally, the multi-functionalization of machine tools for process integration (e.g., five-axis machine tools equipped with two additional rotary axes) is a mainstream technological development to cut complicated geometry parts with high efficiency and accuracy as well as automatization [3,4]. Super multi-tasking and multi-axis machine tools, such as the mill turn center [5], a hybrid machine with a laser for additive manufacturing and/or quenching [6,7], and a built-in robot machining center [8], have also been developed.

Automation using computer technology, such as NC machine tools, is the 3rd industrial revolution following the 1st industrial revolution, in which power was generated using steam engines, and the 2nd industrial revolution, in which power was revolutionized using electric power and motors. Now, the 4th industrial revolution is strongly expected with the background of a shift to the variety and variable production type (i.e., mass customization), accompanied by diversified needs and shortened product lifecycle [9]. It aims to optimize

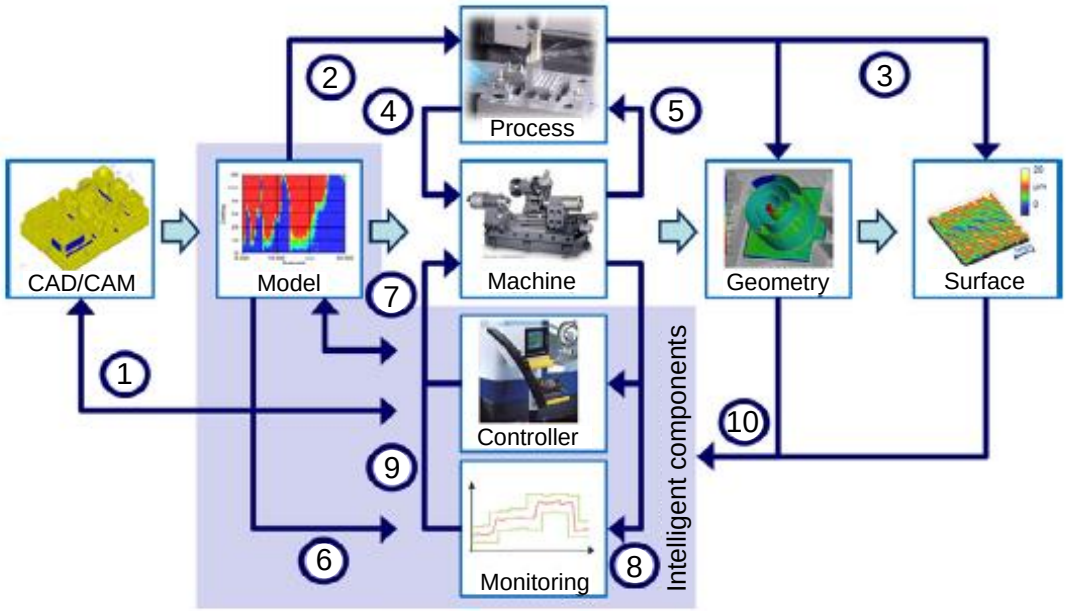

Fig. 1-1 Self-optimizing machining systems [10] (The figure is used with permission from Elsevier.)

the entire production/manufacturing process to enhance its reliability, efficiency, and flexibility by completely using sensor network technologies, denoted as "Internet of Things (IoT)" and virtual digital tools/simulations. An effective use of sophisticated signal processing techniques, including artificial intelligence (AI) and machine learning (ML), is also expected. This concept is currently summarized by the term "Industry 4.0," which was first launched by Germany in 2011. Since then, some other concepts have also been launched in other countries, such as "Industrial Internet" by the United States (2012), "Manufacturing Industry Innovation 3.0" by South Korea (2014), "Made in China 2025" by China (2015), and "Connected Industries" by Japan (2017). The efforts made for transforming the manufacturing system are being promoted and accelerated worldwide.

In the machine tools field, the concept of a highly intelligent system, denoted as "self-optimizing machining system (SOMS)," has emerged to satisfy the above demands. In SOMS, the manufacturing tasks, ranging from the process design to the part inspection, are seamlessly and circularly connected by rich process-related data with or without involving the virtual models and simulations (Fig. 1-1 [10]). Coupling the physical and virtual entities is known as the "cyber-physical system" [11,12] or "digital twin" [13]. Alternatively, using reduced-order mathematical models with only sufficient fidelity, instead of full-dimensional virtual entities such as finite element (FE) model, is called "digital shadow" [14].

SOMS aims to flexibly adapt to the ever-changing manufacturing circumstance and constantly optimize the control strategies/settings for process–machine interaction. In the

most ideal case, this should be done autonomously. According to [10], SOMS comprises the following 10 functionalities (Fig. 1-1).

① Trajectory planning (CAD/CAM) considering characteristics of process, machine, and controller

The first manufacturing task is to define the process kinematics and tool paths, as well as machining parameters and process-related conditions, by using CAD/CAM systems. In addition, trajectory generation from the NC code through real-time interpolation and filtering in the CNC system is included. However, the functions of these systems are independent of each other in the modern manufacturing system. Additionally, these functionalities do not account for the machine tool dynamics. An open and high-level interconnection among CAD/CAM, CNC, and machine-tool dynamics is required. Recently, Sudo and Aoyama proposed an integrated CNC system platform to interoperate the characteristic information belonging to CAD, CAM, NC, operator, and machine through a shared database for realizing accurate machining (Fig. 1-2) [15]. Sencer et al. [16–19] proposed several methods for shaping reference motion trajectories to avoid unwanted inertial vibration while considering the machine structural dynamics. Additionally, Dumanli and Sencer [20,21] proposed a novel method in which the reference trajectory was modified based on a data-driven model of the feed drive system, to achieve perfect tracking.

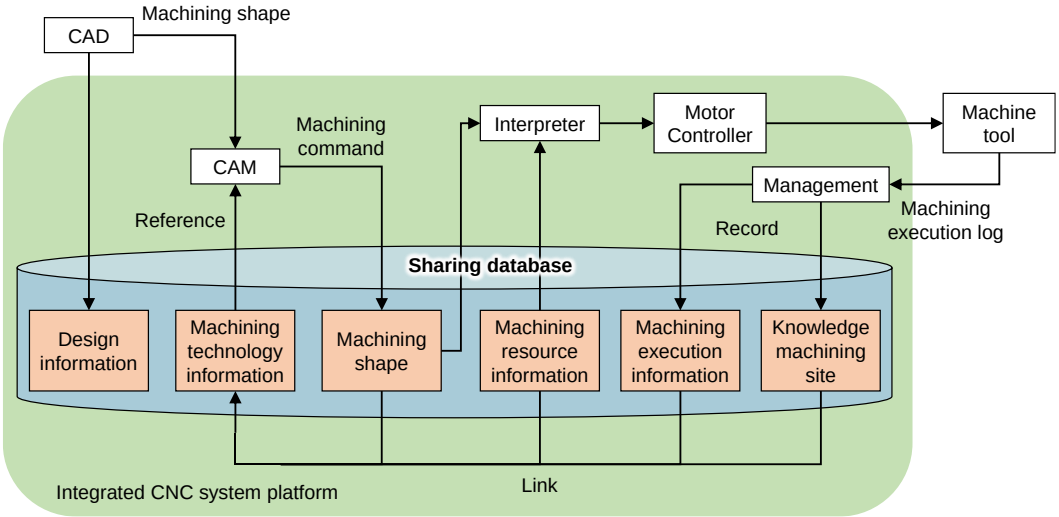

Fig. 1-2 Integrated CNC system platform [15] (The figure is used with permission from Japan Society of Mechanical Engineers.)

② Couple simulation of process–machine interactions (considering models of process, machine, and/or controller)

The process simulation considering process–machine interaction, known as virtual machining technology, is also essential [22,23]. The simulated results should be fed

back to the process design step. The most typical enabling technology is stable process planning by utilizing the stability lobe diagram (SLD) [24,25], which is comprehensively described in subsection 1.4.1. To compute SLD and simulate the process, commercial software systems (e.g., CUTPRO®) have been developed.

③ Prediction of machining results (geometry and surface resulting from process-machine-controller interactions according to process planning designed by CAD/CAM)

The total inspection of machined parts using a virtual model is summarized as "virtual meteorology" (Fig. 1-3 [26]), which is highly expected to realize a total inspection and zero-defect production system [27]. The surface topography is simulated by calculating the cutter-workpiece engagement (CWE) while integrally coupling various information such as the sensor/servo data, FE analysis (FEA), and mathematical model of process-machine interactions [26,28]. Here, the calculation time is not a trivial problem to achieve online virtual inspection in real time or semi-real time. In this case, the digital shadow approach, which constructs an essential mathematical model, is a practical solution [29].

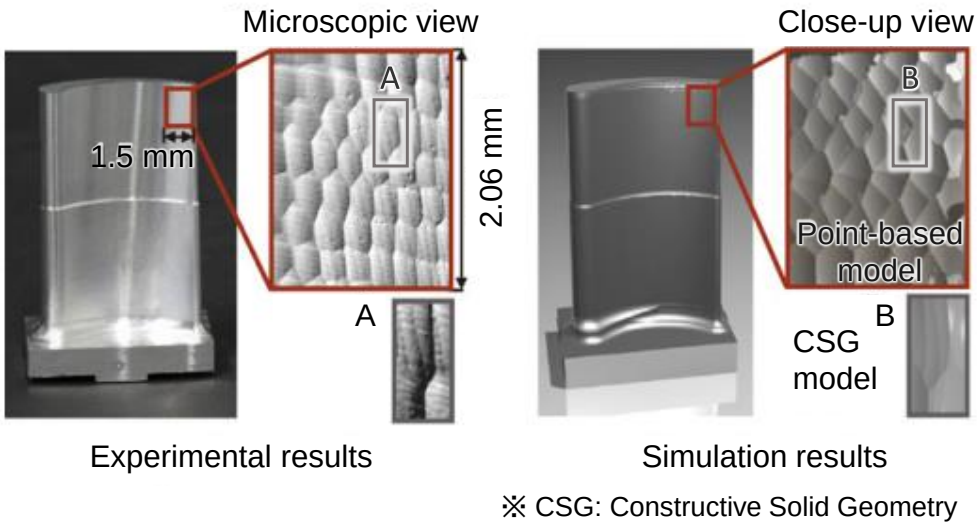

Fig. 1-3 Measured and simulated surface structures in a chattering process [26] (The figure is used with permission from Elsevier.)

④ Multi-physical monitoring (sensor-based process and machine-condition monitoring)

This part represents process and condition monitoring by using single- or multiple sensors. Fujishima et al. [30] developed a conceptual sensory machine tool that can acquire a huge volume of sensing data into the NC or programmable logic controller (PLC) through the developed interface boards and Ethernet (Fig. 1-4). Möhring et al. [31] also developed a sensory machine tool equipped with sensing fixture and an adaptive sensory milling spindle. Additionally, Möhring and his colleague developed a state monitoring system for the wear of a ball screw by measuring the preload of a double nut using a thin film-like sensor [32].

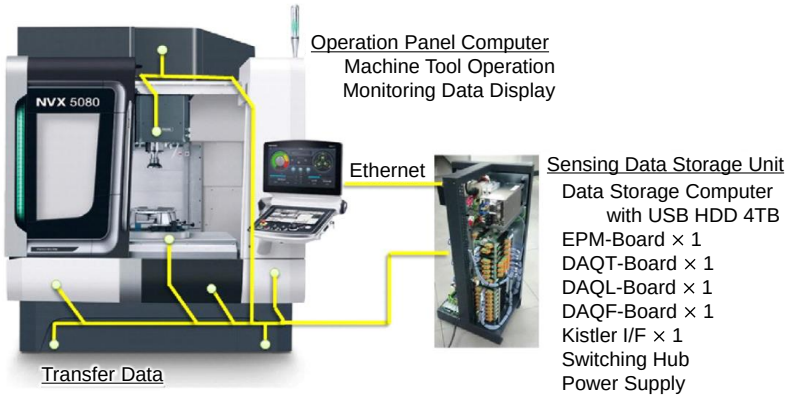

Sensor	Num.	Purpose
Acceleration	6	Spindle and table *x y z* directions
Coolant level	2	Level sensor for coolant tank
Load cell	8	Level adjustment
Electric current	1	Three-phase power supply
Voltage	1	Three-phase power supply
Temperature	3	Spindle and table
Cutting force	3	Kistler dynamometer in *x y z* directions

Fig. 1-4 Sensory machine tool with sensing data storage system [30] (The figure is used with permission from Elsevier.)

⑤ Autonomous adaptronic machine components (including actuators with monitoring and control functions to directly influence the process-machine interactions)

Intelligent components integrating an actuator with the control function, as well as monitoring and signal processing functions, can directly influence the machine or machining process state. A piezoelectric actuator is the most frequently used tool in this filed for various objectives/applications, such as vibration-assisted machining for difficult-to-cut materials [6], vibration damping including chatter [33–35], and compensation of tool deflection [31]. Especially, the functions of a piezoactuator are often integrated in a spindle as an intelligent spindle unit [36,37]. The mechatronics technologies for machine tools are also summarized in [38].

⑥ Model-based teach-less monitoring and its recalibration (digital-twin/digital-shadow process and machine-condition monitoring)

In model-based teach-less monitoring techniques, the reference information of the processes is generated/parameterized in a virtual simulator, and can be utilized to determine the threshold for certain decision-making without trial-and-error and/or extracting high-value process information from the sensor signals (Fig. 1-5) [39]. Therefore, it is expected to realize highly flexible adaptation for mass customization. As an exemplary application, Altintas and Aslan [40] detected tool breakage by comparing the cutting torque estimated in real time from the motor current with that simulated based on the process model and CWE at each tool position. Consequently,

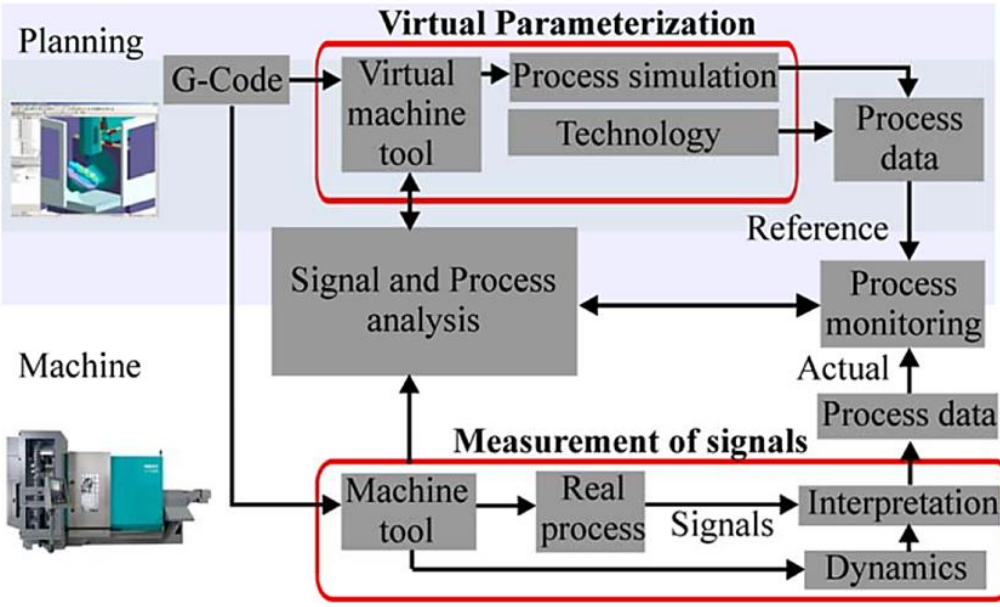

Fig. 1-5 Concept of model-based teach-less process monitoring [39] (The figure is used with permission from Elsevier.)

the tool breakage was robustly detected under the adaptive threshold determined by referring to the simulation result. Nouri et al. [41] converted the measured cutting force signals into the dimensions of the cutting force coefficient using the mechanistic milling model and nominal CWE during the process. As the cutting coefficients are normalized parameters, tool wear monitoring was realized independent of the cutting conditions. Note that the accurate derivation of CWE along the tool path is a key part, as only the abnormal tool states need to be separated from the natural signal variation due to CWE variation [10].

To ensure the integrity of the monitoring system, deterioration detection and recalibration of the simulator or sensor system is also essential. In [31], a procedure was developed to calibrate the sensory fixture system by comparing it to the force sensor signal integrated into the spindle. To address the variation in the environment and/or system state, Putz et al. [42] showed how a self-adaptive monitoring system can be realized by detecting whether the system is in equilibrium.

⑦ Machine simulation including mechanical, thermal, and control behaviors

The virtual machine tool technology configured by a full FE model or a rigid and flexible multi-body model reduced from the FE model can be utilized for not only developing a new machine tool in the design phase but also optimizing the machining process by evaluating it in a computer simulation environment. In particular, a multi-body model comprising rigid links connected through flexible springs allows the virtual assessment of the interaction between a specific CNC control model and

machine tool structure, as well as the modification of control parameters based on the simulation [43,44]. Moreover, the virtual machine tool can be integrated into the numerical cutting process simulation (i.e., simulation of process–machine interactions in ②) and improve its fidelity [45].

⑧ Control-integrated monitoring (based on servo information inside CNC controller)

The most basic representation of this part is the process/condition monitoring performed using the internal information acquired in the CNC of machine tools, such as motor torque, stage position response obtained by the linear encoder, and the motor angle response obtained from the rotary encoder. The motors and encoders are usually installed relatively far from the cutting point. Nevertheless, the internal information still contains rich information regarding the process over a wide frequency band; hence, it is also important to use this information effectively. Many previous studies have proved that the internal information can be effectively used to detect abnormal process states, such as tool wear [46–49], tool breakage [40,50–52], and even high-frequency chatter vibration [53–55].

⑨ Process control (changing process parameters provided by CNC controller)

To realize SOMS, process-control parameters, such as feed rate [40,56–58], stage position [59], tool posture [60], and spindle speed [61], must be modified adaptively in conjunction with the process monitoring system. Besides the process monitoring system, the adaptive process control system may also involve a specific process model for establishing the optimal control strategy. Process control especially focusing on chatter is presented in section 1.4

⑩ Feedback of workpiece quality data (for calibrating the 3rd functions)

The machined surface appears as the final output for all system inputs related to the machining process. In ultimate ideal cases, the intelligent components of SOMS are self-adaptively modified/calibrated by learning the input–output relation of the machining system, and consequently, the desired machined surface can be obtained even in the different machining parts and materials. The developed on-machine and in-process surface metrologies can be used as enabling technologies, which are summarized in [62].

More detailed description and enabling technologies are summarized in [10]. SOMS covers a very wide range of components, and several enabling technologies have been developed, especially in the last two decades. Nevertheless, an intensive implementation and combination of each functionality is not state of the art in the industry and requires further research and development [10].

This dissertation is oriented to SOMS for chatter vibration, and especially addresses the 8th and 9th functionalities presented in Fig. 1-1. For chatter monitoring, a sensorless cutting force estimation technique, only composed of the internal information of machine tools, is employed, and a novel detection algorithm is proposed. Additionally, chatter control strategies are proposed in turning/boring, parallel turning, and parallel milling processes based on the corresponding chatter models constructed considering the process–machine interaction. The only prerequisite for all proposed chatter suppression systems is measurement of the chatter frequency, and no additional actuators are required for chatter control. This chapter first reviews the existing chatter monitoring and avoidance/suppression techniques, and then, presents the aim of the dissertation.

1.2. Basic comprehension of chatter in machining

Chatter vibration in machining processes, resulting in low surface/shape quality, catastrophic tool/machine damage, and limited machining efficiency, is a classical problem first raised in the research field in the late 1950s. Even today, it remains a significant issue in the manufacturing sector, as evidenced from the increasing publications on chatter, and poses a more serious issue when considered in conjunction with the recent trends of highly efficient and/or flexible-parts manufacturing as well as lightweight machine structures required for energy-saving [63–65].

The abnormal vibration in machining processes is roughly classified into forced vibration and (self-excited) chatter vibration. Forced vibration is further divided into force disturbance type and displacement disturbance type. Additionally, the self-excited chatter vibration can be classified into regenerative type and mode coupling type (Table 1-1 [66,67]).

Table 1-1 Abnormal vibration in machining processes [66,67]

Vibration	Type	Factor
Chatter	Regenerative chatter	Regenerative effect caused by previous vibration left on the machined surface
	Mode coupling chatter	Coupling of multi-directional vibrations
Forced	Force disturbance (Process-related)	Intermittent cutting, serrated chip, etc.
	Displacement disturbance (Non-process-related)	Bearing, gears, motor cogging, rotor imbalance, jerk of machine tool, air/oil pressure fluctuation, floor vibration, etc.

The displacement disturbance-type forced vibration is generated by the vibrations from motors, gears, bearings, and floors, and does not depend on the machining process. Therefore, it cannot be avoided by changing the tools and machining conditions. The basic

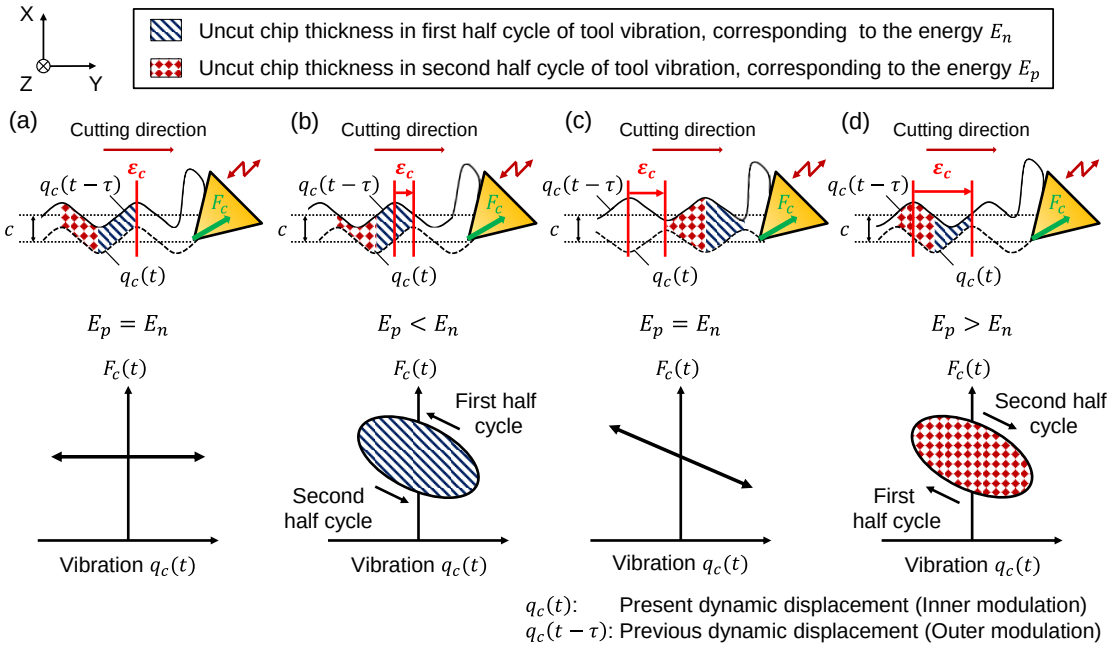

Fig. 1-6 Schematic of basic mechanism of regenerative chatter vibration: (a) $\varepsilon_c = 0, 2\pi$, (b) $0 < \varepsilon_c < \pi$, (c) $\varepsilon_c = \pi$, (d) $\pi < \varepsilon_c < 2\pi$.

countermeasures are isolating/suppressing the vibration source or improving the machine's dynamic rigidity and/or damping. In contrast, the force disturbance type is process-dependent; hence it is important to optimize the machining conditions. For instance, in case of intermittent cutting, such as milling, a periodic cutting force fluctuation composed of a tooth-passing frequency and its harmonics excites the machine as a disturbance. When this synchronizes with the resonance frequency of the machine, a large vibration develops as forced vibration. Therefore, the spindle speed should be shifted so that an integer multiple of the tooth-passing frequency does not synchronize with the resonance frequency.

Self-excited chatter vibration is an instable phenomenon in which vibration develops due to the transfer characteristics of the cutting process and machine structure (i.e., process–machine interaction), even though there is no forced vibration source.

Fig. 1-6 shows the mechanism of regenerative chatter vibration. In this figure, it is assumed that the tool flexibly vibrates in a particular vibration. The present tool vibration (i.e., inner modulation) is transcribed to the workpiece by the machining process, which will cause variation in the uncut chip thickness in the consecutive cut (i.e., regeneration as a previous vibration denoted as outer modulation). Consequently, the fluctuation in the cutting force generated by the fluctuated uncut chip thickness excites the machine tools again, and its present vibration is also transcribed to the workpiece. This process-inherent closed-loop phenomenon is well-known as the regenerative effect, and the process becomes unstable when its closed loop is in an unstable condition.

Some researchers [68–73] have discussed the regenerative chatter mechanism from the

viewpoint of the energy cycle flow according to the chatter vibration cycle, which is also depicted in Fig. 1-6. For destabilization of the machining process, the phase shift between the present and previous vibrations, ε_c [rad], is a key factor. Because the resultant cutting force applied on the tool, $F_c(t)$ [N], always acts on the tool in positive direction, the direction of mechanical work that the tool receives from the cutting force is switched according to the tool's vibration cycle. In the first half vibration cycle where the tool cuts into the workpiece, the negative work acts on the tool, which yields the amount of energy, E_n [J], dissipated through the cutting process. In contrast, the tool receives positive energy, E_p [J], in the second half vibration cycle, where the tool retracts from the workpiece.

In case that the phase shift is zero or 2π (Fig. 1-6(a)), the uncut chip thicknesses in the first and second half vibration cycles are the same; hence, the inflow and consumed energies are the same and the total energy balance in a vibration cycle becomes zero. This is a critical energy stable state. However, this condition is stable because the uncut chip thickness is ideally constant, and the machine is not excited. The case of $0 < \varepsilon_c < \pi$ (Fig. 1-6(b)) is also highly stable as the consumed energy is larger than the inflow energy, and therefore, the vibration is damped out during the cycle, although the machine is excited by the fluctuation in the uncut chip thickness. In case of $\varepsilon_c = \pi$ (Fig. 1-6(c)), the energy cycle is in a critical state where the total energy in the cutter-workpiece system (CWS) is not transferred during the vibration cycle. However, the largest fluctuation in the uncut chip thickness, shown in Fig. 1-6(c), may cause a large vibration and an unstable process as the generated vibration does not decay. The final case of $\pi < \varepsilon_c < 2\pi$ (Fig. 1-6(d)) is an unstable energy condition, because of $E_p > E_n$, whose difference flows into the flexible CWS every vibration cycle. As a result, the mechanical vibration (i.e., regenerative chatter) will develop to divert the net inflow energy, E_f [J], if it exceeds the inherent damping capacity of CWS, as follows [70]:

$$E_f = E_p - E_n > E_d \tag{1-1}$$

where E_d [J] is the amount of energy the machine can absorb in a cycle. From the above, the energy stability of CWS depends on the phase shift, and the unstable phase shift range can be defined as follows:

$$\pi < \varepsilon_c < 2\pi \tag{1-2}$$

which can also be derived from the general stability analysis [24,25]. Almost all machining processes involving rotary motion can be destabilized due to the regenerative effect.

The mode coupling chatter is an unstable phenomenon peculiar to the rotating tools. In a rotary tool, the direction of the cutting force changes depending on the rotational position of the cutting edge. Consequently, instability can occur due to the coupling of vibrations in multiple directions and cutting force fluctuations (Fig. 1-7). Especially in the end milling process, the flexural vibration of the shaft has similar vibration modes in two orthogonal

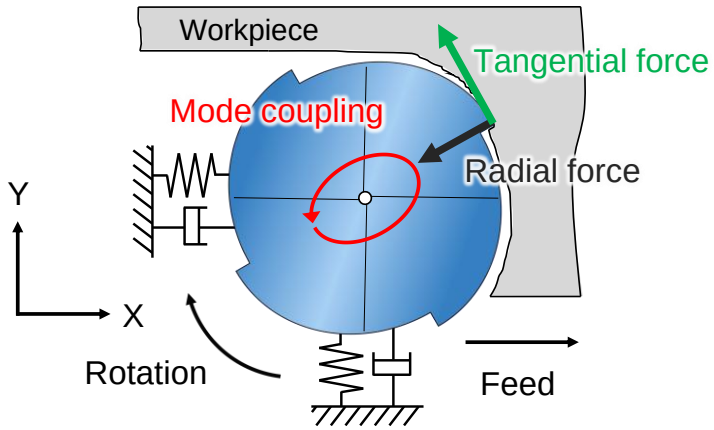

Fig. 1-7 Mode coupling caused by multi-directional vibration mode

directions, and the effect of mode coupling increases when the resonance frequencies match and the cutting forces act in both directions (e.g., slotting). As the mode coupling effect occurs due to the cutting force fluctuations caused by the regenerative effect, both effects simultaneously influence the self-excited chatter onset [67]. Note that it is important to address and avoid all types of the self-excited chatter and forced vibration in an actual production site [74].

1.3. Chatter monitoring techniques

Considering that predictive maintenance and process optimization are performed based on the machine status diagnosis results, it can be stated that condition/process monitoring is the core technology for SOMS. To construct a highly reliable monitoring system, it is important to use appropriate sensors according to the purpose. From this first perspective, chatter monitoring techniques are summarized in subsection 1.3.1.

However, clear process information cannot be obtained in usual cases by simply acquiring the sensor information. It is necessary to perform some data processing and extract the feature quantities or patterns that have strong correlations with the machining state to be monitored. In summary, "data/signal processing" is the second important viewpoint to extract high-value information that cannot be obtained from simple sensor usage. The signal processing techniques for chatter monitoring are summarized in subsection 1.3.2.

1.3.1. Sensor signal selection

Tool condition monitoring (TCM) can be roughly divided into “direct measurement” and “indirect measurement” depending on the sensor used [75]. In the direct method, state changes in the tool shape due to tool wear/breakage, as well as deflection and vibration of

Table 1-2 Physical quantities and sensors for indirect measurement

Physical quantity	Sensor
Cutting force (Torque)	Piezoelectric dynamometer
Tension	Load cell
Temperature	Thermocouple
Vibration	Accelerometer
Sound	Microphone
Acoustic emission	AE sensor

Table 1-3 Characteristics of major sensors for indirect process monitoring

	Dynamometer	AE sensor	Accelerometer	Microphone
Typical frequency range of sensor signal	~5 kHz (size dependent [83])	From 10 kHz to 10 MHz [82]	~10 kHz	From 20 Hz to 20 kHz [83]
Cost	★★★	★★	★★	★
Sensitivity/SN ratio (Reliability)	★★★	★★★	★★	★
Compatibility with machining space	★	★★	★★	★★★
Robustness to sensor-location variation	★★★	★	★	★★

*** High, ** Middle, * Low

Table 1-4 Application of indirect measurement with respect to process monitoring

Application \ Sensor	Dynamometer	Accelerometer	AE sensor	Microphone
Chatter detection	★★★	★★	★	★★★
Tool-breakage detection	★★★	★★	★★★	★★
Tool-wear diagnosis	★★★	★★	★★	★
Part-quality prediction	★★★	★★★	★	★

*** Very effective, ** Effective, * Not effective

the tool tip, are directly detected using sensors such as a vision sensor [76–79] and laser displacement sensor [80,81]. Therefore, the tool status can be monitored with high accuracy. However, these measuring units are generally expensive and difficult to install in the machining space; hence, the indirect method is generally used for real-time TCM.

In the indirect method, the tool state is indirectly estimated from physical quantity data, such as cutting force, vibration, and sound. Table 1-2 shows the measured physical quantities and main sensors used in the indirect method. Additionally, the features of each sensor and its application to process monitoring are summarized in Table 1-3 and Table 1-4 with reference to [75,82,83], in terms of the cutting force, vibration, sound, and AE that are frequently used. The detailed aspects of each physical quantity measurement in process monitoring are summarized below.

Measurement of AE signals:

The tool state, such as tool wear, can be estimated by measuring the elastic wave generated when the material is deformed and sheared at the contact between the tool and workpiece during machining. The frequency band of the AE signal typically ranges from 10 kHz to 10 MHz, which is extremely higher than the process force and environmental noise. Therefore, the AE signal has very high sensitivity and responsiveness, and is known to be effective for detecting instantaneous phenomena, such as tool breakage and contact [82,84]. In addition, as the AE sensor is relatively low cost and highly reliable, it can also be used to enhance the reliability of the process monitoring system by being combined with various sensors [82,85]. Note that it is necessary to focus on the sensor placement and signal overrange by carefully considering the elastic wave transmission path [82]. For chatter detection, Chiou et al. [86] monitored the chatter vibration based on the root mean square (RMS) value of the AE signal and acceleration sensor information in the turning process. However, chatter monitoring using AE signals has been rarely reported.

Measurement of machining sounds:

Delio et al. [87] compared the chatter detection performance in a dynamometer, accelerometer, and microphone in the end-milling process. They concluded that the microphone is most suitable for chatter detection because of its sufficient signal bandwidth and sensitivity. As microphones are inexpensive and do not disturb the machining space due to non-contact measurement, they have been extensively used in chatter monitoring and avoidance applications [63]. However, they have little reliability in a low-frequency region, where the influence of environmental noise cannot be ignored. Therefore, microphones are rarely used at the production site where environmental noise is large, although they are often used at the research level [63,87]. It is important to eliminate or reduce the environmental noise through signal processing, when using a microphone.

Measurement of vibration:

Accelerometers are commonly used in vibration measurement and are extremely easy to handle. Their miniaturization and cost reduction have been progressing due to the development of MEMS technologies. Therefore, they are frequently used for chatter monitoring. Li et al. [88] detected chatter vibrations during the turning process by using a coherence function between two acceleration sensors mounted orthogonally on the tool. Lamraoui et al. [89] performed early chatter detection in the end-milling process based on the acceleration signals transformed into the angular domain through synchronization with the rotary-encoder information of the spindle. When using acceleration sensors, sufficient attention must be paid to process-unrelated vibrations from the floor and rotating parts (e.g., spindle), vibration damping due to mechanical components, and little reliability in the low-frequency range [63,82].

Measurement of cutting force:

As shown in Table 1-4, the cutting force is strongly related to all tool conditions, and a piezoelectric (table) dynamometer, which is a de-facto standard for sufficient bandwidth and accuracy [90], is most frequently used in TCM research [82]. Tlusty et al. [91] stated that cutting force is the most suitable index for chatter monitoring because it is deeply linked to the mutual vibration between the tool and workpiece. Kuljanica et al. [92] compared the signals generated from a rotating cutting-force dynamometer (RCD), an accelerometer mounted on the spindle side, and an AE sensor mounted on the workpiece side. They also obtained similar conclusions. However, the table dynamometer is still expensive and incurs large interference with the machining space. It is also necessary to focus on the thermal drift and signal overrange. Although the interference with the machining space can be minimized using a spindle-integrated force sensor [93–95] or RCD with a wireless data-transfer system [96], the cost will increase beyond that of the ordinal table dynamometer. In addition, it might be necessary to design a spindle system for sensor integration. As a result, dynamometers have not been widely applied to the shop floor from the perspectives of cost, failure frequency, thermal stability, and compatibility with the workspace. Some studies have mentioned that the use of an acceleration sensor is the most preferable when considering the practical viewpoints such as sensor cost [97].

So far, many chatter detection methods using various sensors have been proposed. Note that the method of incorporating a sensor's signal into the control system of a machine tool is also important to acquire variables at a high sampling rate for wideband process monitoring. Simultaneously, a high-capacity storage system is required to utilize the process data, whose size and variety are dynamically increasing due to IoT [9]. In a machine tool, I/O signal lines are frequently connected to the PLC, which commonly performs in the millisecond range and is not suitable for acquiring analog signals at a high sampling rate. Additionally, several machine tool manufacturers adopt an NC system provided by NC manufacturers on behalf of an in-house developed NC system [30]. Accessibility to sensor signals is usually limited by NC manufacturers, which makes it difficult to incorporate the acquired signals into the control system of machine tools.

Besides the above limitations, the use of external sensors inevitably causes problems such as an increase in failure rates and installation/maintenance costs and interference with the machining space. Therefore, several studies have attempted to detect chatter vibrations only from the internal information of machine tools [53–55,98]. Soloman et al. [98] detected chatter vibration based on the variation in the R value (the ratio of RMS values of the static and dynamic components). The R value was calculated from the cutting force estimated by the motor current response and the transfer characteristics of the spindle system. Aslan and Altintas [53] also detected chatter based on the frequency spectrum of a

reference spindle motor current. Kakinuma et al. [54] and Koike et al. [55] constructed a wide-band and type-assorted chatter monitoring system by digitally filtering the cutting torque estimated by a disturbance observer (DOB [99]), which integrates the angle information of the rotary encoder and the spindle motor current. An external sensorless process monitoring that uses internal information of machine tools (i.e., encoder information and motor current) is a sustainable approach, as it does not yield any adverse effect, such as additional costs or constraint of the machining space. Another major advantage is that the process monitoring system can be constructed as an add-on to existing machine tools.

1.3.2. Signal processing for chatter monitoring

The signal processing for process monitoring can be classified into three approaches: signal-, AI/ML-, and model-based approaches [29]. Model-based approaches are currently represented as the term "digital twin" or "digital shadow" (the 6th functions for SOMS). For real-time chatter monitoring/detection, the classical signal-based approaches are commonly employed, although AI/ML-based approaches have appeared recently [100–102]. In the signal-based approach, chatter vibration is indirectly detected based on sensory characteristic features (SCFs), such as the maximum peak [53,87,103], RMS [86,98], variance (or standard deviation) [55,97,104–106], correlation [81,88], singular value entropy [107], energy entropy/ratio [108–113], and/or other statistical indicators [114]. SCFs are extracted in time domain [55,86,97,98,104,107,108], frequency domain using Fourier transform [53,87,103], or time–frequency domain using short-time Fourier transform (STFT) [110,114,115], wavelet transform (WT) including wavelet packet decomposition [105,106], or mode decomposition techniques [109,111–113].

Signal-based chatter detection in time domain:

Soliman et al. [98] demonstrated that the index calculated from the RMS value of the cutting torque reconstructed from the spindle motor current can be utilized for chatter monitoring. Yeh and Lai [104] detected the chatter based on the time transition of the standard deviation extracted from the measured cutting force in the peripheral turning of a slender workpiece. In addition, van Dijk et al. [97] detected chatter in a high-speed milling process by setting a threshold on the variance in the acceleration signals measured at the spindle. Recently, Koike et al. [55] proposed an assorted chatter-detection method by combining the moving variance (MV) and moving Fourier transform (MFT) modified using sliding discrete Fourier transform (SDFT) algorithms [116]. The SDFT and MFT algorithms can analyze a specific frequency with low calculation costs independent of the sample number of the analyzed data (i.e., $O(1)$); hence, they are useful when the desired analysis frequency is accurately known in advance. In [55], the power spectrum density (PSD) of

forced vibrations was calculated by MFT, because forced vibrations are mostly excited at the tooth-passing frequency and its harmonics, which can be calculated from the cutting conditions. The self-excited chatter was detected by subtracting PSD of the forced vibration from the total PSD calculated by MV. Generally, time-domain methods are suitable for real-time calculation (i.e., real-time monitoring and fast detection) because of the low computational load and simple algorithm.

However, the chatter frequency cannot be deduced directly in usual cases, although a few studies have estimated the chatter frequency as with the chatter detection [81,108]. Additionally, the threshold for decision-making is often determined experimentally and empirically through trial and error, as SCFs, such as variance (standard deviation), largely fluctuate under the experimental conditions [117]. One of the solutions is to draw a limit curve by referring to the signal in the first part of the batch where the conditions are assumed to be ideal. However, it is not suitable for a recent single/small batch production system, although it may be sufficient for mass production; hence, setting a robust and optimal threshold over the changes in the machining conditions and environment remains a practical challenge [10].

Signal-based chatter detection in frequency domain:

Delio et al. [87] and Altintas et al. [103] analyzed the fast Fourier transform (FFT) of the cutting sounds acquired by a microphone and determined that it was chatter vibration when the maximum peak value of the frequency spectra exceeded a certain threshold. Aslan and Altintas [53] also imposed an empirical threshold to the magnitude ratio of the highest peak in the comb-filtered DFT of a spindle drive motor current command and the tooth-passing spectrum in an unfiltered signal. Li et al. [88] detected chatter vibration by using the spectral coherence between two acceleration sensor signals. The greatest advantage of chatter detection in the frequency domain is that the chatter frequency can be acquired simultaneously.

However, FFT analysis is usually unsuitable for real-time fast chatter detection, as its calculation order is $O(N_w \log(N_w))$ where N_w $[-]$ is the number of data samples; hence, the required computation cost rapidly increases with the number of samples of the analyzed cutting data [104]. Due to the recent increase in the PC processing capabilities, there are now opportunities for real-time chatter monitoring by using STFT, where FFT is performed by sequentially sliding the small analysis window. Nevertheless, it remains problematic, especially when processing at a high speed in a servo/phase cycle of machine tools and quickly detecting chatter without lowering the frequency resolution [55]. Additionally, the setting of the threshold is a practical issue as in the time-domain methods, considering that the sum of PSDs at all frequencies, except for the DC component, coincides with the variance in the time domain [117].

Signal-based chatter detection in time–frequency domain:

Yoon and Chin [105] applied the discrete wavelet transform to the measured cutting force and detected chatter vibration from the standard-deviation ratio of the wavelet coefficient. Berger et al. [106] also used the discrete wavelet coefficient of the measured cutting force to calculate the mean absolute deviation for chatter detection. WT excels in the analysis of non-stationary signals and can capture the state changes with high sensitivity, as the signal characteristics are localized according to the frequency bands [100]. In addition, the calculation order is $O(N_w)$, which is smaller than that of FFT. Therefore, it is said to be more suitable for chatter monitoring than STFT [63,118]. Comprehensive techniques of WT for process monitoring are summarized in [75]. Furthermore, newly developed time-frequency domain methods, such as ensemble empirical mode decomposition [113] and variation mode decomposition [109,111,112], have also been applied to chatter detection. However, there is no theoretical principle for selecting a suitable wavelet base function and decomposition levels, which significantly influence the analysis results [107,112]. Additionally, the question of how to determine a robust threshold for discriminating the chatter onset remains unanswered, even with WT or other time-frequency domain methods [63].

AI/ML-based chatter detection:

To robustly classify the chatter state under different machining conditions, AI/ML approaches have been employed for the classification problem of the extracted SCFs. Yao et al. [100] recognized the chatter conditions in the boring process by using a least-square support vector machine, and Lamraoui et al. [101] used a neural network for milling chatter detection. In [102], transfer learning was applied to enhance the performance of classifiers with different machining configurations. Note that the key for all AI/ML approaches is to sufficiently train high-quality SCFs that are strongly related to the targeted applications. As the configuration of AI/ML and training data must be carefully considered and prepared, the AI/ML approach generally requires much more labor than simple signal-based methods.

Note that the sensor and SCF fusion is also an important aspect for realizing reliable TCM systems [92,119,120]. More information on TCM methods, including chatter monitoring, is available in the literature [63,65,75,82,83,91,118,121,122].

1.4. Chatter avoidance/suppression techniques

1.4.1. Planning stable process based on stability lobe diagram

To preliminarily avoid chatter vibration, SLD is used, where the critical cutting depth of a tool with respect to the spindle speed is determined based on the machine dynamics

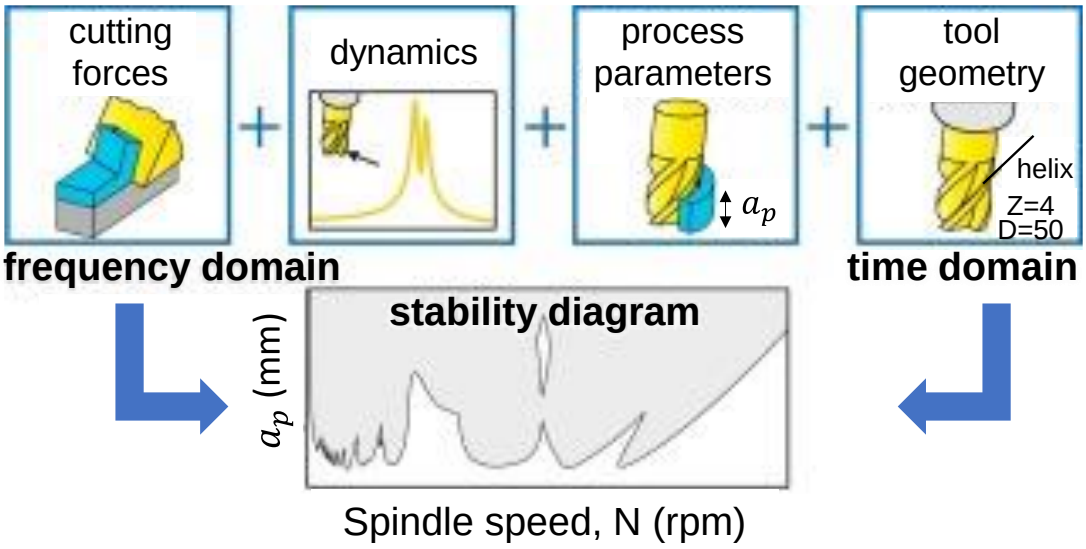

Fig. 1-8 Procedure to obtain SLD [64] (The figure is used with permission from Elsevier.)

(frequency response function, FRF) and cutting process model (Fig. 1-8 [64]).

SLD has a long history, and was first proposed scientifically by Tobias and Fishwick [123] and Tlusty and Polacek [124] at almost the same time during 1950–1960s. They derived the basic stability law between the machine dynamic stiffness and a material's cutting force coefficient in the orthogonal turning process. In particular, Tobias and Fishwick [123] indicated the effect of spindle speed on stability (stability pocket or "lobes") due to the regenerative time delay. Then, Altintas and Budak [125] developed a systematic frequency-domain methodology for stability prediction in the milling process under the assumption of a single dominant frequency (i.e., zeroth-order approximation, ZOA). As ZOA assumes a single chatter frequency, its prediction accuracy is known to deteriorate under low radial immersion, where multiple harmonics of chatter often occur. A general formulation for milling stability in the frequency domain that can consider multiple chatter frequencies has been proposed (i.e., multi-frequency method) [126–128]. Besides the frequency-domain method, various other methods, such as semi-discretization method [129–131], Floquet theory method [132], and full-discretization method [133,134], have been proposed for stability analysis.

To accommodate various machining processes, the stability analyses for specific tools and processes, such as ball end milling [135], serrated tool [136], variable helix tool [137–139], variable pitch tool [140–144], asymmetric dynamics tool [145,146], plunge milling [147], and spindle speed variation [132,148–153], have been performed. Sustained efforts are also being made to develop an authentic process model and a more accurate SLD by accounting for the nonlinearity, such as the interrupted regenerative effect at CWS [154–157] and the ploughing effect including process damping and friction chatter [158–161].

With the advent of multi-tasking machine tools, such as mill-turn center, stability analysis for simultaneous processes with plural tools, such as parallel turning, parallel milling, and turn milling, has also been developed. For the parallel turning process, Budak et al. [162,163] conducted an encompass stability analysis for a general multi-dimensional model of CWS. They analyzed various process stabilities in parallel turning, such as the chatter onset at the tool/workpiece side and the cutting of a shared/different surface. Budak and his colleagues [164] also demonstrated the stability analysis in the parallel milling process and Brecher et al. [165] investigated the holistic machine interaction in parallel milling. Recently, chatter stability in a more complicated turn-milling process [166,167] and robot machining [168] has been analyzed.

Considerable research has been conducted for stability analysis in various machining processes, as described in the literature [24,25,169]. This research direction is essential for not only planning a stable process but also comprehending the phenomenon and the behavior of process stability. However, the SLD approach generally requires time-consuming preliminary tests to accurately identify the machine dynamics and process parameters of CWS. This drawback will become increasingly evident in complex simultaneous processes because it requires the consideration of multiple parameters. In addition, SLD is sensitive to changes in FRFs and excited mode shapes due to the axis position of the machine tool [170], spindle rotation/speed [171,172], cutting points [164,173], and material removal [174,175]. It is known that the FRF identified by an offline method, such as a tap test, is different from that identified under an actual machining condition [176] and often results in the prediction error of SLD. Ensuring reliable stability prediction is still challenging in academia and industry.

To address this issue, considerable efforts have been made, such as in-process identification of machine/workpiece dynamics to track the variation in FRF [177,178], probabilistic chatter prediction considering uncertainty [179,180], creating SLD based on the actual cutting experiments/database [30,181–185], and conducting hardware-in-the-loop test (semi-virtual machining) for process analysis [186,187]. In particular, the stability prediction based on the actual machining results (i.e., database) is expected to become more effective in the future, in conjunction with various accumulating sensors' information in various machining situations through IoT, penetration of AI/ML into production systems, and further improvement in computer performance.

1.4.2. Enhancing machine-inherent stabilizing capacity

Improvements in the inherent stabilizing capacity of machine tools by altering the dynamic stiffness, system damping, and machine assembly have also been extensively studied, which can be classified into passive and active damping with or without additional actuators [118,188].

In passive damping techniques, a tuned mass damper (TMD) is the most commonly used. In TMD, one or more additional masses are attached to the structure of interest to absorb the vibrations [189,190]. As an alternative to the common linear TMD, a nonlinear TMD has also been proposed [191], where the damping performance was further improved by an additional element of elastic support dry (Coulomb) friction exhibiting hysteretic damping mechanism of the sliding friction. To obtain effective damping capability by TMD, it must be designed optimally over the resonance peak of interest. However, as indicated in relation to SLD (subsection 1.4.1), the machine structural dynamics can vary depending on the axis position [170], which should decrease the TMD performance. To address this problem, Burtscher and Fleischer [192] proposed an adaptive TMD system in which the TMD mass can be continuously changed by filling it with a fluid. For the thin-walled milling process, Fei et al. [193,194] developed a moving fixture element, which always supports the workpiece at the back surface of the tool–workpiece contact zone, and consequently, suppresses the vibration and deformation of the workpiece (Fig. 1-9(a)). The moving damper was realized by connecting the support fixture to the spindle unit. Alternatively, Ozturk et al. [195] achieved similar mobile support with the assistance of an industrial robot equipped with a rubber roller (Fig. 1-9(b)). In addition, Zhang et al. [196,197] attenuated the chatter of a flexible workpiece by performing machining in a chamber filled with viscous fluid. Munoa et al. [198] developed a tunable clamping table system to damp out chatter in the thin-walled part by applying the TMD principle.

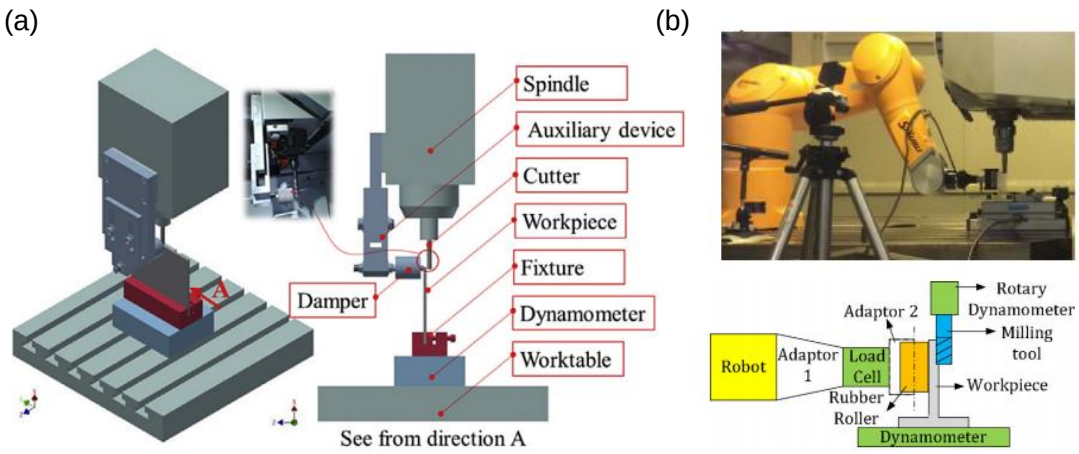

Fig. 1-9 Configuration of moving support for suppressing thin-walled workpiece chatter (a) in [193] and (b) in [195] (The figure is used with permission from Elsevier.)

Note that as the dynamics of the machine structure (e.g., column, headstock, and table) substantially impact the stability against the low-speed heavy-duty machining, it is important to increase the stiffness and/or damping of machine tools in the design phase. It is effective to use a high-damping structural material [199] and/or a high-friction guiding

system, such as a sliding type [200], although it would be conflicting to the high-speed precision positioning and lightweight design. In high-speed machining, the process stability is mainly determined by the system FRF formed by the assembly of the spindle, bearing, holder, and tool. In this case, there is a great opportunity to suppress the tooltip FRF (i.e., enhance chatter stability) by capitalizing on the absorber effect under the dynamic interactions by optimizing the spindle–bearing–holder–tool assembly (e.g., optimally selecting and designing the dimensions/locations of the assembly components) [201–203]. In addition, the stability can be improved by appropriately applying asymmetric stiffness at the tool holder according to the machining conditions (e.g., up or down cut) [204]. In some cases of the simultaneous process, the dynamic coupling between multiple tools can be actively used to enhance the process stability. For instance, in the shared-surface parallel turning with flexible tools, Ozturk et al. [205] and Reith et al. [206] increased the stability limit by detuning the ratio of natural frequency between the two tools.

For the active damping of chatter at the spindle, tool, or workpiece, an additional piezoelectric actuator is most frequently used to directly influence the process [72] or reduce the dynamic compliance [33–35]. Alternatively, an electromagnetic actuator is also used, so that the non-contact electromagnetic force can be applied to suppress the mechanical vibration. Recently, Beudaert et al. [207] developed an easy-to-handle portable damping system for a flexible workpiece, integrating an electromagnetic actuator, an accelerometer for chatter detection, and a model-free autonomous controller for the tuning function.

A low-frequency chatter, such as that induced by structural dynamics, can be actively suppressed using a feed-drive controller of machine tools without an additional actuator. Kakinuma et al. [208] applied a band-limited force control to suppress the low-frequency chatter in a high-precision linear motor-driven lathe. Additionally, Munoa et al. [170] demonstrated an active damping of the structural chatter induced by the bending mode of the ram and torsional mode of the column in heavy-duty face milling with a large milling machine. They fed the sensor signal of the accelerometer at the ram tip back to the feed-drive controller as an additional velocity feedback loop, and then designed the loop transfer function (TF) based on the loop-shaping technique.

1.4.3. Controlling tool path, posture, or geometries

Although the feed rate, which is a process control parameter, does not substantially affect the chatter stability, it can stabilize the process by optimally adjusting other control parameters, such as the tool path and/or tool posture. The feed rate is an important factor for avoiding forced vibration. The underlying concept of tool path/posture control for chatter avoidance is controlling the directional factor [209], as the tool posture/path, resultant cutting-force direction, and regenerative direction are related through CWE. In summary, the tool path/posture should be controlled so as to reduce the work of the regeneration effect

and cutting force over the vibration (i.e., flexible) direction. Shamoto et al. [60] proposed the chatter stability index (CSI), which represents the degree of orthogonality among the vibration, resultant cutting force, and regenerative width vector, for the turning process. They experimentally and theoretically showed that a stable process can be achieved by planning the tool path/posture for a high CSI. Recently, Maulimov and Sencer [210] investigated the CSI for the milling process. Especially in five-axis ball-end milling [211] and robotic machining process [212–214], chatter-free tool path/posture planning is a major concern and very complex because of acting in conjunction with pose-dependent dynamic and static stiffness.

In the multi-point cutter process (e.g., milling process), special geometric tools, such as variable pitch tools (VPCs) [140,144,215–218], variable helix tools [219–221], and serrated tools [222], can be used as an alternative for chatter control. The various design methodologies described in the literature can effectively suppress the chatter. All these tools focus on suppressing the regenerative chatter by discretely or continuously perturbing the delay representing the regenerative effect. Alternatively, it is also effective to increase the process damping effect by applying a cutting-edge chamfer [223] or flank-surface texture [224] for a low apparent clearance angle, which can be applied to not only multi-point but also single-point cutter processes, such as turning and boring.

The serrated tool can be used for the roughing process, although it can increase both the asymptotic stability limit and the number of stability pockets [225]. The variable pitch cutter (VPC) and variable helix cutter (VHC) are expected to have a sufficient chatter suppression if optimally designed. On one hand, VHC is inherently less robust to changes in the axial depth of the cut, although it is robust to changes in chatter frequency. On the other hand, VPC exhibits the opposite property. To address the issue of robustness against changes in chatter frequency in VPCs, Suzuki et al. [215] introduced the regeneration factor (RF) and proposed a novel robust design method to suppress h_m [−] vibration modes by using $2h_m$-flute VPCs. They also proposed an advanced tool design that combines the advantages of VPC and VHC [221]. Note that being robust to the variation in chatter frequency implies being robust to that in spindle speed; hence, it is expected to suppress chatter in a wide spindle speed range.

Although special tools are effective for suppressing chatter, the cost of these tools is higher than that of ordinal tools. Furthermore, to optimally design these special tools, it is generally required to know in advance the used cutting conditions (e.g., spindle speed range and depth of cut) and the corresponding chatter frequency. If the cutting conditions or chatter frequency change substantially, the special tool must be redesigned. The above aspects are the major drawbacks to using special tools in industry.

Even in the parallel tuning process, where the two tools cut the same surface, it has been confirmed that a high chatter stability can be achieved by tuning the angular

positioning of the tools (i.e., pitch angle) [226–228]. This process is referred to as "unequal pitch turning," similar to variable (i.e., unequal) pitch tool, as the pitch differences between two successive cuts perturb the regenerative effect and improve the stability. The stability over the tool chatter (i.e., flexible tools) can only be improved by unequal pitch turning if the tool dynamics are coupled through the machine structure (e.g., when both turrets are attached to the same column) [226]. Additionally, there is no simple rule to design an optimal pitch angle in this case; hence, it is accomplished by the stability analysis based on the machine dynamics.

In contrast, the optimal pitch angle can be simply designed for the workpiece chatter under the same design criterion as that of VPCs, based on the chatter frequency and spindle speed [227]. As it is feasible to provide a pitch difference with the turret-position control system during unequal pitch turning, unlike the variable pitch cutters, the robust and flexible chatter suppression can be expected by adaptively tuning the pitch angle according to the changes in the spindle speed and chatter frequency [228].

1.4.4. Controlling spindle speed/rotation during processes

Spindle speed is the most flexible process control parameter for altering the process stability. Therefore, among the stability improvement techniques, the spindle speed control techniques are widely known to be easy to implement, provide flexibility of design, and be effective in chatter avoidance/suppression. As the spindle speed control can be completely implemented only with the spindle system without any special tool or device, it is highly compatible with SOMS. Spindle speed control can be categorized as discrete spindle speed tuning (DSST) and continuous spindle speed variation (CSSV or simply SSV).

In DSST, the spindle speed is regulated based on the measured chatter conditions, so that the process will enter the stability pocket. In accordance with the important investigation into favorable searching methods for DSST performed by Trang and Lee [229], the spindle speed should be iteratively updated until the chatter is diminished in line with Eq. (1-3), as follows:

$$S_{new} = \frac{60 f_c}{N_c (k_c + 1)} \tag{1-3}$$

where f_c [Hz] is the chatter frequency, N_c [−] is the number of teeth, and k_c [−] is an arbitrary natural number that corresponds to the stability/chatter lobe number. S_{new} [min^{-1}] is the new spindle speed after update.

Eq. (1-3) indicates that the chatter phase shift between the previous and present vibrations on the machined surface by consecutive cuts is set to 0 or 2π, where one of the harmonics of the tooth-pass frequency is synchronized with the measured chatter frequency (Fig. 1-10). The most important point in Eq. (1-3) is that only the observable chatter

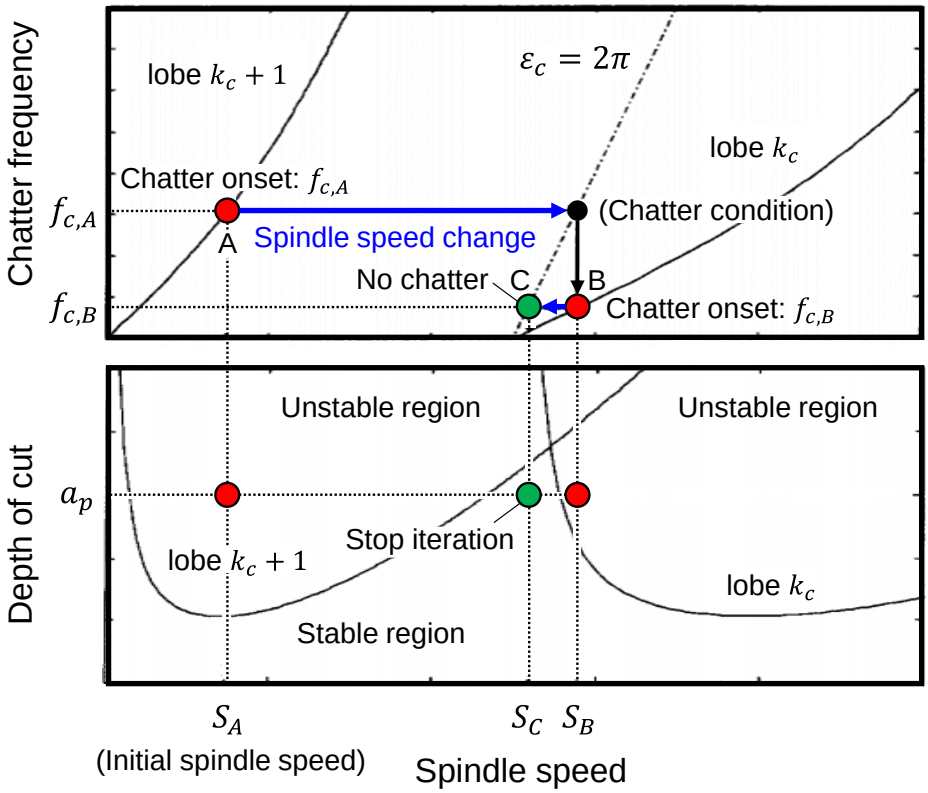

Fig. 1-10 Iterative tuning procedure of spindle speed in DSST based on [229] (The figure is used with permission from Elsevier.)

frequency during the cutting process is required to select the new spindle speed. In addition, there are other searching methods in which the spindle speed monotonically increases until the defined chatter index falls below the threshold [61]. Some of these monitoring-based stable spindle speed searching functions have already been incorporated into commercial machine tools (e.g., Machining Navi M-i and M-g from OKUMA Corporation, Machine Vibration Control from DMG MORI Co., Ltd., and Smooth AI spindle from Yamazaki Mazak Corporation), and are being used in industrial applications.

In SSV, the spindle speed is continuously varied during the cutting process to disrupt the regenerative effect. So far, various CSSV modes have been proposed, such as the sinusoidal [68,230], triangular [231,232], rectangular [233], random [234,235], linear ramped [236], and multi-harmonic [69,237] SSVs. Among these varying shapes of CSSV, the sinusoidal spindle speed variation (SSSV) and the triangular spindle speed variation (TSSV) are commonly observed because of their intuitiveness and effectiveness. The options for SSV have also been prepared in the industrial field (e.g., SSSV obtained by the CNC function from Haas Automation Inc. and TSSV obtained by Machining Navi L-g from OKUMA Corporation).

Some comparison studies have concluded that SSSV is the most efficient approach from the viewpoints of both chatter stabilization and spindle-speed tracking performance

[151,238]. Therefore, the sinusoidal trajectory is the most studied [64]. In contrast, some studies have stated that TSSV is more beneficial in terms of constraints of spindle acceleration [152,231], as the maximum theoretical spindle acceleration of TSSV is less than that of SSSV for the same design parameters. Furthermore, some other studies have experimentally reported that TSSV is more effective in terms of chatter suppression performance [73,232]. This discrepancy is attributable to a transient vibration, called "the beat vibration," which frequently emerges due to a momentary destabilization every SSSV/TSSV cycle and makes the process stability interpretation in a real system much more difficult [151]. Sexton and Stone [239] stated that the improvement in process stability by SSV often becomes modest compared to that observed during the stability simulation. The beat vibration tends to occur around the TSSV/SSSV extremums [232,236,240]. The authors in [232] suggested that TSSV can robustly suppress the beat vibration, and thus, TSSV is more stable than SSSV. This makes sense, as the velocity gradient in SSSV becomes very small at the turnaround points of the spindle speed (i.e., acceleration/deceleration).

However, most studies recommending TSSV overlook the spindle jerk in TSSV, which can be interpreted as a type of multi-harmonic SSSV where an infinite number of odd harmonics are superimposed. Thus, an infinite jerk, and therefore, a very large torque are required at the turnaround points of TSSV [238,241]. To follow the harmonic components of TSSV, a synchronous motor is required instead of the induction motor. A larger (synchronous) motor will lead to an increase in the cost, size, and thermal deformation of the machine tool [241]. However, according to the stability analysis recently conducted in [152], TSSV contains much broader optimal parameter spaces than SSSV, although SSSV shows slight advantage on the improvement in the depth of the cut (i.e., productivity). Therefore, SSSV might be more sensitive to the selection of design parameters.

In most previous studies, SSV was designed using several time-consuming, costly, and complex-stability simulations, which involved varying the amplitude and frequency of SSV to determine the optimal parameters [64,230]; hence, these design procedures cannot be implemented in machine tools as an intelligent function. According to the critical review conducted in [64], only Al-Regib et al. [68] proposed simple criteria to select appropriate design parameters in SSSV by numerically calculating the internal process energy based on the kinematic model of CWS. Their design method only requires the measured chatter frequency; hence, it can be online or integrable in machine tools such as DSST. However, their design criteria do not provide flexible options for considering the machine limitation, such as power, acceleration, and/or bandwidth of the spindle motor [240]. Urbikain et al. [242] stated that the limitations of SSV actually originate from the machines, and the scientific literature does not recommend any realistic value for the tuning of SSV parameters. Therefore, despite the substantial research, the SSV techniques have not yet been sufficiently used in actual manufacturing sectors [243].

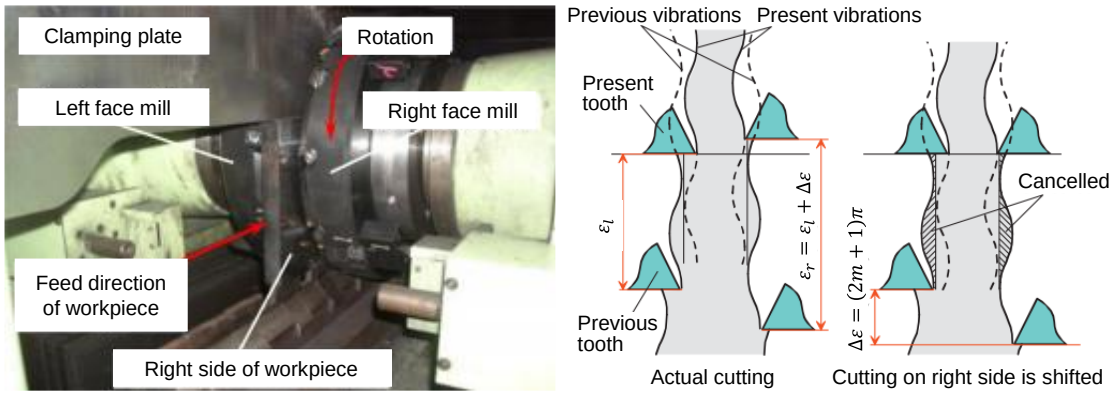

Fig. 1-11 Schematic of SDM in double-sided face milling of a flexible thin plate [245] (The figure is used with permission from Elsevier.)

In the parallel milling process, process stability can be controlled by actively using the dynamic interaction between CWSs by controlling the spindle speed or rotational angle. Brecher et al. [165] showed that the relative angular tool offset (ATO) between multiple milling tools, which yields phase differences of cutting forces at each CWS, substantially affects the stability if the same spindle speed and depth of cut are applied to all tools. In this case, the combination of cutting type (i.e., up/down), besides ATO, considerably alters the process stability [164]. Budak et al. [164] demonstrated that the stability margin of parallel milling with a flexible workpiece can be substantially increased by optimally tuning the spindle speeds of both tools. Only Shamoto et al. [244,245] proposed a simple strategy in which the regenerative effect was comprehensively canceled out by several cutters rotating at different speeds, which is termed as the speed difference method (SDM).

In the SDM, the optimal speed difference originates only from the chatter frequency, based on the similar principle as that of VPCs. The authors in [244,245] presented SDM for a flexible thin plate machined by double-sided face milling rotating in the same direction, where the vibration in a one-dimensional (1D) space perpendicular to the machining surface can be assumed (Fig. 1-11). Considering only regenerative effect in the thickness direction, they clarified the effectiveness of SDM analytically and experimentally. SDM is advantageous because the spindle speed can be flexibly adjusted to adapt to the chatter frequency.

SDM application makes the flexible workpiece more susceptible to forced vibration; hence, for the finishing process with no regenerative chatter, the forced vibration should be suppressed by completely synchronizing the rotation angle between the tools (i.e., zero ATO) as well as the cutting conditions to cancel out the cutting forces as much as possible [246].

1.4.5. Application and selection of chatter suppression techniques

In [64], the guidelines for selecting an appropriate chatter suppression technique have

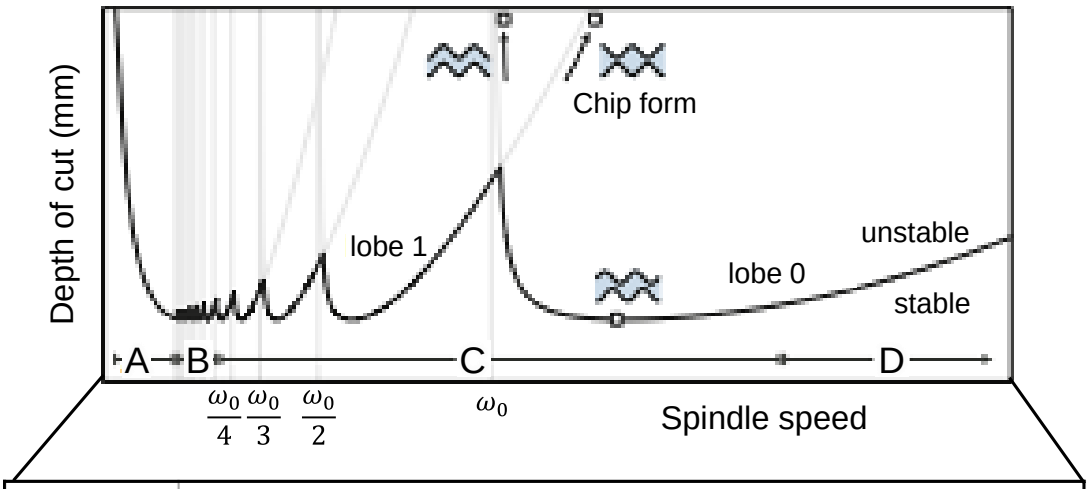

origin	Zones in the stability diagram			
	Zone A	Zone B	Zone C	Zone D
Tool/boring bar	CSSV Passive damper Variable helix	Passive damper CSSV Variable helix Variable pitch	DSST SLD Passive damper Variable pitch	Increase spindle speed
Spindle	CSSV Variable helix Edge geometry	CSSV Variable helix Variable pitch	DSST SLD Variable pitch	Increase spindle speed
Workpiece	CSSV Variable helix Increase stiffness	CSSV variable helix Increase stiffness	DSST Increase stiffness	Increase spindle speed
Fixture	CSSV Variable helix Passive damper	Passive damper Increase stiffness	SLD Passive damper Increase stiffness	Increase spindle speed
Machine structure	CSSV Passive damper	Passive damper CSSV Increase stiffness Active damping	Passive damper Increase stiffness Active damping	Increase spindle speed

Application targeted in this dissertation

Fig. 1-12 Chatter suppression strategies according to different zones in SLD and chatter origins [64] (The figure is used with permission from Elsevier.)

been compiled. As the first step in finding the best solution for the chatter problem, it is important to evaluate the cause of chatter and the number of complete waves per tooth-passing period produced by the chatter, i.e., chatter lobe number: $k_c \rightarrow f_c/f_z$ (Fig. 1-12) where f_z [Hz] is the tooth-passing frequency. The relative locations in SLD are categorized in the following four zones: (A) process damping zone ($k_c \geq 10$), (B) intermediate zone ($10 > k_c \geq 3$), (C) high-speed zone ($3 > k_c \geq 0.5$), and (D) ultra-high-speed zone ($0.5 > k_c$).

In zone D, as a stable region expands considerably as the spindle speed increases,

increasing the spindle speed is always a promising option if the machinability and motor limitation (e.g., cutting speed and motor power) are satisfied. Note that this zone is rarely reached as other chatter is induced by higher-frequency modes.

In zone C, the stability can be drastically increased by selecting a spindle speed that coincides with that of the stability pockets. Additionally, this zone is often dominated by clear local modes of tool, spindle, workpiece, or fixture. Thus, stable process planning by SLD or online stability pocket searching by DSST can be applied with reasonable reliability. Therefore, the SLD and DSST approaches are usually employed for high-spindle-speed machining, such as the high-speed aluminum-alloy milling process.

In contrast, CSSV is always an envisaged solution in zones A and B. Therefore, the CSSV is usually promising in low-spindle-speed processes, such as not only turning/boring but also grinding and heavy-duty milling. For an effective chatter suppression over a wide range of spindle speeds, Bediaga et al. [247] conceptualized a flexible system that automatically switches between DSST and CSSV according to the observed chatter lobe number. However, no simple optimal design rule for CSSV has been established yet.

If the process parameters cannot be changed because of machinability limitations, VPC, VHC, and other special edge geometry tools, which enhance the process damping effect, are also good alternatives, although they require the optimization of geometries in advance. In the roughing process with large chip load and cutting depth, the serrated tool or high-feed inserts is a good alternative independent of the zone. In addition, the improvement in

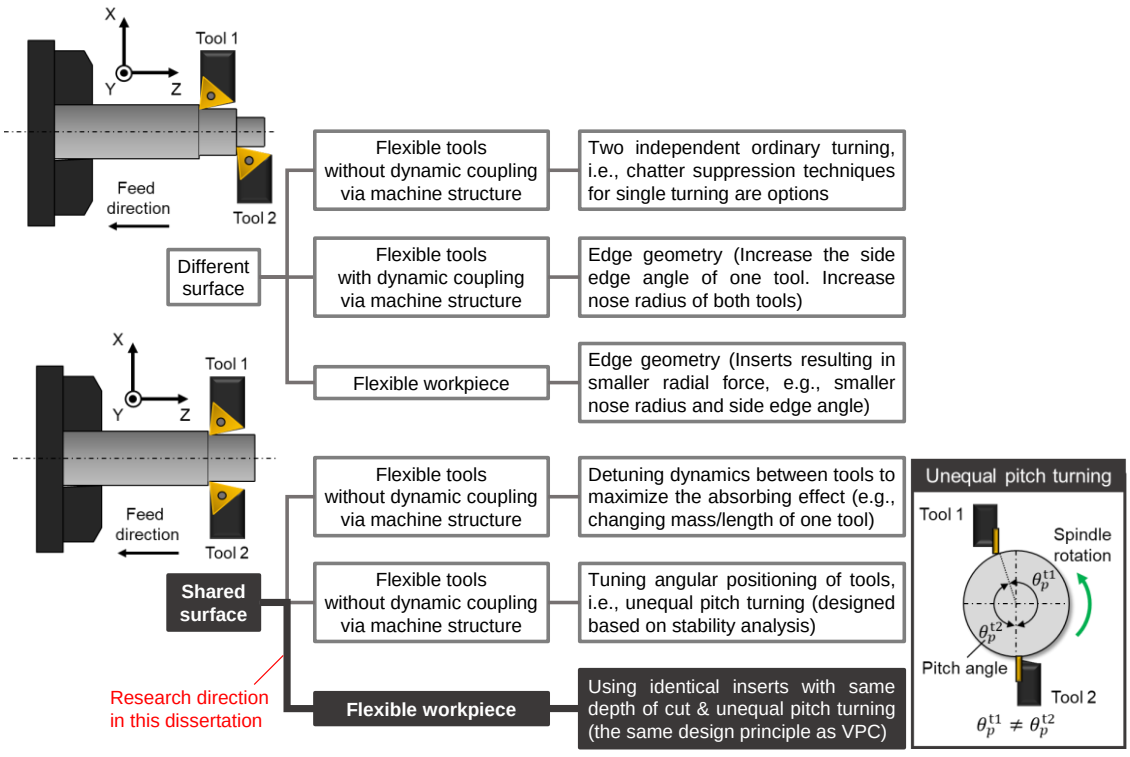

Fig. 1-13 Existing chatter suppression strategies in parallel turning process

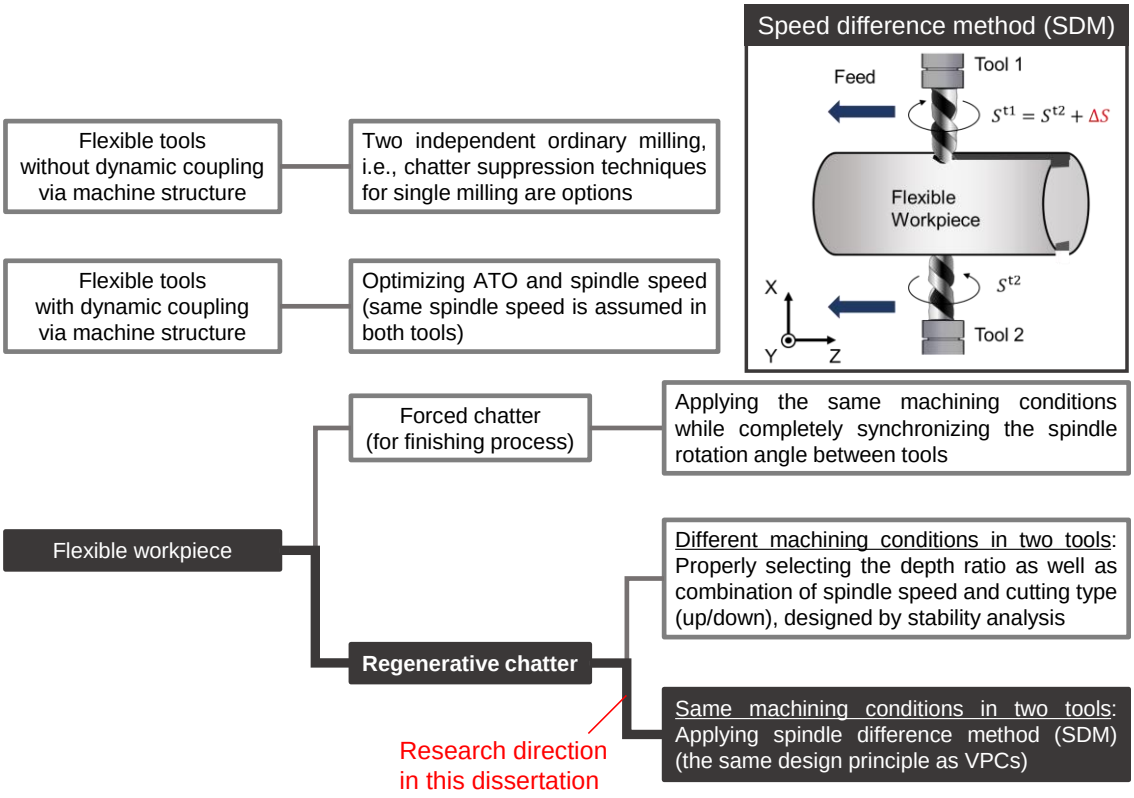

Fig. 1-14 Existing chatter suppression strategies in the parallel milling process

stiffness or damping is effective in most cases. This is preferable, especially when the process parameters and tool are fixed, other chatter solutions are not enough, or the machine tool performs different machining tasks highly limited by the structural chatter.

In the simultaneous machining processes, a process-specific solution for the chatter problem is available depending on the experimental setup. To date, some findings have been obtained to avoid chatter in the parallel turning/milling process, as described in the previous subsections. The guidelines for chatter suppression strategies in the parallel tuning and milling processes are summarized in Fig. 1-13 and Fig. 1-14, respectively.

1.5. Research purpose

1.5.1. Motivations and objectives

SOMS has great potential to realize a highly intelligent manufacturing system with sufficient flexibility and autonomy to handle mass customization. Machining chatter is a major issue that SOMS should address, as it remains a major impediment to productivity. This study aims to develop novel enabling techniques for SOMS so that the machine tool can self-actively suppress the chatter vibration according to the monitored chatter state. For this purpose, only the internal servo information and actuator (i.e., servo/spindle motor)

of the machine tool are used to monitor and suppress the chatter, which correspond to the 8th (i.e., control-integrated monitoring) and 9th (i.e., process control) functions of the categorized SOMS functionality, respectively (Fig. 1-1). All methodologies for chatter detection/suppression proposed in this dissertation are based on the physical mechanism of chatter vibration.

As previously mentioned in subsection 1.3.1, the cutting force is the most valuable physical quantity for process monitoring and control. However, the piezoelectric dynamometer has not been widely used on the shop floor because of concerns such as costs, failure frequency, thermal stability, and compatibility with the workpiece, although it is frequently used in the research and development phase in laboratories. Therefore, in this consistent study, the existing DOB techniques are employed to estimate the cutting force, including the high-frequency components induced by the chatter. The estimated cutting force is utilized in the developed chatter monitoring system.

To date, several chatter detection techniques have been proposed, as summarized in subsection 1.3.2. However, only a few studies have discussed a simple threshold setting and type-assorted detection of abnormal vibrations. Furthermore, some signal processing approaches proposed for chatter detection are too complicated to be integrated with the NC system. In practice, the chatter detection system should meet the following requirements: (1) type-assorted chatter detection for appropriate countermeasures according to the abnormal-vibration type, (2) small computation load for recognizing abrupt state changes in the real time, and (3) a unique threshold independent of the cutting conditions for mass customization. To meet these requirements, this paper proposes a novel online chatter detection technique, involving the novel concept of "phase shift monitoring." As this concept is based on the chatter mechanism, setting a unique threshold is feasible. To determine the phase shift in the machining process, the novel indices of the mechanical power factor (MPF) [248,249] and mechanical energy factor (MEF) are introduced for type-assorted chatter monitoring, inspired from the power factor (PF) theory in an AC electrical circuit.

For chatter suppression, many enabling technologies have already been established, as summarized in section 1.4. In particular, the chatter suppression approach, which controls process parameters such as tool posture, trajectory, feed rate, and spindle speed on a monitoring basis, is very advantageous and compatible for SOMS, as the process-control parameters can be easily adjusted without any special device to influence the process. DSST is practically used for high-speed machining in industry at a mature level. However, a simple optimal design methodology for CSSV, which can be online or integrable in machine tools, such as DSST, have not yet been established. For an effective chatter suppression system that supports various machining types and spindle speed ranges, an SOMS-oriented optimal design method not only for DSST but also for CSSV is indispensable. To address this challenge, in this study, a practical design methodology for an optimal SSSV is proposed

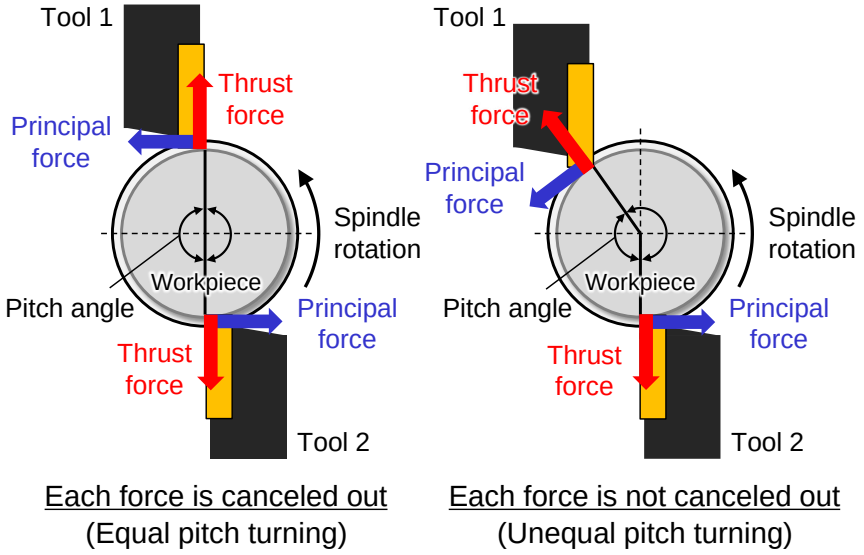

Fig. 1-15 Problem in unequal pitch turning for flexible workpiece

based on the novel analysis of the process energy balance.

In addition, the investigation of process control strategies for chatter suppression in an advanced simultaneous machining process is not sufficient. Simultaneous machining with multiple tools, especially in a flexible workpiece, is of great interest to both industry and academia, as the process stability can be substantially improved by a process-specific solution that makes good use of dynamic coupling of CWSs.

In the shared-surface parallel turning of a flexible workpiece, the VPC-inspired unequal-pitch turning can effectively suppress the chatter [227,228]. Only the chatter frequency at the used spindle speed is required to be designed, and the pitch angle can be flexibly changed by turret-position control. The unequal pitch turning is also advantageous in terms of machinability limitation, as the cutting speed (i.e., spindle speed) is sometimes limited by the cutting insert and may not be selected arbitrarily [226]. Therefore, unequal pitch turning is one of the most promising techniques for SOMS. However, there is a concern regarding the eccentricity of the flexible workpiece, as the sum of the force vectors cannot perfectly cancel each other when applying an unequal pitch (Fig. 1-15). This viewpoint has never been evaluated. If the cutting insert can tolerate a change in the cutting speed, controlling the spindle speed is also an effective and flexible technique to suppress chatter vibration and maximize the material removal rate. From this viewpoint, this paper also proposes a novel chatter suppression technique in parallel turning assisted with tool swing motion (TSM) flexibly provided by the feed-drive system. As the regenerative effect (i.e., the delay between two consecutive cuts) is perturbed by TSM, the proposed TSM process is expected to effectively suppress the chatter. Additionally, as both tools swing in the circumferential direction of the workpiece while maintaining equal pitch, the imbalance of the force vector is not caused ideally. The TSM provided by feed-drive system has bandwidth

advantage over the SSV provided by the spindle system.

In the parallel milling process of a flexible workpiece, SDM, proposed by Shamoto et al. [244,245], is a promising technique for an SOMS-oriented autonomous chatter suppression system for the same reason as that for unequal-pitch turning (i.e., simple design criterion based on the chatter frequency inspired from VPC and flexible redesign by adjusting the process parameter, i.e., spindle speed). The authors in [244,245] assumed double-side face milling rotating in the "same" direction and a thin plate with flexibility perpendicular to the machining surface (i.e., tool axis direction) (Fig. 1-11). However, the effectiveness of SDM in other machining situations has not been clarified yet. For instance, if there are flexibilities on a plane perpendicular to the tool axis direction, two tools should be rotated in opposite direction to balance the cutting forces. In addition, dynamic variations of the cutting width will dominantly occur on this plane, which must be considered. A part of this study discusses anew the effectiveness of SDM in this scenario based on the developed process model, and then experimentally shows that the chatter suppression performance can be enhanced by the adaptive SDM system based on real-time chatter monitoring.

The research direction of chatter suppression techniques dealt with in this study is depicted in Fig. 1-12 to Fig. 1-14. Although considerable individual techniques for chatter monitoring and suppression/avoidance have been proposed, the most important challenge in SOMS is to achieve system integration such that multiple functionalities act as one system for self-optimizing machining processes and produce high added value (i.e., system of systems). This study presents active process control strategies with monitoring-based optimal design based on the process models in the specific applications, and realizes system integration of the control-integrated process monitoring and control for autonomous chatter suppression. The proposed techniques and discussion in this dissertation can help in the automation of solutions toward realizing full-fledged SOMS.

1.5.2. Organization of the dissertation

Fig. 1-16 summarizes the organization of the dissertation. Chapter 1 provides an overview of the functionalities of SOMS, which is a novel concept for addressing the recent manufacturing issues. Then, focusing on the critical machining chatter problem, the state of the art in terms of chatter monitoring and suppression/avoidance techniques is summarized. Based on the state of the enabling technologies for SOMS in the chatter issue, the motivation and purpose of this dissertation are declared while indicating the specific research direction.

Chapter 2 describes the existing sensorless cutting force estimation techniques using the internal servo information of the machine tool. The cutting force estimation formula is derived from the motion equations of the modeled feed-drive system based on the disturbance estimation theory. As several approaches have been proposed to date, the

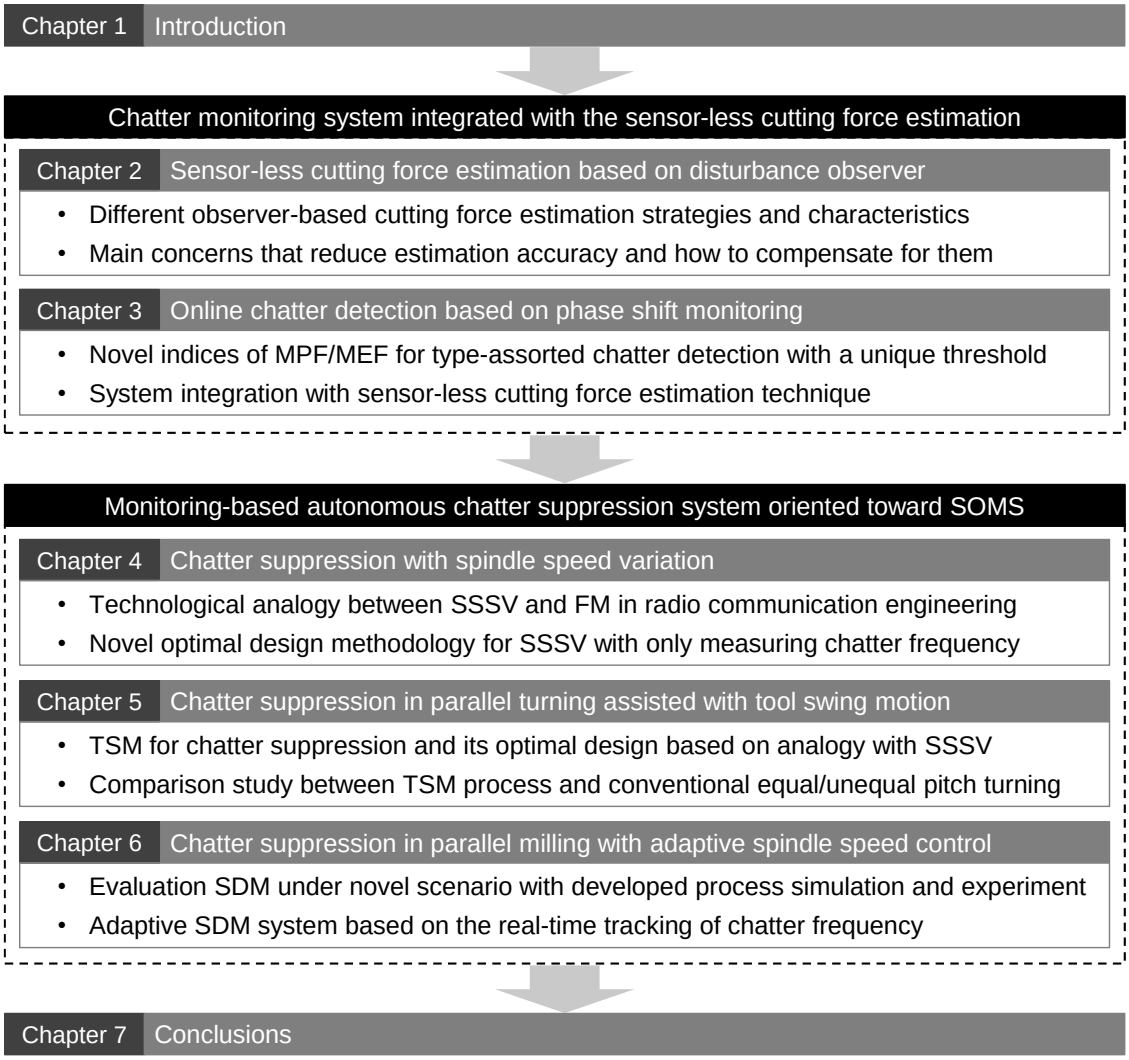

Fig. 1-16 Organization of dissertation

characteristics of each cutting force observer are compared analytically and experimentally with a developed prototype three-axis ball-screw-driven machine tool. In addition, the main concerns in achieving an accurate cutting force estimation and the compensation techniques are proposed. If the proposed compensation techniques can be applied successfully, the accuracy of the sensorless cutting force estimation system can be substantially enhanced with the sufficient bandwidth.

In Chapter 3, the online chatter detection method is proposed based on the novel concept of phase shift monitoring by using MPF and MEF, which are proposed anew as indices for chatter detection, inspired from the PF theory in an AC circuit. The MPF and MEF in the machining process represent the phase differences between the cutting force and tool velocity/displacement and can be utilized to detect the forced and (regenerative) chatter vibration, respectively. The detailed methodologies for detecting forced and chatter vibration by MPF/MEF and its efficient calculation for an online system, as well as the

system integration with the sensorless cutting estimation technique, are described. The effectiveness of the proposed method is verified with a developed high-precision liner-motor-driven lathe. After investigating the influence of the window length on computing MPF/MEF with oscillation tests, the performance of the proposed system is evaluated using a series of outside turning tests.

In Chapter 4, the practical design methodology for an optimal SSSV is proposed based on the novel analysis of the process energy balance. Through mathematical treatment of the chatter vibration in SSSV, an analogy can be found between the SSSV characteristics and the frequency modulation (FM) techniques used in radio communication engineering, defining the modulation index (MI) for SSSV. The analytical kinematic energy model can be expressed with the Bessel function having MI as an argument. It provides design candidates for selecting the optimal amplitude of SSSV, which effectively dissipates the chatter energy. In addition, the limit criteria for SSSV frequency, according to the variation amplitude, are discussed to ensure the SSSV effect and prevent the beat vibration. The proposed design methodology is verified by a series of time-domain simulations and a series of boring tests with a commercial large-scale double-column-type machining center.

In Chapter 5, the TSM process for chatter suppression is proposed in parallel turning under the following assumption: rigid tools with the same depth of cut and insert geometries machine the shared surface of a flexible workpiece. In the TSM process, the two tools are swung in the circumferential direction of the workpiece in a sinusoidal manner while maintaining equal pitch. The systematic design procedure for TSM is also introduced based on the analogy with the SSSV process. In a prototype multi-tasking machine tool modified to be flexibly controlled, the chatter stabilization performance and workpiece runout in the proposed TSM process are experimentally evaluated and compared with the conventional equal- and unequal-pitch turning.

In Chapter 6, the SDM is described under the assumption that a slender workpiece, which is flexible on a plane perpendicular to the tool axis direction, is simultaneously machined by two end mills rotating in opposite directions. As the effectiveness of SDM has not yet been elucidated for this scenario, it is evaluated through a series of process simulations in the time and frequency domains, which are developed in this study. Based on the findings, an adaptive SDM system is also developed. The difference in the spindle speed is adaptively optimized during the process according to the chatter frequency tracked from the cutting force estimated by a sensorless cutting force observer. Its effectiveness is also verified in the prototype multi-tasking machine tool, and the results show that the developed real-time adaptive SDM system can suppress the chatter vibration more robustly.

In Chapter 7, conclusions of the dissertation are summarized.

2. Sensorless cutting force estimation based on disturbance observer

To date, several sensorless cutting estimation techniques using the servo information of the machine tool have been proposed. The formulas of existing observer-based cutting force estimation are derived in section 2.2, based on the defined physical model of feed drive system in section 2.1. The main characteristics and informative knowledges of each techniques are summarized in section 2.3 and 2.4, while demonstrating milling tests with a prototype three-axis ball-screw-driven machine tool. In section 2.5, the compensation techniques for deterioration in cutting force estimation, induced by position-dependent model parameters and/or complex structure dynamics, are proposed [250,251] to overcome the limitations for accurate cutting force estimation in the existing sensorless techniques.

2.1. Physical model of feed drive system in machine tools

Fig. 2-1 shows the most used ball-screw-driven feed-drive system in the machine tool, which comprises many mechanical elements, such as the driven body (table + workpiece), guide, ball screw shaft, nut, support bearing, servo motor, and coupling; hence, it usually has multiple modes. There are two typical modes: the torsional and axis modes resulting from the ball screw shaft. These have a substantial impact on the control system stability and positioning accuracy. The torsional resonance frequency of a ball screw is generally higher than the axial resonance frequency. If high-frequency vibration does not impair the stability of the servo system [252], a dual-inertial model that models only the primary mode in the axial direction is available [253–256] (Fig. 2-2). In the dual-inertia model, rotating mechanical elements (e.g., motor, coupling, and ball screw shaft) and translational elements (e.g., nut and movable stage) are both regarded as one mass. This enables the description

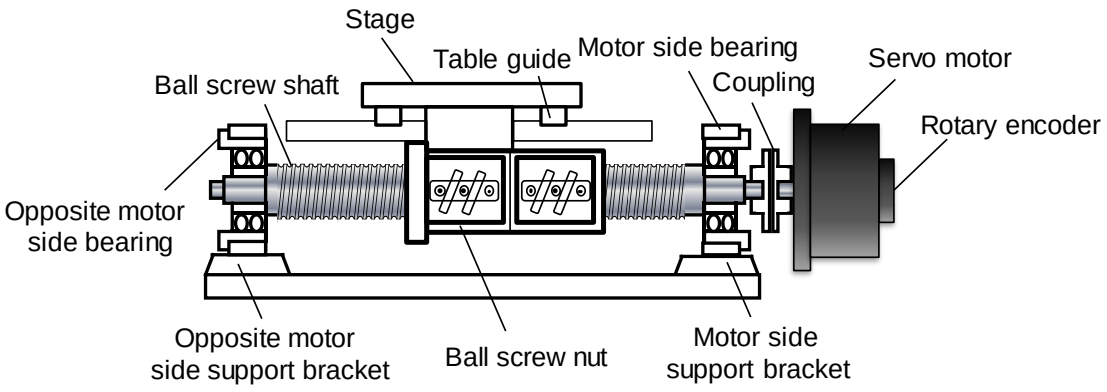

Fig. 2-1 Mechanical element of ball-screw-driven system

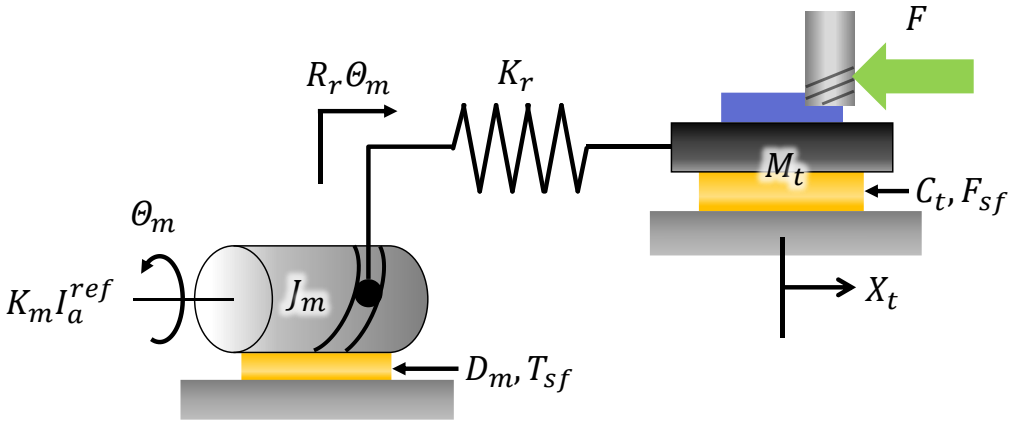

Fig. 2-2 Dual-inertia model of ball-screw-driven system

of the dynamic behavior of each mass due to the primary mode in the axial direction. The dual inertial model is advantageous in terms of simplicity and intuitiveness, and consequently, widely used for system design, such as control system and disturbance observer. Note that the structural damping between two masses is not included in this study. In addition, two or more vibration modes cannot be considered in the dual-inertia model. The driven body (i.e., movable translational mass) cannot often be regarded as a simple rigid body depending on the machine tool kinematic chain. This is a major obstacle in achieving accurate sensorless cutting force estimation with sufficient bandwidth, as will be described later in subsection 2.5.2.

From Fig. 2-2, the motion equations of the dual-inertia model can be described as follows.

$$J_m\ddot{\Theta}_m + K_r(R_r\Theta_m - X_t)R_r + D_m\dot{\Theta}_m = K_m I_a^{ref} - T_{sf} \tag{2-1}$$

$$M_t\ddot{X}_t + K_r(X_t - R_r\Theta_m) + C_t\dot{X}_t = -F - F_{sf} \tag{2-2}$$

where J_m [kg · m^2] is a total inertia of rotational elements, M_t [kg] is a movable mass, K_r [N/m] is a total stiffness of feed-screw system, D_m [N · m · s/rad] is a damping coefficient of rotational elements, C_t [N · s/m] is a damping coefficient of translational elements, K_m [N · m/A] is a torque coefficient. F_{sf} [N], T_{sf} [N · m], F [N] is a friction force, friction torque, and cutting force, respectively, which applied on feed-drive system as load forces/torques. Additionally, I_a^{ref} [A], Θ_m [rad], and X_t [m] are motor current reference, motor angle, and stage position, respectively. These three signals can be obtained in CNC as servo information according to types of stage drive (i.e., linear-motor-driven or ball-screw-driven system) and position control (i.e., semi-closed or full-closed control). Here, R_r [m/rad] is a transform coefficient for rotational to translational motion, which is calculated from the lead length of screw shaft, l_p [m], as $R_r = l_p/(2\pi)$. The parameters are also summarized in the Nomenclature.

Although the actual load applied to the machine elements includes Coriolis force and centrifugal force, these are ignored because they are sufficiently smaller than the friction force/torque and the cutting force. Note that the armature current is assumed to be equivalent to the motor current reference value, as the bandwidth of the current loop is sufficiently high in general. Here, Eqs. (2-1) and (2-2) can be rewritten in the following matrix format:

$$\begin{bmatrix} J_m & 0 \\ 0 & M_t \end{bmatrix}\begin{Bmatrix} \ddot{\Theta}_m \\ \ddot{X}_t \end{Bmatrix} + \begin{bmatrix} D_m & 0 \\ 0 & C_t \end{bmatrix}\begin{Bmatrix} \dot{\Theta}_m \\ \dot{X}_t \end{Bmatrix} + \begin{bmatrix} K_r R_r^2 & -K_r R_r \\ -K_r R_r & K_r \end{bmatrix}\begin{Bmatrix} \Theta_m \\ X_t \end{Bmatrix} = \begin{Bmatrix} K_m I_a^{ref} - T_{sf} \\ -F - F_{sf} \end{Bmatrix} \tag{2-3}$$

Furthermore, by applying Laplace transform and rearranging it, Eq. (2-3) can be transformed as follows:

$$\begin{aligned} \begin{Bmatrix} R_r\Theta_m(s) \\ X_t(s) \end{Bmatrix} &= \frac{\alpha_r}{M_t^2 s D_r(s)}\begin{bmatrix} M_t s^2 + C_t s + K_r & K_r \\ K_r & (J_m/R_r^2)s^2 + (D_m/R_r^2)s + K_r \end{bmatrix}\begin{Bmatrix} K_m I_a^{ref}/R_r \\ -F \end{Bmatrix} \\ &= \frac{\alpha_r}{M_t s D_r(s)}\begin{bmatrix} s^2 + 2\zeta_t\omega_t s + \omega_t^2 & \omega_t^2 \\ \omega_t^2 & \frac{1}{\alpha_r}s^2 + 2\zeta_m\omega_t s + \omega_t^2 \end{bmatrix}\begin{Bmatrix} K_m I_a^{ref}/R_r \\ -F \end{Bmatrix} \end{aligned} \tag{2-4}$$

where $\alpha_r\,[-]$ is inertia ratio, and $D_r(s)$ is defined as:

$$D_r(s) = s^3 + 2\omega_t(\alpha_r\zeta_m + \zeta_t)s^2 + \{\omega_r^2 + 4\alpha_r\zeta_m\zeta_t\omega_t^2\}s + 2\alpha_r(\zeta_m + \zeta_t)\omega_t^3 \tag{2-5}$$

$$\alpha_r = \frac{M_t}{J_m/R_r^2}, \omega_t = \sqrt{\frac{K_r}{M_t}}, \omega_r = \omega_t\sqrt{\alpha_r + 1}, \zeta_m = \frac{D_m/R_r^2}{2\omega_t M_t}, \zeta_t = \frac{C_t}{2\omega_t M_t} \tag{2-6}$$

where ω_t [rad/s] is an anti-resonance frequency at motor side, ω_s [rad/s] is a resonance frequency in dual inertia system, $\zeta_m\,[-]$, and $\zeta_t\,[-]$ are damping ratio of rotational elements, and translational elements, respectively. Note that, for simplicity, the friction terms are omitted here in Eq. (2-4).

If the axial rigidity is sufficiently high and the elastic deformation between the translational and rotating systems can be ignored, the ball-screw-driven system can be expressed as a one-inertia (i.e., rigid body) model. Assuming that the operating efficiency from the rotating system to the translational system is unity, the ball-screw-driven system as the single-inertia model is expressed as follows:

$$M_a\ddot{X}_m + C_a\dot{X}_m = \frac{1}{R_r}K_m I_a^{ref} - \frac{1}{R_r}T_{sf} - F_{sf} - F \tag{2-7}$$

$$M_a = J_m/R_r^2 + M_t, C_a = D_m/R_r^2 + C_t, X_m = R_r\Theta_m \tag{2-8}$$

where M_a [kg] and C_a [N · s/m] are a total mass and damping coefficient in rigid body motion, respectively. X_m [m] is an equivalent value of Θ_m in translational motion.

Here, the linear-motor-driven system with a linear encoder is also utilized for high-precision machine tools. In the linear-motor-driven system, the linear motor directly drives the stage for translational motion without mechanical elements for rotation–translation conversion, such as a ball screw. Generally, the linear-motor-driven system is also modeled as an inertia model, as follows:

$$M_t\ddot{X}_t = K_t I_a^{ref} - F_{sf} - F \tag{2-9}$$

where K_t [N/A] is a thrust-force coefficient. Note that viscous friction is neglected in the above equation as it should have a small value in the linear-motor-driven system.

2.2. Observer-based sensorless cutting force estimation

2.2.1. Disturbance observer

DOB [99] was originally constructed for estimating disturbance in a single-inertia plant, such as a servomotor, based on the input motor current and output motor angle information. In a broad sense, DOB includes the feed-forward compensation to the current control system by the compensation motor current equivalent to the estimated disturbance. By canceling the disturbance including the load force and parameter fluctuations, robust motion control can be realized. As DOB is a model-based method, the nominal values of mechanical parameters are used for disturbance estimation. If the errors between the nominal values and the actual parameters are explicitly shown, Eq. (2-7) can be rewritten with parameter fluctuations, as follows:

$$(M_{an} + \Delta M_a)\ddot{X}_m + (C_{an} + \Delta C_a)\dot{X}_m = \frac{1}{R_r}(K_{mn} + \Delta K_m)I_a^{ref} - \frac{1}{R_r}T_{sf} - F_{sf} - F \tag{2-10}$$

where $(\ \ )_n$ and Δ denote the nominal values and variation in parameters, respectively.

From Eq. (2-10), the disturbance force, F_{dis} [N], including the parameter-fluctuation-induced forces, frictional forces and cutting force can be derived as follows:

$$F_{dis} = \frac{1}{R_r}K_{mn}I_a^{ref} - M_{an}\ddot{X}_m - C_{an}\dot{X}_m \tag{2-11}$$

where

$$F_{dis} \equiv \frac{1}{R_r}T_{sf} + F_{sf} + F - \Delta K_m I_a^{ref} + \Delta M_a\ddot{X}_m + \Delta C_a\dot{X}_m \tag{2-12}$$

The motor current reference value is observable information. In addition, velocity and acceleration information can be estimated by differentiating the motor angle signal obtained from the rotary encoder attached to the servomotor. Therefore, the disturbance force can be estimated based on Eq. (2-11). This is the principle of the disturbance estimation theory (i.e., DOB). Note that as differential processing amplifies high-frequency noise, a low-pass filter (LPF) should be applied for noise reduction.

When the parameter errors are sufficiently reduced by prior identification, the disturbance in Eq. (2-12) can be regarded as comprising cutting and friction forces during machining; hence, by applying the disturbance estimation theory and subtracting the friction terms identified in advance (i.e., $T_{sf} \to \hat{T}_{sf}, F_{sf} \to \hat{F}_{sf}$, $\hat{}$ indicates estimated value), the cutting force is estimated as follows:

$$\hat{F}^{DOB} = G_{LPF}\left(\frac{K_{mn}}{R_{rn}} I_a^{ref} - M_{an}\ddot{X}_m - C_{an}\dot{X}_m - \frac{1}{R_{rn}}\hat{T}_{sf} - \hat{F}_{sf}\right) \tag{2-13}$$

where $\hat{F}^{DOB}$ [N] is the cutting force estimated in DOB and G_{LPF} indicates LPF.

Eq. (2-13) is the cutting force observer based on the single-inertia model in the ball-screw-driven system. Here, the principle of conventional motor-current-based cutting force estimation, $\hat{F}^{CUR}$ [N], can be simply expressed as:

$$\hat{F}^{CUR} = G_{LPF}\left(\frac{K_{mn}}{R_{rn}} I_a^{ref} - \frac{1}{R_{rn}}\hat{T}_{sf} - \hat{F}_{sf}\right) \tag{2-14}$$

In the linear-motor-driven system modeled as single inertia of Eq. (2-9), the estimation manner is derived similar to that in Eqs. (2-13) and (2-14):

$$\hat{F}^{DOB} = G_{LPF}\left(K_{tn} I_a^{ref} - M_{tn}\ddot{X}_t - \hat{F}_{sf}\right) \tag{2-15}$$

$$\hat{F}^{CUR} = G_{LPF}\left(K_{tn} I_a^{ref} - \hat{F}_{sf}\right) \tag{2-16}$$

Fig. 2-3(a) and (b) shows the block diagram of Eqs. (2-13) and (2-15), respectively. The estimation accuracy is improved by compensating the phase lag between the servo signals induced by the current loop, servo amplifier, and signal communication [257–259], which is also explicitly depicted in Fig. 2-3. In Fig. 2-3, ω_L [rad/s] is bandwidth of current loop, T_a [s], T_m [s], and T_t [s] are dead times at servo amplifier, motor, and stage, respectively. The phase lag compensation by 1st order LPF with ω_{Ln} and dead-time components with T_1 [s], T_2 [s], and T_3 [s] should be applied if required.

2.2.2. Load-side disturbance observer

Recently, machine tools inherently equipped with a linear encoder have become mainstream due to the demand for part accuracy assurance (i.e., full-closed-loop control).

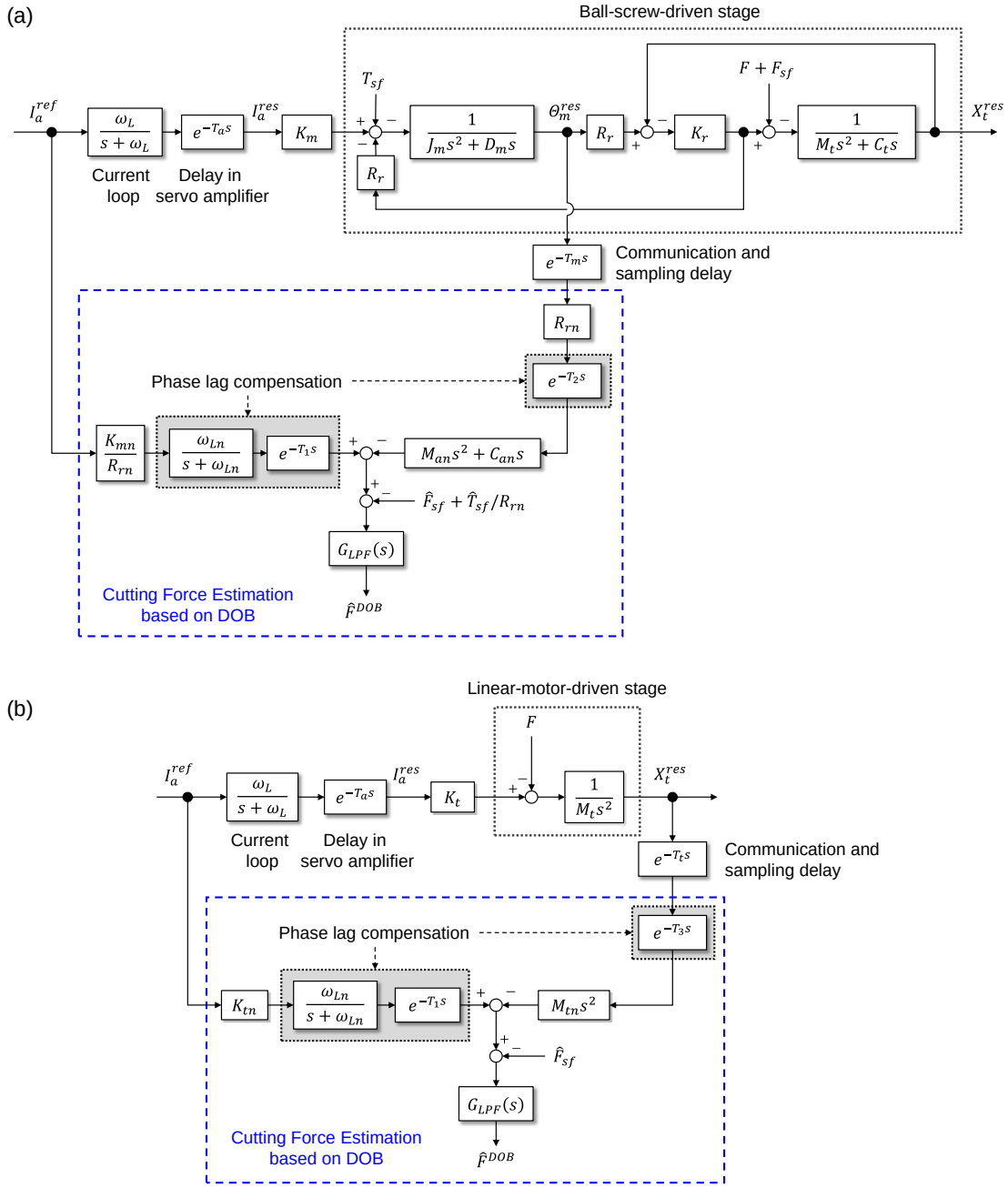

Fig. 2-3 Block diagram of cutting-force-estimation system based on DOB: (a) in ball-screw-driven system, (b) in linear-motor-driven system

In a fully closed ball-screw-driven system, the disturbance estimation technique for the dual-inertia model is available.

The load-side disturbance observer (LDOB) [260] is one of these techniques, and is based on the motion equation of the translational (i.e., load side) system in Eq. (2-3), as follows:

$$M_t\ddot{X}_t + C_t\dot{X}_t + K_r\left(X_t - R_r\Theta_{m,q}\right) = -F - F_{sf} \tag{2-17}$$

Consequently, the estimation method of the cutting force in LDOB can be derived based

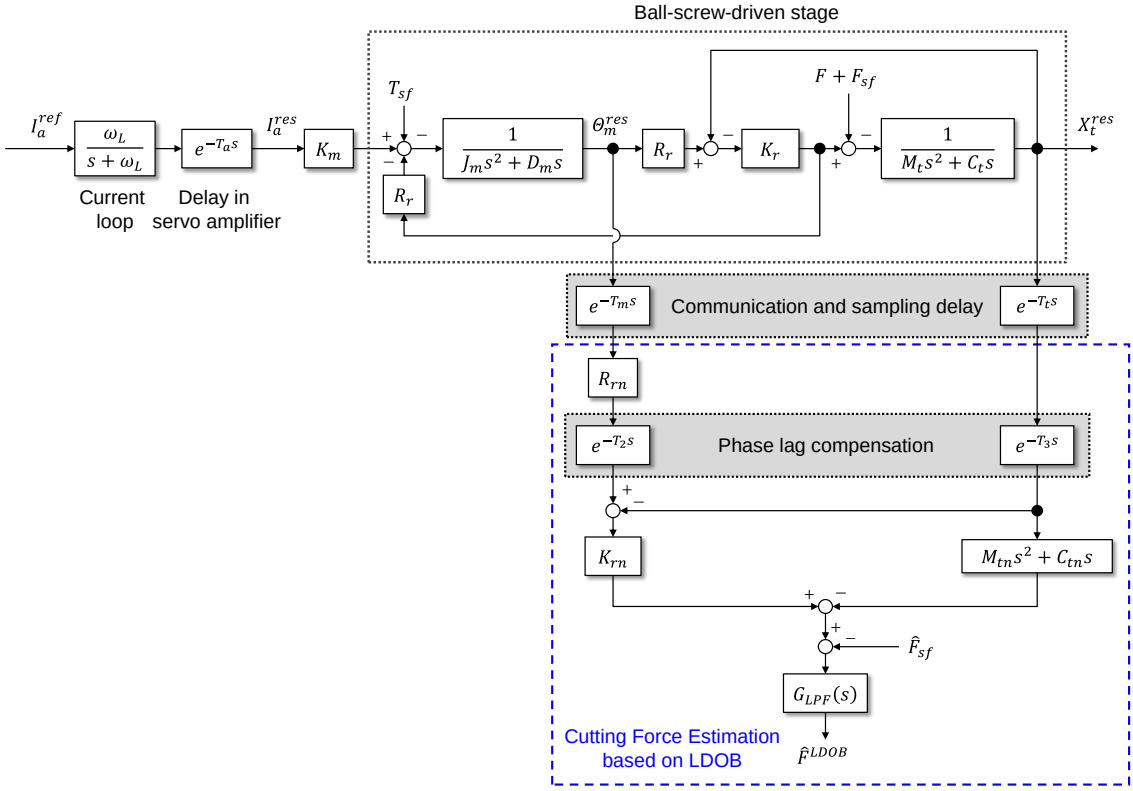

Fig. 2-4 Block diagram of cutting-force-estimation system based on LDOB

on Eq. (2-17) according to the same procedure as that used for DOB:

$$\hat{F}^{LDOB} = G_{LPF}\left(-M_{tn}\ddot{X}_t - C_{tn}\dot{X}_t + K_{rn}X_r - \hat{F}_{sf}\right) \tag{2-18}$$

where $\hat{F}^{LDOB}$ [N] is cutting force estimated in LDOB and X_r [m] is relative displacement between the motor and stage:

$$X_r = R_r\Theta_m - X_t = X_m - X_t \tag{2-19}$$

Based on Eq. (2-18), the cutting force is estimated using the multi-encoder signals and the identified friction force. The block diagram of LDOB is shown in Fig. 2-4, where phase lag compensations are also explicitly depicted.

2.2.3. Multi-encoder-based disturbance observer

Another method of disturbance estimation in dual-inertial model is the multi-encoder-based disturbance observer (MEDOB) [261,262], which can also be utilized for cutting force estimation in machine tools [257]. By correlating the motor- and load-side motion equation in Eq. (2-3) to eliminate the interaction term of $K_r(R_r\Theta_m - X_t)$, the following equation can be obtained:

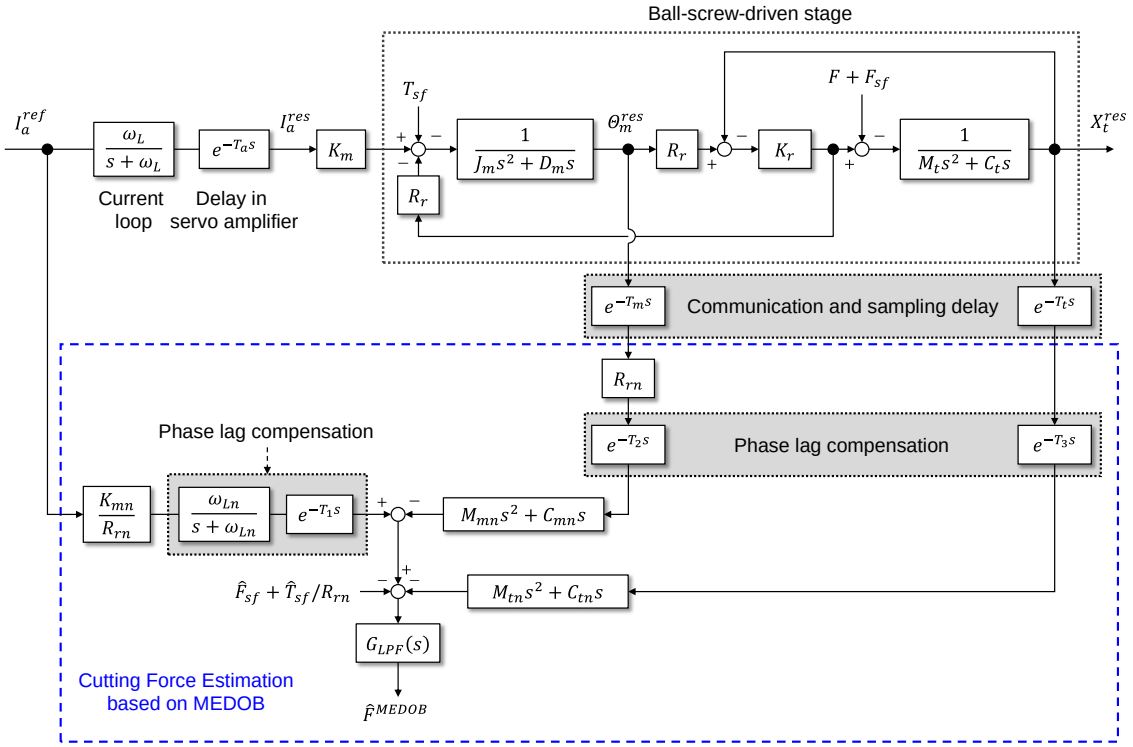

Fig. 2-5 Block diagram of cutting-force-estimation system based on MEDOB

$$\frac{1}{R_r}J_m\ddot{\Theta}_m + \frac{1}{R_r}D_m\dot{\Theta}_m + M_t\ddot{X}_t + C_t\dot{X}_t = \frac{K_m}{R_r}I_a^{ref} - \frac{1}{R_r}T_{sf} - F - F_{sf}$$
$$\rightarrow M_m\ddot{X}_m + C_m\dot{X}_m + M_t\ddot{X}_t + C_t\dot{X}_t = \frac{K_m}{R_r}I_a^{ref} - \frac{1}{R_r}T_{sf} - F - F_{sf} \quad (2\text{-}20)$$

where M_m [kg] and C_m [N · s/m] are equivalent value of J_m [kg · m^2] and D_m [N · m · s/rad] in translational motion, respectively:

$$M_m = J_m/R_r^2\,,\, C_m = D_m/R_r^2 \quad (2\text{-}21)$$

The method of estimating the cutting force in MEDOB, $\hat{F}^{MEDOB}$ [N], can be derived as

$$\hat{F}^{MEDOB} = G_{LPF}\left(\frac{K_{mn}}{R_{rn}}I_a^{ref} - M_{mn}\ddot{X}_m - C_{mn}\dot{X}_m - M_{tn}\ddot{X}_t - C_{tn}\dot{X}_t - \frac{1}{R_{rn}}\hat{T}_{sf} - \hat{F}_{sf}\right) \quad (2\text{-}22)$$

Unlike Eq. (2-13) for a single-inertia model, Eq. (2-22) treats the rotational and translational motions independently; hence, each motion can be considered even around the resonance frequency, where the rotational and translational parts move in opposite phases. As the interaction term of axial stiffness is eliminated in MEDOB, the cutting force is estimated by focusing on the movements of the two masses at both ends, instead of directly considering the relative motion between the rotational and translational systems due to the

spring. In a real system, this makes a difference in the estimation results in each estimation technique, as discussed in sections 2.3 and 2.4. An advantage of MEDOB is that it is not necessary to identify the axial stiffness, which may be position-dependent [263], as discussed later. The block diagram of the cutting force estimation system based on MEDOB is shown in Fig. 2-5.

2.2.4. Mode-decoupled disturbance observer

The methods of cutting force estimation in DOB, LDOB, and MEDOB are directly derived in the physical-space-coordinate system from the motion equation of the dual-inertia model. Recently, mode-decoupled cutting force estimation in an equivalent SDoF (i.e., modal-space coordinate) system has been proposed [258,259]. In the dual-inertia model of the ball-screw-driven system, there are two vibration modes: a rigid-body mode, which represents the center-of-mass motion, and a vibration mode, which represents the relative motion between the rotational and translational parts induced by the spring element. In the physical-space-coordinate system, these two modes are mixed, but become mutually independent in the modal space. A conceptual figure of modal decomposition in the dual-inertia model of the ball-screw feed-drive stage is depicted in Fig. 2-6.

Thus, each mode can be handled individually as an equivalent SDoF system. As a first step toward modal decomposition, Eq. (2-3) is rewritten as follows:

$$[\boldsymbol{M}]\{\ddot{\boldsymbol{X}}\} + [\boldsymbol{C}]\{\dot{\boldsymbol{X}}\} + [\boldsymbol{K}]\{\boldsymbol{X}\} = \{\boldsymbol{F}\} \tag{2-23}$$

where

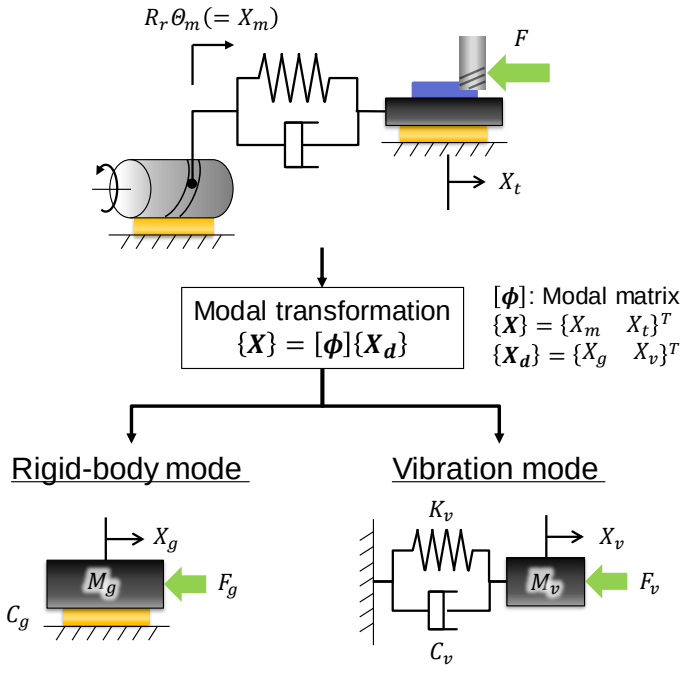

Fig. 2-6 Conceptual figure of modal decomposition in dual inertia model

$$[\boldsymbol{M}] = \begin{bmatrix} M_m & 0 \\ 0 & M_t \end{bmatrix}, [\boldsymbol{C}] = \begin{bmatrix} C_m & 0 \\ 0 & C_t \end{bmatrix}, [\boldsymbol{K}] = \begin{bmatrix} K_r & -K_r \\ -K_r & K_r \end{bmatrix} \tag{2-24}$$

$$\{\boldsymbol{X}\} = \begin{Bmatrix} X_m \\ X_t \end{Bmatrix}, \{\boldsymbol{F}\} = \begin{Bmatrix} K_m I_a^{ref}/R_r - T_{sf}/R_r \\ -F - F_{sf} \end{Bmatrix} \tag{2-25}$$

As there are off-diagonal terms in the stiffness matrix, the rotational and translational motions are coupled in the physical-space-coordinate system. Here, it is assumed that the following relationship holds between the modal- and physical-space coordinates through the modal transformation matrix:

$$\{\boldsymbol{X}\} = [\boldsymbol{\phi}]\{\boldsymbol{X_d}\} \tag{2-26}$$

where $(\ \ )_d$ indicates value in modal-space coordinate.

By multiplying the transpose matrix of $[\boldsymbol{\phi}]$ from the left side after substituting Eq. (2-26) into Eq. (2-23), Eq. (2-23) can be decomposed as follows:

$$[\boldsymbol{M_d}]\{\ddot{\boldsymbol{X}}_{\boldsymbol{d}}\} + [\boldsymbol{C_d}]\{\dot{\boldsymbol{X}}_{\boldsymbol{d}}\} + [\boldsymbol{K_d}]\{\boldsymbol{X_d}\} = [\boldsymbol{\phi}]^T\{\boldsymbol{F}\} \tag{2-27}$$

where

$$[\boldsymbol{M_d}] = [\boldsymbol{\phi}]^T[\boldsymbol{M}][\boldsymbol{\phi}], [\boldsymbol{C_d}] = [\boldsymbol{\phi}]^T[\boldsymbol{C}][\boldsymbol{\phi}], [\boldsymbol{K_d}] = [\boldsymbol{\phi}]^T[\boldsymbol{K}][\boldsymbol{\phi}] \tag{2-28}$$

To specifically obtain the modal matrix of the dual-inertia model in a ball-screw-driven system, the free vibration in Eq. (2-23) is considered, that is, the right-hand side of Eq. (2-23) is set to zero. Then, the solution of free vibration is assumed as follows:

$$\{\boldsymbol{X}\} = \{\boldsymbol{\varphi}\}e^{\lambda_r t} \tag{2-29}$$

where λ_r is the eigenvalue and $\{\boldsymbol{\varphi}\}$ is the corresponding eigenvector.

Consequently, the characteristic equation is derived as follows:

$$(\lambda_r^2[\boldsymbol{M}] + \lambda_r[\boldsymbol{C}] + [\boldsymbol{K}])\{\boldsymbol{\varphi}\}e^{\lambda_r t} = \{\boldsymbol{0}\} \tag{2-30}$$

For Eq. (2-30) to have meaningful solutions, the determinant on the left-hand side in Eq. (2-30) must be zero. However, as it becomes a quadratic equation of the eigenvalue, it cannot be solved analytically in general; hence, the proportional viscosity damping is assumed, as follows:

$$[\boldsymbol{C}] = \alpha_c[\boldsymbol{M}], \text{ where } \alpha_c = C_m/M_m = C_t/M_t \tag{2-31}$$

where $\alpha_c\,[\mathrm{N \cdot s/(m \cdot kg)}]$ is a constant for proportional damping. Viscous damping is assumed to be proportional to mass only, as structural damping is not modeled in this study.

By substituting Eq. (2-31) into Eq. (2-30), Eq. (2-30) can be rearranged as follows:

$$(-p_r^2[\boldsymbol{M}] + [\boldsymbol{K}])\{\boldsymbol{\varphi}\}e^{\lambda_r t} = \{\boldsymbol{0}\} \tag{2-32}$$

where

$$p_r^2 = -(\lambda_r^2 + \alpha_c\lambda_r) \tag{2-33}$$

As the determinant on the left-hand side of Eq. (2-32) becomes a quadratic equation for p_r^2, it can be analytically solved as follows:

$$(-p_r^2 M_m + K_r)(-p_r^2 M_t + K_r) - K_r^2 = 0 \;\rightarrow \therefore p_{r1}^2 = 0, p_{r2}^2 = \frac{M_m + M_t}{M_m M_t}K_r \tag{2-34}$$

As a result, the eigenvectors of the rigid-body and vibration modes can be defined by substituting the solutions of Eq.(2-34) into Eq. (2-32):

$$\begin{bmatrix} K_r & -K_r \\ -K_r & K_r \end{bmatrix}\{\boldsymbol{\varphi_1}\}e^{\lambda_{r1}t} = \begin{Bmatrix} 0 \\ 0 \end{Bmatrix} \rightarrow \{\boldsymbol{\varphi_g}\} \equiv \{\boldsymbol{\varphi_1}\} = \begin{Bmatrix} 1 \\ 1 \end{Bmatrix} \tag{2-35}$$

$$\begin{bmatrix} K_r/\alpha_r & K_r \\ K_r & \alpha_r K_r \end{bmatrix}\{\boldsymbol{\varphi_2}\}e^{\lambda_{r2}t} = \begin{Bmatrix} 0 \\ 0 \end{Bmatrix} \rightarrow \{\boldsymbol{\varphi_v}\} \equiv \{\boldsymbol{\varphi_2}\} = \begin{Bmatrix} 1 \\ -1/\alpha_r \end{Bmatrix} \tag{2-36}$$

Finally, the modal matrix is defined based on Eqs. (2-35) and (2-36), as follows:

$$[\boldsymbol{\phi}] = \begin{bmatrix} \{\boldsymbol{\varphi_g}\} & \{\boldsymbol{\varphi_v}\} \end{bmatrix} = \begin{bmatrix} 1 & 1 \\ 1 & -1/\alpha_r \end{bmatrix} \tag{2-37}$$

where $(\;)_g$ and $(\;)_v$ are values in rigid-body and vibration mode, respectively.

By applying the derived modal matrix based on Eqs. (2-26), (2-28), and (2-31), the physical-space system is transformed into modal-space system:

$$\{\boldsymbol{X_d}\} = [\boldsymbol{\phi}]^{-1}\{\boldsymbol{X}\} \;\rightarrow \therefore \begin{Bmatrix} X_g \\ X_v \end{Bmatrix} = \frac{1}{\alpha_r + 1}\begin{Bmatrix} X_m + \alpha_r X_t \\ \alpha_r(X_m - X_t) \end{Bmatrix} \tag{2-38}$$

$$\begin{aligned}
[\boldsymbol{M_d}] &= [\boldsymbol{\phi}]^T[\boldsymbol{M}][\boldsymbol{\phi}] = \begin{bmatrix} M_m + M_t & 0 \\ 0 & (1 + 1/\alpha_r)M_m \end{bmatrix} = \begin{bmatrix} M_g & 0 \\ 0 & M_v \end{bmatrix} \\
[\boldsymbol{K_d}] &= [\boldsymbol{\phi}]^T[\boldsymbol{K}][\boldsymbol{\phi}] = \begin{bmatrix} 0 & 0 \\ 0 & (1 + 1/\alpha_r)^2 K_r \end{bmatrix} = \begin{bmatrix} 0 & 0 \\ 0 & K_v \end{bmatrix} \\
[\boldsymbol{C_d}] &= [\boldsymbol{\phi}]^T[\boldsymbol{C}][\boldsymbol{\phi}] = \alpha_c[\boldsymbol{\phi}]^T[\boldsymbol{M}][\boldsymbol{\phi}] = \begin{bmatrix} \alpha_c M_g & 0 \\ 0 & \alpha_c M_v \end{bmatrix} = \begin{bmatrix} C_g & 0 \\ 0 & C_v \end{bmatrix}
\end{aligned} \tag{2-39}$$

Eqs. (2-38) and (2-39) show that the center-of-mass motion independent of the spring element is extracted in the rigid-body mode by multiplying the inertia ratio as a weight with the stage position. In contrast, the vibration mode represents the relative motion between two masses, as it accounts for the difference in positions. In addition, all off-

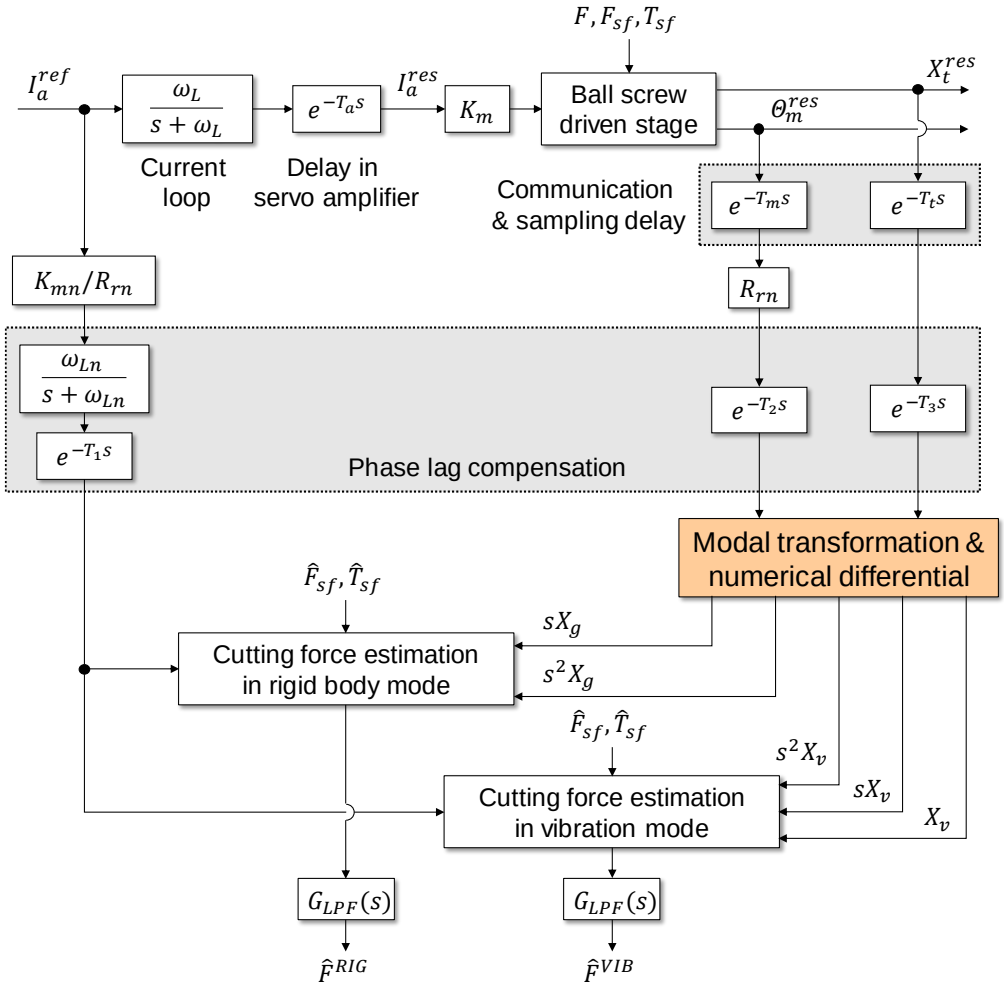

Fig. 2-7 Schematic block diagram of cutting force estimation in modal space

diagonal terms become zero, which means that each mode is an SDoF system that does not interfere with the other systems.

The explicit form of the motion equation in modal space can be expressed as follows:

$$\begin{bmatrix} M_g & 0 \\ 0 & M_v \end{bmatrix} \begin{Bmatrix} \ddot{X}_g \\ \ddot{X}_v \end{Bmatrix} + \begin{bmatrix} C_g & 0 \\ 0 & C_v \end{bmatrix} \begin{Bmatrix} \dot{X}_g \\ \dot{X}_v \end{Bmatrix} + \begin{bmatrix} 0 & 0 \\ 0 & K_v \end{bmatrix} \begin{Bmatrix} X_g \\ X_v \end{Bmatrix} = \begin{bmatrix} 1 & 1 \\ 1 & -1/\alpha_r \end{bmatrix} \begin{Bmatrix} (K_m I_a^{ref} - T_{sf})/R_r \\ -F - F_{sf} \end{Bmatrix} \tag{2-40}$$

Therefore, based on Eq. (2-40), the estimation method of the cutting force can be derived in both rigid-body and vibration modes by the same procedure as the conventional disturbance estimation techniques:

$$\hat{F}^{RIG} = G_{LPF}\left(\frac{K_{mn}}{R_{rn}} I_a^{ref} - M_{gn}\ddot{X}_g - C_{gn}\dot{X}_g - \frac{1}{R_{rn}}\hat{T}_{sf} - \hat{F}_{sf}\right) \tag{2-41}$$

$$\hat{F}^{VIB} = G_{LPF}\left\{-\alpha_{rn}\left[\frac{K_{mn}}{R_{rn}} I_a^{ref} - \left(M_{vn}\ddot{X}_v + C_{vn}\dot{X}_v + K_{vn}X_v\right) - \frac{1}{R_{rn}}\hat{T}_{sf} + \frac{1}{\alpha_{rn}}\hat{F}_{sf}\right]\right\} \tag{2-42}$$

where $\hat{F}^{RIG}$ [N] and $\hat{F}^{VIB}$ [N] are cutting forces estimated in rigid-body and vibration modes, respectively.

A schematic block diagram of the cutting force estimation in modal space is shown in Fig. 2-7. Note that the estimation formula of the rigid-body mode in Eq. (2-41) is proven to be equivalent to that of MEDOB in Eq. (2-22) [259]. Therefore, the rigid-body mode is not dealt with in later comparative studies.

2.3. Characteristics of each observer

In this section, the characteristics of cutting force techniques based on DOB, LDOB, MEDOB, and vibration mode-based disturbance observer (VMDOB) are discussed through numerical simulations. By substituting Eq. (2-4) into Eq. (2-13) in Laplace domain, so that $X_m = R_r\Theta_m$ disappears, the following equation can be derived:

$$\hat{F}_{ls}^{DOB} = -G_{LPF}(s)\cdot\frac{\alpha_r(s+2\zeta_t\omega_t)^2 s^2}{sD_r(s)}\cdot\frac{K_m}{R_r}I_a^{ref} + G_{LPF}(s)\cdot\frac{\omega_r^2 s^2 + 2\alpha_r(\zeta_r+\zeta_t)\omega_t^3 s}{sD_r(s)}\cdot F_{ls} \tag{2-43}$$

where F_{ls} [N] is load force at the load side such as cutting force.
Note that the friction terms and parameter errors of the nominal values are ignored for simplification. Eq. (2-43) shows that the disturbance TF between the load force (i.e., cutting force in machining process) and the estimated force based on DOB in a dual-inertia-modeled ball-screw-driven system can be described as follows:

$$\frac{\hat{F}_{ls}^{DOB}}{F_{ls}} = G_{LPF}(s)\cdot\frac{\omega_r^2 s^2 + 2\alpha_r(\zeta_r+\zeta_t)\omega_t^3 s}{sD_r(s)} \tag{2-44}$$

Fig. 2-8 shows an exemplary disturbance TF of Eq. (2-44). The physical parameters of

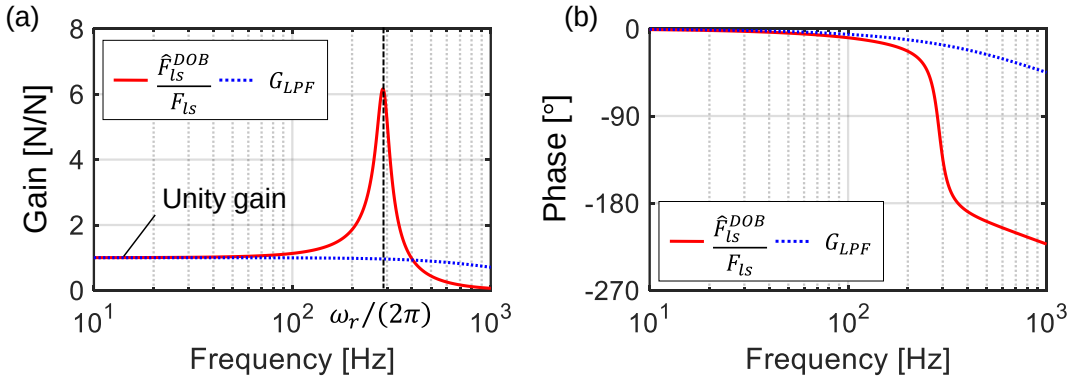

Fig. 2-8 Disturbance TF between actual cutting force and estimated force based on DOB in dual-inertia-modeled ball-screw-driven system: (a) gain characteristic, (b) phase characteristic (physical parameters are the same as X-axis of the experimental system shown in Table 2-1: $M_t = 7.9$ kg, $M_m = 100$ kg, $C_t = 2.4\times10^3$ N·s/m, $C_m = 2.8\times10^3$ Ns/m, $K_r = 24$ N/μm, $l_p = 5.0$ mm. Additionally, LPF of $G_{LPF}(s) = g_{LPF}/(s+g_{LPF})$ with $g_{LPF} = 1000$ rad/s is applied as an example.)

the ball-screw-driven system in the simulation coincide with the values identified in the X-axis of the real experimental setup in section 2.4 (Table 2-1).

In the low-frequency region where the rotational and translation systems together behave as a nearly rigid-body motion, almost a unity gain of disturbance TF can be observed (i.e., the estimated cutting force is expected to be accurate). However, the disturbance TF obtains high gain around the axial resonance frequency, that is, the cutting force is overestimated in this vicinity. In addition, the gain characteristics are considerably attenuated with a large phase delay over the actual cutting force in the higher-frequency region. This is because the mechanical transfer characteristics from the stage to the motor act as LPF. In summary, Fig. 2-8 indicates that a bandwidth with a reliable accuracy of the DOB-based cutting force estimation is limited due to the axial mode of the ball-screw-driven system. When the DOB is applied to the linear-motor-driven stage (Fig. 2-3(b)), the disturbance TF ideally exhibits the same characteristic as the applied LPF, as the estimation method of DOB is derived based on the motion equation of a single-inertia model (blue-dot line in Fig. 2-8).

As LDOB, MEDOB, and VMDOB are derived based on the dual-inertia model, their disturbance TF ideally follows the characteristic of the applied LPF even in the ball-screw-driven system. This means that the estimated cutting force is ideally the same in all techniques. Nevertheless, as the component forces contributing to the estimated cutting force differ due to the different estimation method, the characteristics of each method also differ. Fig. 2-9 shows the gain characteristics of disturbance TF of the estimated cutting force in each technique. This figure is obtained from the stage-position/motor-angle response and current reference when applying the swept (cutting) force to the movable stage, emulated in the servo simulator of the ball-screw-driven system. Simultaneously, the disturbance TFs in terms of each component forces are also depicted.

In MEDOB (Fig. 2-9(a)), the contribution of the equivalent motor-thrust force $K_{mn}I_a^{ref}/R_{rn}$ dominates the cutting force estimation, although its gain is not unity; that is, the equivalent inertia force of rotating mass compensates for the gain characteristic of the resultant estimated cutting force. Around the resonance frequency (i.e., 286 Hz), both inertia forces of rotational and translational masses have high gain. However, the inertia forces cancel each other out because of their opposite phases, and consequently, the other component forces contribute to the cutting force estimation. Overall, in MEDOB, the cutting force is reconstructed through an elaborate balance of many component forces. This indicates that MEDOB is sensitive to the phase differences between signals that upset the delicate signal balances. This is especially noticeable near the resonance frequency, where the phase difference between two masses changes sharply. In the enlarged view of Fig. 2-9(a), the gain characteristics of MEDOB slightly deteriorate around the resonance, even in a very ideal simulation. This suggests that the estimated cutting force in MEDOB is

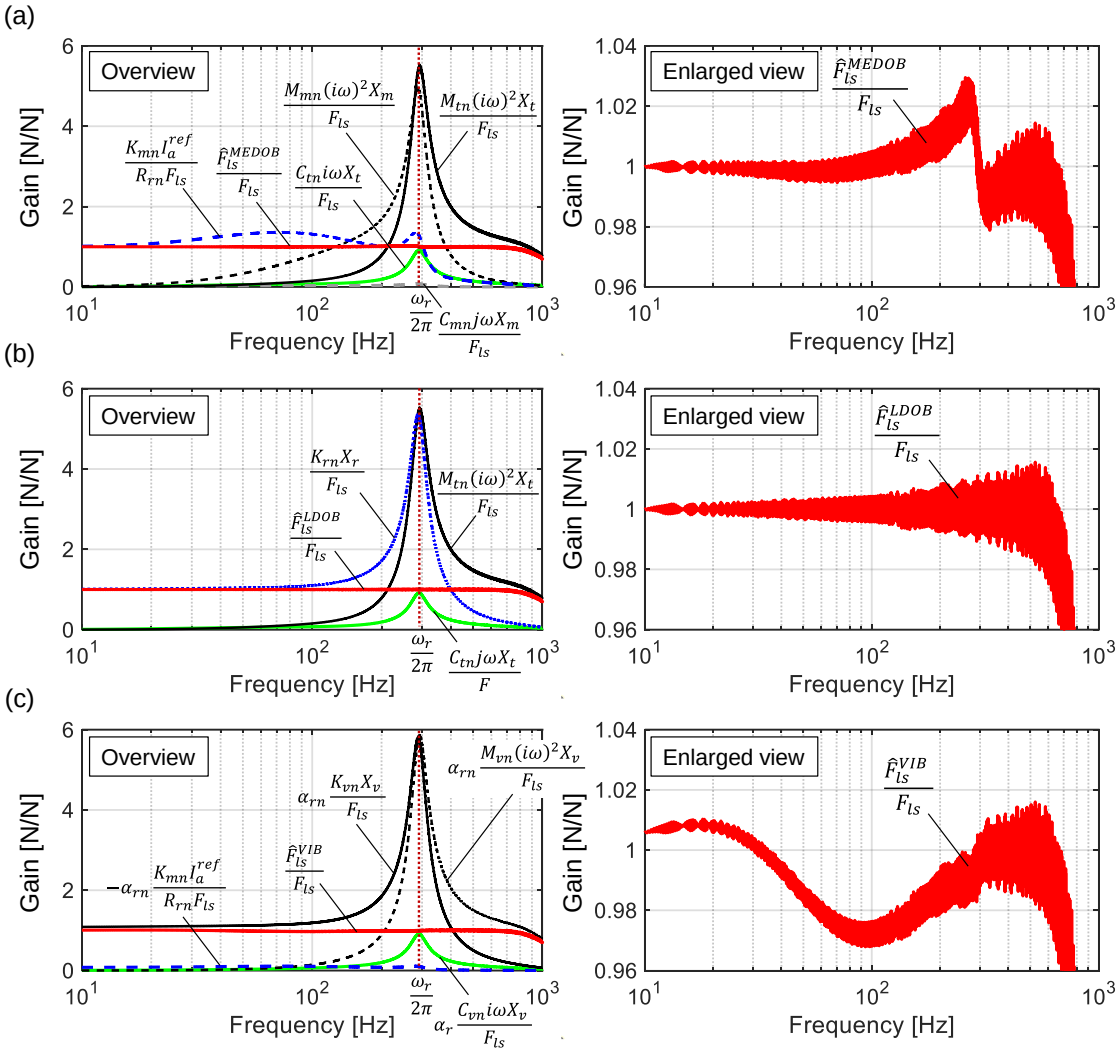

Fig. 2-9 Gain characteristics of disturbance TF between the actual cutting force and estimated force in a dual-inertia-modeled ball-screw-driven system: (a) MEDOB, (b) LDOB, (c) VMDOB (parameter conditions remain the same as those in Fig. 2-8)

sensitive to the slight deviation in the balance of component forces, including phase shift, which might be induced by numerical differential processing. Note that the enlarged view looks noisy because of the numerical signal processing for calculation. It is not evitable and has no notable meaning.

In LDOB (Fig. 2-9(b)), the balance between the component forces is simple, because of only focusing on the load-side motion equation. Almost only the restoring force represented by axial stiffness contributes to the estimated cutting force in a low-frequency region. At the resonance frequency, although the gains of inertia force and restoring force are amplified, they cancel each other out because of their opposite phase shifts. Consequently, the contribution of the damping force relatively increases. In a very high-frequency region, almost only inertia force contributes to the cutting force estimation. As the restoring force is directly considered, LDOB is less sensitive to the deviation of the force-component

balance than MEDOB, as seen in the enlarged view.

VMDOB appears similar to LDOB in the gain characteristic (Fig. 2-9(c)). Expanding Eq. (2-42) into a form expressed by physical parameters yields the following equation:

$$\hat{F}^{VIB} = G_{LPF}\left[-\alpha_{rn}\frac{K_{mn}}{R_{rn}}I_a^{ref} + M_{tn}\ddot{X}_r + C_{tn}\dot{X}_r + (1+\alpha_{rn})K_{rn}X_r + \frac{\alpha_{rn}}{R_n}\hat{T}_{sf} - \hat{F}_{sf}\right] \tag{2-45}$$

When the inertia ratio is very small, as in the simulation conditions (i.e., $\alpha_r = 0.079$), the terms weighted by the inertia ratio can be neglected. Furthermore, the motor vibrational velocity/acceleration induced by the cutting force are expected to be much smaller than that on the stage side (i.e., $\ddot{X}_r \approx -\ddot{X}_t,\ \dot{X}_r \approx -\dot{X}_t$). Consequently, the estimation method of VMDOB can be regarded as

$$\hat{F}^{VIB} \approx G_{LPF}\left(-M_{tn}\ddot{X}_t - C_{tn}\dot{X}_t + K_{rn}X_r - \hat{F}_{sf}\right) \tag{2-46}$$

This is the same as the estimation method of LDOB in Eq. (2-18). In summary, VMDOB and LDOB are almost the same in a machine with a low inertia ratio.

However, the gain characteristic of disturbance TF in VMDOB is deteriorated, as observed in the enlarged view of Fig. 2-9(c). This is because the physical parameters in the simulation are inconsistent with the proportional viscous damping in Eq. (2-31), which is assumed for deriving Eq. (2-42): $C_m/M_m = 30, C_t/M_t = 304 \rightarrow C_m/M_m \neq C_t/M_t$. Although VMDOB would be useful when integrated with the existing process monitoring techniques established for the SDoF system, an exact assumption of the proportional viscous damping rarely holds in real machine tools. Therefore, LDOB might be a more reasonable strategy.

It has been confirmed that VMDOB can estimate the cutting force less than the maximum static friction force in the stopped axis, whereas MEDOB cannot [259]. This is because VMDOB directly considers the restoring force induced by the axial stiffness term. As LDOB is similar to VMDOB, it is inferred that LDOB can also capture the cutting force in the stopped axis. Here, the axial stiffness of the ball-screw-driven system can be theoretically expressed by a series connection of several springs of mechanical components:

$$K_r = \frac{1}{\frac{1}{K_b}+\frac{1}{K_s}+\frac{1}{K_{nut}}} = \frac{1}{\frac{1}{K_{bs}}+\frac{1}{K_{nut}}} \tag{2-47}$$

where K_b [N/m], K_s [N/m], and K_{nut} [N/m] are axial stiffnesses of bearing, screw shaft, and nut, respectively. K_{bs} [N/m] is the summation of K_b and K_s. Note that the attachment rigidities of the nut and bearing are ignored as they are sufficiently high in general.

When the screw shaft is doubly anchored at both ends by using the support bearings, the sum of axial stiffness of the bearing and screw shaft is expressed as follows:

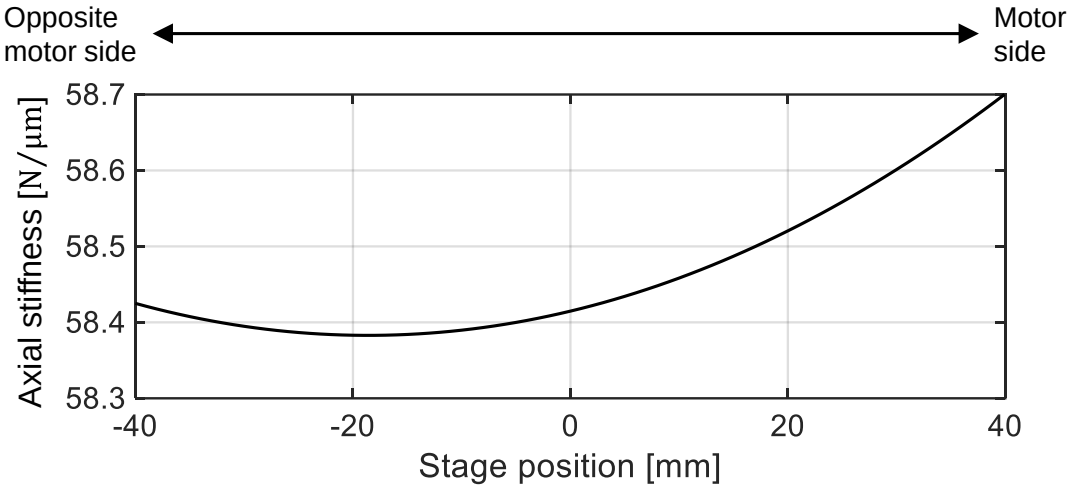

Fig. 2-10 Exemplary theoretical characteristic of axial stiffness in double-anchored ball-screw-driven stage (design values in X-axis of the prototype double-column-type machine tool are used: $K_{b1} = 104$ N/μm, $K_{b2} = 94$ N/μm, $K_{nut} = 98.6$ N/μm, $E_s = 206 \times 10^9$ Pa, $d_s = 15$ mm, $L_s = 280$ mm)

$$K_{bs} = \frac{1}{\frac{1}{K_b} + \frac{1}{K_s}} = \frac{1}{\frac{1}{K_{b1}} + \frac{4X_A}{\pi d_s^2 E_s}} + \frac{1}{\frac{1}{K_{b2}} + \frac{4(L_s - X_A)}{\pi d_s^2 E_s}} \tag{2-48}$$

where X_A [m] is absolute stage position from the motor-side bearing, d_s [m] is diameter of screw shaft, E_s [Pa] is Young's modulus of screw shaft, L_s [m] is length of screw shaft, K_{b1} [N/m] is axial stiffness of bearing at the motor side, and K_{b2} [N/m] is axial stiffness of bearing at opposite motor side.

Therefore, the resultant axial stiffness depends on the stage position under the condition of double anchor support. An example profile of axial stiffness to indicate its tendency according to the stage position is shown in Fig. 2-10. The design values on the X-axis of the developed three-axis ball-screw-driven machine tool (subsection 2.4.1) are used for the calculation, although Young's modulus is set as a literature value of steel. Note that the plotted data are shifted so that the zero position denotes the center of the screw shaft, and the view around the center position from -40 to 40 mm is enlarged in Fig. 2-10. As shown in Fig. 2-10, the axial stiffness increases around both ends of the motor and anti-motor sides. Especially, the axial stiffness has a large deviation around the motor side; hence, the nominal stiffness value in LDOB and VMDOB must be compensated depending on the stage position for an accurate cutting force estimation. If the compensation is difficult, MEDOB is advantageous, that it, is not necessary to identify the stiffness, although MEDOB has difficulty in estimating the cutting force in the stopped axes under the effect of static friction [259].

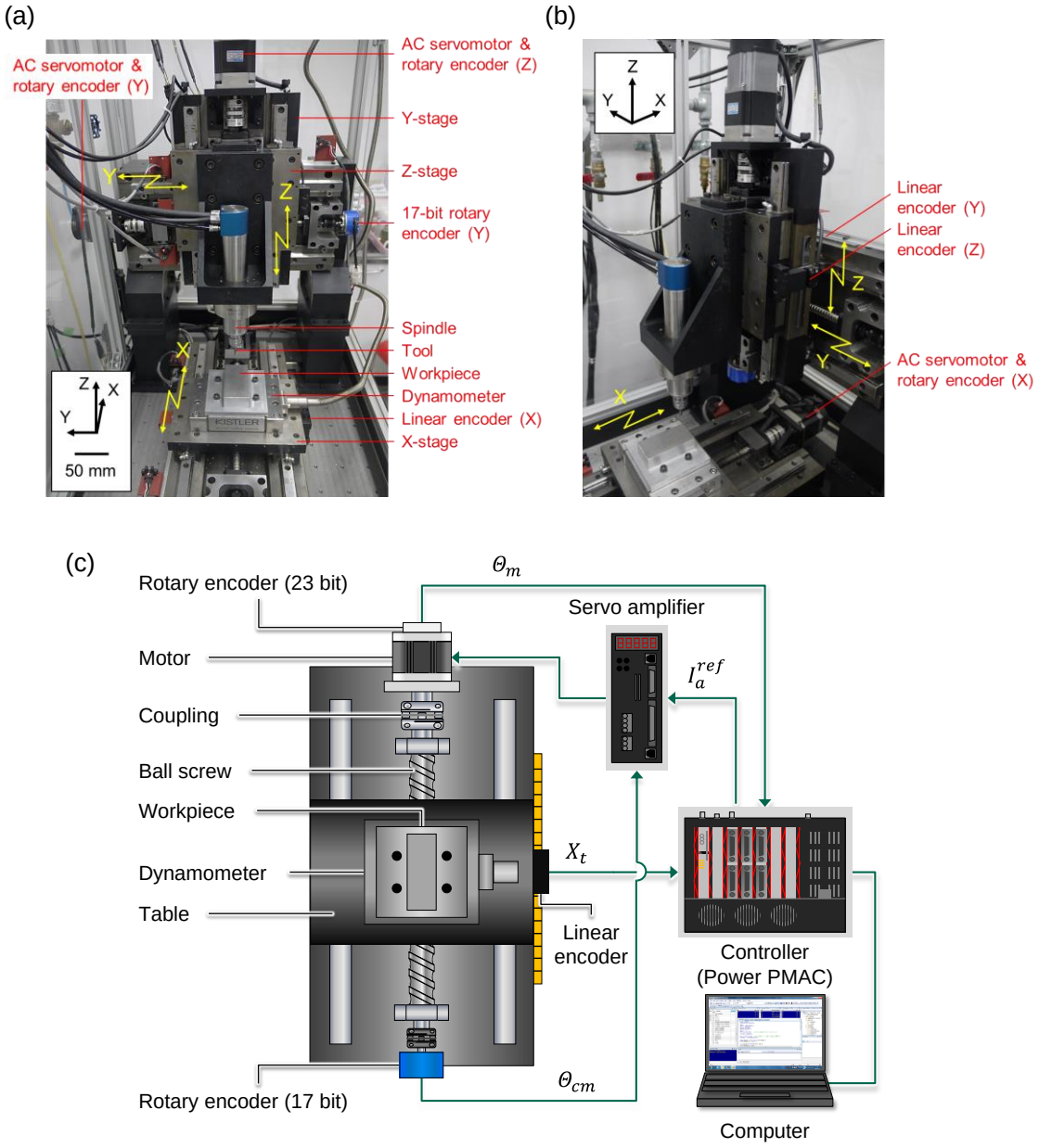

Fig. 2-11 Configuration of prototype three-axis double-column-type machine tool with ball-screw-driven stage: (a) Front view, (b) oblique view, and (c) signal flow of control system

2.4. Experimental comparison

2.4.1. Experimental setup

Fig. 2-11 shows a three-axis double-column prototype machine tool with a ball-screw-driven system. The ball screw is connected to a synchronous AC servomotor with a low cogging torque through a disc-type coupling and has a small torque fluctuation depending on the nut position. In addition, rotary and linear encoders are mounted on all translational axes; hence, the motor current, motor angle, and stage position can be used as the internal

information. Each encoder has a high resolution to reduce the quantization error associated with differential processing in the high-frequency region. An additional rotary encoder (17 bit) is also installed on the anti-motor side to calculate the motor electric angle, although it is not used for cutting force estimation. The workpiece is fixed on the X-stage. A piezoelectric table dynamometer (Type 9129AA from Kistler) is equipped under the workpiece to measure the cutting force as a reference. A spindle unit is installed on the Z-stage, which is attached on the Y-stage.

In Fig. 2-11(c), the configuration of the machine tool control system is also described. Although only the configuration of the X-stage is shown as a representative, the signal flow is the same for all axes. As three encoders are attached to each axis (i.e., XYZ), nine position information are fed back to the controller. The signals from the 23-bit rotary and linear encoders are sent directly to the controller, whereas those from the 17-bit rotary encoders are sent to the controller through the servo amplifier. In the controller, a torque command is generated for each servo cycle by calculating the corresponding current command based on the feedback signals obtained from the 23-bit rotary encoder and linear encoder. After the current command value is converted to the voltage command value, the voltage command is D/A converted in the interface card and applied to the servo amplifier. To perform the current control of the motor in the servo amplifier, the angle information of the 17-bit rotary encoder is used for calculating the electric angle. The 17-bit rotary encoder is not used for cutting force estimation.

In this study, a P-P controller with feed-forward compensation for disturbance cancellation by MEDOB is adopted as the positioning control system, instead of the P-PI controller generally used for machine tools. Additionally, velocity and acceleration feed-forward commands are applied to enhance the responsiveness. Note that the controller specifications for positioning do not affect the cutting force estimation, as the cutting force observers are assembled inside the position and velocity feedback loop. The detailed specifications of the experimental setup are summarized in **Appendix A**.

Fig. 2-12 shows the FRFs obtained from the equivalent motor thrust force to the stage acceleration and the equivalent motor acceleration in translational motion, obtained by a sinusoidal motor swept excitation. The excitation frequency was swept logarithmically from 0.1 Hz to 1 kHz, and the tests were applied to the XY-axes. In an ideal dual-inertia model without system delay times, the phase delay of FRF between the motor-angular acceleration and the motor current does not fall below 0°. Similarly, the phase delay of FRF between the stage acceleration and motor current does not fall below -180°. However, the phase lags of FRFs continue to increase with the frequency if there are time delay elements in the system. As this phenomenon was observed in the experimental system and could not be ignored, the phase-lag compensations were applied before calculating the FRFs. The amount of phase-

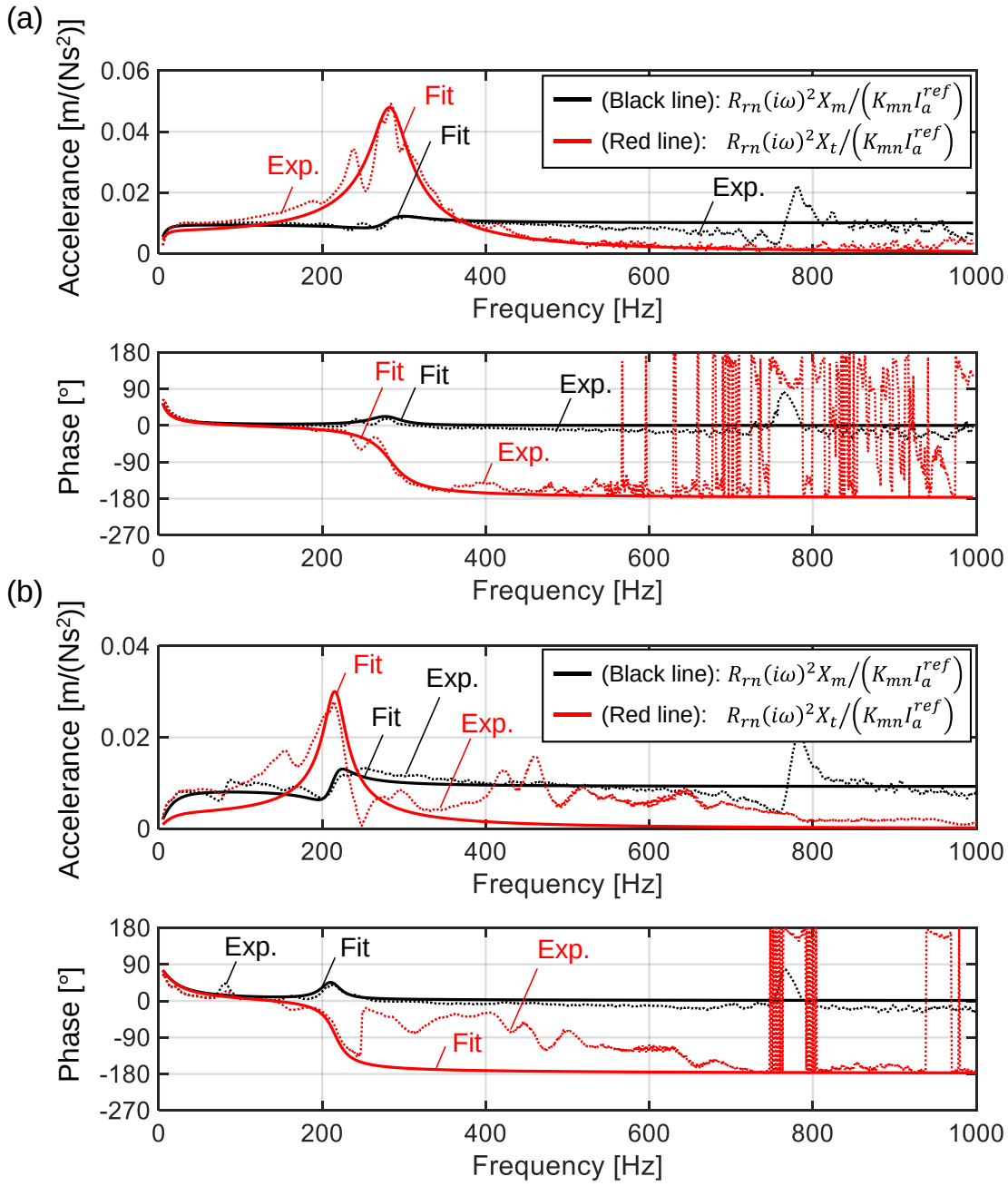

Fig. 2-12 Experimental FRFs from the equivalent motor thrust force to encoder accelerations: (a) X-axis, (b) Y-axis (pitch length is 5 mm in both XY-axes, and therefore, the rotation-to-translation transform coefficient is $R_{rn} = 7.96 \times 10^{-4}$ m/rad)

lag compensation was determined by trial and error, so that the resultant phase shifts of FRFs become flat in a high-frequency region, similar to an ideal dual-inertia model.

Next, the physical parameters of the dual-inertia model were iteratively tuned using the MDoF curve-fitting technique with a nonlinear least square method (LSM) [264,265], such that the sum of residual errors between the model FRFs based on Eq. (2-4) and the experimental FRFs would be minimized in the defined frequency range.

Table 2-1 Physical parameters for dual inertia model identified by motor sine swept excitation

Axis	X	Y
Resonance frequency in dual-inertia system $\omega_r/2\pi$ [Hz]	286	228
Total inertia of motor, coupling, and ball screw J_{mn} [kg·m^2]	6.3×10^{-5}	6.9×10^{-5}
Equivalent value of J_m in translational motion M_{mn} [kg]	1.0×10^{2}	1.1×10^{2}
Total movable mass M_{tn} [kg]	7.9	24
Inertia ratio α_r [-]	0.079	0.22
Damping coefficient of rotational element D_{mn} [N·m·s/rad]	1.8×10^{-3}	8.1×10^{-3}
Equivalent value of D_m in translational motion C_{mn} [N·s/m]	2.8×10^{3}	1.3×10^{4}
Damping coefficient of translational element C_{tn} [N·s/m]	2.4×10^{3}	4.2×10^{3}
Axial stiffness of feed screw system K_{rn} [N/μm]	24	40
Bandwidth of current loop ω_{Ln} [rad/s]	5000 (catalogue value)	
Dead time T_a, T_m, T_t [ms]	0.2, 0.2, 0.2	
Dead time for phase lag compensation T_1, T_2, T_3 [ms]	0.4, 0, 0	

Table 2-2 Minimum detectable force fluctuation per sampling period

Axis	X	Y
Inertia force of rotational elements, $M_{mn}\ddot{X}_m$ [N]	5.9	6.5
Inertia force of translational elements, $M_{tn}\ddot{X}_t$ [N]	0.19	0.59
Damping force of rotational elements, $C_{mn}\dot{X}_m$ [N]	0.017	0.076
Damping force of translational elements, $C_{tn}\dot{X}_t$ [N]	0.0059	0.010
Restoring force induced by axial stiffness, $K_{rn}X_r$ [N]	0.0059	0.0098
Inertia force in vibration modal space, $M_{vn}\ddot{X}_v$ [N]	2.4	2.7
Damping force in vibration modal space, $C_{vn}\dot{X}_v$ [N]	0.074	0.047
Elastic force in vibration modal space, $K_{vn}X_v$ [N]	0.080	0.054
Sampling frequency [kHz]	10	
Resolution of stage response [nm]	0.244	
Resolution of angular response [nm]	0.596	

Table 2-1 shows the identified physical parameters of dual-inertia model for using the observers. As the signal flow is the same in the XY-axes, dead times in the system become almost the same on both axes. The design values of $[M_m, M_t]$ are roughly [111, 10] kg and [111, 21] kg in X- and Y-axis, respectively; hence, the identified values for the dual-inertia model expressing axial resonance appear reasonable.

Table 2-2 shows the theoretical resolution of each acting force calculated based on the identified physical parameters and machine specifications, such as the sampling frequency and encoder resolutions. Note that the minimum detectable forces of restoring force and vibration mode were calculated based on the specification of a high-resolution linear encoder. The resolutions of both rotary and linear encoders were designed to be sufficiently high to sense the very high-frequency small cutting force (e.g., 2–3 kHz). In this machine, it was confirmed that the 17-bit rotary encoder, whose resolution in translational motion is 38 nm,

was not sufficient to estimate the high-frequency cutting force variation, since the dynamic variation of angle responses induced by load forces significantly decreases in the high frequency range due the structure and friction damping, especially in such low-inertia machine tool [266]. Consequently, quantization errors in angle measurement become non-negligible especially when applying differential processing. Since the contribution of inertia force to the estimated cutting force significantly increases in high frequencies, it is important to enhance the resolutions of both linear and rotary encoders.

Fig. 2-12 shows that, overall, the dual-inertia model fits well in the X-axis, although another high-frequency mode can be observed around 800 Hz. This mode has been confirmed to be a torsional mode of a ball screw; hence, it is clearly observed in motor angular acceleration. As the XY-axes use the same ball screw, the torsional mode is observed at the same frequency on the Y-stage as well. Nevertheless, almost no resonance peak due to torsional mode appears on the stage accelerations in both X-and Y-axis.

Unlike the X-axis, the experimental FRFs between the motor thrust force and encoder accelerations on the Y-axis cannot be expressed reasonably by the dual inertia model overall, as shown in Fig. 2-12(b). Especially, the gain characteristic of FRF between the motor thrust force and the stage acceleration obtained by linear encoder (i.e., red line) does not fit well with the dual inertia model. This is attributable to the excited structural dynamics, including the Z-stage and spindle units, attached on the Y-stage. The result suggests that the multi-body dynamics on the Y-stage is not negligible, and the reliability of the observer-based cutting force estimation is strongly limited, even in the low-frequency region.

2.4.2. Exemplary results representing observer characteristics

A comparative study in terms of the cutting-force-estimation performance in each observer technique was conducted through a series of actual cutting tests. To evaluate the observer performances, the cutting force measured by the piezoelectric table dynamometer was used as a reference. In previous studies done by Yamada et al. [257,259,266], the influence of error factors in sensorless cutting force estimation, such as delay times in control system, disturbance fluctuations (e.g., torque ripple), and quantization errors in angle/position measurements, has been evaluated in detail; hence, such error factors are not discussed in this subsection. Only experimental results to explain the essential properties in observer techniques are demonstrated.

Fig. 2-13 shows a schematic for the experimental procedure. The cutting forces in XY-direction were simultaneously estimated by the observer techniques implemented in the X- and Y-axis ball-screw-driven system while feeding the X- or Y-stage (Fig. 2-11). The cutting and system conditions are tabulated in Table 2-3. As a yawing mode of the X-stage was observed around 800 Hz in addition to the torsional modes of the ball screws in XY-axes, the cutoff frequency of LPF was set to 500 Hz to eliminate the influence of these modes. In

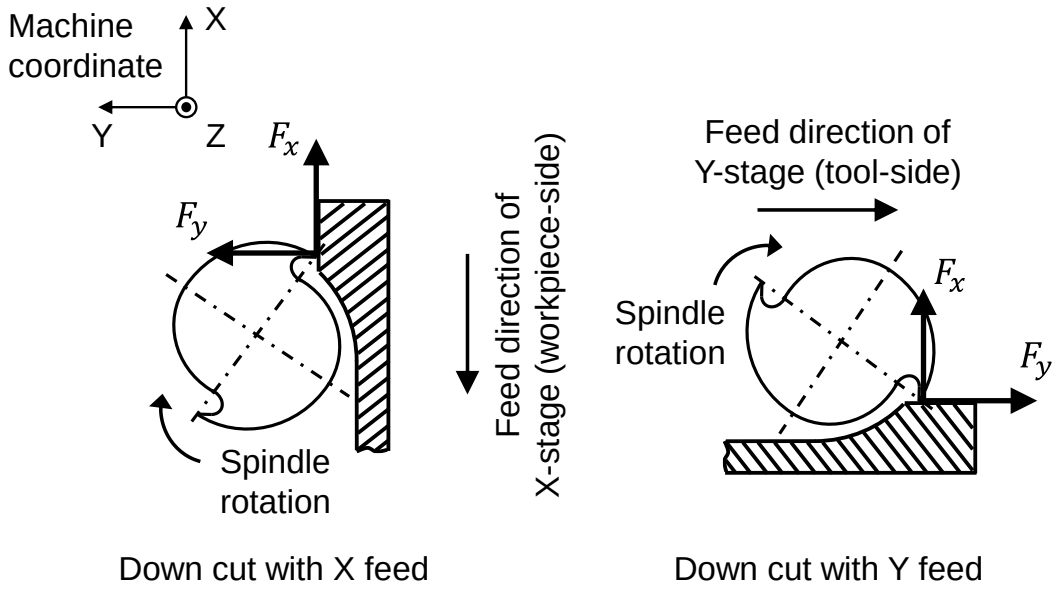

Fig. 2-13 Schematic of the cutting tests for comparative study

Table 2-3 Cutting conditions for comparative study

Tool type	Square endmill ($D = 6$ mm, $N_c = 2$)
Feed per tooth [μm]	30
Spindle speed [min^{-1}]	1000, 7000, 13000
Cutting type	Down cut
Axial depth of cut [mm]	2.0
Radial depth of cut [mm]	1.5 (quarter immersion)
Sampling frequency of signals [kHz]	10
Cutoff frequency of LPF for observer [Hz]	500

MEDOB, LDOB, and VMDOB, the cutting force is estimated based on the dual inertia model representing axial dynamics of ball-screw-driven system; hence, for accurate cutting force estimation, the LPF should be set to avoid the effect of other higher frequency modes.

When the cutting force was estimated in the stage-moving axis, the friction force was compensated by the recording method using the same approach as that used by Yamada et al. [257,259]. In the recording method, the air-cutting data obtained by the preliminary idling test in advance are subtracted from each servo signal under cutting to extract the cutting force. Note that the friction forces often change according to the table position, workpiece mass, and the use of chip cover [267]. Nevertheless, the position-dependent fluctuation of friction force has high repeatability [257,267,268]. Therefore, the recording method can most reliably compensate for the friction forces in the cutting force observer, although it results in double process time. To avoid the preliminary air cutting test in each process, the model-based approach with an established friction model, such as the Tustin model [269], Lund-Grenoble (LuGre) model [40,270], or generalized Maxwell-slip (GMS) model [20,271], is a practical option, although the position-dependent friction cannot be

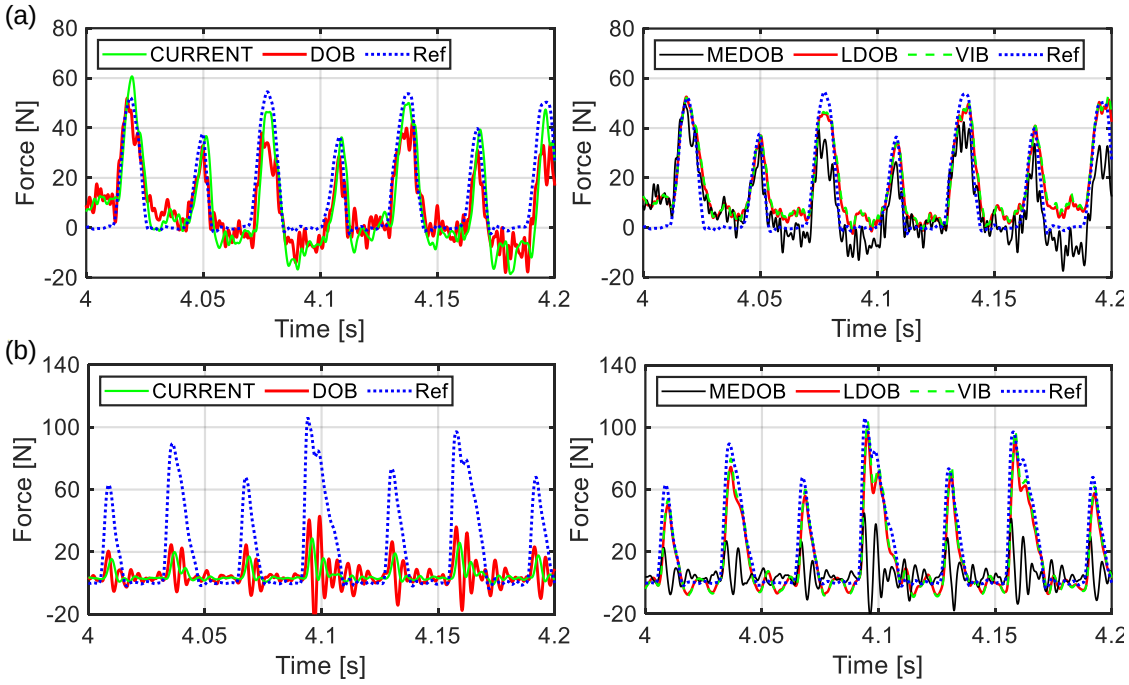

Fig. 2-14 Cutting force in X-direction estimated by each observer technique under 1000 min^{-1}: (a) feeding X-stage (Y-stage stop), (b) feeding Y-stage (X-stage stop)

directly treated. On the stage-fixed axis, friction compensation was not performed.

Fig. 2-14 shows the estimation results of X-direction cutting force under 1000 min^{-1} (i.e., spindle rotational and tooth-passing frequencies are 16.7 and 33.3 Hz, respectively). In Fig. 2-14(a) (i.e., X-stage is fed), the dynamic fluctuations in the cutting force were estimated with relatively high accuracy in all methods. There were no large differences in the estimation results based on the motor current ($\hat{F}^{CUR}$), DOB ($\hat{F}^{DOB}$), and MEDOB ($\hat{F}^{MEDOB}$). This indicates that the inertia force contributed little to the cutting force estimation because of the low-frequency process force. Even in DOB and MEDOB, the motor current information dominantly contributes the cutting force estimation when the process frequencies are much lower than the axial resonance (e.g., 286 Hz in this case) of the ball-screw-driven system.

In contrast, the relative displacement between the motor angle and stage position (i.e., deformation of the ball screw) dominantly contributes to the estimation of the low-frequency force in LDOB ($\hat{F}^{LDOB}$). Furthermore, as the inertia ratio was very small (i.e., $\alpha_r = 0.079$), VMDOB ($\hat{F}^{VIB}$) became almost the same as LDOB, as discussed in Fig. 2-9. Because the estimated results of LDOB and VMDOB were relatively accurate in both Fig. 2-14(a) and (b), the identified axial stiffness was considered valid.

In Fig. 2-14(b), LDOB and VMDOB estimated the cutting force on the stationary axis without friction compensation, whereas $\hat{F}^{CUR}$, $\hat{F}^{DOB}$, and $\hat{F}^{MEDOB}$ do not capture the cutting force at all. This difference is attributed to whether the restoring force induced by

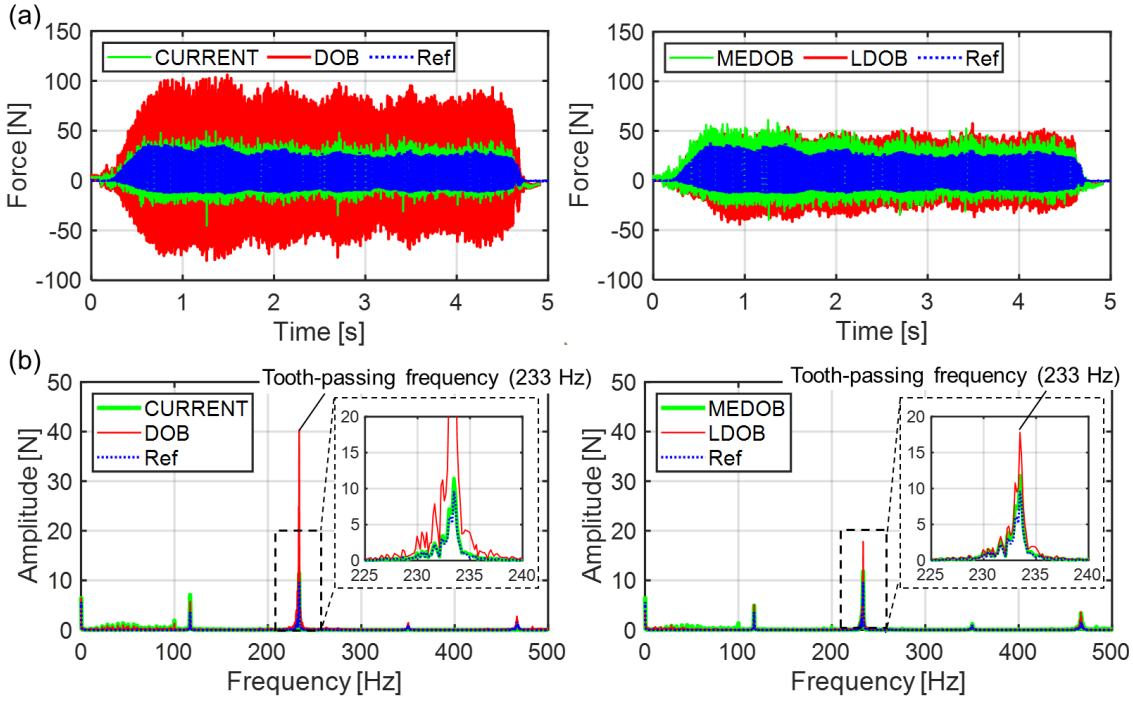

Fig. 2-15 Cutting force in X-direction estimated by each observer technique while feeding X-stage under 7000 min-1: (a) Overview of time waveform, (b) FFT

axial stiffness is directly considered [259]. In the current-based method, it is difficult to estimate the cutting force less than the maximum static friction force on the stationary axis [257,259,272]. In the developed system, a kinetic friction force of ~120 N was confirmed; hence, the static friction force should be larger than 120 N. As the cutting force was less than 120 N, it could not be estimated even using DOB or MEDOB, where the motor-current information is dominated in the low-frequency region. In contrast, LDOB and VMDOB could successfully estimate the cutting force less than the maximum static friction force.

Fig. 2-15 shows the estimated cutting force in X-direction while feeding the X-stage under 7000 min^{-1}, where the tooth-passing frequency of 233.3 Hz was near the axial resonance frequency. Note that the estimation result in VMDOB is omitted here because it is almost the same as LDOB. DOB significantly overestimated the cutting force at the tooth-passing frequency (i.e., around the axial resonance frequency) due to the assumption of a rigid-body single-inertia system, as discussed in Fig. 2-8. In contrast, MEDOB and LDOB based on a dual-inertia model improved estimation accuracy. although they still overestimated the cutting force. This may be because of the modeling error around the resonance frequency. Another small mode neighboring the fitted axial resonant mode can be observed in Fig. 2-12. The observer-based approach is considerably affected by the modeling error under the assumption of a dual-inertia model.

Here, the cutting force was reasonably estimated by simply using the motor current. In the region below the resonant frequency, the disturbance TF from the load force to an

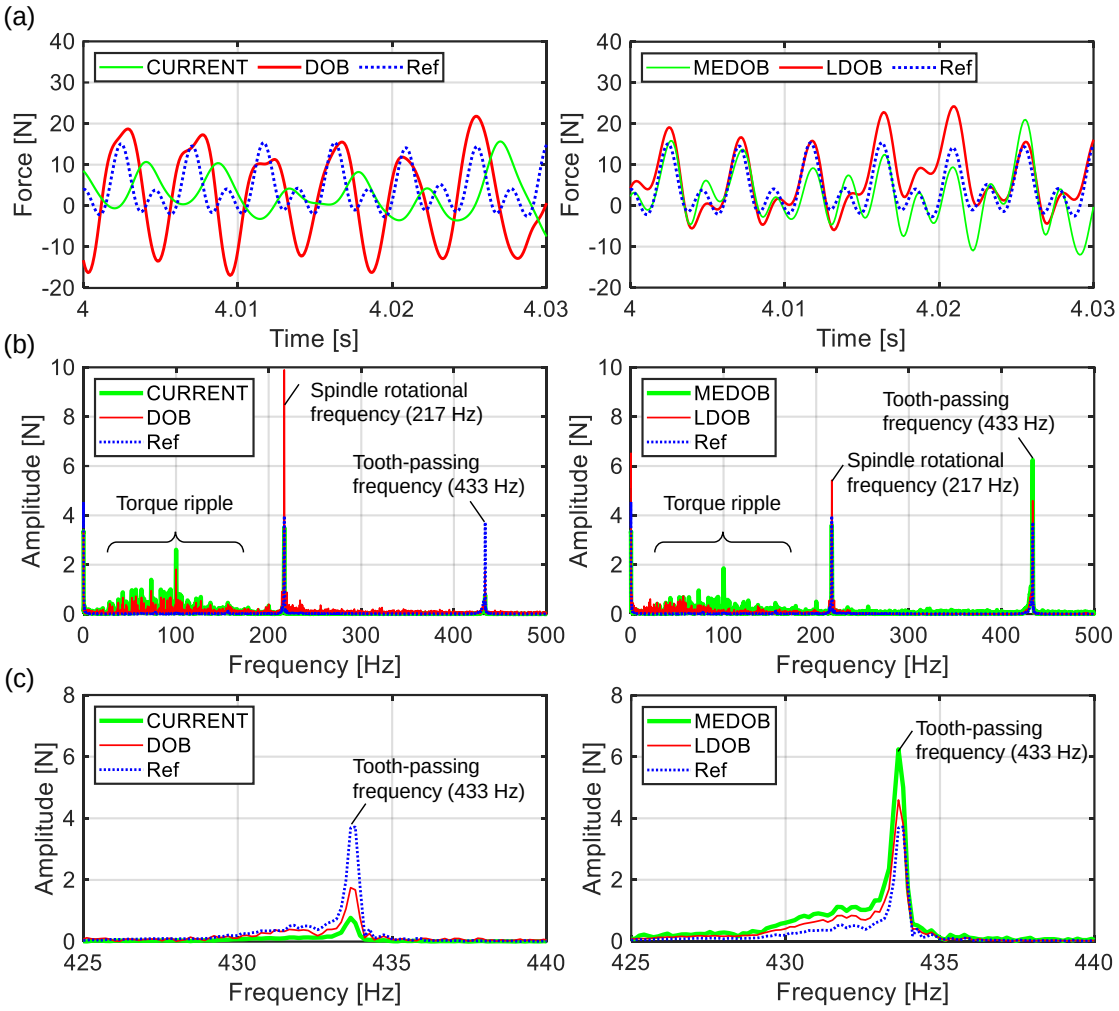

Fig. 2-16 Cutting force in X-direction estimated by each observer technique while feeding X-stage under 13000 min^{-1}: (a) Time waveform, (b) FFT, (b) enlarged view around tooth-passing frequency

equivalent motor thrust force (i.e., blue dash line in Fig. 2-9(a)) does not deviate much from the unity gain, although it is not ideally unity. However, the transfer gain (i.e., sensitivity) decreases sharply when the resonance frequency is exceeded. This suggests that the bandwidth for high sensitivity in current-based estimation is constrained by the less-dominant mode of the ball-screw-driven system.

Fig. 2-16 shows the results obtained at a higher spindle speed of 13000 min^{-1}. The cutting force in the X-direction was estimated while feeding the X-stage. The result of VMDOB is also omitted, as that in Fig. 2-15. In DOB, the spindle rotational component of 216.7 Hz induced by tool eccentricity was overestimated, because it is near the axial resonance frequency where the DOB is significantly deteriorated (also see Fig. 2-15). In the current-based method in Fig. 2-16, the estimation of the tooth-passing component was dull, although the spindle rotational frequency matches the measured value well. This is because the tooth-passing frequency of 433.3 Hz is much higher than the axial resonance frequency of 286 Hz, and the sensitivity of the motor current has already dropped significantly.

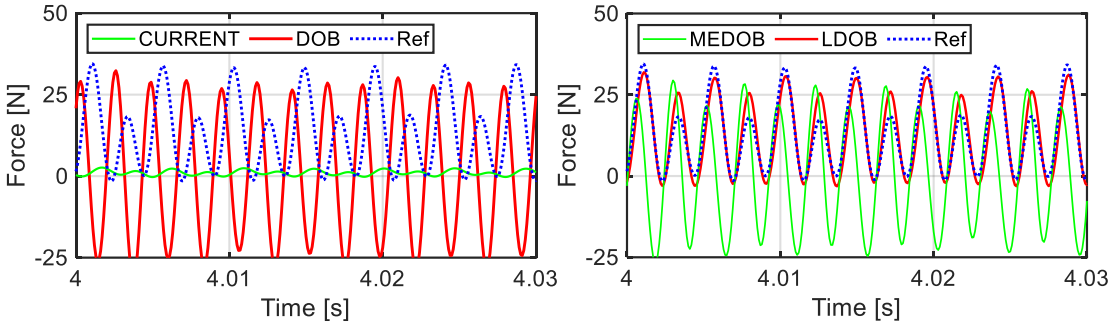

Fig. 2-17 Estimated cutting force in X-direction while feeding Y-stage under 13000 min^{-1}

Consequently, the current-based estimation did not reflect the dynamic variations in the cutting force well, as seen in Fig. 2-16(a).

In contrast, LDOB and MEDOB reasonably captured the dynamic cutting force while maintaining high sensitivity. By integrating the load-side stage acceleration obtained from high-resolution linear encoder, a high sensitivity against a high-frequency process force can be maintained even in the case of high damping guideways, such as the sliding type [273]. Here, the torque ripples, which were not eliminated by the recording method, appear strongly in the current-based method, DOB, and MEDOB, as seen in Fig. 2-16(b). In contrast, LDOB was not much affected by this torque ripple. As LDOB does not use the motor current, it is less susceptible to error factors from the motor.

Fig. 2-17 shows the cutting force in the X-direction while feeding Y-stage (i.e., estimation in cross-feed direction) under 13000 min^{-1}. As observed in Fig. 2-14 as well, the motor-current-based method could not estimate the cutting force to be less than the maximum static friction force on the stationary axis. In DOB and MEDOB, the estimated signals oscillated in response to the dynamic cutting force, unlike the motor thrust force. This is because the signals in DOB and MEDOB were dominantly constructed by the inertia force (i.e., acceleration signal), as the tooth-passing frequency (i.e., 433.3 Hz) was much higher than the resonant frequency of 286 Hz (Fig. 2-9(a)). As the inertia force reflected the vibrational state of motor/stage acceleration, the resultant estimated cutting force could capture the high-frequency dynamic variation of the cutting force even on the stationary axis. However, the estimated accuracy of DOB and MEDOB in Fig. 2-17 was unreliable as well, because the motor-current information was unreliable. The resultant estimated cutting force is determined by the balance between the inertia force and motor-thrust force. Especially, the estimation of low-frequency components—including the DC component, where the motor current is in charge—was not valid at all. In contrast, LDOB accurately estimated the cutting force on the stationary axis even under a high spindle speed of 13000 min^{-1} as well as a low spindle speed, as shown in Fig. 2-14(b). Note that the result obtained for VMDOB was the same as that obtained for LDOB in Fig. 2-17.

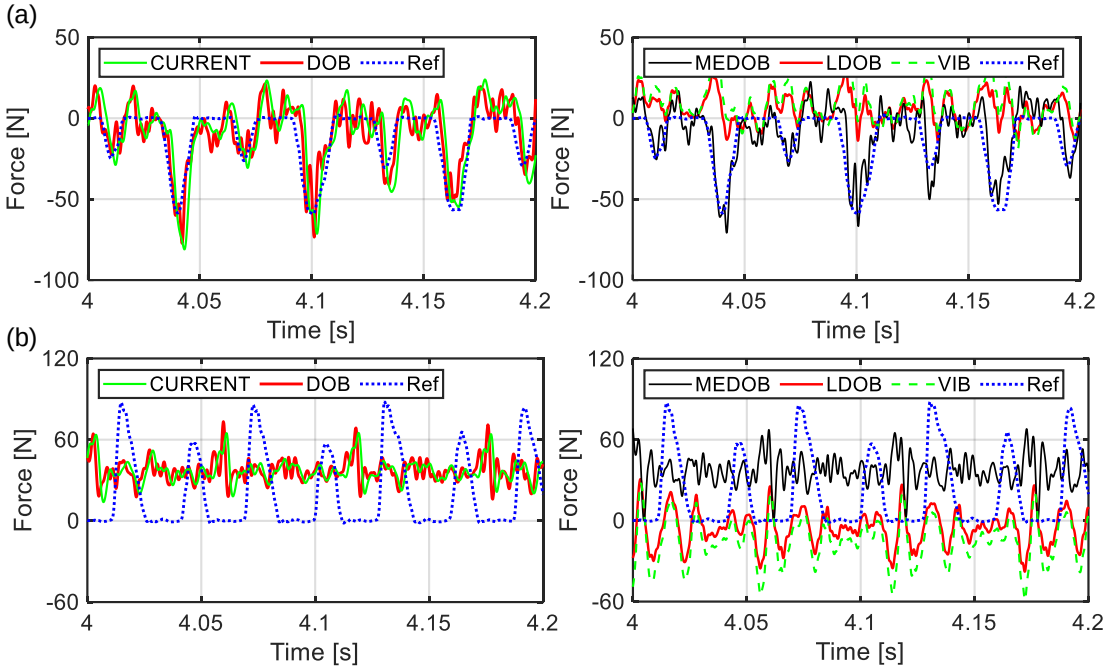

Fig. 2-18 Cutting force in Y-direction estimated by each observer technique under 1000 min^{-1}: (a) Feeding Y-stage (X-stage stop), (b) feeding X-stage (Y-stage stop)

Fig. 2-18 shows the results of cutting force estimation in the Y-direction at a spindle speed of 1000 min^{-1}. As shown in Fig. 2-18(a), the signals in $\hat{F}^{CUR}$, $\hat{F}^{DOB}$, and $\hat{F}^{MEDOB}$ could capture the dynamic cutting force without large deviations, although they were vibratory, compared to Fig. 2-14, due to the complex dynamics on the Y-axis. As already discussed in Fig. 2-14, the motor current information dominantly contributes to the cutting force estimation in these methods when the frequency components of the process force are much lower than the axial resonance of the ball-screw-driven system (e.g., 228 Hz on the Y-axis).

However, the cutting force could not be estimated in LDOB and VMDOB at all. This result suggests that it is difficult to use LDOB and VMDOB when the dynamics of the ball-screw-driven system cannot be modeled as a dual-inertia model well. On the Y-axis, the motor and encoder are installed far from the cutting point through some mechanical units (see Fig. 2-11). The vibration from the structural modes was superimposed on the stage displacement, and consequently, the waveform of the low-frequency process force reconstructed from the relative displacement might deteriorate. It is also necessary to focus on the reliability of the identified parameters, because of the forcible fitting by the dual-inertia model on the Y-axis. As LDOB and VMDOB did not function properly, the cutting force on the stationary axis could not be estimated, as shown in Fig. 2-18(b). The results of VMDOB and LDOB were slightly different because the inertia ratio is slightly larger on the Y-axis (i.e., $\alpha_{r,y} = 0.22$), although the difference in the result was not significant.

Fig. 2-19 shows the estimated cutting force in the Y-direction while feeding the Y-stage under 7000 min^{-1}, where the tooth-passing frequency of 233.3 Hz was near the axial

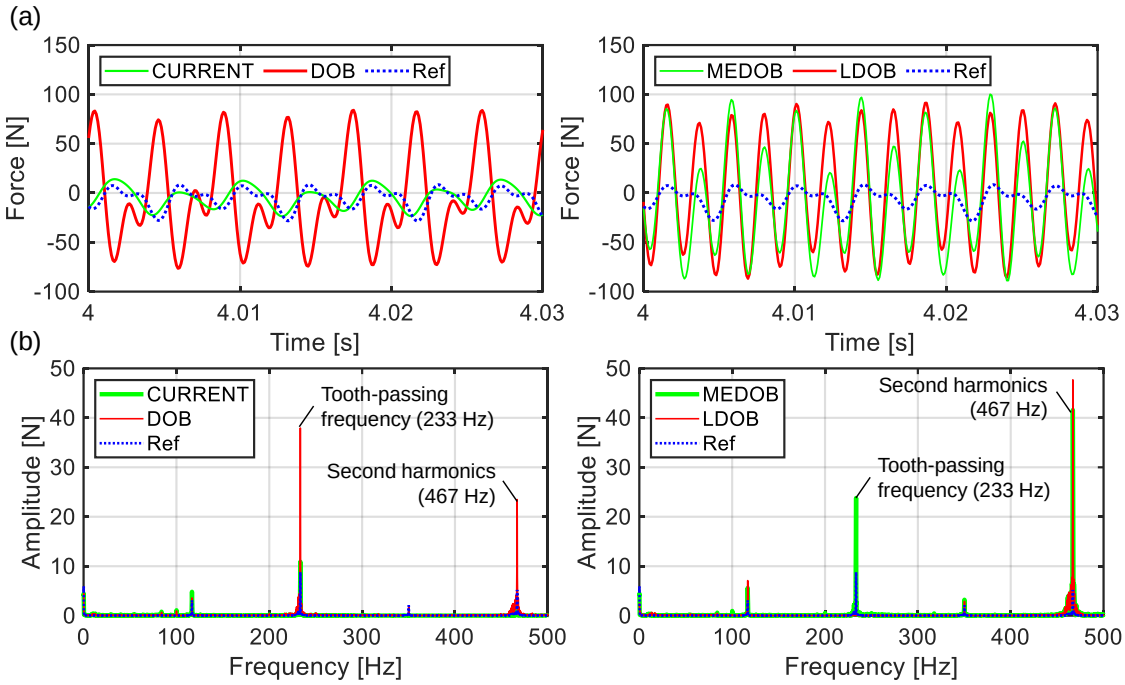

Fig. 2-19 Cutting force in Y direction estimated by each observer technique while feeding the Y-stage under 7000 min^{-1}: (a) Overview of time waveform, (b) FFT

resonance frequency of 228 Hz. The estimation result in VMDOB is omitted because it was not much different from LDOB. DOB substantially overestimated the tooth-passing frequency, which was close to the resonance frequency. Also, LDOB and MEDOB significantly overestimated the cutting force, especially at the second harmonic (i.e., high frequency dominated by the inertia force induced by vibratory acceleration), although they sensitively react to the dynamic cutting forces. This is because the Y-axis has a large modeling error, especially in the high-frequency region, as shown in Fig. 2-12(b). When the ball-screw-driven system has multiple-inertia dynamics, including flexible structural modes, the observer system significantly deteriorates (i.e., overestimates or underestimates the cutting force) due to the unmodeled modes even when dual-inertia-mode-based observer techniques are used. To realize a reliable cutting force estimation with a sufficient bandwidth in this complex situation, the deterioration of disturbance TF induced by the machine structure must be compensated, as described in subsection 2.5.2.

Only a simple current-based method reasonably estimated the cutting force in Fig. 2-19. Although the current-based method should be also affected by the flexible structural dynamics at the stage side [40,274], the influence of load-side dynamics on the disturbance TF for the motor-thrust force was small because of the low inertia ratio. As discussed in Fig. 2-16, however, the motor current cannot capture the dynamic cutting force at even a higher spindle speed, because of the low sensitivity caused by the mechanical transfer characteristic of the ball-screw-driven system from the stage to the motor side.

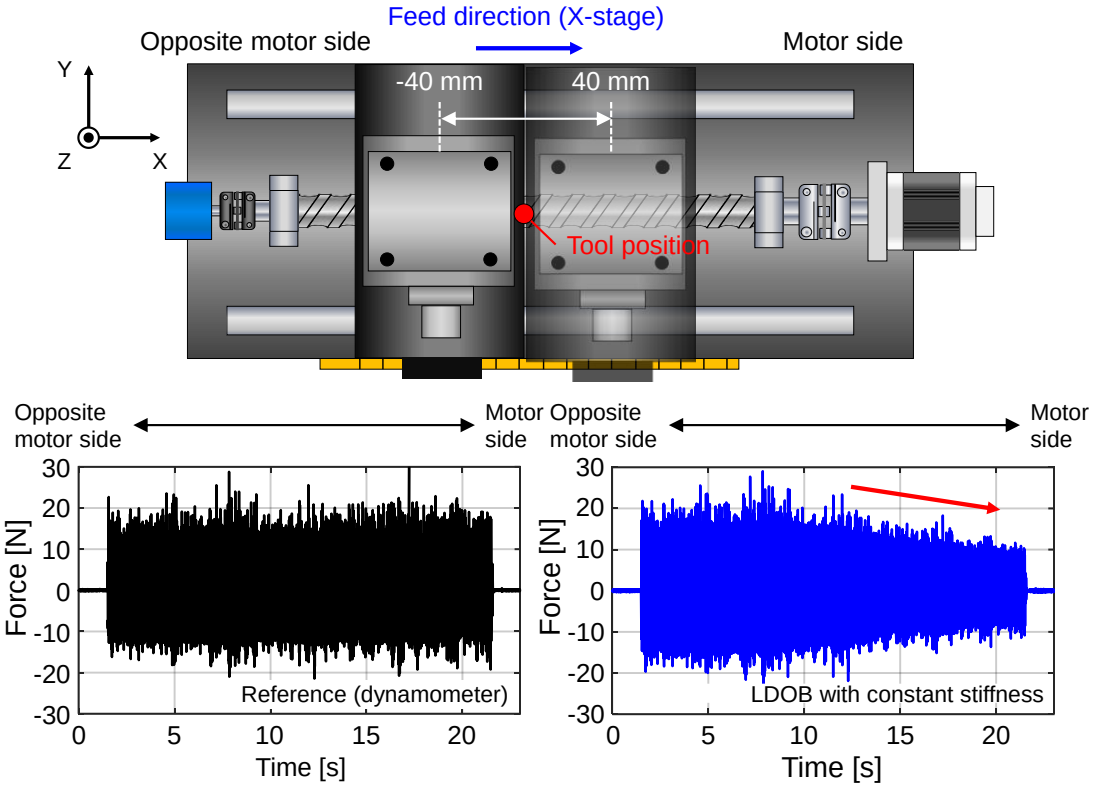

Fig. 2-20 Exemplary result representing the impact of position-dependent stiffness on LDOB-based cutting force estimation in X-axis (X-stage is fed from the position of -40 mm to 40 mm. Feed per tooth: 20 μm, Spindle speed: 6000 min^{-1}, Axial depth of cut: 0.2 mm, Slotting)

If the ball-screw-driven systems fit the dual-inertia model relatively well, such as on the X-axis, LDOB or VMDOB (i.e., relative motion-based method) has great potential to estimate the cutting force most accurately in both feed and cross-feed directions, as discussed in Fig. 2-14–Fig. 2-17. In LDOB and VMDOB, the identification of the stiffness parameter is especially important, as the restoring force affects the estimation result over a wide range of frequency, especially in the low-frequency region (Fig. 2-9(b)(c)). However, the axial stiffness of this system depends on the stage position, as discussed in Fig. 2-10, which affects the relative motion-based cutting force estimation.

Fig. 2-20 shows an exemplary result representing the impact of position-dependent stiffness on LODB-based cutting force estimation. The cutting conditions are denoted in the caption. The cutting force was estimated on the X-axis while feeding the X-stage from an absolute position of -40 mm to 40 mm. The center of the stage stroke was defined as the zero position. As it approaches the motor side, the dynamic cutting force was underestimated because of the changes in axial stiffness depending on the stage position. A compensation for position-dependent stiffness to maintain an accurate cutting force estimation in LDOB is introduced in subsection 2.5.1.

2.5. Compensation of cutting force estimation system

2.5.1. Position-dependent stiffness of ball-screw-driven system

LDOB is a very simple strategy and has great potential to estimate the cutting force most accurately in both feed and cross-feed directions, if the ball-screw-driven system fits the dual-inertia model relatively well (e.g., as on the X-axis of Fig. 2-12(a)). However, it is necessary to carefully focus on the position dependency of machine dynamics, especially the position-dependent stiffness term.

In Fig. 2-12, the model parameters of the dual inertia model are identified from the FRFs between the equivalent motor-thrust force and encoder signals obtained by motor sweep excitation tests. The physical parameters are extracted by curve fitting to FRFs in the frequency method. However, it is difficult to identify the continuous characteristics of position-dependent dynamics by using this approach; hence, a direct identification in time domain by LSM with a single sinusoidal motor excitation is proposed. During the motor excitation, the cutting force does not exist. The friction term is concentrated in the DC and low-frequency regions and the high-frequency noise can be eliminated from the obtained signals by using a peak/band-pass filter. When a sine wave signal is input as a velocity command and the stage is oscillated at a constant frequency, the dynamic components (i.e., restore force and damping force) are balanced with the inertia force at the stage side, which is expressed as follows:

$$M_t \ddot{X}_t = K_r X_r - C_t \dot{X}_t \tag{2-49}$$

Here, the sum of squares of the residuals, ϵ_e [N^2], at a certain window length, N_w [−], is expressed as follows:

$$\epsilon_e = \frac{1}{2}\sum_{h=1}^{N_w}\left\{M_t \ddot{X}_{t(h)} - \left(K_r X_{r(h)} - C_t \dot{X}_{t(h)}\right)\right\}^2 \tag{2-50}$$

If the parameter vector is defined as $\boldsymbol{\lambda} = \{K_r, C_t\}^T$, the following relation in terms of the identified parameters should be satisfied to minimize the residual sum square:

$$\frac{\partial \epsilon_e}{\partial \boldsymbol{\lambda}} = 0 \rightarrow \therefore \begin{cases} \dfrac{\partial \epsilon}{\partial K_r} = K_r \displaystyle\sum_{h=1}^{N_w} X_{r(h)}^2 - C_t \sum_{h=1}^{N_w} X_{r(h)} \dot{X}_{t(h)} - M_t \sum_{h=1}^{N_w} X_{r(h)} \ddot{X}_{t(h)} = 0 \\ \dfrac{\partial \epsilon}{\partial C_t} = -K_r \displaystyle\sum_{h=1}^{N_w} X_{r(h)} \dot{X}_{t(h)} + C_t \sum_{h=1}^{N_w} \dot{X}_{t(h)}^2 + M_t \sum_{h=1}^{N_w} \dot{X}_{t(h)} \ddot{X}_{t(h)} = 0 \end{cases} \tag{2-51}$$

Thus, the parameters are identified as follows:

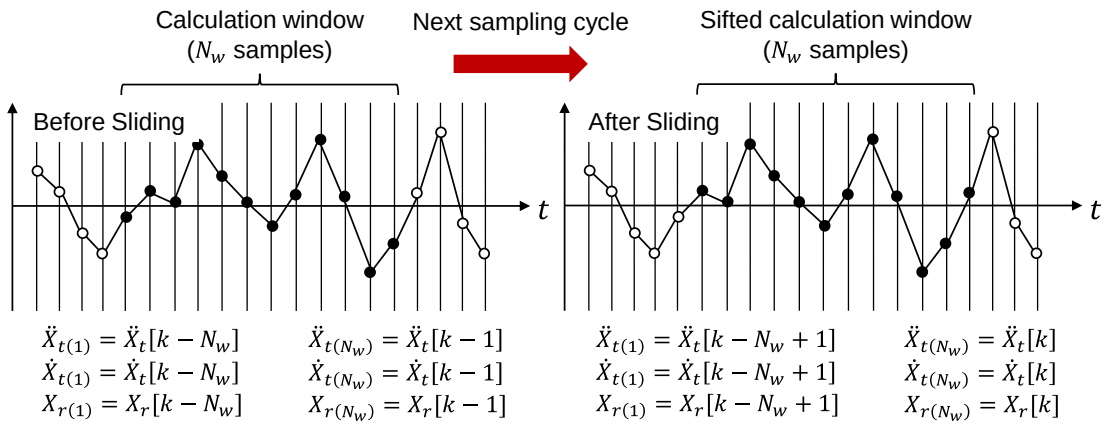

Fig. 2-21 Calculation scheme for time-domain identification while shifting the data window

$$\boldsymbol{\lambda} = \boldsymbol{A}^{-1}\boldsymbol{b} \tag{2-52}$$

$$\boldsymbol{A} = \begin{bmatrix} \sum_{h=1}^{N_w} X_{r(h)}^2 & -\sum_{h=1}^{N_w} X_{r(h)}\dot{X}_{t(h)} \\ -\sum_{h=1}^{N_w} X_{r(h)}\dot{X}_{t(h)} & \sum_{h=1}^{N_w} \dot{X}_{t(h)}^2 \end{bmatrix}, \boldsymbol{b} = \left\{ M_t \sum_{h=1}^{N_w} X_{r(h)}\ddot{X}_{t(h)} \quad -M_t \sum_{h=1}^{N_w} \dot{X}_{t(h)}\ddot{X}_{t(h)} \right\}^T \tag{2-53}$$

To capture the position-dependent characteristic of stiffness, the above calculation is repeated in every sampling period while sliding the calculation window (Fig. 2-21). The calculation cycle can be set arbitrarily. Here, the movable mass, M_t, needs to be known to employ the proposed method. As a case study, the design value was simply set in this dissertation. The identified position-dependent stiffness is subsequently installed in LDOB. Note that the damping coefficient of the translational element is also identified simultaneously. The identified damping term can also be installed in LDOB, whereas the stiffness term is more important.

Fig. 2-22 shows the position-dependent axial stiffness of the double-anchored ball-screw-driven system on the X-axis identified by the proposed procedure. A sinusoidal motor velocity command with an amplitude of 1.0 mm/s and frequency of 200 Hz was superimposed while feeding the X-stage at 4.0 mm/s (i.e., the same speed as that in Fig. 2-20). The X-stage was fed from -40 mm to 40 mm around the stroke center. The 2nd-order IIR peak filter having a peak frequency of 200 Hz was applied, and the calculation window length was set to 1000 samples under 10 kHz sampling. As the stage moved from the center to the motor side, the identified axial stiffness increased. In contrast, stiffness was identified as a nearly constant value in the opposite side of the motor from the center, which is almost the same as the value identified by the motor sweep test around the center position

in Fig. 2-12(a). The tendency of Fig. 2-22 is similar to the theoretical analysis shown in Fig. 2-10, although the absolute value is different. Note that the periodic small fluctuation in the identified values was induced by the lead length of the screw shaft, although it was relatively small compared to the global variation according to the stage position.

Fig. 2-23 shows the result of the cutting force estimation in LDOB with position-dependent axial stiffness. The position dependency can be handled by creating a stiffness function according to the stage position based on Fig. 2-22 and recording the absolute stage position during the process. Compared to Fig. 2-20, the estimation accuracy on the motor side was clearly improved in Fig. 2-23. Fig. 2-24 summarizes the root mean square error (RMSE) of the cutting forces estimated by LDOB with or without considering the position-dependent axial stiffness relative to the reference values measured by the dynamometer. The RMSEs were calculated for each 10 mm section. Before calculating the RMSE, the signals of the dynamometer and LDOB were synchronized.

Note that the dynamic characteristics (e.g., stiffness and damping) can also vary depending on the amplitude of the exciting disturbance force due to pre-sliding friction, known as nonlinear spring characteristics in the microdisplacement region [275,276]. The nonlinear spring in the microdisplacement region affects the cutting force estimation by LDOB/VMDOB, particularly on the stationary axis, but does not significantly affect the estimation when the stage is moving [250]. The force-amplitude-dependent model characteristic can be captured by the same methodology while varying not only the stage position but also the excitation amplitude of the motor velocity command. LDOB/VMDOB can be compensated by a created position and force-amplitude-dependent stiffness/damping function according to the absolute stage position and the amplitude of relative displacement during the process as arguments [250]. As a moving identification test was conducted in Fig. 2-22, the motor-excitation amplitude did not change the identification result significantly.

In the exemplary results shown in Fig. 2-22–Fig. 2-24, the tooth-passing frequency of the end milling test was the same as the excitation frequency in the identification test. It was confirmed that the cutting force could be estimated reasonably even if the tooth-pass frequency and excitation frequency for the identification tests were different, although the best performance was exhibited when the tooth-pass frequency coincided with the excitation frequency. However, the excitation frequency for the identification test must not be close to the resonance frequency, as the conditions of $\boldsymbol{A}$ matrix in Eq. (2-53) will change, and consequently, the axial stiffness tends to be underestimated [250]. Empirically, the ratio of resonant frequency to excitation frequency should be set as below 0.8 at least. It is expected that an approximate resonance frequency will be estimated theoretically.

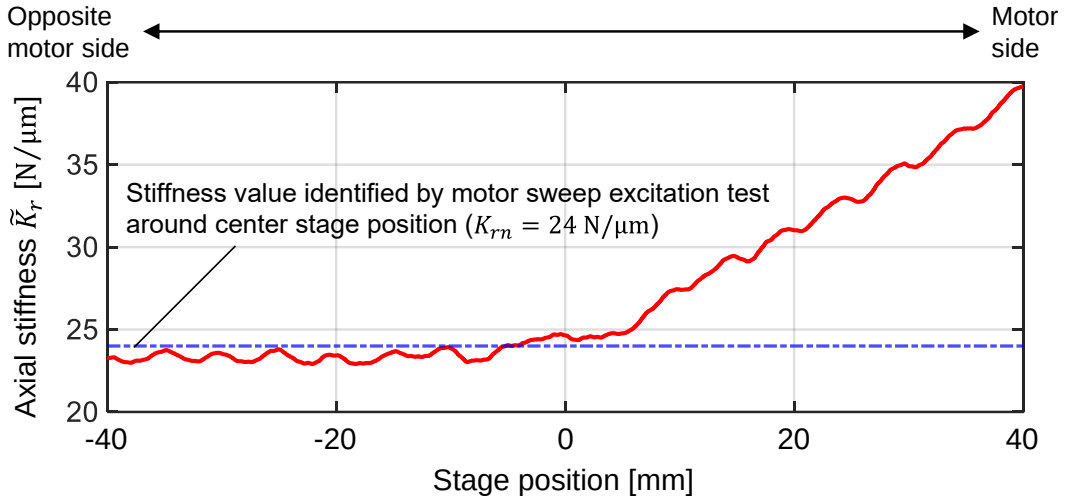

Fig. 2-22 Identified position-dependent axial stiffness in X-axis

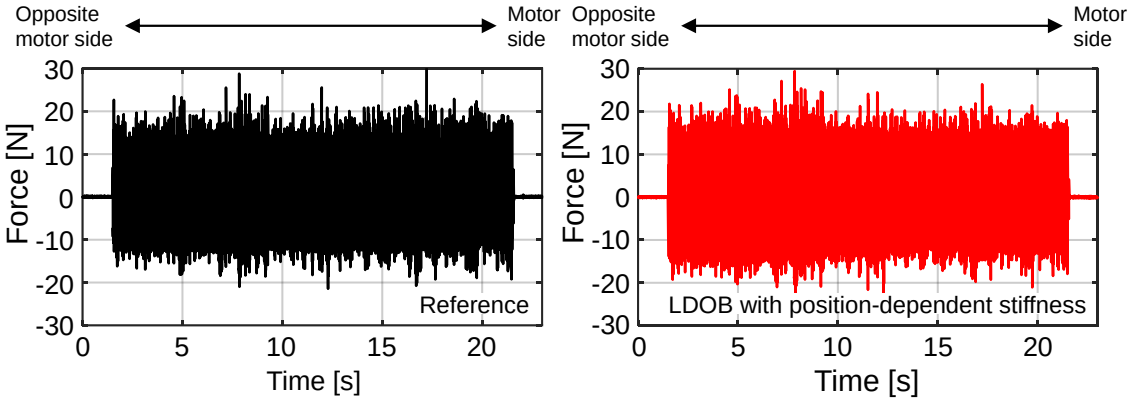

Fig. 2-23 Cutting force estimation in LDOB when considering the position dependency of axial stiffness identified in Fig. 2-22 (Cutting data in Fig. 2-20 are utilized)

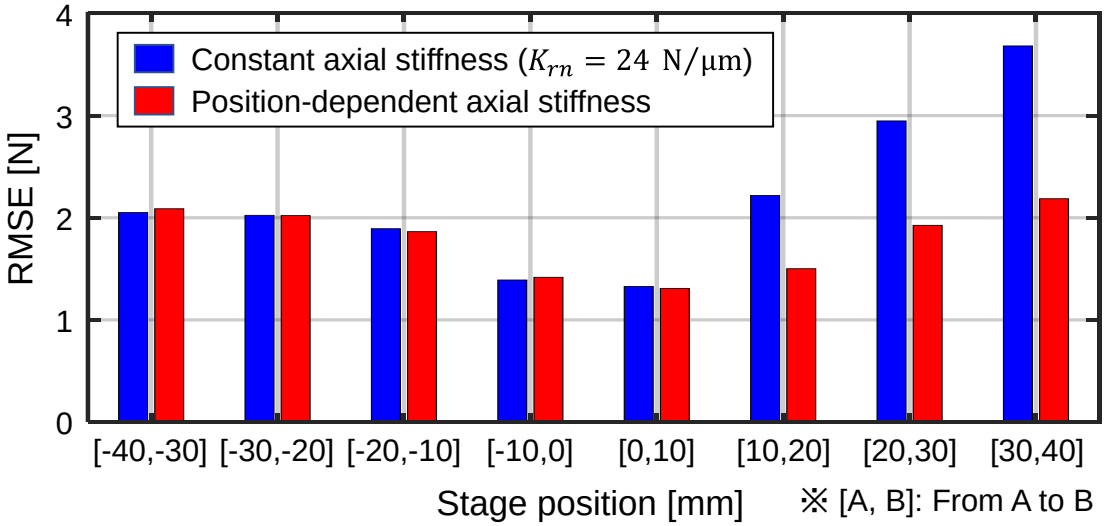

Fig. 2-24 RMSE of cutting force estimated by LDOB with or without considering position-dependent axial stiffness, relative to the reference cutting force measured by the dynamometer

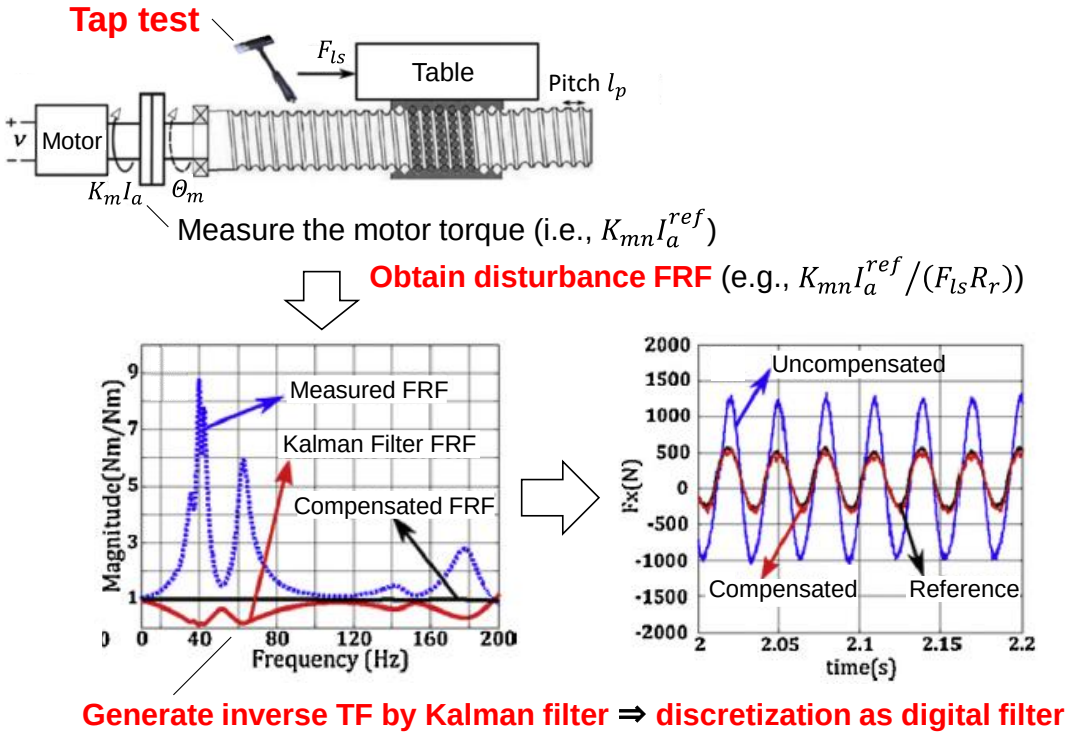

Fig. 2-25 Compensation procedure with Kalman-filter-based inverse digital filter proposed in [40] (The figure is used with permission from Elsevier.)

2.5.2. Disturbance transfer function induced by structural modes

When the ball-screw-driven system cannot be regarded as dual-inertia dynamics, the reliable bandwidth of the sensorless cutting-force-estimation system is substantially limited, as discussed in Fig. 2-18 and Fig. 2-19. This is an essential limit of the sensorless cutting force estimation by model-based observer techniques. Note that the motor current information also becomes more affected by the structural dynamics from the stage side as the inertia ratio increases. Although the accuracy can be improved by increasing the order of the assumed model, additional encoders/accelerometers corresponding to the assumed degree of freedom are required. Additionally, identification of observer parameters has become very time-consuming, and the consideration of where to install additional sensors has not yet been systematized; hence, this approach is not realistic in industry.

Recently, Altintas and Aslan [40,94] compensated the disturbance TF for the current-based cutting force estimation system deteriorated by structural dynamics, by using a digital filter that exhibits inverse characteristics of disturbance FRF obtained by the tap test. They generated a strictly proper inverse filter by applying Kalman filter theory (Fig. 2-25). However, the reliable bandwidth of the compensated signal was still limited to 200 Hz, because it is not easy to accurately measure the disturbance FRF due to the effect of pre-sliding friction on the stationary axis as well as the low sensitivity of the motor current

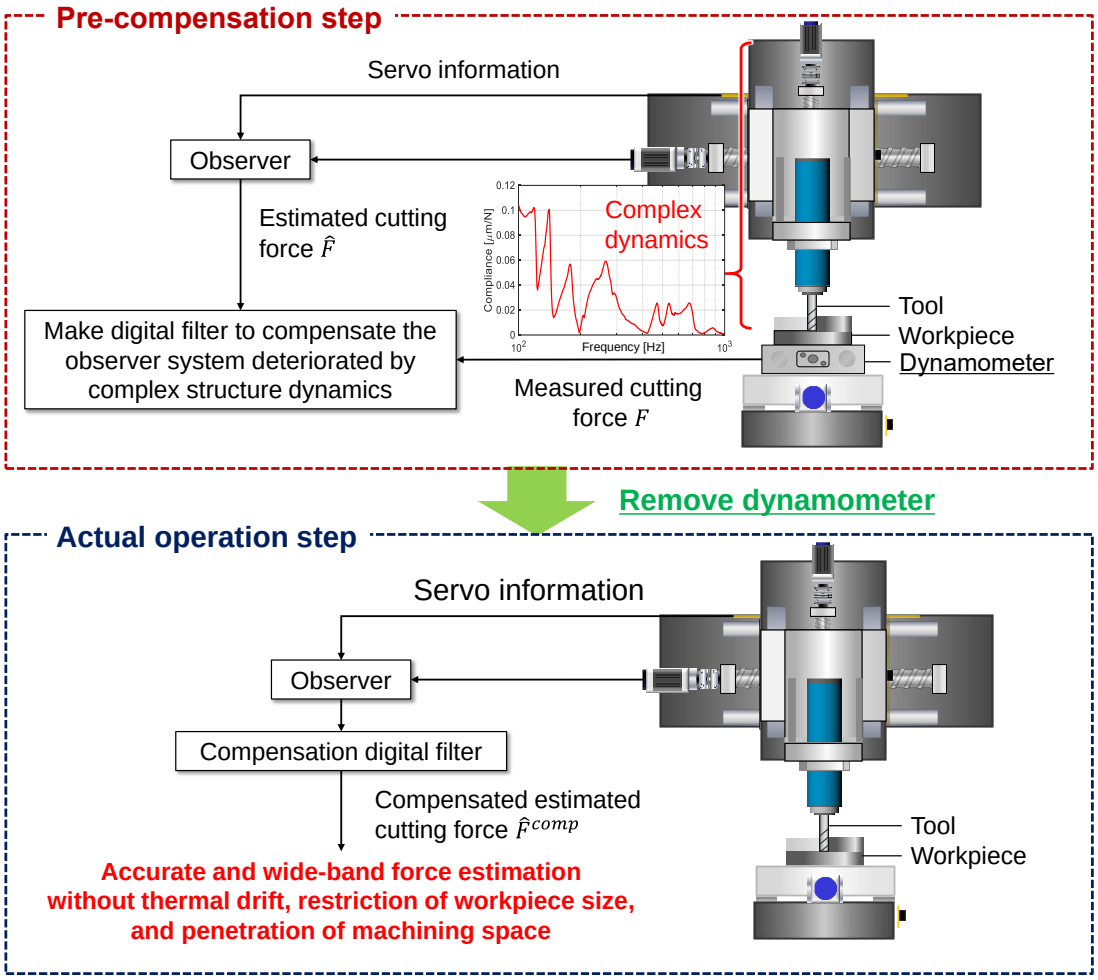

Fig. 2-26 Concept of pre-compensation for sensorless cutting force estimation system

in a high-frequency region (e.g., discussion in Fig. 2-14 and Fig. 2-16).

Alternatively, this subsection presents a novel concept to directly generate a compensation filter based on the actual cutting tests for the sensorless cutting-force-estimation system (Fig. 2-26) [251]. The performance deterioration of the model-based observer techniques induced by the modeling error, including structural dynamics, is pre-compensated through iterative milling tests in the development phase, denoted as the pre-compensation step. In this step, a digital filter for compensation is directly self-adjusted by the proposed optimization loop, referring to the cutting force measured by the dynamometer. In particular, observer techniques integrated with linear encoder information offers a good opportunity to obtain a reasonable compensation filter, as a high sensitivity to the cutting force is maintained over a wide frequency range. If the sensitivity is nearly zero in the high-frequency range, such as the current-based estimation, an infinite power of filters is required to obtain unity gain. This filter becomes unstable, and thus, cannot be realized.

The proposed approach can reduce the uncertainties and manual operation induced from the tap test for measuring the disturbance FRF; hence, it is more reliable. The

dynamometer is removed in the actual operation on the shop floor after completing the pre-compensation step. Consequently, the sensorless cutting force estimation system compensated by the self-generated digital filter can accurately sense the cutting force without any drawback induced using the dynamometer on the shop floor, such as thermal drift, overload, limitations of workpiece size, and machining-space invasion. The concept of pre-compensation is inspired from precision measurement instruments such as coordinate measuring machine (CMM), which are always calibrated before use.

The estimated cutting force is compensated by 1D digital filtering, whose general proper form (i.e., numerator and denominator have the same order) can be expressed as follows:

$$G_l(z) = \frac{b_0 + b_1 z^{-1} + b_2 z^{-2} + \cdots b_l z^{-l}}{1 + a_1 z^{-1} + a_2 z^{-2} + \cdots a_l z^{-l}} \tag{2-54}$$

where $a_l\,[-]$ and $b_l\,[-]$ $(l = 0, 1, 2, \ldots)$ are filter coefficients in denominator and numerator, respectively. Consequently, the compensated estimated cutting force at the k-th sampling point can be expressed as a recursive function with the coefficient vector of the l-th-order digital filter as follows:

$$\begin{aligned} &\hat{F}^{comp} = G_l(z)\hat{F} = \frac{b_0 + b_1 z^{-1} + b_2 z^{-2} + \cdots b_l z^{-l}}{1 + a_1 z^{-1} + a_2 z^{-2} + \cdots a_l z^{-l}}\hat{F} \\ &\rightarrow \hat{F}^{comp}[k] = \boldsymbol{b_l} \cdot \left\{\hat{F}[k], \hat{F}[k-1], \ldots, \hat{F}[k-l]\right\} - \boldsymbol{a_l} \cdot \left\{\hat{F}^{comp}[k-1], \ldots, \hat{F}^{comp}[k-l]\right\} \\ &\qquad\qquad \text{where } \boldsymbol{\lambda} = \{\boldsymbol{a_l}, \boldsymbol{b_l}\} = \{[a_1, a_2, \ldots, a_l], [b_0, b_1, \ldots, b_l]\} \end{aligned} \tag{2-55}$$

where $\hat{F}^{comp}$ [N] is the compensated signal of the estimated cutting force, $\hat{F}$ [N]. By regarding $\boldsymbol{\lambda}$ as a variable tuning vector, the filter coefficients are directly adjusted by nonlinear programming so that the compensated force matches the reference cutting force, F^{ref} [N], measured by the dynamometer.

Fig. 2-27 shows the self-tuning procedure, which comprises two optimization loops. In the inner optimization loop, the filter coefficients at a specific filter order are tuned to minimize the set error function. The phase of the compensated force is shifted due to digital filtering. In addition, the sensor signals and servo signals are not usually synchronized; hence, time-domain tuning may not be suitable. From the above viewpoints, gain-based tuning in the frequency domain is applied. The error function, J_e [N], is defined as

$$\mathbf{e} = \mathbf{R_G} - \mathbf{U_G^{comp}} \rightarrow J_e = \sqrt{\mathbf{e}\mathbf{e}^T} \text{ where } \mathbf{R_G} = \text{Abs}(\text{FFT}[\mathbf{r}]), \mathbf{U_G^{comp}} = \text{Abs}(\text{FFT}[\mathbf{u}^{comp}]) \tag{2-56}$$

The gain vectors $\mathbf{R_G}$ and $\mathbf{U_G^{comp}}$ are obtained by the FFT of the time-series dataset of the reference signal and that of the tuning signal (i.e., compensated signal) derived by filtering the original estimation signal. The datasets of $\mathbf{r}$, $\mathbf{u}^{comp}$, and $\mathbf{u}$ contain signal values at each sampling point corresponding to F^{ref} (i.e., cutting force measured by the

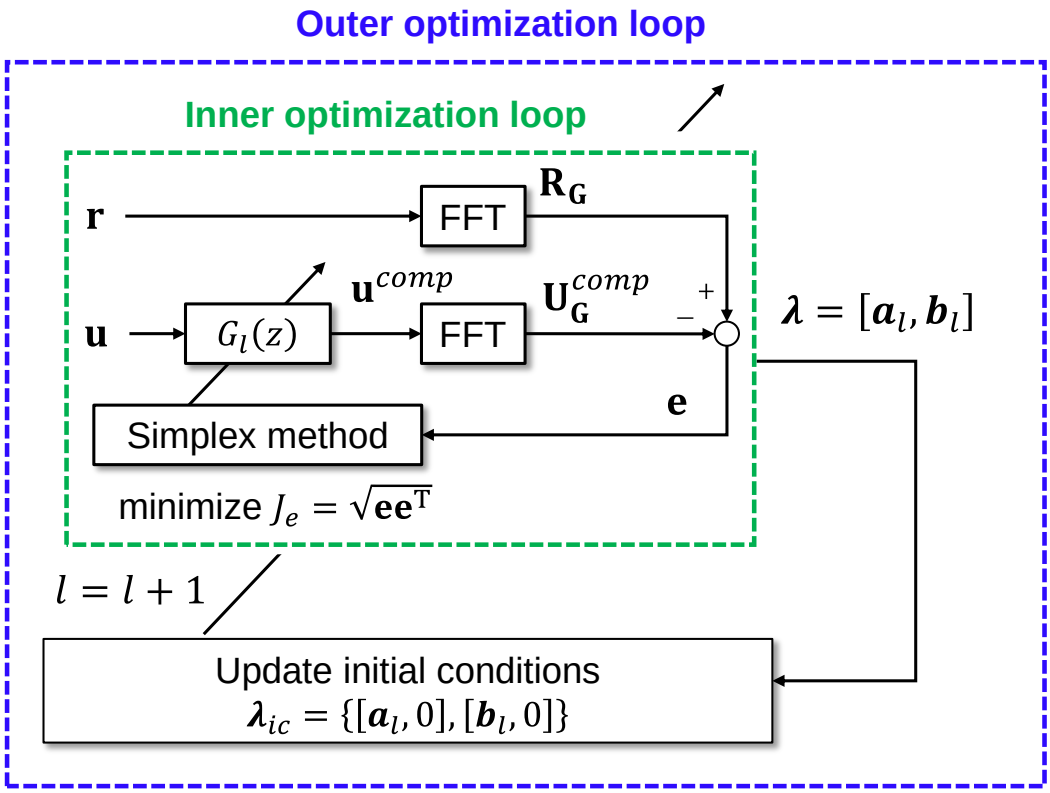

Fig. 2-27 Dual optimization loop for self-adjustment of digital filter

dynamometer), $\hat{F}^{comp}$, and $\hat{F}$, respectively. The filter coefficient vector is automatically adjusted by the Simplex method to minimize the error function. By restoring the spectrum amplitude, including that from DC to the Nyquist frequency in the gain vectors, an overfitting that ignores filter stability can be avoided.

Here, setting the initial conditions is not trivial for nonlinear optimization. In addition, an appropriate filter order should be self-determined. An outer optimization loop addresses these challenges. In the outer loop, the filter order is increased gradually, and the inner loop runs for each order and outputs the filter coefficient vector optimally tuned at that order. The outer loop also updates the initial conditions for the inner iteration by reusing the filter-coefficient vector tuned in the previous order (Fig. 2-28). This procedure can eliminate the need to set the initial condition and gradually find a better optimal point with reduced iteration time, although the tuned coefficient vector is not necessarily a global optimal solution. If the residual error function does not decrease even for an increase in the filter order, the filter adjustment is terminated. The outer optimization loop inputs the non-filtering condition (i.e., $G_0 = b_0 = 1$) to the inner loop as the first initial condition. Therefore, the iteration ends if filtering is not required. In Fig. 2-28, the iterative tuning of the cascade optimization loop is completed at the filter order of 4, as the changing rate of the residual error function drops below 0.1 %; hence, the 3rd-order digital filter in the previous step and the corresponding adjusted filter coefficients are employed.

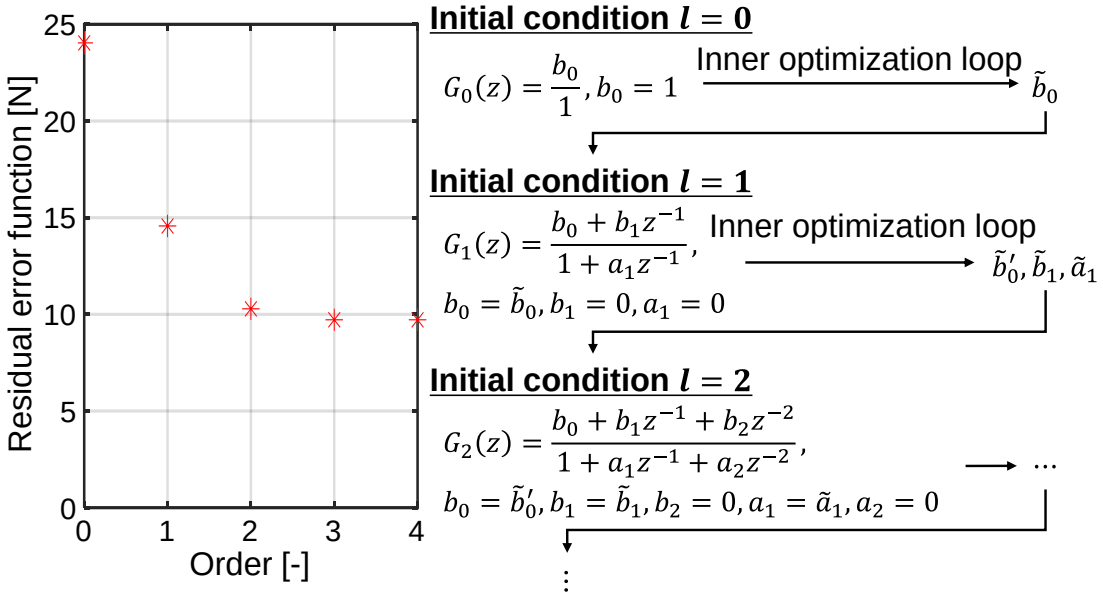

Fig. 2-28 Update procedure of filter order and initial conditions

For a reliable optimization in the frequency domain, the steady-state excitation through the milling test at a constant spindle speed should be conducted. Therefore, all frequencies cannot be excited, like that in the tap test, which makes it impossible to generate the digital filter at once to compensate for the entire frequency range. To address this problem, iterative experimental tuning for the cascaded compensation filter is conducted based on the machine-in-the-loop concept (Fig. 2-29).

The compensation filter is gradually completed by cascading each filter generated through iterative milling tests while discretely varying the spindle speed, as follows:

$$G_c(z) = G^{(1)}(z) \cdot G^{(2)}(z) \cdot \cdots \cdot G^{(n-1)}(z) \cdot G^{(n)}(z) \tag{2-57}$$

where $G^n(z)$ is a digital filter generated by passing the dual optimization loop (i.e., Fig. 2-27) in the n-th cutting test. If n experiments for pre-compensation are performed, total n filters are generated. Note that the filter coefficient vectors behave unlike filter ($G_0^{(n)}(z) = 1$) if not needed. Consequently, the resultant cascade filter, G_c, represents the compensator (compensation TF) for the disturbance TF in the cutting force estimation system.

When a new filter is generated, all previous experimental datasets and generated compensation filters must be considered; hence, the reference and original estimation datasets input into the filter-tuning program are extended as

$$\mathbf{r} = \left[\mathbf{r}^{(1)}, \mathbf{r}^{(2)}, \ldots, \mathbf{r}^{(n-1)}, \mathbf{r}^{(n)}\right], \quad \mathbf{u} = \left[\mathbf{u}^{(1)}, \mathbf{u}^{(2)}, \ldots, \mathbf{u}^{(n-1)}, \mathbf{u}^{(n)}\right] \tag{2-58}$$

where $\mathbf{r}^n$ and $\mathbf{u}^n$ are the reference and original datasets gathered by the n-th cutting test. Before inputting the extended original dataset of the estimated cutting force into the tuning

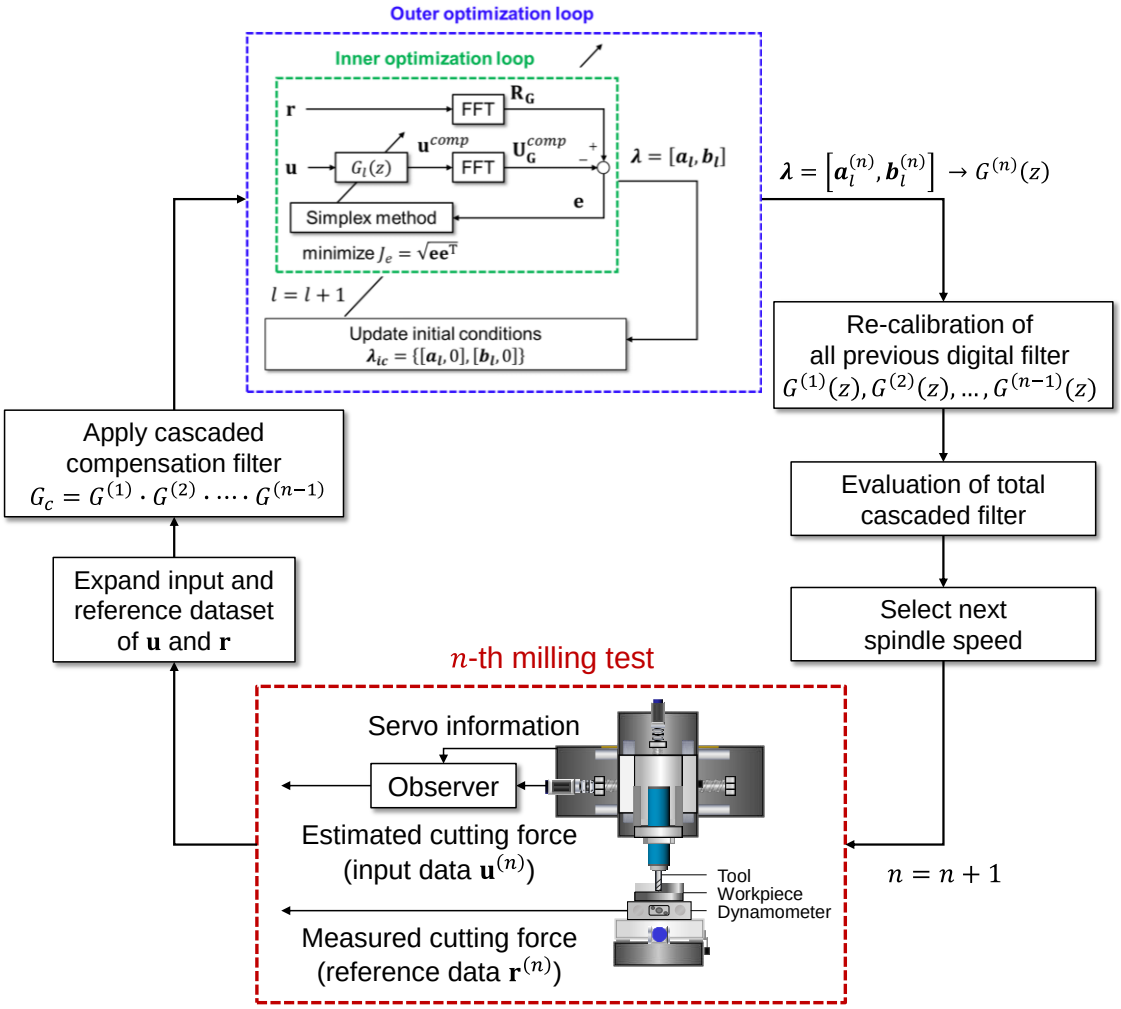

Fig. 2-29 Iterative milling test procedure for generating a cascaded compensation digital filter

program, it is filtered by the cascaded filter composed of all previous filters (i.e., $G_c(z) = G^{(1)}(z) \cdot G^{(2)}(z) \cdot \cdots \cdot G^{(n-1)}(z)$). Then, a new filter is generated to fill in the insufficient part and the total characteristic of the cascaded digital filter is changed.

Fig. 2-30 shows the concrete recalibration step of each filter. It is also important to prevent overfitting at certain frequencies, as the filter is tuned based on the discrete-frequency excitation through milling tests. In this step, all previous filters are readjusted by the Simplex method in order, considering the other filters. During the recalibration of one filter, coefficient vectors of the others and its own filter order are fixed. Consequently, overall, the total cascaded filter fits better for all input frequencies. Although the next spindle speed for learning should be designed within a certain spindle speed range after evaluating the frequency-domain distribution of the residual error function, the spindle speeds ranging 1000–15000 min^{-1} with 1000 min^{-1} increments (i.e., 15-times milling tests) are applied in this dissertation as a case study.

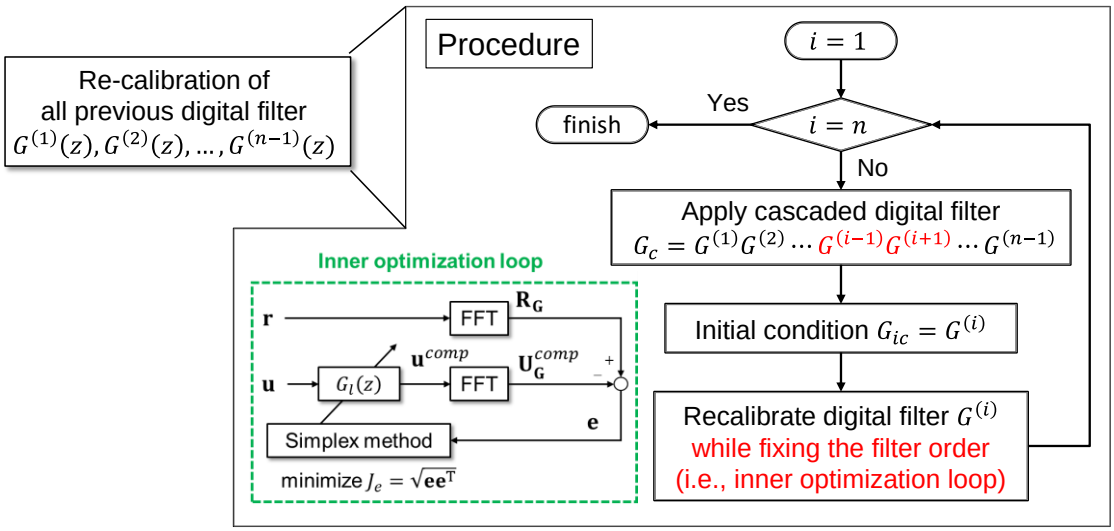

Fig. 2-30 Recalibration procedure of all previous digital filters

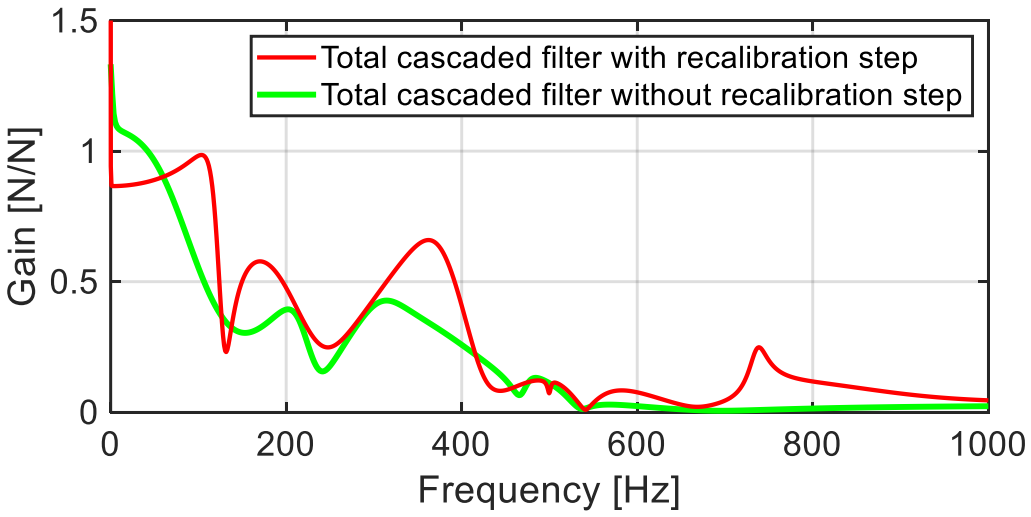

Fig. 2-31 Gain characteristic of self-optimized cascaded digital filter

Fig. 2-31 shows the gain characteristic of the cascaded digital filter to compensate for the MEDOB system on the Y-axis, self-optimized by the proposed procedure. The iterative straight cutting tests were conducted by providing feed in the Y-direction and down-milling aluminum alloy 7075 with a two-flute 6-mm-diameter end mill. The feed per tooth, axial depth of cut, and radial depth of cut were set as 30 μm, 2.0 mm, and 1.5 mm (quarter immersion), respectively. The friction compensation was achieved using the recording method, although various friction models can be used. Here, since the disturbance TF in the high frequency region deteriorated by unmodelled high-frequency modes can be compensated through the proposed method, an LPF with wider cut-off frequency can be applied. Therefore, a LPF with 1 kHz cut-off frequency is applied to the MEDOB system in this section, although the cut-off frequency of 500 Hz was applied in previous sections (Table

2-3), to eliminate the influence of high-frequency modes, even for the X-axis.

The filters are gradually generated and self-adjusted to complement each other through 15 tests conducted at spindle speeds ranging 1000–15000 min^{-1} with 1000 min^{-1} increments. The characteristic of the total cascaded filter is modified as the iterative milling tests progress. Only the final cascaded compensation filter (i.e., $G_c(z) = G^{(1)}(z) \cdot G^{(2)}(z) \cdot \cdots \cdot G^{(15)}(z)$) is depicted in Fig. 2-31. Note that the DC gain of the cascaded filter is also modified so that the error function, including the friction compensation error, will decrease overall. To show the impact of the recalibration step in Fig. 2-30, the total cascaded filter generated without the recalibration step is also shown in Fig. 2-31. Some of the training results obtained in the pre-compensation step are shown in **Appendix B**, which verify that the self-shaping process of the cascaded compensation digital filter is functioning successfully.

To verify the generated compensation filter, additional straight milling tests in the Y-direction were conducted with various combinations of spindle speed and cutting depth, which were not used in the pre-compensation step. Note that the LPF with 1 kHz cut-off frequency was applied to both the compensated and non-compensated signals of the estimated cutting force, for a fair comparison.

Fig. 2-32 compares the compensated and uncompensated MEDOB signals; the conventional motor-current-based estimation is also depicted. The cutting condition is presented in the caption. The MEDOB-based cutting force estimation system was improved by the self-optimized cascaded digital filter with the recalibration step in Fig. 2-31. As shown in Fig. 2-32(b), there is no large deviation in all estimation results at the tooth-pass frequency of 113 Hz, because of the relatively low-frequency region. However, there is a large error in the normal MEDOB at the second harmonic of 226 Hz. This error was successfully compensated by the generated digital filter. The time waveform of the current-based cutting force estimation appears dull. This is because the motor current did not sensitively reflect the vibrational state at the third harmonic of 339 Hz. As already discussed (Fig. 2-9 and Fig. 2-16), the gain of disturbance TF of the motor-current-based estimation can substantially decrease in the high-frequency region over the resonance frequency of the ball-screw-driven system (e.g., 228 Hz on the Y-axis). The compensated MEDOB system appropriately estimated all frequency components.

To show the impact of the recalibration step, the estimation result of the compensated MEDOB without the recalibration step is shown in Fig. 2-33. The compensation performance is generally enhanced by applying the recalibration step sequentially, although the time required to tune the filters become longer. In Fig. 2-33, the RMSE in the time waveform showed an improvement by ~23% by applying the recalibration step, over the RMSE in the compensation without the recalibration step.

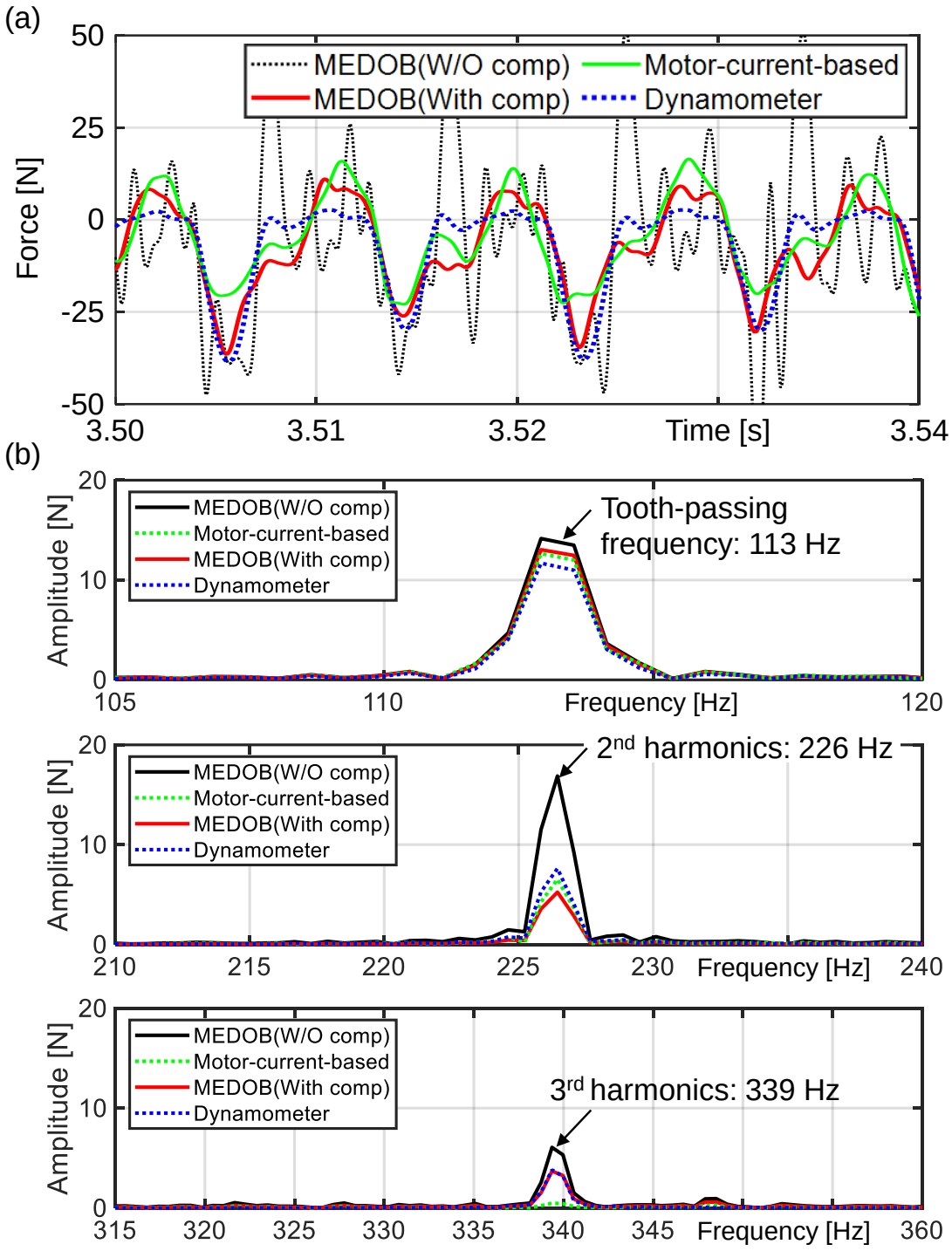

Fig. 2-32 Comparison of the cutting force in Y-direction while feeding Y-stage estimated by the motor current, uncompensated MEDOB, and compensated MEDOB ($S = 3400\ \mathrm{min}^{-1}, a_p = 2.5\ \mathrm{mm}, a_e = 1.0\ \mathrm{mm}$, down cut with two-fluted 6-mm-diameter end mill and a feed per tooth of 30 μm): (a) Time waveform, (b) enlarged FFT results at tooth-passing frequency as well as 2nd and 3rd harmonics

Fig. 2-34 shows the additional results obtained at higher spindle speeds of 8300 and 12500 min^{-1} in both time and frequency domains. In brief, the estimation accuracy of MEDOB was substantially improved by the proposed compensation system in both cases. The spectrum error at the tooth-passing frequency became ~9% and 17% at 8300 and 12500

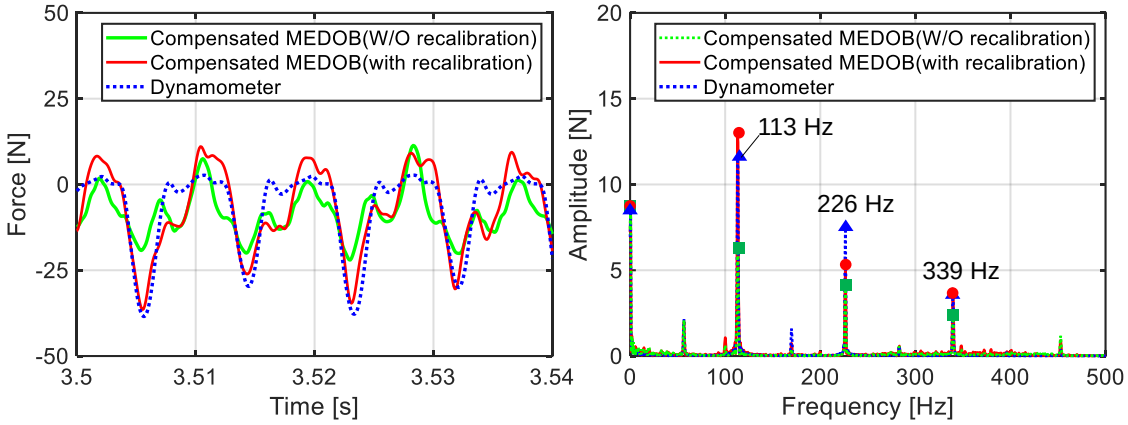

Fig. 2-33 Comparison of the cutting force in Y-direction while feeding Y-stage estimated by the compensated MEDOB with or without recalibration step (same data as those used in Fig. 2-32 are used here)

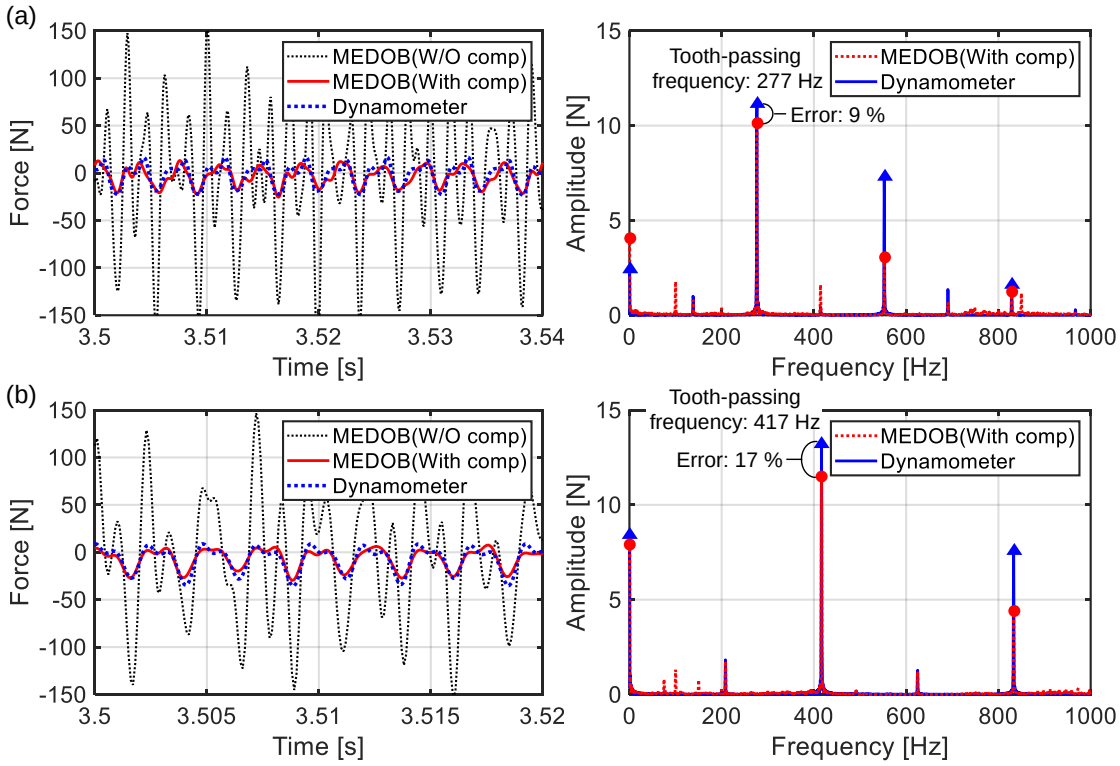

Fig. 2-34 Cutting force in the Y-direction while feeding the Y-stage estimated by MEDOB with or without compensation (down cut with two-fluted 6-mm-diameter end mill and a feed per tooth of 30 μm): (a) $S = 8300\ \mathrm{min}^{-1}, a_p = 1.5\ \mathrm{mm}, a_e = 3.0\ \mathrm{mm}$ (b) $S = 12500\ \mathrm{min}^{-1}, a_p = 2.5\ \mathrm{mm}, a_e = 1.5\ \mathrm{mm}$

min^{-1}, respectively, whereas ~200% or more errors were induced in the uncompensated MEDOB system in both cases.

Note that the estimation accuracy in high harmonics was still not sufficient. This is because the frequency-spectrum distribution in the training dataset concentrated on the relatively low-frequency region, since the undesigned 15-times tests with 1000 min^{-1} increments ranging from 1000 to 15000 min^{-1} were simply conducted in the pre-

compensation step. In this case, the compensation accuracy can be enhanced by increasing the dataset with a high spindle speed and/or many teeth, so that many high frequencies will be included. It is also important to establish a systematic experiment design method for the pre-compensation. Furthermore, because of the gain-based tuning for filter generation, the phase characteristic of the compensated signal is not considered; hence, the time waveform of the saw-like cutting force can be corrupted after compensation due to the phase delay of digital filtering. As the frequency response of the force sensing system is ideally desired to have a unity gain and low phase delay for the widest frequency range [94], this problem must be solved in the future.

2.6. Summary

This chapter introduced the existing sensorless cutting-force-estimation techniques based on disturbance estimation theories or the motor current. In-depth characteristics in each technique, as well as challenges and compensations for accurate cutting force estimation, were described through simulations (i.e., theoretical aspects) and actual cutting tests with the prototype three-axis machine tool having a fully closed ball-screw-driven system. The contents are summarized as follows.

1. In the dual-inertia model of the ball-screw-driven system, estimation by a simple DOB (i.e., rigid-body single-inertia model basis) will significantly deteriorate around the unmodeled axial resonance frequency. DOB can be useful for the linear-motor-driven stage modeled as a rigid body. By applying a dual-inertia-model approach, such as MEDOB, LDOB, or VMDOB, the unity gain of the disturbance transfer function can be ideally obtained. This means that the estimated cutting force is ideally the same for all techniques. Nevertheless, the estimation characteristics differ depending on the method, as the component forces contributing to the estimated cutting force are different. MEDOB, LDOB, and VMDOB can be implemented in a fully closed ball-screw-driven system. By integrating the high-resolution load-side linear encoder information, the high detectable-force resolution and sensitivity to dynamic cutting force in the high-frequency region can be maintained.

2. Only LDOB and VMDOB can estimate the cutting force regardless of whether the stage is moving or not, even when the cutting force is less than the maximum static friction force. This is because of the relative motion-based estimation, which directly considers the restoring force induced by the axial stiffness of the ball-screw-driven system. In case of a low inertia ratio, VMDOB will become almost the same as LDOB. Additionally, LDOB does not use the motor current, which has large error factors in some cases. LDOB is a more reasonable strategy than VMDOB because of its theoretical simplicity.

3. As the observer technique is model-based, the estimation accuracy substantially depends on the modeling accuracy. In LDOB/VMDOB, the identification of axial stiffness is particularly important. In machine tools, axial stiffness may have position dependency depending on the anchor type of the ball-screw-driven system. The position-dependent variation from a nominal value in the axial stiffness deteriorates the estimation accuracy of LDOB and VMDOB. In this case, the estimation accuracy can be improved by handling the stiffness function identified in advance according to the absolute stage position during the process. Alternatively, MEDOB is useful because there is no need to identify the axial stiffness; however, it cannot estimate the cutting force less than the maximum static friction on the stationary axis.

4. When the ball-screw-driven system cannot be regarded as a dual-inertia model due to the complex structural dynamics, the reliable estimation bandwidth is substantially limited. This is an essential limit of sensorless cutting force estimation by model-based observer techniques. To address this challenge, a practical compensation technique with a cutting-data-driven self-optimized compensation digital filter, which is learned through iterative milling tests in the pre-compensation step, is proposed.

3. Online chatter detection based on phase shift monitoring

3.1. Introduction and concept

In this chapter, a novel online type-assorted chatter detection, based on the concept of "phase shift monitoring" and inspired by the PF theory in AC circuits, is proposed.

The PF is an index used to represent the energy-transmission efficiency in an electrical system and varies from −1 to 1. A high PF indicates that the electric power is consumed effectively in the electrical devices. Fig. 3-1(a) shows a schematic of a simple AC circuit. A complex power, which includes an active and a reactive power, develops after the current starts flowing in the circuit. The active power, P_{act} [W] is consumed at the load, while the reactive power, P_{react} [W] is not consumed at the load.

Fig. 3-1(b) shows the geometric relationship between the active and the reactive powers in a complex coordinate system. The complex power, P_c [W] can be expressed as follows:

$$P_c = P_{act} + iP_{react} \tag{3-1}$$

The PF is defined by the ratio of the active power to the norm of the complex power (i.e., apparent power, P_{app} [W]) as follows:

$$PF = \frac{P_{act}}{P_{app}} = \cos\theta_{IE} \tag{3-2}$$

$$P_{app} \equiv |P_c| = \sqrt{\frac{1}{T_w}\int_{t'}^{t'+T_w} I_e^2(t)\,dt}\sqrt{\frac{1}{T_w}\int_{t'}^{t'+T_w} E_e^2(t)\,dt} \tag{3-3}$$

$$P_{act} = \frac{1}{T_w}\int_{t'}^{t'+T_w} I_e(t)E_e(t)\,dt \tag{3-4}$$

where I_e [A] and E_e [V] are the AC current and voltage, respectively, and θ_{IE} [rad] is the phase angle between $I_e(t)$ and $E_e(t)$. In addition, T_w [s] is the calculation window length.

Focusing on the analogy between electrical and mechanical systems, Mizoguchi et al. [248,249] converted the PF into an MPF. They used the MPF as an indicator of motion efficiency in a motion-control system [277,278].

Here, based on Eq. (3-2), the PF can be also interpreted as an indicator of the phase shift between the current and voltage. Considering the system analogy, the MPF also indicates a phase shift between the velocity and load force in the mechanical system. By

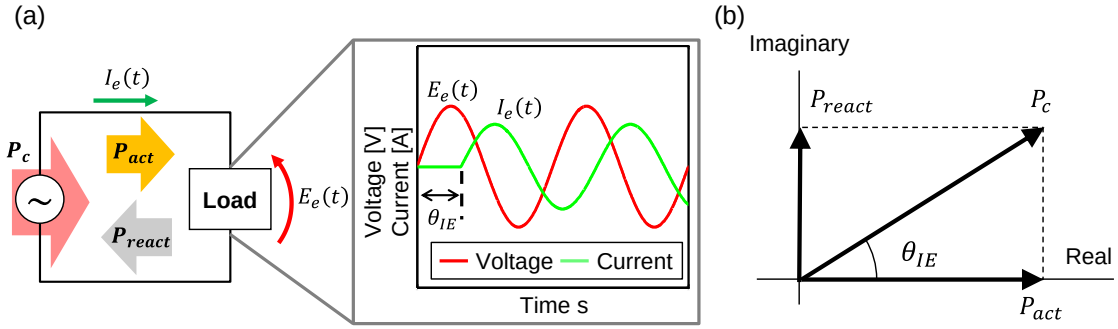

Fig. 3-1 Conceptual figure of PF: (a) electrical AC circuit; (b) vector diagram of power relationship

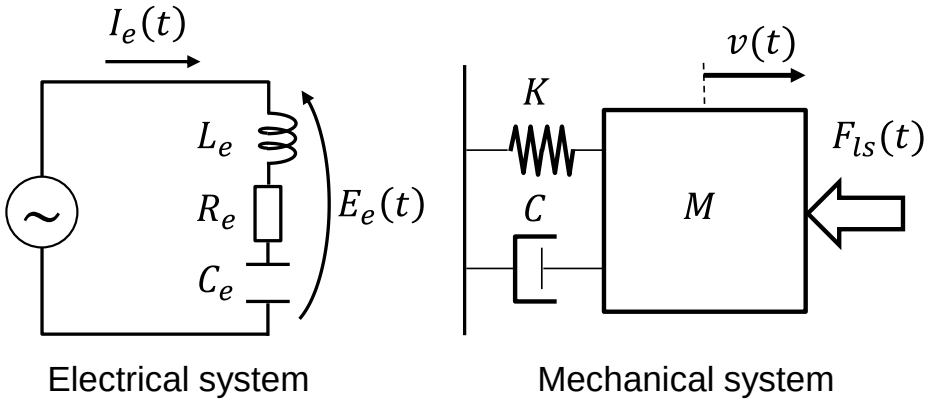

Fig. 3-2 Analogy between electrical and mechanical systems

extending the MPF concept, a novel index, namely the MEF, which indicates the phase difference between the displacement and load force is also proposed in this study.

In a machining system, the phase shift is a key factor for the onset of chatter (see Fig. 1-6). Consequently, both the MPF and MEF can be applied to the chatter detection system. In the following sections, a detailed methodology for constructing a type-assorted chatter detection, with a unique threshold by the MPF and MEF is described. Additionally, the construction of a system that integrates sensorless cutting force estimation is also depicted.

3.2. Methodology

3.2.1. Mechanical power factor for abnormal forced vibration detection

To introduce the MPF, a differential equation of an electrical system is applied to a mechanical system. The RLC circuit is the most basic model for the electrical system, which corresponds to an SDoF vibration model in the mechanical system (see Fig. 3-2). The circuit and motion equations are, respectively shown as follows:

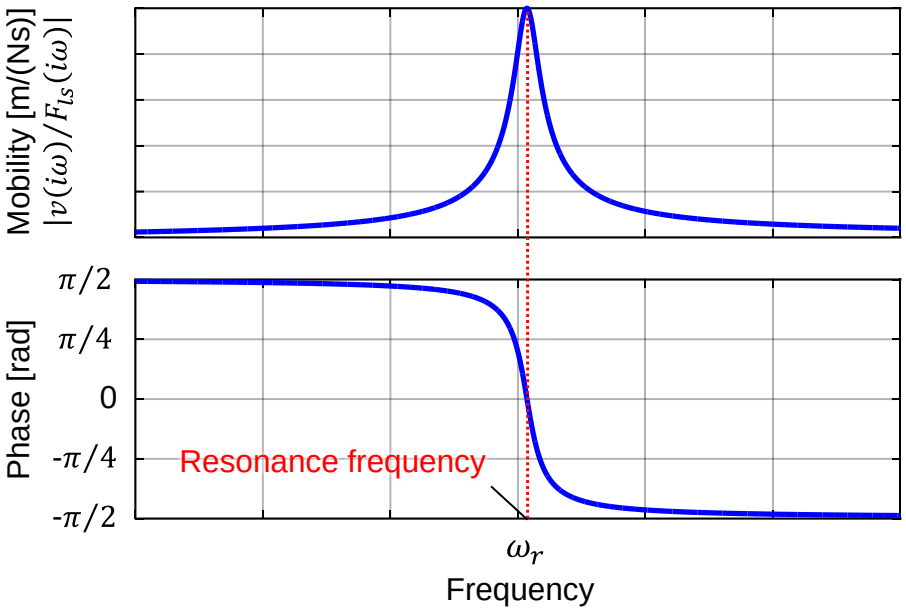

Fig. 3-3 Schematic diagram of mobility in an SDoF system

$$L_e \frac{d}{dt} I_e(t) + R_e I_e(t) + \frac{1}{C_e} \int I_e(t)\, dt = E_e(t) \tag{3-5}$$

$$M \frac{d}{dt} v(t) + Cv(t) + K \int v(t)\, dt = F_{ls}(t) \tag{3-6}$$

where, on one hand, L_e [H], R_e [Ω], and C_e [F] are the inductance, resistance, and capacitance in electrical system, respectively. On the other hand, M [kg], C [N · s/m], and K [N/m] are the mass, damping, and stiffness in mechanical system, respectively.

As expressed in Eqs. (3-5) and (3-6), the current and voltage in the electrical system correspond to the velocity, v [m/s] and load force, F_{ls} [N] in the mechanical system, respectively. As a result, the MPF can be defined with active and apparent mechanical powers, W_{act} [W] and W_{app} [W] by employing Eqs. (3-2)–(3-4), as follows:

$$MPF = \frac{W_{act}}{W_{app}} = \cos\theta_{vF} \tag{3-7}$$

$$W_{app} = \sqrt{\frac{1}{T_w}\int_{t'}^{t'+T_w} v^2(t)\, dt} \sqrt{\frac{1}{T_w}\int_{t'}^{t'+T_w} F_{ls}^2(t)\, dt} \tag{3-8}$$

$$W_{act} = \frac{1}{T_w}\int_{t'}^{t'+T_w} v(t) F_{ls}(t)\, dt \tag{3-9}$$

Table 3-1 Number of calculations required to obtain the MPF

	Addition/subtraction	Multiplication/division
1. Square of each velocity and force	—	$2N_w$
2. Each average calculation of ①	$2(N_w-1)$	2
3. Each root value of ②	—	2
4. Multiplication of each RMS value of ③	—	1
5. Multiplication of velocity and force	—	N_w
6. Average calculation of ⑤	N_w-1	1
7. Division of ⑥ by ④	—	1
Total number of MPF calculations	$3N_w-3$	$3N_w+7$

where θ_{vF} [rad] is the phase difference between $v(t)$ and $F_{ls}(t)$.

Here, the abnormal forced vibration is a type of a resonance phenomenon. If the frequency of the cutting force components corresponds to the resonance frequency of the machine, the machine will vibrate significantly because of the resonance phenomenon. If the CWS can be modeled as an SDoF system, the resultant phase of the vibrational tool displacement is delayed by $\pi/2$ rad compared that of the dynamic force at the resonance frequency. In other words, as the phase of the velocity leads by $\pi/2$ rad compared to the displacement, the phase shift of mobility under an abnormal forced-vibration condition should be close to 0 as shown below (see Fig. 3-3):

$$\angle \frac{v(i\omega_r)}{F_{ls}(i\omega_r)} = \theta_{vF} = 0 \tag{3-10}$$

As an MPF value of close to 1 indicates that the phase difference between the velocity and load force is almost 0 rad, it is expected that the MPF can be used to detect abnormal forced vibration. Note that the actual information that can be obtained during the machining is a discrete-time value, sampled in each sampling period. Therefore, the continuous expressions in Eqs. (3-7)–(3-9) are discretized as follows:

$$MPF[k] = \frac{W_{act}[k]}{W_{app}[k]} \tag{3-11}$$

$$W_{app}[k] = \sqrt{\frac{1}{N_w}\sum_{h=0}^{N_w-1} v^2[k-h]}\sqrt{\frac{1}{N_w}\sum_{h=0}^{N_w-1} F_{ls}^2[k-h]} \tag{3-12}$$

$$W_{act}[k] = \frac{1}{N_w}\sum_{h=0}^{N_w-1} v[k-h]F_{ls}[k-h] \tag{3-13}$$

Table 3-2 Number of calculations required to obtain the MPF by emplying the MA algorithm

	Addition/subtraction	Multiplication/division
1. Square of each velocity and force at the sample number k	0	2
2. Each moving average calculation of ①	4	2
3. Each root value of ②	—	2
4. Multiplication of each RMS value of ③	—	1
5. Multiplication of velocity and force at the sample number k	—	1
6. Moving average calculation of ⑤	2	1
7. Division of ⑥ by ④	—	1
Total number of MPF calculations	6	10

where N_w $[-]$ is the corresponding number of sample data: $N_w = \mathrm{Floor}(T_w/\text{sampling period})$.

If the MPF is calculated using Eqs. (3-11)– (3-13), the total number of calculation steps increases in proportion to N_w, as given in Table 3-1. Nevertheless, the calculation steps of both the apparent and active mechanical powers include calculation of an average, which suggests that the average value is continuously calculated with a small calculation load, when the moving average (MA) algorithm is used in the discrete-time system. The MA algorithm is expressed as:

$$\bar{u}[k] = \bar{u}[k-1] + (u[k] - u[k-N_w])/N_w \tag{3-14}$$

where $u[k]$ and $\bar{u}[k]$ are the analyzed signal and its average value, at k-th sample number, respectively.

Consequently, if $\bar{u}[k-1]$, $u[k]$, and $u[k-N_w]$ are known, the new average value $\bar{u}[k]$ can be calculated by adding/subtracting twice and multiplying/dividing once. The total number of MA calculations will not change even if the number of samples increases. The MA algorithm can be implemented easily by retaining the signals past N_w samples using a ring buffer. By applying the MA algorithm to determine the MPF and MEF, the apparent and active mechanical powers can be obtained with a low computation cost independent of the size of the sampling as follows:

$$W_{app}[k] = \sqrt{\overline{v^2}[k]\overline{F_{ls}^2}[k]} = \sqrt{\overline{v^2}[k-1] + \frac{v^2[k]-v^2[k-N_w]}{N_w}}\sqrt{\overline{F_{ls}^2}[k-1] + \frac{F_{ls}^2[k]-F_{ls}^2[k-N_w]}{N_w}} \tag{3-15}$$

$$W_{act}[k] = \overline{vF_{ls}}[k] = \overline{vF_{ls}}[k-1] + \frac{v[k]F_{ls}[k] - v[k-N_w]F_{ls}[k-N_w]}{N_w} \tag{3-16}$$

As a result, $MPF[k]$ can continue to be computed at every sampling period by adding/subtracting six times and multiplying/dividing ten times as shown in Table 3-2.

3.2.2. Mechanical energy factor for chatter detection

As described in Eq. (1-2), the unstable region owing to the regenerative chatter can be represented in terms of a phase shift, ε_c [rad], as $\pi < \varepsilon_c < 2\pi$. According to [25], the relationship between the phase shift, ε_c and the phase angle of the compliance TF, θ_{xF} [rad] in the SDoF system can be related as follows:

$$\varepsilon_c = 3\pi + 2\theta_{xF} \tag{3-17}$$

Consequently, the chatter condition can be determined by employing the phase difference between the tool displacement and dynamic cutting force as follows:

$$-\pi < \theta_{xF} = \angle\frac{x(i\omega_c)}{F_{ls}(i\omega_c)} < -\frac{\pi}{2} \tag{3-18}$$

where ω_c [rad] is the chatter frequency. The chatter vibration has a strong relationship with θ_{xF}. As the range of θ_{xF} is between $-\pi$ and $-\pi/2$, the range of cosine value of θ_{xF} under the chatter condition is as follows:

$$-1 < \cos\theta_{xF} < 0 \tag{3-19}$$

For detecting chatter vibration, based on Eq. (3-19), a novel index, namely MEF is proposed. In the MPF, the cosine value of θ_{vF} is derived from the velocity and dynamic force by introducing the apparent and active mechanical powers. In other words, the velocity and force are correlated to the power dimension. Similarly, the cosine value of θ_{xF} can be obtained by employing the displacement and dynamic force. As the multiplication of displacement and force has the dimensions of energy, a new indicator for self-excited chatter detection is preferable to be defined in relation to the energy. From this viewpoint, the apparent and active mechanical energy, E_{app} [J] and E_{act} [J] can be defined as follows:

$$E_{app} = \sqrt{\frac{1}{T_w}\int_{t'}^{t'+T_w} x(t)^2\,dt}\sqrt{\frac{1}{T_w}\int_{t'}^{t'+T_w} F_{ls}(t)^2\,dt} \tag{3-20}$$

$$E_{act} = \frac{1}{T_w}\int_{t'}^{t'+T_w} x(t)F_{ls}(t)\,dt \tag{3-21}$$

Then, the MEF indicating the phase difference between the displacement and the load force is defined as follow:

$$MEF = \frac{E_{act}}{E_{app}} = \cos\theta_{xF} \tag{3-22}$$

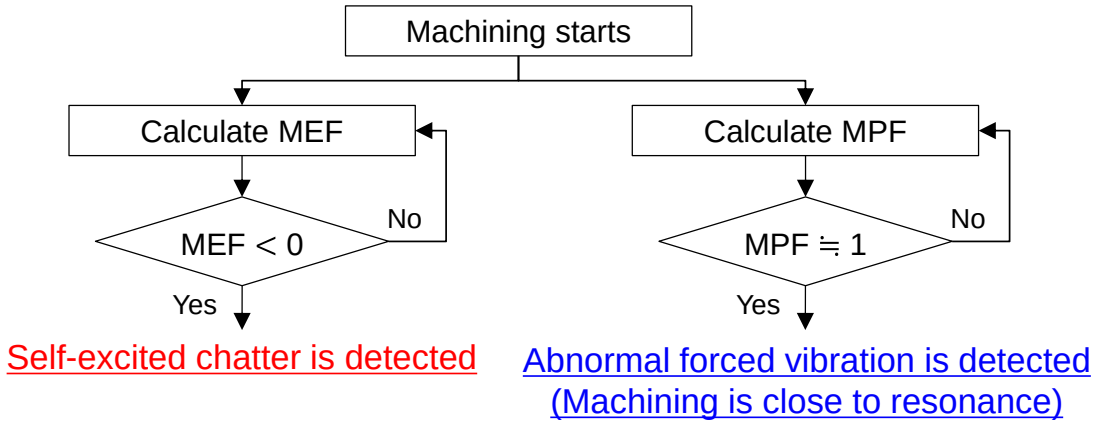

Fig. 3-4 Flowchart of the proposed chatter detection system

Owing to the nature of Eq. (3-19), the value of MEF is less than 0 when the chatter vibration occurs, i.e., the chatter detection is possible based on the phase shift monitoring without setting a threshold for the vibration magnitude. Consequently, the threshold will be determined uniquely, independent of the cutting condition or workpiece material.

Similar to the MPF, the MEF is also discretized as follows:

$$MEF[k] = \frac{E_{act}[k]}{E_{app}[k]} \tag{3-23}$$

$$E_{app}[k] = \sqrt{\overline{x^2}[k]\overline{F_{ls}^2}[k]} = \sqrt{\overline{x^2}[k-1] + \frac{x^2[k]-x^2[k-N_w]}{N_w}}\sqrt{\overline{F_{ls}^2}[k-1] + \frac{F_{ls}^2[k]-F_{ls}^2[k-N_w]}{N_w}} \tag{3-24}$$

$$E_{act}[k] = \overline{xF_{ls}}[k] = \overline{xF_{ls}}[k-1] + \frac{x[k]F_{ls}[k] - x[k-N_w]F_{ls}[k-N_w]}{N_w} \tag{3-25}$$

Based on Eqs. (3-23)–(3-25), the MEF is also computed at every sampling period with six iterations of addition/subtraction, and ten iterations of multiplication/division, independent of the number of data samples. Finally, a type-discrimination chatter detection can be constructed by monitoring both the MPF and MEF, as shown in Fig. 3-4. The MPF and MEF are continuously computed with a low computation cost, and the thresholds for detecting forced and chatter vibration can be set uniquely as follows:

$$\begin{cases} \text{MPF} \approx 1 & \text{if forced vibration occurs} \\ \text{MEF} < 0 & \text{if chatter vibration occurs} \end{cases} \tag{3-26}$$

3.3. Experimental system configurations

3.3.1. Experimental setup and procedure

Fig. 3-5(a) shows the prototype precision lathe, including a work spindle supported by an aerostatic bearing and an XZ-stage driven by shaft-type linear motors along two linear ball guideways. Fig. 3-5(b) also depicts the schematic of CWS where the tool approach angle was approximately 90°. Optical linear encoders with a resolution of 10 nm were attached to the stage in each direction. The detailed specifications of the developed linear motor-driven high-precision lathe are also summarized in **Appendix A**.

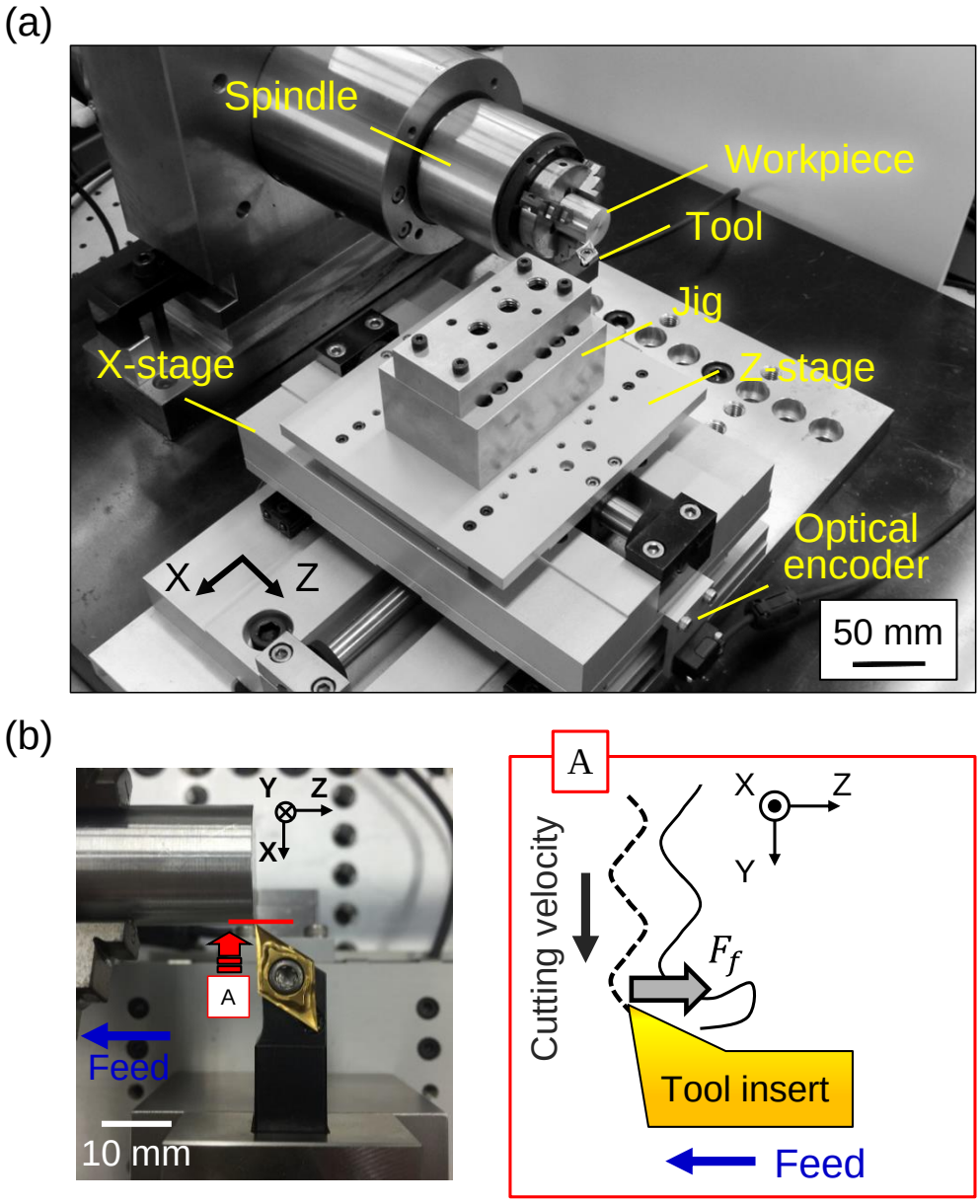

Fig. 3-5 Experimental setup: (a) prototype linear motor-driven high-precision lathe; (b) schematic of corresponding CWS

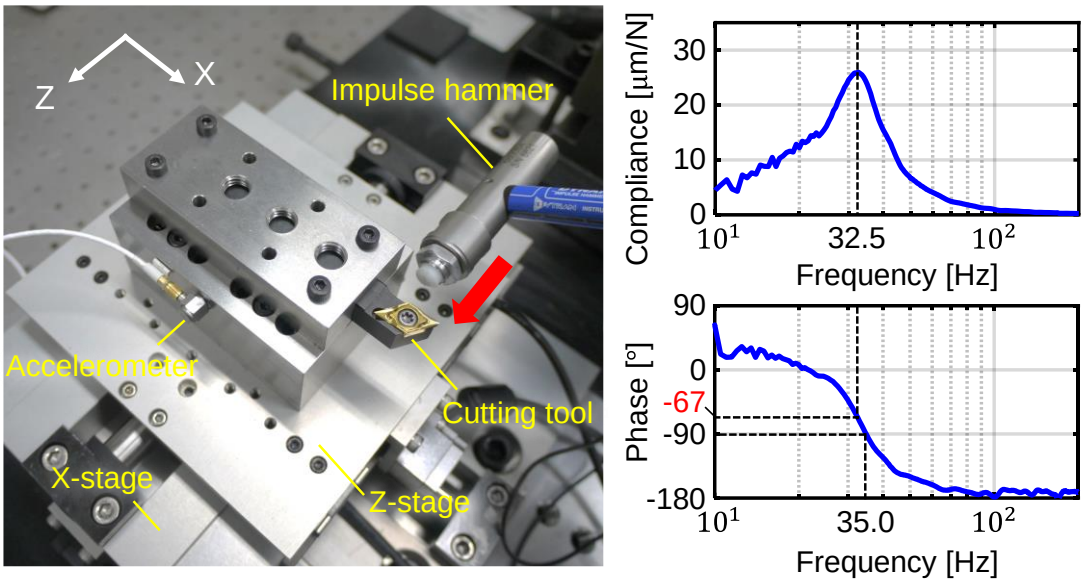

Fig. 3-6 Compliance FRF from the tool-tip to the jig under the fixed-position control

Fig. 3-6 shows the experimental compliance FRF from the tool tip to the Z-stage, obtained by a preliminary tap test under the fixed-position control. It agreed well with that from the tooltip to the Z-stage and can be regarded as an SDoF system. Here, the resonant frequency of 32.5 Hz was slightly different from the frequency of 35. 0 Hz, where the phase difference was -90 degree owing to influence of the controller. Because the MEF/MPF follows the phase characteristic, this difference would influence the reliability of the phase shift monitoring, especially for the MPF. It should be compensated to achieve a more accurate monitoring. However, it was not practical to set the threshold to "exactly" 1. Furthermore, the forced vibration would pose a problem when the disturbance frequency was "around" the resonant frequency, as the magnitude of compliance was already high around the resonance. In fact, the amplitude of compliance was still high at 35.0 Hz. As the phase of mobility at 32.5 Hz should be 23 ° (i.e., the cosine value was 0.92), the threshold of the MPF for forced vibration detection was set to 0.90 in this study. Empirically, an approximate value of 0.8 – 0.9 may be a reasonable threshold for the MPF for detecting forced vibration.

3.3.2. MPF/MEF monitoring system applying a DOB

In machining process, the dynamic load force corresponds to the cutting force (i.e., $F_{ls} \rightarrow F$); hence, the dynamic cutting force must be monitored to apply the MPF and MEF for chatter detection. In this study, the dynamic cutting force is estimated by applying a DOB to the control system of the linear motor-driven stage. The shaft-type linear motor in the developed lathe is suitable for estimating the high-precision force because of its friction-less and cogging-less structure. The cutting force estimation manner of the DOB in a linear

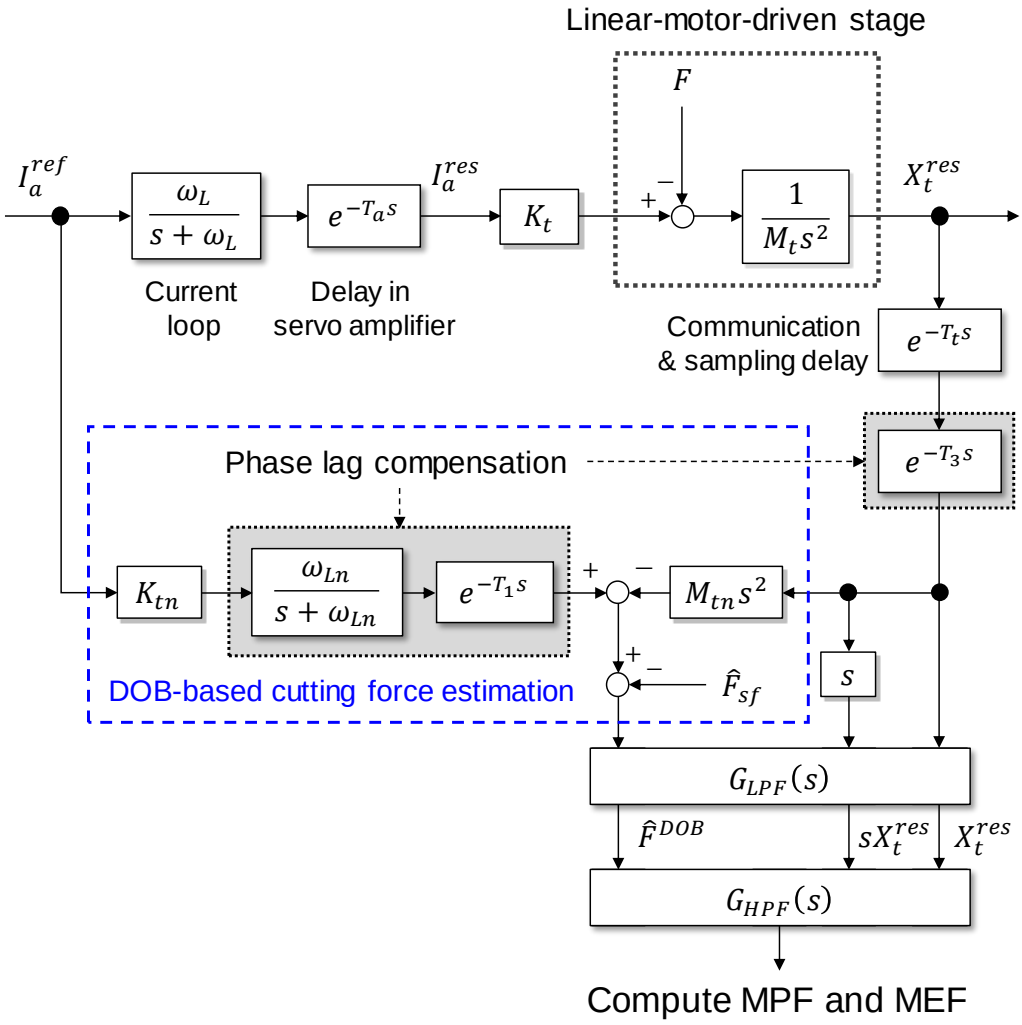

Fig. 3-7 Block diagram of the MPF/MEF monitoring system

motor-driven system has been described in Eq. (2-15).

To compute the MPF/MEF, the tool vibrational displacement and velocity are also needed. In this study, the tool displacement is directly obtained from the linear encoder, as the developed high-precision lathe has an SDoF characteristic from the tool-tip to the linear encoder (see Fig. 3-6). The velocity response is calculated by numerically differentiating the obtained position information.

Fig. 3-7 shows a block diagram of the MPF/MEF monitoring system, integrated with the DOB-based cutting force estimation. Note that the same LPF as the cutting force observer was inserted into the velocity and displacement information before the MPF/MEF calculation to eliminate the relative phase lag caused by the LPF. In addition, a high-pass filter (HPF) was applied to all the information to cut off the DC components, because only the dynamic component, essential for the chatter as well as the PF is originally defined in the AC circuit. Consequently, the compensation of the friction force in the DOB became unnecessary. Note that the pass-through filters cause an additional phase shift of the

Table 3-3 Parameters for the monitoring system

	X-stage	Z-stage
Sampling time [μs]	80	
Nominal movable mass, M_{tn} [kg]	7.2	3.0
Nominal thrust-force coefficient, K_{tn} [N/A]	18.5	20.5
Cutoff frequency of LPF, g_{LPF} [rad/s]	500	1000
Cutoff frequency of HPF, g_{HPF} [rad/s]	—	4π

signals. However, they do not pose a problem for chatter detection by the MPF/MEF, if the same type and number of filters are inserted in all the signals, as the MPF/MEF captures the "relative" phase shift between the signals. Therefore, the phase lag compensations are also important if needed. After the filtering process, the MEF and MPF were calculated at every servo cycle.

Table 3-3 lists the parameters for the monitoring systems. A second order LPF and a bi-quad HPF were employed. Phase lag compensations were not applied in this system. Note that the bandwidth of the LPF must be higher than the expected chatter frequency so that the chatter component was not eliminated. The nominal movable masses and thrust-force coefficients in the X- and Z- stages were simply determined from the design values. As shown in Fig. 3-5(b), the vibration direction of the width of cut corresponded to the feed direction (i.e., the Z-direction), and the process force in the Z-direction fluctuated dynamically. Therefore, the proposed chatter-detection method was applied to the Z-stage.

3.4. Experimental results

Using the above experimental setup, three types of experiments were conducted. In the first experiment, the oscillation test was conducted to evaluate the influence of the calculation window length, T_w, on the calculation accuracy of the MPF and MEF (see Fig. 3-8). The calculation window length was varied from 1 to 200 ms under several oscillation frequencies. The obtained results were evaluated with the peak-to-peak (P-P) values of the resultant MPF and MEF. In the second and third experiments, outside turning tests were conducted, while gradually increasing the radial depth of the cut and spindle speed during the process, respectively. The performance of the proposed method was evaluated by comparing the results of the machined surface quality and frequency analyses.

3.4.1. Oscillation test

The oscillator applied a vibration of approximately 9.25 Hz as the low-frequency and 40 Hz as the high-frequency to the Z-stage in the Z-direction. Fig. 3-9(a) shows the results of the estimated force and velocity during the oscillation. The phase difference between the

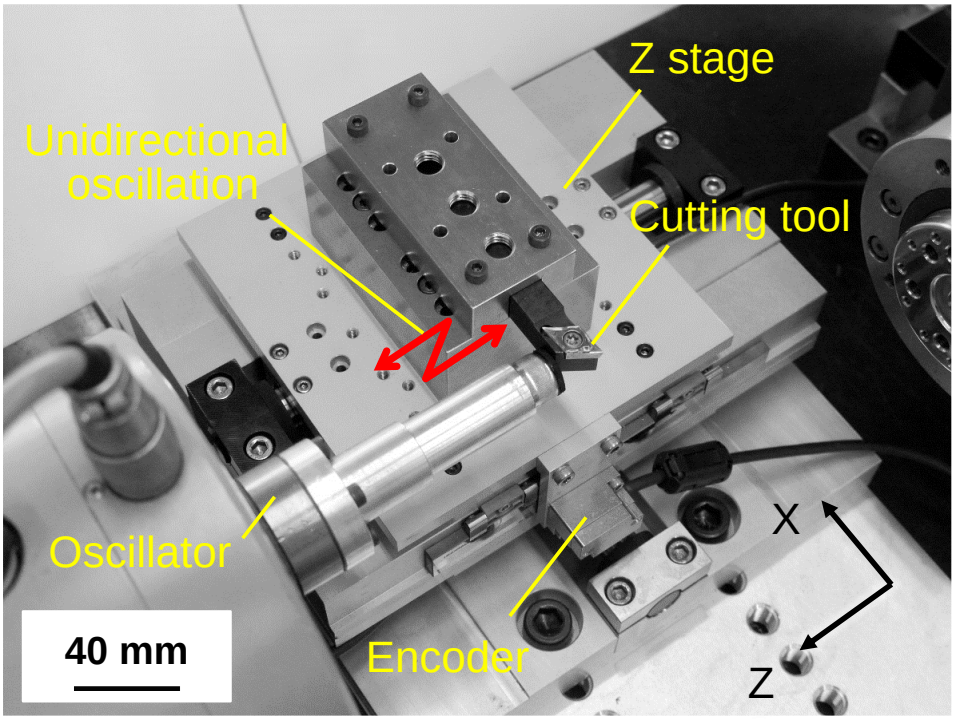

Fig. 3-8 Experimental setup for the oscillation test

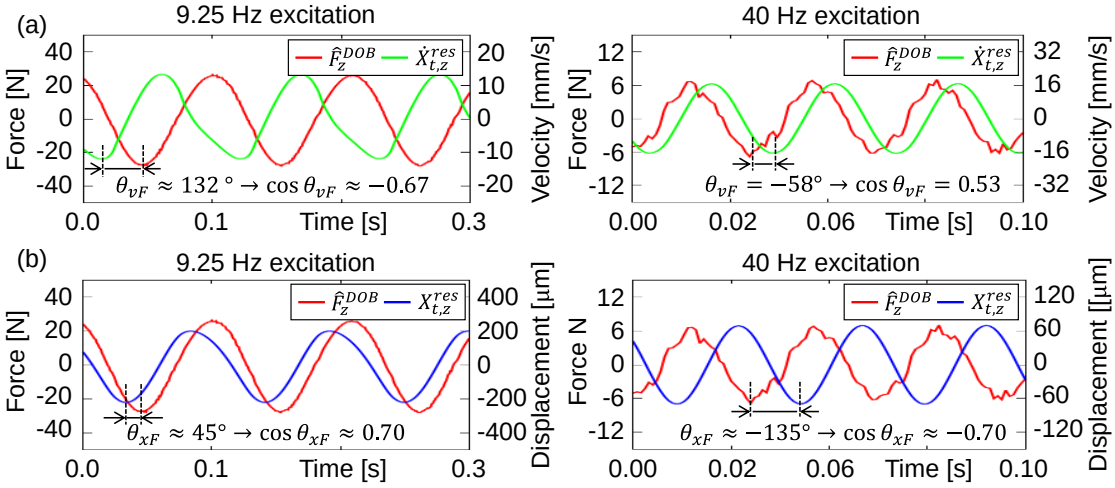

Fig. 3-9 Response of the estimated force, and (a) velocity, (b) displacement in the oscillation test

force and velocity was approximately 132° (2.31 rad) at 9.25-Hz excitation and –58° (–1.01 rad) at 40-Hz excitation, respectively; hence, the MPF values were expected to become approximately –0.67 and 0.53 at each frequency. Similarly, Fig. 3-9(b) shows the result of the estimated force and displacement response. The phase difference between the force and displacement was approximately 45° (0.79 rad) at 9.25-Hz excitation and –135° (–0.70 rad) at 40 Hz; hence the MEF values should be 0.70 and −0.70 at each frequency.

Fig. 3-10 shows the behavior of the MEF with window lengths of 10 and 200 ms. The MPF calculation exhibited a similar tendency. As shown in Fig. 3-10, the accuracy of the

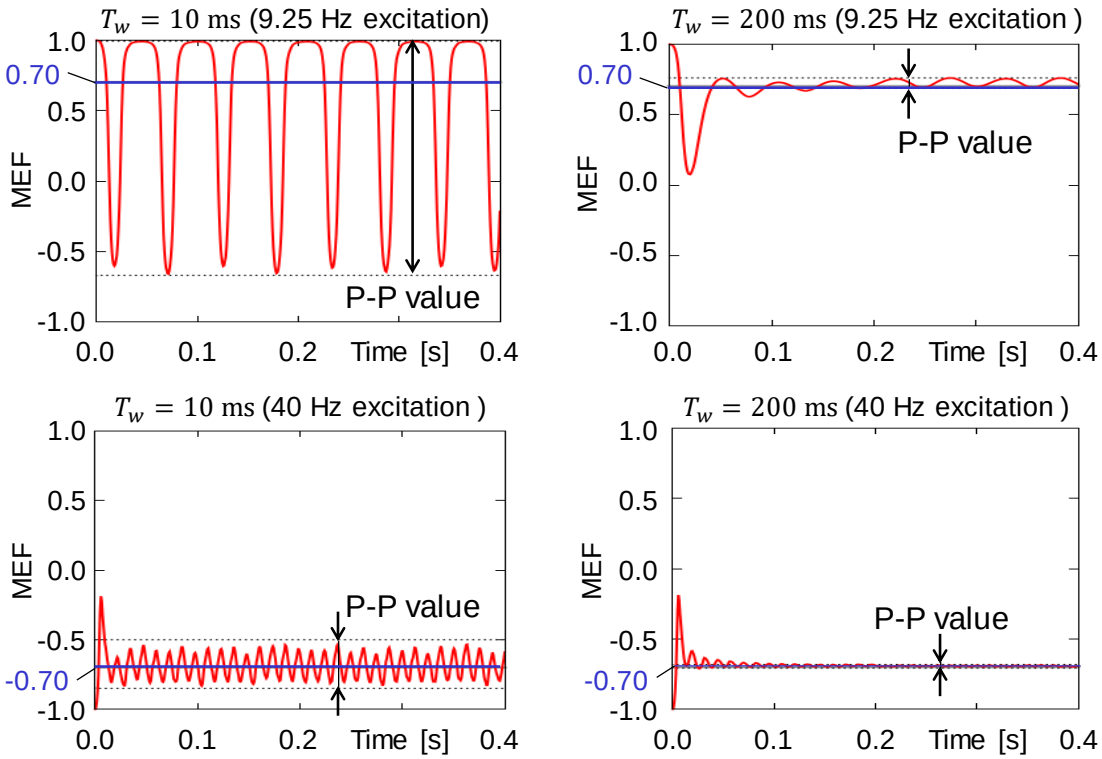

Fig. 3-10 Representative results of MEF monitoring with different window lengths and input frequencies

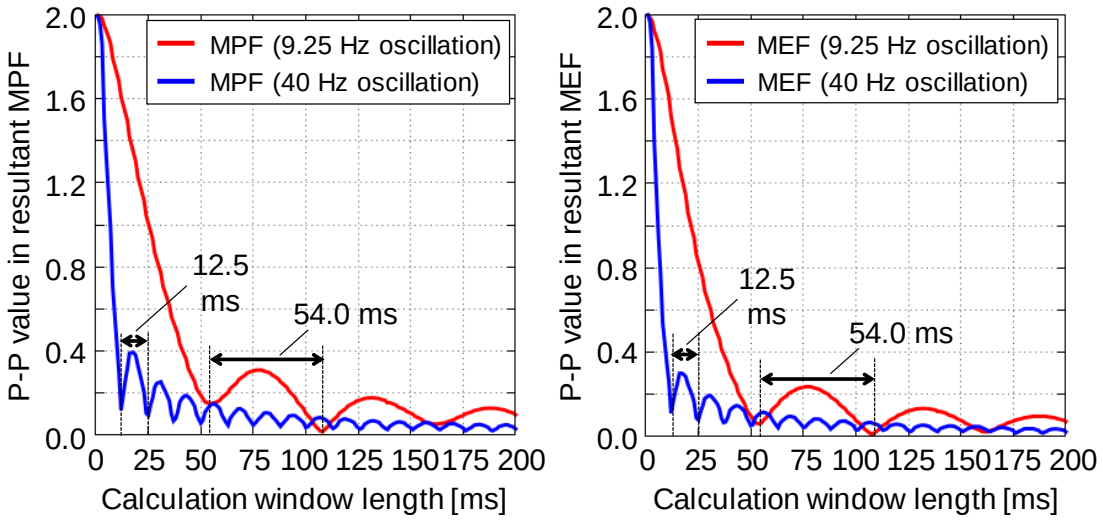

Fig. 3-11 Summary of the P-P value of the resultant MPF/MEF for each window length

MEF/MPF calculation depended on the window length according to the input frequency.

Fig. 3-11 summarizes the P-P values of the MEF and MPF at every calculation window length, and shows that the calculation accuracy tended to reduce every half period of the input oscillation (i.e., $1/(2 \times 9.25\ \text{Hz}) = 54\ \text{ms}$, $1/(2 \times 40\ \text{Hz}) = 12.5\ \text{ms}$). It suggests that the ratio of the window length to the input oscillation period was important. In particular, it was preferable to set the window length to an integer multiple of half of the input

oscillation period. In AC electrical circuits, T_w is set to correspond to the frequency of the AC current/voltage, and is usually known in advance. However, the optimal window length is unclear in the machining process because the chatter frequency is usually unknown. Here, as seen in Fig. 3-10, the MPF/MEF value fluctuated significantly with a low-frequency input with the same window length; hence, the window length should be set considering the lower frequency component of the analytical object rather than the higher frequency component.

From the above analysis, the window length was set to the same period of the spindle speed in the outside turning tests, as the rotational frequency was generally lower than the chatter/resonance frequency. The integer number of waves generated in the spindle period should be sufficiently large to alleviate the calculation error. Consequently, the chatter can be detected at least after one spindle rotation, when the chatter occurs, because all the data in each sliding window was updated after one spindle rotation.

3.4.2. Turning test increasing the depth of cut

To verify the performance of the proposed chatter detection method, an outside turning test was conducted, while increasing the depth of the cut, in the second experiment. The cutting conditions are summarized in Table 3-4. The calculation window length was set to 67 ms (i.e., $T_w = 67\ \text{ms} \rightarrow N_w = \text{Round}(67\ \text{ms}/80\ \mu\text{s}) = 838\ \text{samples}$) so that it coincided with the spindle-rotation frequency, as discussed in the previous subsection.

Fig. 3-12(a) shows the machined surface quality evaluated along with its roughness curve measured using the stylus profiling instrument (Surfcom Flex-50A; Tokyo Seimitsu Co., Ltd, see Fig. 3-13). The machining time according to the feed length during the turning is also shown in Fig. 3-12(b). The chatter mark (i.e., the deteriorated surface) can be clearly observed after a machining time of 22 s.

Fig. 3-14 shows the off-line STFT analysis of the estimated cutting force. Before 22 s, the component of 15 Hz corresponding to a spindle rotation of 900 min^{-1} was dominant, while the 41-Hz component could be observed after 17 s. From 17 to 22 s, the cutting process might be in a transition region from being stable to unstable. After 22 s, chatter was generated with a peak frequency of 41 Hz, which corresponded to neither the spindle rotational frequency nor the resonance frequency; hence, it could be considered to be a chatter vibration, and not an abnormal forced vibration.

Table 3-4 Cutting conditions for outside truning, while increasing the depth of cut

Cutting tool	Carbide
Workpiece	A5056B (ϕ 20 mm × 30 mm)
Feed rate in Z-direction [μm/rev]	36.0
Feed rate in X-direction [nm/rev]	67.0
Spindle speed [min^{-1}]	900
Calculation window length [ms]	67
Depth of cut [μm]	150 – 178

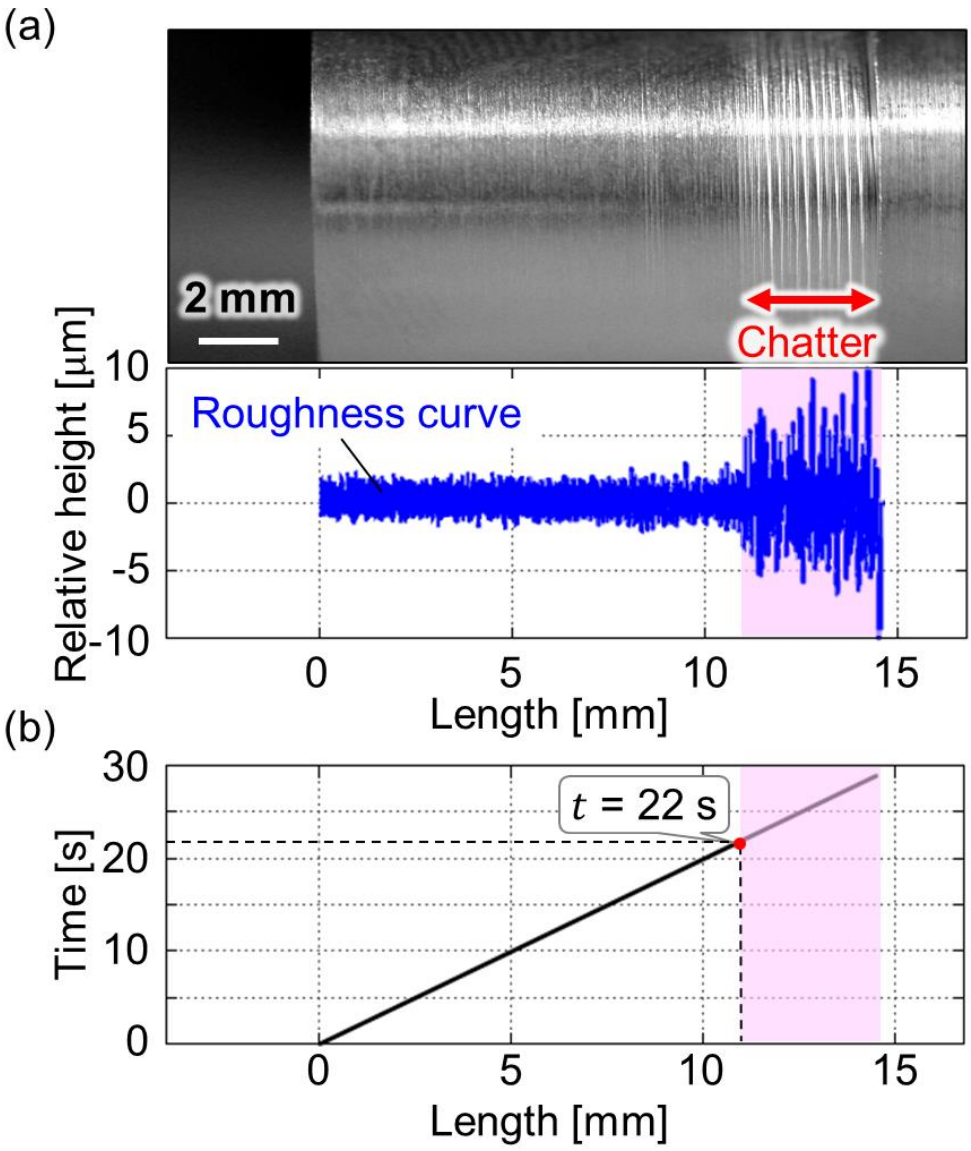

Fig. 3-12 Results in outside turning, while increasing the depth of the cut: (a) picture and roughness curve of the machined surface, (b) machining time along feed length

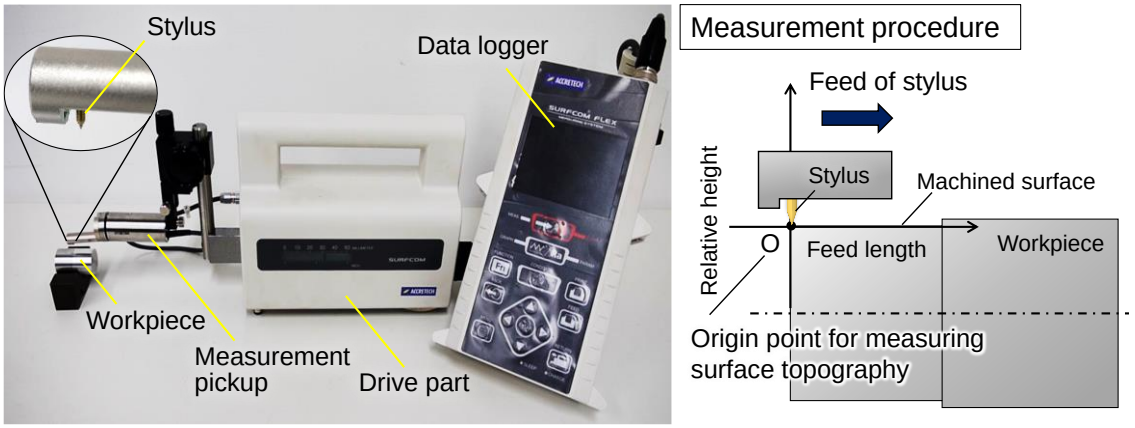

Fig. 3-13 Measurement instrument for surface topography (e.g., surface roughness/waviness)

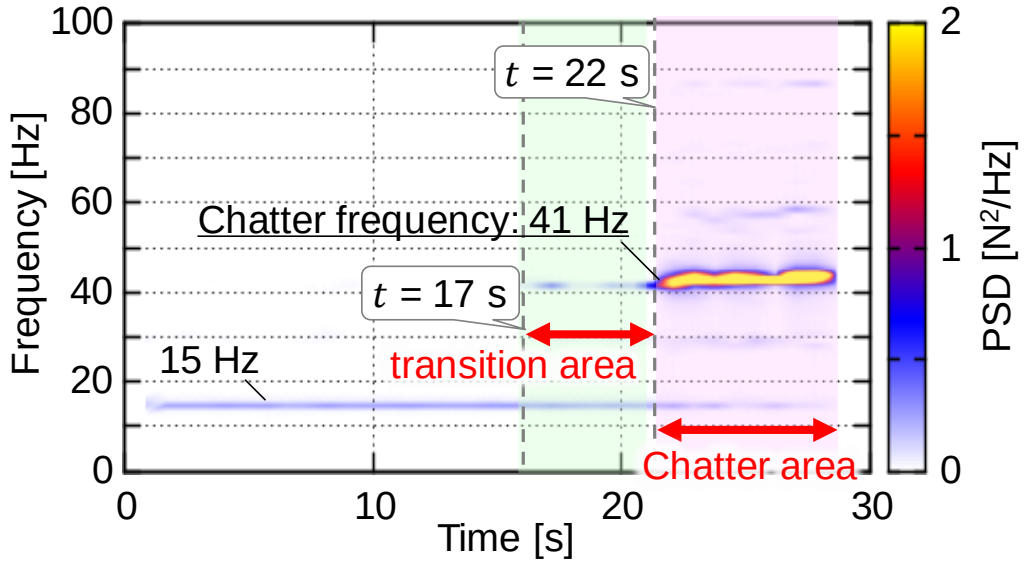

Fig. 3-14 STFT of the cutting force estimated by DOB in outside turning, while increasing the depth of the cut

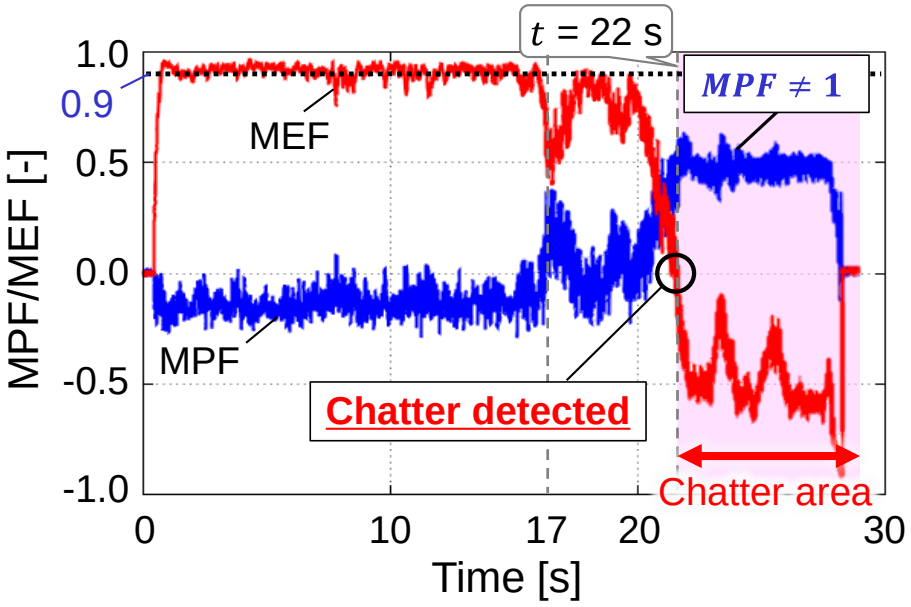

Fig. 3-15 Monitoring MPF and MEF in outside turning, while increasing the depth of cut

Based on Fig. 3-14, it may be inferred that chatter detection is feasible if a real-time implementation of STFT is possible. However, it may be difficult to detect the chatter quickly because of the computational cost as well as the relatively long analysis section to ensure the frequency resolution. Additionally, an appropriate threshold must be considered carefully for robust autonomous detection, and may be reconsidered if the experimental conditions are changed, as the spectrum amplitude depends on the cutting conditions.

Fig. 3-15 shows the results of the online MPF and MEF monitoring. Both the MEF and MPF began to fluctuate from 17 s (i.e., the transition area determined from the STFT

analysis). This is because the chatter component and the spindle rotational component were mixed in this area. However, each factor remained in a stable area, as the stable component was still dominant. After 22 s, the MEF value suddenly become negative and remained negative during the self-excited chatter. In this area, the MPF was not close to 1 (i.e., lower than the threshold of 0.9, as discussed in Fig. 3-6), although it approached 1. As a result, it can be considered that the resonance did not occur, which corresponded to the analysis presented in the machined surface and STFT. The results show that the chatter could be detected, while distinguishing it from the abnormal forced vibration by comprehensively monitoring the MPF and MEF.

Here, the PF originally indicated the energy-transmission efficiency in the AC circuit, i.e., how much energy supplied from the power supply was consumed at the load. Considering the analogy between the electrical and mechanical systems, to sum up, the MPF suggested how much energy supplied from the cutting force was consumed as the vibration of the machine took place. Under the (regenerative) chatter condition, the energy flowed into the tool side continuously and was consumed as the vibration continued (refer Fig. 1-6). That is why the MPF also approached 1 when the chatter occurred. When the MPF was equal to 1, the energy supplied from the cutting force was converted into vibration energy most efficiently, which implied that a resonance occurred.

3.4.3. Turning test increasing the spindle rotational speed

Another outside turning test was conducted, while increasing the spindle speed under a constant depth of cut, as the third experiment. Table 3-5 lists the cutting conditions. Here, the calculation window length was adaptively changed during the process, in response to the changes in the spindle speed.

Fig. 3-16 shows the machined surface quality with its roughness and waviness curve (Fig. 3-16(a)) measured by the stylus profiling instrument similar to the second experiment (see Fig. 3-13) as well as the machining time according to the feed length(Fig. 3-16(b)). As seen in Fig. 3-16, the surface roughness deteriorated in the feed length from 4.3 to 7.9 mm, and after 12.3 mm. From 7.9 to 12.3 mm, the waviness deteriorated, whereas the deterioration of the surface roughness could not be observed in this area.

Table 3-5 Cutting conditions for outside truning while increasing the spindle speed

Cutting tool	Carbide
Workpiece	A5056B (ϕ 20 mm × 30 mm)
Feed rate in Z-direction [μm/rev]	36.0
Feed rate in X-direction [nm/rev)	0.0
Spindle speed [min^{-1}]	500 – 2290 (100 min^{-1}/s)
Calculation window length [ms]	60/Spindle speed × 10^3
Depth of cut [μm]	180

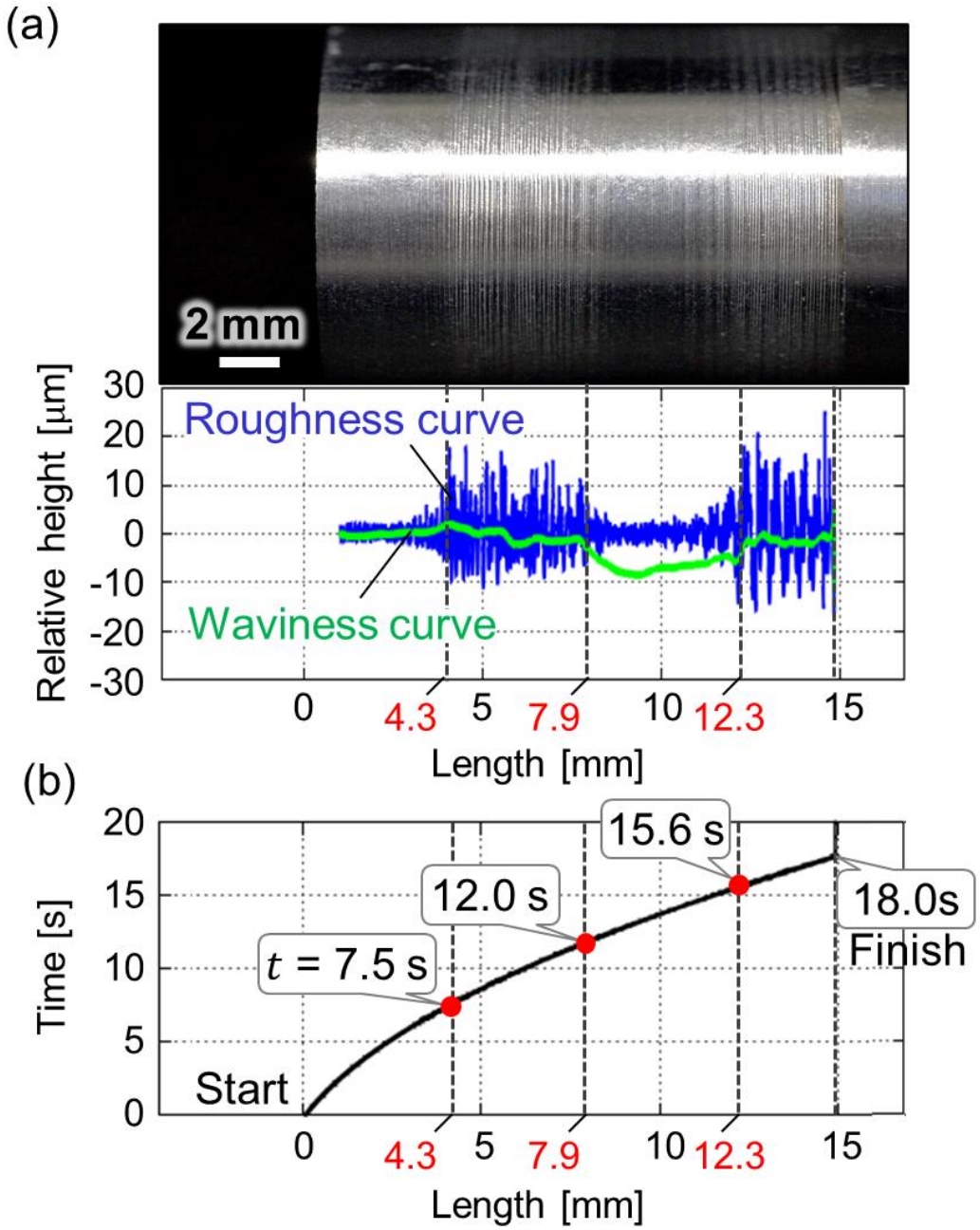

Fig. 3-16 Results in the outside turning, while the spindle speed was increased: (a) picture, roughness curve, and waviness curve of the machined surface, (b) machining time along feed length

Fig. 3-17 shows the estimated cutting force after the HPF in the Z-direction and its off-line STFT result. As soon as the machining started, a vibration with a frequency of 8.4 Hz caused by the spindle rotation of 500 min^{-1} was generated. Subsequently, the frequency component gradually increased in response to an increase in the spindle speed. The frequencies of about 38 and 76 Hz were excited suddenly from 7.5 s (a spindle speed of 1240 min^{-1}), and dominated the frequency component in the cutting force until 12.0 s (a spindle speed of 1690 min^{-1}). The vibration amplitude of the estimated cutting force also increased in this area. Because these frequencies were in discord with the higher harmonics of the

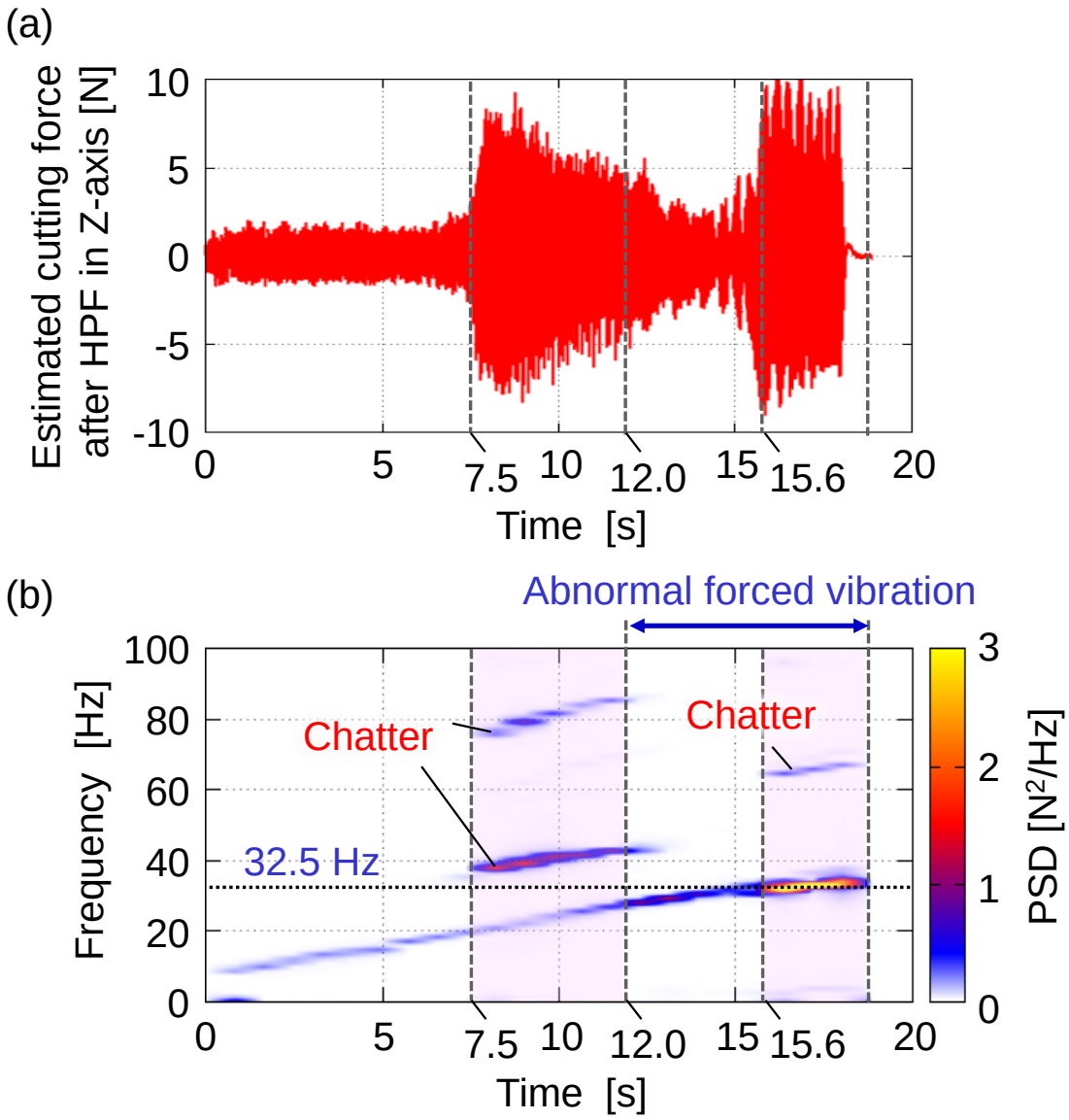

Fig. 3-17 The cutting force estimated by DOB in outside turning, while increasing the spindle speed: (a) time waveform, (b) STFT analysis

spindle rotational frequency, it can be concluded that the (regenerative) chatter occurred from 7.5 to 12.0 s (i.e., between the spindle speeds of 1240 to 1690 min^{-1}).

The amplitude of the estimated cutting force decreased and the chatter seemed to disappear from 12.0 s. On the other hand, the spectrum of the spindle-rotation frequency around the resonance appeared to be excited (i.e., an abnormal forced vibration occurred). Instead of the surface roughness, the waviness began to deteriorate from 12.0 s.

In the turning process, surface roughness resulted from the cusp height. However, the cusp height might not increase when the spindle-rotation frequency was sufficiently close to the resonant frequency, as the tool displacement per spindle rotation was approximately the same in each cycle (Fig. 3-18). As a result, the waviness deteriorated when the abnormal forced vibration occurred, whereas the surface roughness did not worsen in this experiment.

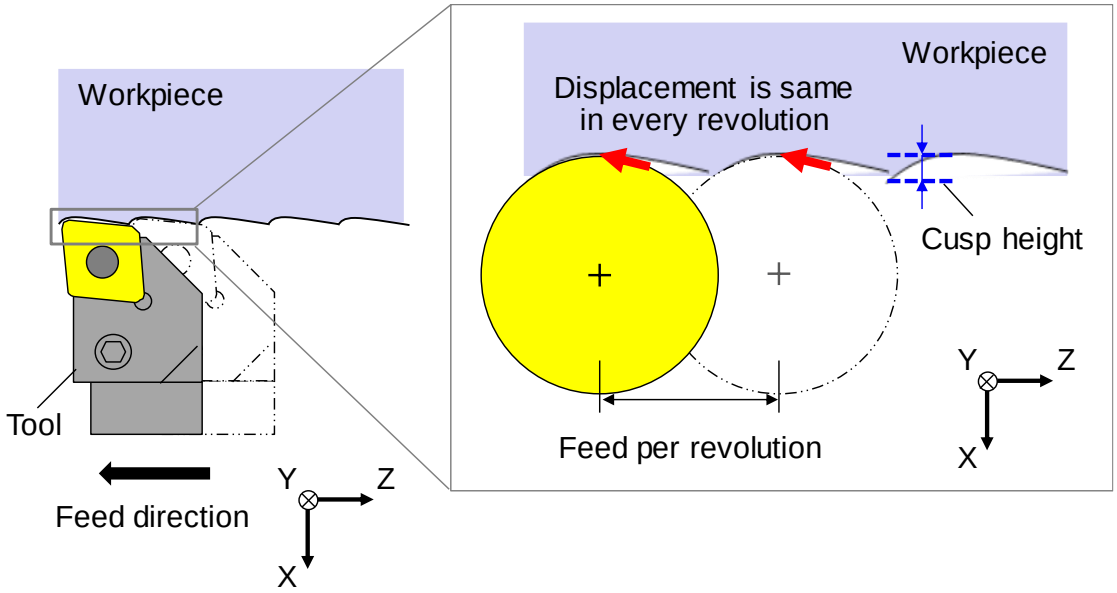

Fig. 3-18 Tool displacement and cusp height in resonance

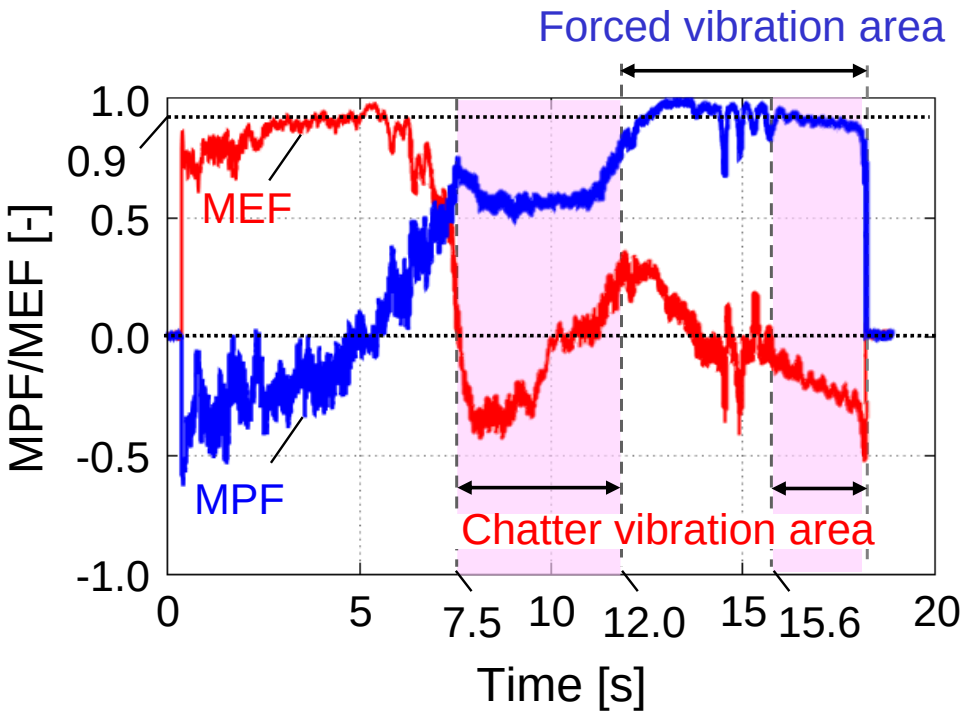

Fig. 3-19 Monitoring results of MPF and MEF in the outside turning, while increasing the spindle speed

In general, an increase in the waviness causes a deterioration in the form accuracy of the machined parts; therefore, detecting the abnormal forced vibration is also critical in practical applications.

Here, it appears that the chatter of approximately 65 Hz occurred again at the same time. The amplitude of the estimated cutting force also increased in this area. As synchronization between the tool vibration and spindle rotation collapsed due to the chatter

vibration, it could be considered that the surface roughness, and not the surface waviness, deteriorated again from 15.6 s (i.e., a spindle speed of 2050 min^{-1}), as shown in Fig. 3-16.

Fig. 3-19 shows the online MPF and MEF monitoring results. The MEF value suddenly became negative when the first chatter vibration occurred, although the MPF remained approximately at 0.5; hence the first chatter from 7.5 s was clearly detected by the MEF. According to the result in Fig. 3-15, the MEF was expected to continue displaying a negative value during the chatter vibration. However, the MEF remained approximately zero after 10 s, and finally transitioned to a positive value before 12.0 s. In the STFT analysis of Fig. 3-17(b), it can be seen that the spindle-rotation frequency began to be slightly excited from approximately 10.0 s. Consequently, it changed the MEF to a positive value. At the same time, the MPF began to approach 1.0. From 12.0 to 15.6 s, when only the abnormal forced vibration occurred, the MPF evidently tended to stay close to 1. Assuming a threshold of 0.9 for the MPF, the abnormal forced vibration was successfully monitored by the MPF.

Shortly before 15.6 s, both the MPF and MEF fluctuated largely, which was similar to the transition phenomenon seen in Fig. 3-15. In fact, the chatter reoccurred after 15.6 s in this experiment. As the chatter and forced vibrations occurred (or the chatter occurred very close to the resonant frequency) after 15.6 s, the MEF transitioned to a negative value. However, the MEF already showed a negative value at 13.8 s, and the MPF gradually decreased by a small extent owing to the influence of the chatter frequency of 65 Hz. When either the chatter or the abnormal forced vibration occurred individually, the type-assorted detection of abnormal vibration was feasible by the monitoring of both the MPF and MEF. However, if some dominant components existed, the reliability of the proposed chatter detection system would deteriorate, although the tendency of the cutting state could be captured.

3.5. Summary

This chapter describes a chatter detection methodology based on two novel indices, namely the MPF and MEF. The findings from this chapter can be summarized as follows:

1. In machining processes, MPF and MEF represent the phase differences between the dynamic cutting force on the one hand, and the velocity or displacement on the other hand, in the CWS, respectively. Based on the onset mechanism of abnormal vibrations, the MPF and MEF could be utilized to monitor the forced and chatter vibration, respectively.

2. The MPF and MEF could be calculated during the process with a low computational cost, independent of the calculation window length, by employing the MA algorithm. Based on the results of the oscillation tests, the window length was set to the spindle-

rotation period in the turning process. Consequently, a fast chatter/forced detection could be achieved, at least after one spindle rotation.

3. By combining with the observer-based cutting-force estimation, the MPF and MEF were successfully obtained without using any additional sensors. Note that the proposed method has the potential to be developed on a sensor-based system, such as a dynamometer, displacement sensor, and accelerometer.

4. In the outside turning tests, the MEF rapidly became negative as soon as the (regenerative) chatter occurred, and remained negative during the chatter condition. In addition, the MPF was fairly close to 1 during the abnormal forced vibration (i.e., resonance), whereas it did not become 1 during the stable cutting or only the regenerative-chatter generation. However, when some dominant frequency components existed, the reliability of the proposed method could deteriorate.

The proposed method could help distinguish between a stable cutting, chatter, and forced vibration using unique thresholds. The threshold of the MEF was clear (i.e., MEF < 0). Although the exact threshold of the MPF was 1, a range of 0.8–0.9 is reasonable in practice. Because the aforementioned thresholds were determined from the chatter mechanism, they were expected to be independent of the workpiece materials or the cutting conditions; hence, there is ideally no need to reconsider the thresholds for each experiment.

Here, the concept of proposed method can be applied to a ball-screw-driven stage, wherein a sensorless detection system with an observer-based cutting force estimation can also be achieved if the chatter-induced process force can be estimated accurately. Note that, in this study, the stage displacement measured by linear encoder were simply used for the calculation of MPF and MEF, as the tool and stage vibrated together as a SDoF system (see Fig. 3-6). However, when chatter results from a local mode of tool/workpiece/spindle, MPF/MEF calculation considering a transfer function from the vibration element and stage must be achieved. Another option is sensor-based direct measurement of vibration and cutting force near the cutting point. In particular, system integration to the adaptronic machine components (fifth functionality of SOMS in Fig. 1-1), such as intelligent/sensory spindle unit [36,37] integrating sensors and monitoring functions, may be effective. For chatter in a rotating flexible tool/workpiece, the sensorless phase shift monitoring by MPF/MEF in angular domain (with or without coordinate transformation), calculated from the estimated cutting torque and angular velocity/displacement of spindle, is also interesting. Additionally, further improvements to the detection algorithm may be necessary, especially in processes with intermittent cutting and/or 2DoF system.

4. Chatter suppression with spindle speed variation

4.1. Assumptions and concepts

In this chapter, a practical design methodology for optimal sinusoidal SSV (SSSV), oriented towards SOMS is proposed that can be simply integrated into machine tools to realize autonomous chatter suppression with an in-situ optimal design. As described in Fig. 1-6, the regenerative chatter mechanism can be interpreted from the viewpoint of the internal process energy balance as follows (same formula as Eq. (1-1)):

$$E_f = E_p - E_n > E_d \tag{4-1}$$

As the total inflow energy in the SSV cycle is changed by a phase shift perturbation owing to the spindle speed variation, the optimal design methodology for SSSV is proposed to properly control the process energy balance [279]. The net inflow of energy, E_f [J] in a section $[t_b, t_e]$ can be defined kinematically with the resultant dynamic cutting force vector, $\boldsymbol{F_c}$ and vibration vector, $\boldsymbol{q_c}$ as follows:

$$E_f = \int_{t_b}^{t_e} \boldsymbol{F_c}(t) \cdot \dot{\boldsymbol{q}}_{\boldsymbol{c}}(t)\, dt \tag{4-2}$$

Note that this study only considers the net inflow of energy to be minimized because the damping capacity should always work positively for process stabilization. To estimate E_d, the machine dynamics must be identified, as was done in the SLD approach [70].

By only considering the minimization of Eq. (4-2), the self-acting selection of proper SSV parameters can be achieved, based on the observable chatter frequency during the process. For analytically calculating Eq. (4-2), the cutting force and vibration have to be modeled first. In the next subsection, the details of the process modeling for obtaining the internal process energy is described. Fig. 4-1 shows a general SDoF turning process, assuming that the tool vibrates in a flexible manner in a particular vibration direction in a 3D space. Through chatter modeling, a novel interpretation of the SSSV process is provided, using the analogy of frequency modulation (FM) techniques used in radio communication engineering.

4.2. Process modeling

4.2.1. Vibration model and novel interpretation of SSSV

In many machining applications, only one dominant elastic mode usually becomes unstable and yields a single dominant chatter frequency. This hypothesis, known as ZOA,

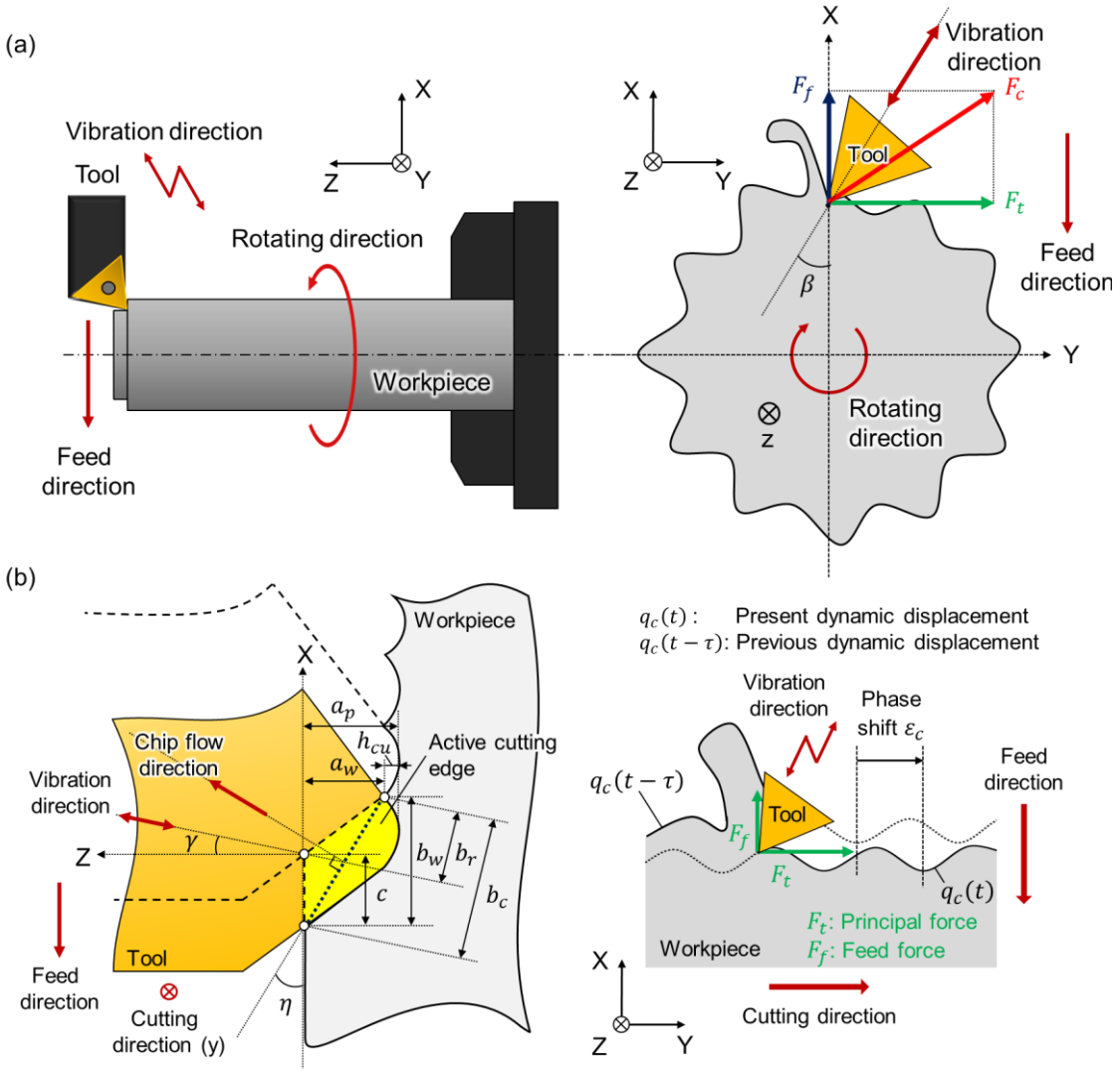

Fig. 4-1 Schematic illustration of general SDoF turning process (for example, the tool is fed in the X-direction and it vibrates flexibly in a certain vibration direction in a 3D space): (a) overview; (b) enlarged view of the cutting edge

is widely used even in the milling process. Especially, this should be true in non-periodic processes, such as turning and boring processes. The chatter vibration is expressed as a simple harmonic motion with a unit vector in the vibration direction $\mathbf{e_q}$, as follows:

$$\boldsymbol{q_c}(t) = q_c(t)\mathbf{e_q} = A_c \cos(\omega_c t + \psi_c)\,\mathbf{e_q} \tag{4-3}$$

$$\therefore \boldsymbol{q_c}(t-\tau) = q_c(t-\tau)\mathbf{e_q} = A_c \cos(\omega_c t - \omega_c \tau + \psi_c)\,\mathbf{e_q} \tag{4-4}$$

where $q_c(t)$ [m] is a present chatter vibration in a certain direction, and A_c [m], ω_c [rad/s], and ψ_c [rad] are its amplitude, frequency, and initial phase, respectively.

Here, $q_c(t-\tau)$ is the previous vibration (i.e., regeneration), and the time delay, τ [s] is constant (i.e., $\tau = \tau_n$) in a constant spindle speed (CSS). In CSS, it matches the tooth-pass

period as follows:

$$\tau_n = \frac{60}{N_c S_n} \tag{4-5}$$

where S_n [min^{-1}] is a nominal spindle speed, and N_c [−] is the number of teeth. The nominal delay term matches the spindle rotational period in a single-point cutter, such as turning and boring process (i.e., $N_c = 1$). Note that the number of teeth is explicitly indicated to retain the general expression.

In SSV, the delay term continuously varies with time because of time-varying spindle speed, $S(t)$. The variation profile of SSSV around the nominal value is defined as follows:

$$S(t) = S_n(1 + R_A \sin(\omega_s t)) \tag{4-6}$$

where R_A [−] and ω_s [rad/s] (or f_s [Hz]) are the relative variation amplitude (RVA) and frequency of the spindle speed variation, respectively. These are design parameters for the SSSV. $R_A = 0$ implies an ordinary CSS process.

In SSV, the time-varying delay term cannot be usually expressed in a straightforward manner, as in Eq. (4-5) (i.e., the reciprocal of the tooth-passing frequency). However, by assuming that the relative variation frequency of the spindle speed over the tooth-pass frequency (i.e., RVF) is small, it can be approximated as follows [240]:

$$\tau(t) \approx \tilde{\tau}(t) = \frac{60}{N_c S(t)} = \frac{60}{N_c S_n(1 + R_A \sin(\omega_s t))} = \frac{\tau_n}{1 + R_A \sin(\omega_s t)} \tag{4-7}$$

where $\tilde{(\ )}$ indicates the approximated value, and nominal values in SSSV denotes the "center" values (e.g., S_n and τ_n denote the center spindle speed and center delay time, in the SSSV process, respectively). Here, the RVF, R_F [−] is generally defined as follows:

$$R_F = \frac{60 f_s}{N_c S_n} = f_s \tau_n = \frac{\omega_s \tau_n}{2\pi} \tag{4-8}$$

Eq. (4-7) has a sine function in its denominator. This expression is still inconvenient because it is a non-closed form for the integral in Eq. (4-2). In [240] and here, Eq. (4-7) is transformed to a simpler expression with the sine function in the numerator, considering the absolute amplitude of the delay variation as follows:

$$\begin{aligned} \tau(t) \approx \tilde{\tau}(t) \approx \tilde{\tilde{\tau}}(t) &= \tau_n - \frac{\max\left(\tilde{\tau}(t)\right) - \min\left(\tilde{\tau}(t)\right)}{2} \sin(\omega_s t) \\ \rightarrow \tilde{\tilde{\tau}}(t) &= \tau_n \left(1 - \frac{R_A}{1 - R_A^2} \sin(\omega_s t)\right) \end{aligned} \tag{4-9}$$

By employing Eq. (4-9), the regenerative vibration in Eq. (4-4) with a time-varying delay

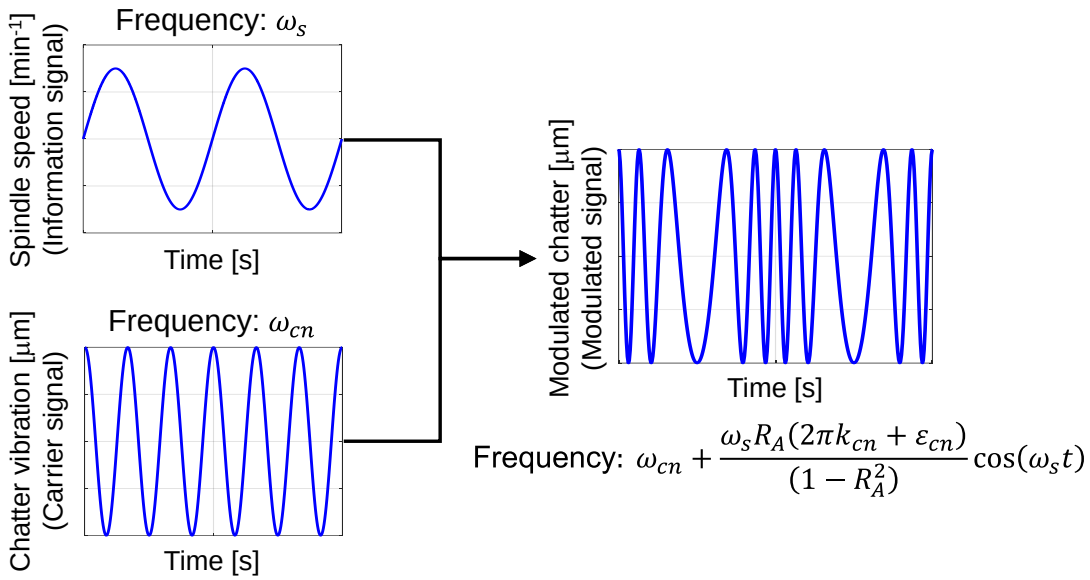

Fig. 4-2 Schematic diagram of the technological analogy between SSSV and FM (The chatter frequency as carrier signal is modulated by the spindle speed variation as the input message wave).

owing to the SSSV effect, can be expressed as follows:

$$q_c\big(t-\tau(t)\big) \approx A_c \cos\left(\omega_{cn} t - \varepsilon_{cn} + \frac{R_A(2\pi k_{cn} + \varepsilon_{cn})}{1 - R_A^2} \sin(\omega_s t) + \psi_c\right) \tag{4-10}$$

Here, k_{cn} [−] and ε_{cn} [rad] are the nominal chatter lobe number ($k_c \in \mathbb{N}_0$) and nominal phase shift between the present and previous vibrations over the center spindle speed of S_n, respectively. These parameters can be obtained using the following relationship as:

$$\frac{60 f_{cn}}{N_c S_n} = k_{cn} + \frac{\varepsilon_{cn}}{2\pi} \;\rightarrow\; \omega_{cn}\tau_n = 2\pi k_{cn} + \varepsilon_{cn} \tag{4-11}$$

Note that the chatter frequency in the CSS process with S_n explicitly shown as ω_{cn}.

Eq. (4-10) indicates that the relative phase between the present and previous vibrations fluctuates with time when SSSV is applied. Interestingly, it is equivalent to the phase modulation (PM) principle defined in radio communication engineering. PM is a type of frequency modulation (FM); hence, the chatter vibration in the SSSV process, represented by Eq. (4-10), can be reinterpreted based on the analogy with FM technology. In short, the spindle speed corresponds to the information signal in FM. In addition, the regenerative chatter vibration before the SSSV, and chatter after the SSSV correspond to the carrier signal and modulated signal, respectively (see Fig. 4-2). Based on Eq. (4-10), the instantaneous frequency of the modulated chatter in SSSV is derived as follows:

$$\omega_c(t) = \omega_{cn} + \Delta\omega_c \cos(\omega_s t)\,, \text{where } \Delta\omega_c = \omega_s \frac{R_A(2\pi k_{cn} + \varepsilon_{cn})}{1 - R_A^2} \tag{4-12}$$

In the FM technology, the ratio of the maximum shifted frequency, $\Delta\omega_c$ [rad/s] to the information signal frequency, ω_s is defined as the modulation index (MI), which represents the degree of modulation. In this study, MI, m_f [−] is redefined for the SSSV process as a novel design index, utilizing the analogy, as follows:

$$MI \equiv m_f = \frac{\Delta\omega_c}{\omega_s} = \frac{R_A(2\pi k_{cn} + \varepsilon_{cn})}{1 - R_A^2} \tag{4-13}$$

Consequently, Eq. (4-10) can be further rewritten as follows:

$$\begin{aligned} &q_c\big(t-\tau(t)\big) \approx A_c \cos\big(\omega_{cn}t - \varepsilon_{cn} + m_f \sin(\omega_s t) + \psi_c\big) \\ &= A_c \cos(\omega_{cn}t - \varepsilon_{cn} + \psi_c)\cos\big(m_f \sin(\omega_s t)\big) - A_c \sin(\omega_{cn}t - \varepsilon_{cn} + \psi_c)\sin\big(m_f \sin(\omega_s t)\big) \end{aligned} \tag{4-14}$$

Note that this model represents that the previous vibration appears to be modulated, whereas the present vibration is not modulated, assuming that the chatter frequency is constant. This assumption is similar to the analytical model in some of the previous studies [68,73,230,240]. However, the resultant present vibration is also modulated by the SSSV. Recently, Nam et al. [232] empirically discussed the chatter frequency shift during the SSV. A comprehensive discussion for the FM phenomenon in Eq. (4-12), associated with [232], is given in **Appendix C**. Here, the special form in Eq. (4-14) can be further expanded by using a Bessel function of the first kind as follows:

$$\begin{aligned} \cos\big(m_f \sin(\omega_s t)\big) &= J_0\big(m_f\big) + 2\sum_{l=1}^{\infty} J_{2l}\big(m_f\big)\cos(2l\omega_s t) \\ \sin\big(m_f \sin(\omega_s t)\big) &= 2\sum_{l=1}^{\infty} J_{2l-1}\big(m_f\big)\sin\big((2l-1)\omega_s t\big) \end{aligned} \tag{4-15}$$

where $J_l\big(m_f\big)$ is the l-th order Bessel function of the first kind, with MI as an argument (see Fig. 4-3). By substituting Eq. (4-15) for Eq. (4-14) and rearranging the resultant equation, the infinite order expression of the approximated regenerative chatter vibration with modulation can be finally derived as follows:

$$q_c\big(t-\tau(t)\big) \approx A_c \sum_{l=-\infty}^{\infty} J_l\big(m_f\big)\cos\big((\omega_{cn} + l\omega_s)t - \varepsilon_{cn} + \psi_c\big) \tag{4-16}$$

where

$$J_{-l}\big(m_f\big) = (-1)^l J_l\big(m_f\big) \tag{4-17}$$

According to Eq. (4-16), an infinite number of side-band frequencies, $\omega_{cn} \pm l\omega_s$ ($l = 1,2,\ldots,\infty$), are generated in SSSV in accordance with its frequency. This is also pointed out in [151,230]. Eq. (4-16) includes the CSS process, as $J_0\big(m_f\big)$ is 1 and all other order Bessel functions are zero under $R_A = 0$ (i.e., $m_f = 0$).

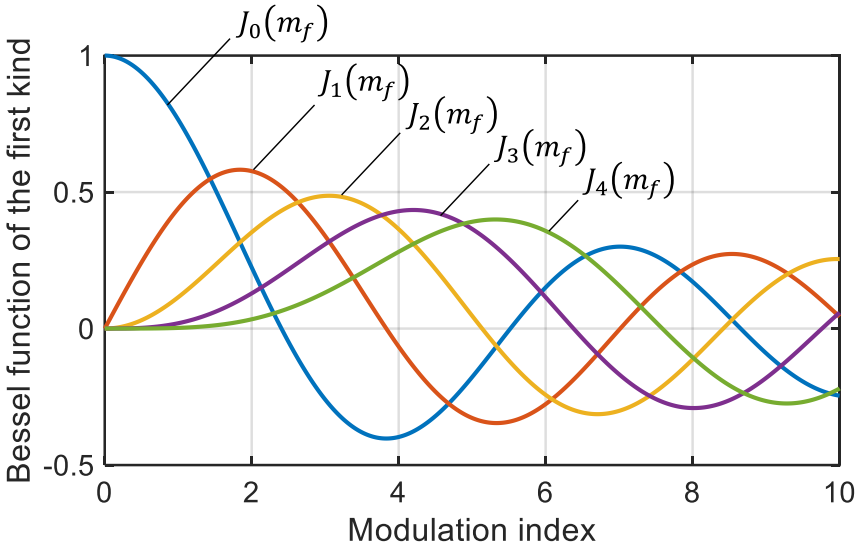

Fig. 4-3 Bessel function of the first kind with the modulation index as an argument

4.2.2. Derivation of analytical net inflow of process energy

The regenerative chatter model with Eq. (4-7) is a non-closed form, which means that the energy calculation in Eq. (4-2) is not integrable. Therefore, Al-Regib et al. [68] solved Eq. (4-2) using numerical integration. They plotted the corresponding energy minimum point based on the results obtained in numerous energy simulations, while varying the combination of SSSV design parameters and the nominal spindle speed. Then, they heuristically derived the optimal design criteria for SSSV to attain an effective chatter energy dissipation. On the other hand, Eq. (4-2) can be solved analytically with an approximation of Eq. (4-16). Here, a dynamic cutting force vector, $\boldsymbol{F_c}$ can be defined with a dynamic cutting area, A_s [m^2], and a specific cutting force vector, $\mathbf{K_c}$, as follows:

$$\boldsymbol{F_c}(t) = A_s(t) \cdot \mathbf{K_c} \tag{4-18}$$

By utilizing the well-known Colwell's empirical chip flow rule (i.e., the chip flows along the cutting width vector), the specific cutting force vector can be expressed as:

$$\mathbf{K_c} = \{\mu_f K_{tc} \sin\eta \quad K_{tc} \quad \mu_f K_{tc} \cos\eta\}^{\mathrm{T}} \tag{4-19}$$

where K_{tc} [Pa] and μ_f [−] are a cutting force constant in principal force and a constant ratio of the force in the chip flow direction to the principal force, respectively, and η [rad] is a chip flow angle. Note that the components of $\mathbf{K_c}$ are generally positive, as the forces act on the tool along the positive directions in the XYZ-coordinate system, as shown in Fig. 4-1.

Furthermore, the cutting width vector is defined as:

$$\mathbf{b_c} = \{a_w \quad 0 \quad b_w\}^{\mathrm{T}} \tag{4-20}$$

where a_w [m] and b_w [m] are the cutting chord lengths projected onto the Z- and X-axis, in Fig. 4-1, respectively.

In a general turning process, the vibration before one rotation is not always regenerated over the entire cutting width, and the regenerative width vector, $\mathbf{r_c}$ is defined as follows:

$$\mathbf{r_c} = \{a_w \quad 0 \quad b_w - c\}^{\mathrm{T}} \tag{4-21}$$

where c [m] is a feed per tooth. Note that the Y-direction component of each width vector is always zero because it does not change the cutting area. The dynamic cutting area can be obtained by the inner product of vibration and each width vector as follows:

$$\begin{aligned} A_s(t) &= -\mathbf{b_c} \cdot \boldsymbol{q_c}(t) + \mathbf{r_c} \cdot \boldsymbol{q_c}(t-\tau) \\ &= -b_c q_c(t) + b_r q_c(t-\tau) = b_c\big(-q_c(t) + \mu_c q_c(t-\tau)\big) \end{aligned} \tag{4-22}$$

where b_c [m] $(= \mathbf{b_c} \cdot \mathbf{e_q})$ and b_r [m] $(= \mathbf{r_c} \cdot \mathbf{e_q})$ are the cutting width and regenerative width in the vibration direction, respectively, and $\mu_c (= b_r/b_c\,;\ 0 \le \mu_c \le 1)$ is known as the overlap factor. The unit direction vector of vibration, $\mathbf{e_q}$ is defined with γ [rad] and β [rad] (i.e., vibration-direction angles on the XZ- and XY-plane in Fig. 4-1, respectively), as follows:

$$\mathbf{e_q} = \{\sin\gamma\cos\beta \quad \sin\beta \quad \cos\gamma\cos\beta\}^{\mathrm{T}} \tag{4-23}$$

Consequently, the process energy balance can be obtained from Eqs. (4-2), (4-18), (4-19), (4-22), and (4-23) as follows:

$$E_f = \int_{t_b}^{t_e} -K_{tc} b_c d_f q_c(t)\dot{q}_c(t)\,dt + \int_{t_b}^{t_e} \mu_c K_{tc} b_c d_f q_c(t-\tau)\dot{q}_c(t)\,dt \tag{4-24}$$

$$d_f = \mu_f \sin\eta \sin\gamma \cos\beta + \sin\beta + \mu_f \cos\eta \cos\gamma \cos\beta \tag{4-25}$$

Note that the energy related to the static cutting force is dropped from Eq. (4-24), as it does not affect the chatter stability. Furthermore, the first term of Eq. (4-24) can be neglected, as it is not related to the regenerative effect. In fact, it can be easily shown that the first term becomes zero in every chatter vibration cycle. This is understandable, as the process becomes unstable owing to the regenerative effect. As a result, the approximated solution of Eq. (4-24), with Eq. (4-3) and Eq. (4-16), can be finally obtained as follows:

$$\begin{aligned} E_f &= \int_{t_b}^{t_e} \mu_c K_{tc} b_c d_f q_c\big(t-\tau(t)\big)\dot{q}_c(t)\,dtz \\ &\approx -\frac{1}{2}\mu_c K_{tc} b_c d_f A_c^2 \omega_{cn} \times \sum_{l=-\infty}^{\infty} J_l(m_f) \left\{ \begin{array}{c} \displaystyle\int_{t_b}^{t_e} \sin\big((2\omega_{cn} + l\omega_s)t - \varepsilon_{cn} + 2\psi_c\big)\,dt \\ \displaystyle -\int_{t_b}^{t_e} \sin(l\omega_s t - \varepsilon_{cn})\,dt \end{array} \right\} \end{aligned} \tag{4-26}$$

where

$$\int_{t_b}^{t_e} \sin\big((2\omega_{cn} + l\omega_s)t - \varepsilon_{cn} + 2\psi_c\big)\, dt = \frac{-1}{(2\omega_{cn} + l\omega_s)}\Big[\cos\big((2\omega_{cn} + l\omega_s)t - \varepsilon_{cn} + 2\psi_c\big)\Big]_{t_b}^{t_e} \tag{4-27}$$

$$\int_{t_b}^{t_e} \sin(l\omega_s t - \varepsilon_{cn})\, dt = \begin{cases} \dfrac{-1}{l\omega_s}[\cos(l\omega_s t - \varepsilon_{cn})]_{t_b}^{t_e} & n \neq 0 \\ -\sin\varepsilon_{cn}\,[t]_{t_b}^{t_e} & n = 0 \end{cases} \tag{4-28}$$

Here, Eq. (4-27) should be negligibly small compared to Eq. (4-28), as the chatter frequency is usually much higher than the SSSV frequency; hence, Eq. (4-26) should be regarded as a simpler form as follows:

$$E_f \approx \frac{1}{2}\mu_c K_{tc} b_c d_f A_c^2 \omega_{cn} \sum_{l=-\infty}^{\infty} J_l(m_f) \int_{t_b}^{t_e} \sin(l\omega_s t - \varepsilon_{cn})\, dt \tag{4-29}$$

4.3. Self-acting optimal design for SSSV

To realize a self-acting optimal design that can be online or integrable in CNC machine tools, the information required for the design procedure should be known from the cutting conditions or can be observed unmanned. This section proposes a novel design for SSSV based on MI to attain an effective chatter energy dissipation, by selecting a proper RVA. Furthermore, the novel criteria in terms of the limitations of the SSSV frequency are proposed for preventing the beat vibration and ensuring an expected SSSV effect. The proposed method requires only the chatter frequency and a nominal spindle speed similar to the DSST. Additionally, the proposed method presents some candidates for a proper design, thus enabling a flexible design, considering the constraints of the machines and cutting conditions.

4.3.1. Design criterion for selecting a proper RVA

In the CSS process, the integral section for Eq. (4-29) should be set to the chatter vibration cycle (i.e., $[t_b, t_e] = [0, 2\pi/\omega_{cn}]$) or an integer multiple of it. In the SSSV process, however, a long-term energy cycle is generated according to the variation frequency of the spindle speed. Therefore, the integral section is set to coincide with the SSSV cycle as $[t_b, t_e] = [0, 2\pi/\omega_s]$, even though Al-Regib et al. [68] used $[0,\ 1/\omega_s]$ in an earlier study. If the integral section is not equal to the SSSV cycle, the result of the energy balance changes depending on the integral section, as the system is constantly changing in certain time portions of the SSSV cycle. By setting $[t_b, t_e] = [0, 2\pi/\omega_s]$, it can be found that all the terms related to the sideband components become zero in Eq. (4-29), and the process energy

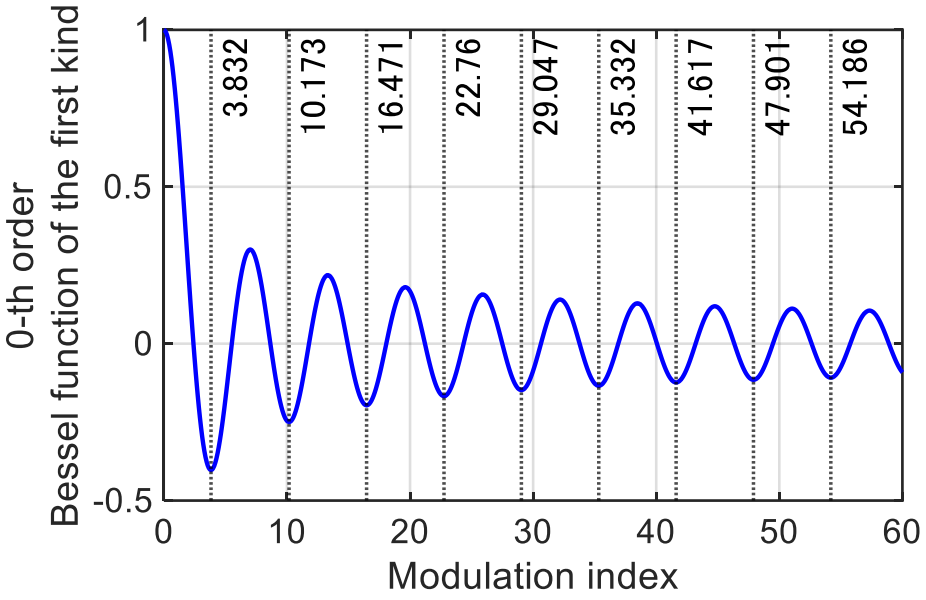

Fig. 4-4 Zeroth order Bessel function of the first kind with the MI and its local minimum points

Table 4-1 List of modulation indices corresponding to the local minimum point of $J_0(m_f)$

#	Modulation index	#	Modulation index		Modulation index
1	3.832	6	35.332	11	66.753
2	10.173	7	41.617	12	73.037
3	16.471	8	47.901	13	79.320
4	22.760	9	54.186	14	85.604
5	29.047	10	60.469	⋮	⋮

balance in the SSSV cycle can be derived as follows:

$$E_f \to -\frac{\pi \mu_c K_{tc} b_c d_f A_c^2 \omega_{cn} J_0(m_f)}{\omega_s} \sin \varepsilon_{cn} \tag{4-30}$$

Eq. (4-30) indicates that only the original chatter component is related to the total energy balance in the SSSV cycle, i.e., the corresponding 0-th order Bessel function of the first kind with the MI is dominant. In the CSS process, $J_0(m_f) = J_0(0) = 1$, $\omega_s \to \omega_{cn}$, and the chatter happens in $\pi \le \varepsilon_{cn} < 2\pi$ (i.e., Eq. (1-2)); hence, the energy balance of Eq. (4-30) is positive under the chatter condition, considering that the other coefficients are positive. It should be stated that the directional factor d_f [−], can be negative depending on the vibration direction. In this case, the chatter frequencies are lower than the natural frequency [209], which implies that the unstable phase shift range becomes $0 < \varepsilon_{cn} \le \pi$ in the SDoF system. To sum up, the process energy balance of Eq. (4-30) is always positive in the CSS at least in a state of regenerative chatter.

However, the overall energy inflow in the SSSV cycle can be controlled by utilizing the

MI, through the 0-th order Bessel function of the first kind, shown in Fig. 4-4. From Fig. 4-4, it can be noticed that the chatter energy can be effectively dissipated by setting the MI corresponding to the local minimum points of the 0-th order Bessel function of the first kind, a part of which is listed in Table 4-1. As a result, the optimal design criterion of RVA ($R_A > 0$) can be proposed from the relational expression of Eq. (4-13) as follows:

$$R_A = \frac{-(2\pi k_{cn} + \varepsilon_{cn}) + \sqrt{(2\pi k_{cn} + \varepsilon_{cn})^2 + 4m_f^2}}{2m_f}, m_f = 3.832, 10.173, 16.471, \ldots \tag{4-31}$$

This proposed design criterion for RVA has two important features of practical use. Firstly, the RVA is designed only from the observable chatter frequency using Eq. (4-5) and (4-11), as the nominal spindle speed is known from the cutting conditions. Secondly, Eq. (4-31) presents multiple proper design candidates of RVA, which indicates that a proper flexible design is feasible, considering the machine constraints of the spindle drive motor. As a result, the practicality and realization of effective chatter suppression by SSSV is significantly enhanced.

Here, the RVA design criterion is heuristically derived following Al-Regib et al. [68] as:

$$R_A = \frac{\varepsilon_{cn}}{2\pi k_{cn}} \tag{4-32}$$

where measuring the chatter frequency as well as Eq. (4-31) are the only requirements. Eq. (4-32) roughly corresponds to the first local minimum point in Eq. (4-31) (i.e., $m_f = 3.832$), although the energy integral section considered for Eqs. (4-31) and (4-32) is originally different (i.e., $t_e = 1/\omega_s$ in Eq. (4-32); $t_e = 2\pi/\omega_s$ in Eq. (4-31)).

The comparison of Eq. (4-31) corresponding to $m_f = 3.832$ and Eq. (4-32) proposed by Al-Regib et al. is shown in Fig. 4-5. The black lines show the boundaries of the RVA and the corresponding negative energy balance around $m_f = 3.832$ (see Fig. 4-4), i.e., over a range of $2.405 < m_f < 5.502$. In Eq. (4-32), the recommended RVA increases monotonically as the nominal phase shift approaches 2π from π at a certain lobe number. This is because Eq. (4-32) is inspired from the DSST, even though Al-Regib et al. derived it in terms of the minimum energy balance. In fact, the maximum spindle speed, S_m, of SSSV with the RVA in Eq. (4-32) is itself a part of the strategy of DSST, shown in Eq. (1-3), as follows:

$$S_{max} = S_n\left(1 + \frac{\varepsilon_{cn}}{2\pi k_{cn}}\right) = S_n\frac{\omega_{cn}\tau_n}{2\pi k_{cn}} = \frac{60 f_{cn}}{Z k_{cn}} \tag{4-33}$$

As a result, the variation of the optimal RVA in Eq. (4-32) is sensitive to the nominal phase shift, especially in cases involving a low lobe number (i.e., relatively high spindle speed over the chatter frequency). The above points can also be comprehended visually from

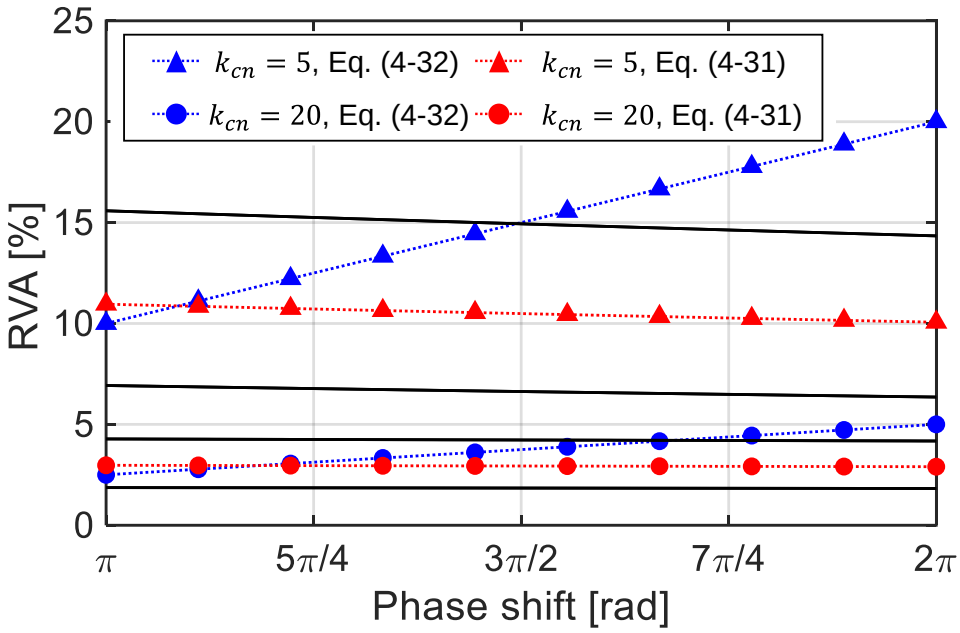

Fig. 4-5 Comparison of the design criteria for RVA corresponding to first minimum point of $J_0(m_f)$ (i.e., m_f = 3.832) and the one proposed by Al-Regib et al. (the black lines are the boundary for the negative energy balance around $J_0(3.832)$, i.e., $2.405 < m_f < 5.520$)

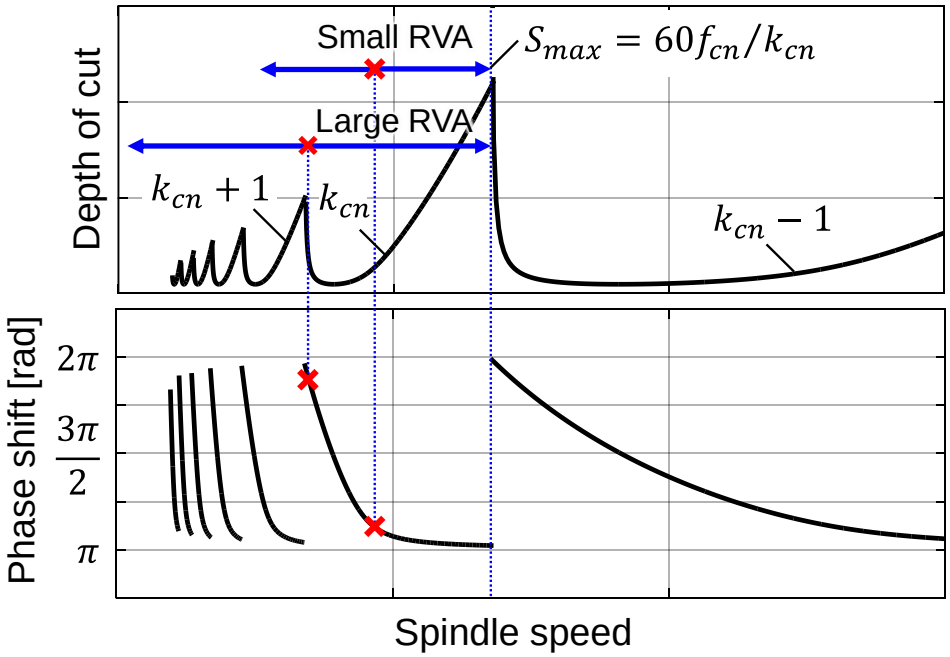

Fig. 4-6 SLD-based comprehension of the design criterion for RVA proposed by Al-Regib et al. [68]

a correspondence with the SLD, as shown in Fig. 4-6. Even though the energy integral sections considered for Eqs. (4-31) and (4-32) are different, the RVA recommended by Eq. (4-32) is close to the one suggested by Eq. (4-31), having m_f = 3.832, especially, in the case of $\varepsilon_{cn} < 3\pi/2$. Note that, as Eq. (4-32) gives only one option for selecting the RVA, there is no opportunity to consider the machine constraints for the users.

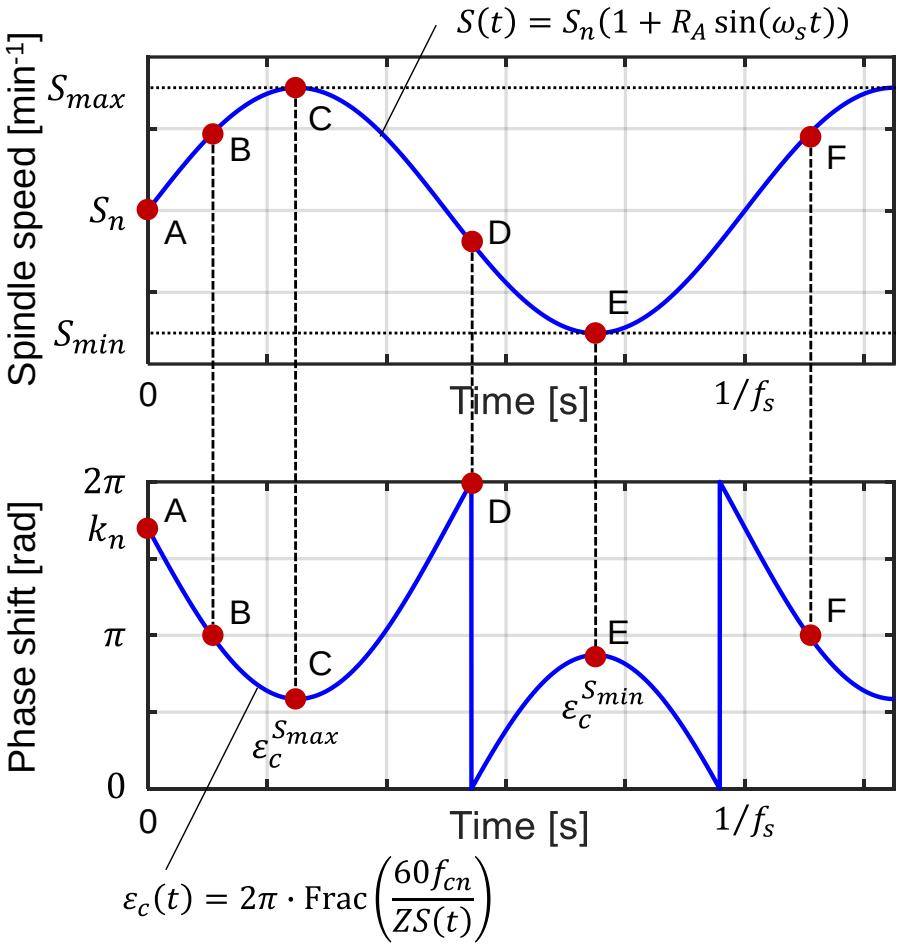

Fig. 4-7 Schematic diagram of the spindle speed and corresponding time-varying phase shift profile in the SSSV process (instantaneous phase shift varies with time owing to the spindle speed variation).

4.3.2. Lower limit criterion for variation frequency of spindle speed

In general SSV techniques, the RVA affects the chatter stability more significantly than the RVF [151,280]. Nevertheless, some studies, based on simulations and/or experiments suggested the existence of a lower limit value of the SSV frequency for an effective chatter suppression [68,73,230,238,281]. Unless the SSV frequency exceeds a specific value, an effective SSV process cannot be obtained.

According to Al-Regib et al. [68], the SSV frequency represents how fast the energy is dissipated from the CWS (i.e., how fast the energy cycle can rotate in the SSV to dissipate the energy). From this perspective, they also proposed the criterion in terms of a lower limit of the SSV frequency, so that the chatter energy will begin to be dissipated (i.e., the process enters a stable phase region ranging from 0 to π) within at most one tooth path after applying the SSV. In summary, the lower limit criterion for the SSSV frequency, $\omega_{s(min)}^{AB}$ [rad] was proposed so that the time-varying phase shift will pass through the section AB in Fig. 4-7, within one tooth pass as suggested in [68]:

$$\frac{60\omega_{cn}}{N_c S_B} = 2\pi k_{cn} + \pi, S_B = S_n\left(1 + R_A \sin\left(\omega_s \frac{60}{N_c S_n}\right)\right)$$
$$\rightarrow \omega_{s(min)}^{AB} = \frac{ZS_n}{60}\sin^{-1}\left(\frac{2\pi k_{cn} + \varepsilon_{cn}}{R_A(2\pi k_{cn} + \pi)} - \frac{1}{R_A}\right) \tag{4-34}$$

However, the existence of the lower limit of the SSV frequency may be related to the beat vibration; hence, Eq. (4-34) may not be robust, considering that the beat vibration tends to occur around the extrema of the spindle speed [232,236]. From this viewpoint, the unstable transition regions are newly regarded as sections CD and EF in Fig. 4-7 after reaching the extremum values of the spindle speed. It is necessary to pass through an unstable transition region as soon as possible. As the phase shift becomes 2π with the spindle speed, S_D [min^{-1}], at point D, the following equation holds good:

$$\frac{60f_{cn}}{ZS_D} = k_c^{S_{max}} + \frac{2\pi}{2\pi} \rightarrow \therefore S_D = \frac{60f_{cn}}{N_c\left(k_c^{S_{max}} + 1\right)} \tag{4-35}$$

where $k_c^{S_{max}}$ [−] is the instantaneous lobe number at the maximum spindle speed, S_{max} [min^{-1}] and can be expressed as follows:

$$k_c^{S_{max}} = \mathrm{Int}\left(\frac{60f_{cn}}{N_c S_{max}}\right) = \left\lfloor\frac{60f_{cn}}{N_c S_n(1 + R_A)}\right\rfloor = \left\lfloor\frac{k_{cn} + \frac{\varepsilon_n}{2\pi}}{1 + R_A}\right\rfloor \tag{4-36}$$

Note that the chatter frequency is assumed to be constant here (i.e., f_{cn} in the CSS process).

Considering that the spindle speed reaches S_D after N_r number of teeth passes from S_{max}, the following equation also holds good:

$$S_D = S_n\left(1 + R_A \cos\left(\omega_s \frac{60N_r}{N_c S_{max}}\right)\right) \tag{4-37}$$

By combining Eqs. (4-35) and (4-37), a novel criterion, $\omega_{s(min)}^{CD}$ [rad] can be proposed as:

$$\omega_{s(min)}^{CD} = \frac{N_c S_{max}}{60N_r}\cos^{-1}\left(\frac{2\pi k_{cn} + \varepsilon_{cn}}{R_A\left(2\pi k_c^{S_{max}} + 2\pi\right)} - \frac{1}{R_A}\right) \tag{4-38}$$

Similarly, another criterion for the SSSV frequency for section EF, $\omega_{s(min)}^{EF}$ [rad] can be obtained as follows:

$$\omega_{s(min)}^{EF} = \frac{N_c S_{min}}{60N_r}\cos^{-1}\left(\frac{1}{R_A} - \frac{2\pi k_{cn} + \varepsilon_{cn}}{R_A\left(2\pi k_c^{S_{min}} - \pi\right)}\right) \tag{4-39}$$

where S_{min} [min^{-1}] is the minimum spindle speed; $k_c^{S_{min}}$ [−] is the phase shift at the minimum spindle speed and can be written as:

$$k_c^{S_{min}} = \mathrm{Int}\left(\frac{60 f_{cn}}{N_c S_{min}}\right) = \left\lfloor \frac{60 f_{cn}}{N_c S_n (1 - R_A)} \right\rfloor = \left\lfloor \frac{k_{cn} + \frac{\varepsilon_{cn}}{2\pi}}{1 - R_A} \right\rfloor \tag{4-40}$$

The larger of the results of Eqs. (4-38) and (4-39) is utilized as the lower limit for the SSSV frequency, which is generally more restrictive than that suggested by Eq. (4-34). The chatter amplitude grows exponentially every tooth pass or spindle rotation when the instantaneous phase shift enters the unstable region. The instantaneous phase shift should pass out of the unstable region before the momentary chatter grows significantly to avoid the beat vibration. Note that $N_r = N_c$ may be reasonable, as $N_r = 1$ in multi-point tool (i.e., the phase shift will pass through the defined section within one tooth pass) is very restrictive in Eqs. (4-38) and (4-39).

Here, Assuming an SDoF system of CWS, the damping dissipated energy, E_d [J], in a chatter cycle is as follows [70]:

$$E_d = \int_0^{\frac{2\pi}{\omega_{cn}}} C \dot{q}_c^2(t)\, dt = 2\pi A_c^2 \omega_{cn} \zeta_r \frac{K}{\omega_r} \tag{4-41}$$

where C [N · s/m], K [N/m], ζ_r [−], and ω_r [rad/s] are the modal damping coefficient, modal stiffness, modal damping ratio, and modal frequency, respectively. This suggests that when the flexible part has a low modal damping and/or a high resonance with a low modal mass, the chatter vibration momentarily grows very quickly owing to a low inherent damping capacity. In that case, Eqs. (4-38) and (4-39) should be satisfied to avoid the beat vibration by an adequate margin.

4.3.3. Upper limit criterion for variation frequency of spindle speed

As mentioned in Eq. (4-7), the time-varying delay, $\tau(t)$ cannot be generally expressed in a straightforward manner, as in Eq. (4-5) in the SSV process; hence, Eqs. (4-7) and (4-9) are derived under the assumption of a low RVF. To be precise, the following equation in in terms of $\tau(t)$ must hold [240]:

$$\int_{t'-\tau(t)}^{t'} \frac{2\pi S(t)}{60} dt = \frac{2\pi}{60} \int_{t'-\tau(t)}^{t'} S_n (1 + R_A \sin(\omega_s t))\, dt = \frac{2\pi}{N_c} \tag{4-42}$$

Eq. (4-42) can be solved in terms of $\tau(t)$ using numerical methods, such as the Newton–Raphson method, once the time-varying profile of the spindle speed is determined.

Fig. 4-8 shows the example results of the time delay terms, calculated from Eqs. (4-7), (4-9), and (4-42) according to the RVF under a commanded spindle speed of 1200 min^{-1} and an RVA of 10%. As seen in Fig. 4-8(a), all time-delay terms have almost the same behavior in case of a small RVF of 10%. However, the actual value deviates from the expected

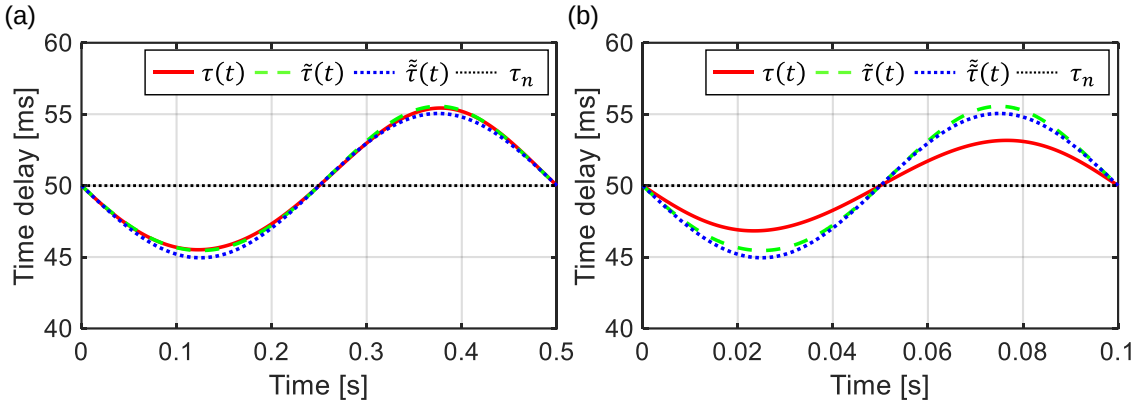

Fig. 4-8 Comparison of time-varying time delay terms in SSSV (i.e., Eqs. (4-7), (4-9), and (4-42)) under $S_n = 1200$ min^{-1} and $RVA = 10\%$: (a) $RVF = 10\%$; (b) $RVF = 50\%$

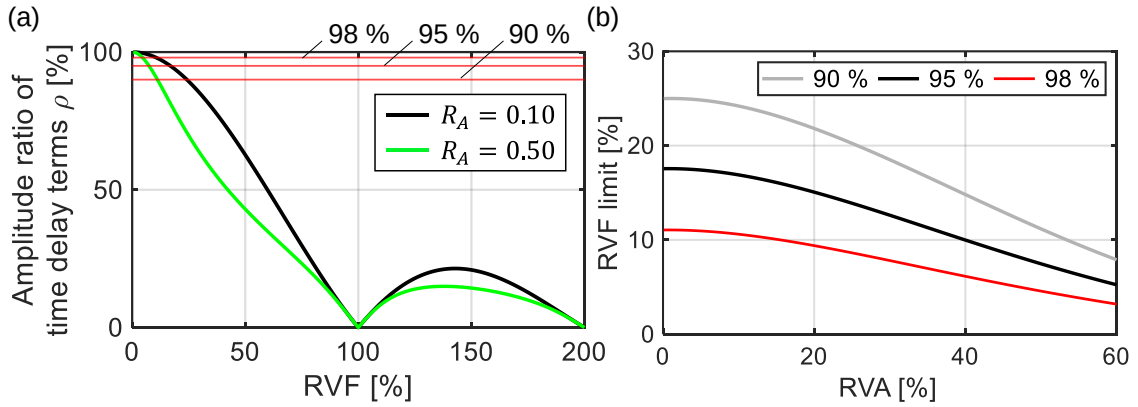

Fig. 4-9 Upper limit criterion for SSSV frequency: (a) ratio of the expected and exact variation amplitude in terms of the process time delay (Eq. (4-43)); (b) RVF limit curves according to RVA

expression, as RVF increases, as shown in Fig. 4-8 (b).

Fig. 4-9(a) shows the ratio of the expected and the exact variation amplitude of the time delay terms ($\tilde{A}_\tau$ [s] and A_τ [s]), which is defined as follows:

$$\rho = \frac{\{\max(\tau(t)) - \min(\tau(t))\}/2}{\left\{\max\left(\tilde{\tilde{\tau}}(t)\right) - \min\left(\tilde{\tilde{\tau}}(t)\right)\right\}/2} = \frac{A_\tau}{\tilde{A}_\tau} \tag{4-43}$$

The amplitude ratio, ρ [−], can be utilized as an index for the efficiency of the SSSV process, as the real amplitude becomes $\rho\tilde{A}_\tau$, whereas the expected one is $\tilde{A}_\tau$. The SSSV efficiency decreases as the RVF increases, and becomes zero when the RVF is 100% (i.e., the SSSV frequency is equal to the tooth-passing frequency). This means that the apparent delay does not vary, and the process appears similar to the CSS even though the SSSV is applied. Therefore, the SSSV frequency should be applied where ρ is close to 100%. This area become narrows as the RVA increases. Note that the approximate delay of $\tilde{\tau}(t)$ and $\tilde{\tilde{\tau}}(t)$ have the same behavior in terms of Eq. (4-43), as Eq. (4-9) is derived by taking the peak to peak value of Eq. (4-7).

Fig. 4-9(b) shows the limit curves of RVF according to RVA for ensuring efficiencies of 98%, 95%, and 90%, respectively. The strict constraint on SSSV efficiency ensures the expected SSV effect, whereas the limit curve of RVF becomes smaller. It should be determined, as required by the user. By applying a polynomial curve fitting to Fig. 4-9(b), the upper limit for the RVF according to RVA, $R_{F(max)}$ [−] can be made regardless of S_n, since the RVA and RVF are the normalized design parameters, e.g., a 95% limit curve can be made as:

$$R_{F(max)} = -0.5243R_A^4 + 1.2404R_A^3 - 0.9219R_A^2 + 0.0147R_A + 0.1755 \tag{4-44}$$

Next, the corresponding upper limit of SSSV frequency, $\omega_{s(max)}$ [rad/s] (or $f_{s(max)}$ [Hz]) can be calculated as follows:

$$\omega_{s(max)} = \frac{2\pi R_{F(max)}}{\tau_n} \rightarrow f_{s(max)} = \frac{R_{F(max)}}{\tau_n} \tag{4-45}$$

4.3.4. Priority of design candidates

The proper RVA candidates are derived from the perspective of the energy minimum points in long term SSSV cycle. They have the potential to effectively dissipate the chatter vibration energy. However, the negative energy balance in the SSSV cycle does not always make the process stable. Conversely, the process does not always become unstable even if the energy balance is positive. This is because a positive energy balance simply suggests that effect of the unstable region is larger than that of the stable one in an SSSV cycle.

In general, for SSV, a large RVA value can robustly suppress the chatter vibration [282], as it results in a quick passage through the unstable region with a high spindle acceleration. In addition, a larger RVA yields a larger modulation index; hence, the chatter vibration is modulated in a wider range of frequency band. As the chatter tends to occur near the resonance, the vibration frequency moves further away from the resonance at a certain time portion when a larger RVA is applied. It may moderate the momentary growth of chatter vibration in the unstable portion. As a result, the SSV with a large RVA has chance to robustly suppress the chatter even in case of fast growth rate of the chatter with high depth of cut. Furthermore, a large RVF generally yields a stable process owing to a faster passage through the unstable region [73], although too high an RVF is counterproductive.

From the above perspective, the RV factor is introduced for considering the priority of the parameter candidates. The RV factor, RV [−] is defined as follows [242]:

$$RV \equiv R_A \cdot R_F = R_A f_s \tau_n = \frac{R_A \omega_s \tau_n}{2\pi} \tag{4-46}$$

Here, the maximum acceleration and also maximum jerk of the SSSV trajectory are

proportional to RV factor as follows:

$$\dot{S}(t)\big|_{max} = S_n R_A \omega_s = \frac{2\pi S_n}{\tau_n} \cdot \frac{R_A \omega_s \tau_n}{2\pi} = \frac{2\pi N_c S_n^2}{60} \cdot RV \tag{4-47}$$

$$\ddot{S}(t)\big|_{max} = S_n R_A \omega_s^2 = \frac{4\pi^2 S_n}{\tau_n^2} \cdot \frac{\omega_s \tau_n}{2\pi} \cdot \frac{R_A \omega_s \tau_n}{2\pi} = \frac{4\pi^2 N_c^2 S_n^3}{3600} \cdot R_F \cdot RV \tag{4-48}$$

In summary, the RV factor is an indicator of the spindle speed acceleration/jerk. A larger RV factor will induce a larger spindle acceleration and also a spindle jerk. Referring to [232,236], the larger acceleration rate of the spindle speed tends to robustly suppress the chatter. On the other hand, the maximum allowable acceleration of the spindle system will be restricted by the machine. Some studies imposed constraint on the maximum spindle acceleration or the RV factor as a machine limitation [231,242]. For instance, the RV was kept below 1.35% in [242]. It was recommended that a candidate with as high an RV factor as possible be selected for robust chatter suppression, considering the machine constraints.

Note that the maximum acceleration in the triangular SSV (TSSV) would be smaller than that indicated in Eq. (4-47). However, the maximum jerk in TSSV would be infinite, which may cause a much larger instantaneous torque in TSSV than that in SSSV [238,241], although the spindle jerk perspective is often overlooked.

4.3.5. Summary of the design procedure for an optimal SSSV process

The procedure for the proposed SSSV design methodology is summarized below:

(1) The chatter frequency, ω_c, is measured during the process.
(2) The nominal lobe number, k_{cn}, and the nominal phase shift, ε_{cn}, are calculated from the measured chatter frequency and the commanded spindle speed, S_n, using Eq. (4-11).
(3) RVA candidates corresponding to the MI in Table 4-1 are obtained using Eq. (4-31). The RVA candidates are constrained by a maximum value that the users set according to the machine specification or the machinability limitations (e.g., cutting speed), depending on the workpiece material. Empirically, the RVA is often set to less than 20% to avoid the adverse effects of SSSV, such as excessive amount of motor energy and undesirable tear of the workpiece [242].
(4) The lower limit of the SSSV frequency at each RVA candidate is calculated using Eqs. (4-38) and (4-39). The higher of the two values is utilized for the limitation. Additionally, the upper limit of the SSSV frequency is calculated based on the fitted limit curve. The 95% limit curve is employed in this study (e.g., Eq. (4-44)). The candidates, whose lower limit of frequency exceeds the spindle bandwidth or the upper limit value, are excluded.

(5) Based on the combination of the remaining RVA candidates and the corresponding lower-limit frequency, a possible candidate with the highest RV factor is selected, considering the acceptable maximum spindle acceleration. Finally, the applied SSSV frequency is determined so that all the limit criteria will be satisfied.

4.4. Time-domain process simulation

4.4.1. Simulation conditions

To evaluate the proposed design method, a series of time-domain plunge turning simulations were carried out. In the plunge turning process, the cutting edge was assumed to be ideally sharp and furthermore, it was assumed that the vibration direction was entirely the same as the chip flow direction; hence, $\eta = \gamma = 90°$, $\beta = 0°$; and $b_c = b_r = a_p = a_{pn}$ (i.e., $\mu_c = 1$) in Fig. 4-1. Referring to [232], the modal mass, damping coefficient, and stiffness were set to 0.1247 kg, 45.97 N · s/m, and 1.063×10^7 N/m, respectively (i.e., the resonant frequency was 1469 Hz). Additionally, the specific cutting force of K_{tc} and μ_f were set to 1284 MPa and 0.5537 (i.e., $\mu_f K_{tc} = 711$ MPa), respectively. Following [232], the process was considered stable when the vibration amplitude of the maximum frequency spectrum, $|q_c(i\omega)|_{max}$, was less than 1.5 μm_{0-p}. The process was determined as chatter in the case of $|q_c(i\omega)|_{max} \geq 1.5$ μm_{0-p}. Each simulation lasted 30 s with a sampling frequency of 10 kHz. Nonlinearities [283], such as the jumping effect of CWS were considered (i.e., the cutting forces would become zero when the negative uncut chip thickness was calculated). Note that the multiple regenerative effect [284] was not considered, although it was confirmed that the trends of the results did not change even when it was considered. As the cutting conditions, the nominal spindle speed of $S_n = 1393\ \mathrm{min}^{-1}$ and a feed rate of $c = 0.080$ mm/rev were used in all the simulations. The spindle-rotation frequency was significantly smaller than the resonance frequency and the predicted asymptotic stability limit was 0.61 mm. The time delay was accurately calculated based on Eq. (4-42) in the simulation. The static displacement was eliminated by HPF with a 50-Hz cut-off frequency in the displayed results.

4.4.2. Comprehensive description of beat vibration

Fig. 4-10 shows the results of the CSS and SSSV processes with $R_A = 5.5\%$ and $f_s = 1.0$ Hz, when the cutting width b_c was set to 0.915 mm (i.e., 1.5 times the asymptotic stability limit). Chatter was observed at 1500 Hz in the CSS process (Fig. 4-10(c)).

In the example SSSV process, the vibration was significantly amplified periodically (i.e., the beat vibration). Its enlarged view is shown in Fig. 4-10(b), where the profiles of the spindle speed and time-varying phase shift are also depicted. It can be confirmed that the

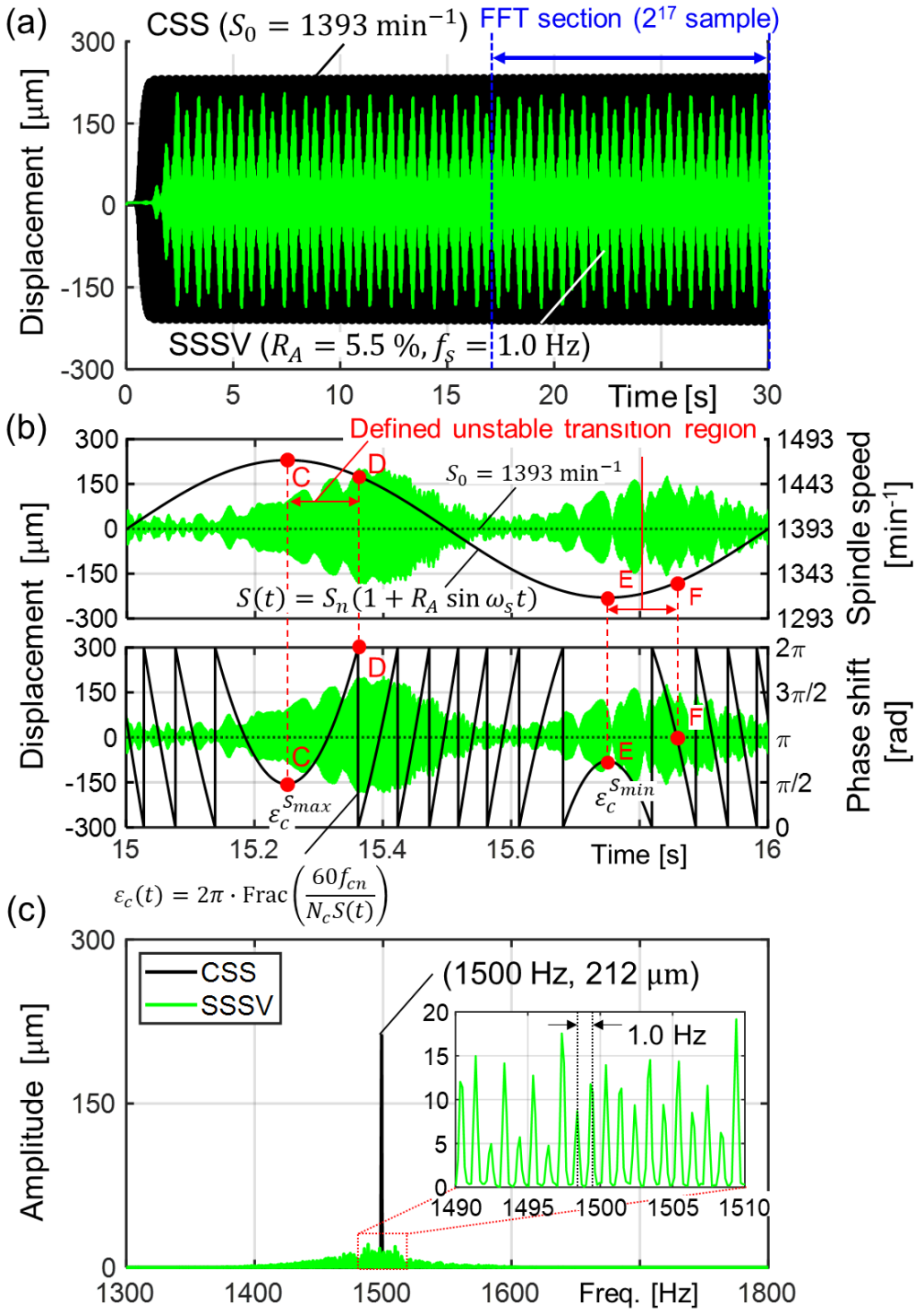

Fig. 4-10 Typical chatter results in CSS and SSSV ($b_c = 0.915$ mm, $S_n = 1393$ min^{-1}, $R_A = 5.5$ %, and $f_s = 1.0$ Hz): (a) overview; (b) enlarged view associated with the time-varying spindle speed and phase shift (refer Fig. 4-7); (c) FFT analysis

beat vibration tended to be amplified around the defined unstable transition region (refer Fig. 4-7); hence it is reasonable to pass through these regions as fast as possible before the chatter develops significantly. As seen in Fig. 4-10(c), the spectrum peak often looked

significantly small in the SSSV process even when a large beat vibration occurred in the time-domain. This is because the spectrum energy was distributed by the frequency modulation of the SSV process. The frequency spacing of each spectrum (i.e., side-band frequency) coincided with the SSSV frequency as predicted by Eq. (4-16).

Based on $f_c = 1500$ Hz and $S_n = 1393$ min^{-1}, the nominal chatter lobe number and the phase shift were calculated as 64 and 219°, respectively. Then, the SSSV would be designed by the proposed design procedure.

4.4.3. Results of the design candidates

Fig. 4-11 shows the behavior of the energy balance in the SSSV cycle according to the RVA. The energy was normalized by constant coefficients. Both the analytical energy model of Eq. (4-30) and the numerical one with the non-closed-form integration are depicted for comparison. As seen in Fig. 4-11, the analytical model predicted the energy behavior well in the low RVA (i.e., MI) region, whereas there was a discrepancy in the higher RVA/MI region owing to the approximations from Eqs. (4-7) – (4-9). Nevertheless, the notable point is that the locations of the extrema in the approximated and exact energy were very well matched, although the correspondence of the extrema was opposite in some RVA values. This suggests that the local minimum/maximum energy points in SSSV cycle were strongly dominated by $J_0(m_f)$.

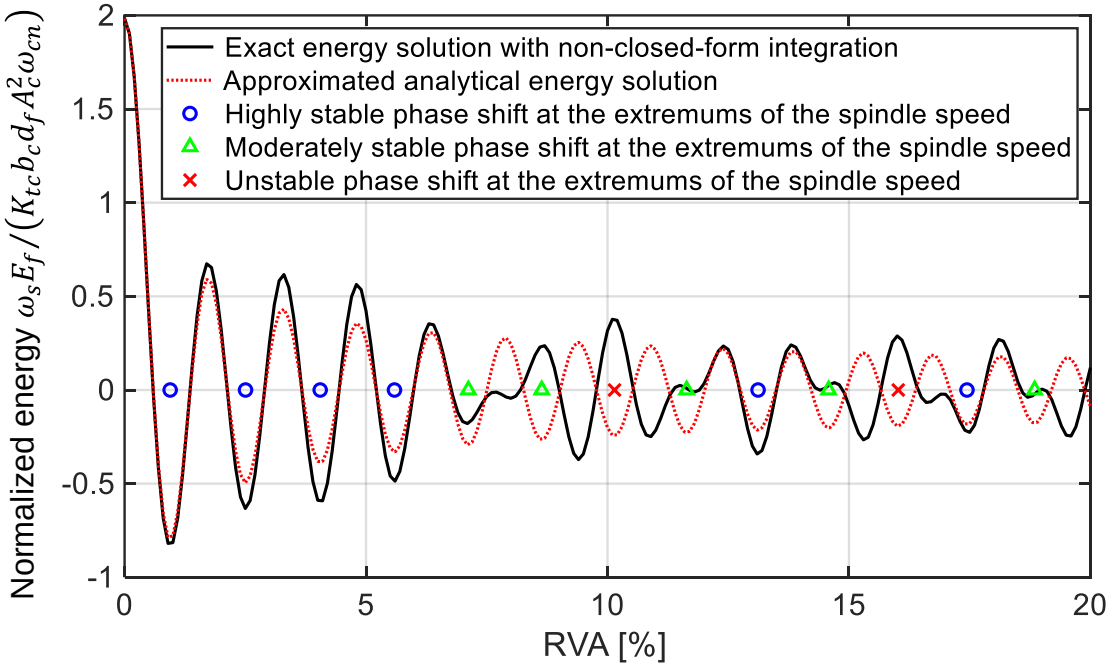

Fig. 4-11 Comparison of the analytical energy (i.e., Eq. (4-30)) and numerical models with non-closed form integration under $k_{cn} = 64, \varepsilon_{cn} = 219°$ and $f_s = 1.0$ Hz (the categorized phase shift stability based on Eq. (4-49) is also depicted)

Considering that the beat vibration would emerge especially around the extrema of the spindle speed, the instantaneous phase stability at S_{max} and S_{min} were investigated. The phase shift at the maximum and minimum spindle speeds $\varepsilon_c^{S_{max}}$ [rad] and $\varepsilon_c^{S_{min}}$ [rad], respectively, can be obtained as follows:

$$\begin{aligned}\varepsilon_c^{S_{max}} &= 2\pi \cdot \mathrm{Frac}\left(\frac{60 f_{cn}}{N_c S_{max}}\right) = 2\pi\left(\frac{k_{cn} + \frac{\varepsilon_{cn}}{2\pi}}{1 + R_A} - k_c^{S_{max}}\right), \\ \varepsilon_c^{S_{min}} &= 2\pi \cdot \mathrm{Frac}\left(\frac{60 f_{cn}}{N_c S_{min}}\right) = 2\pi\left(\frac{k_0 + \frac{\varepsilon_0}{2\pi}}{1 - R_A} - k_c^{S_{min}}\right)\end{aligned} \tag{4-49}$$

If $\varepsilon_c^{S_{max}}$ and/or $\varepsilon_c^{S_{min}}$ fall into the unstable phase region, the beat vibration may be aggravated instantaneously. The phase stability is categorized into three levels, highly stable (HS), moderately stable (MS), and unstable (US). In case of HS phase stability, both $\varepsilon_c^{S_{max}}$ and $\varepsilon_c^{S_{min}}$ remain in the stable phase region (i.e., $0 \le \varepsilon_c < \pi$). On the other hand, if both of them remain in the unstable region (i.e., $\pi \le \varepsilon_c < 2\pi$) the phase is regarded as a US phase. If only either $\varepsilon_c^{S_{max}}$ or $\varepsilon_c^{S_{min}}$ is unstable, while the other is stable, then it is considered as an MS phase. Fig. 4-11 also shows the results of phase stability for the RVA candidates corresponding to MI in Table 4-1. The good correlation between the energy stability and phase stability can be observed. In the US condition, the energy balance tends to be positive in spite of a local minimum point of $J_0(m_f)$. On the other hand, a large negative energy balance tends to exist in case of HS stability. The energy balance tends to approach zero in under MS stability.

Table 4-2 summarizes the design criteria calculated by following the proposed design procedure. Note that $N_r = N_c = 1$ was assumed in Eqs. (4-38) and (4-39). The upper limits for the variation of the frequency were calculated based on the polynomial fitting to the 95% upper limit curve in Eq. (4-44). In the first and second candidates, the lower limit value of SSSV frequency exceeded the upper limit value; hence, the expected SSSV effect could not be secured. Furthermore, the 14th candidate was excluded, as its RVA value exceeded 20% [242]. Therefore, a series of SSSV turning simulations using the third to 13th candidates were conducted. In each simulation, the SSSV frequency was set to the corresponding lower limit value (i.e., $\omega_s = \omega_{s(min)}$).

4.4.4. Verification of design candidates

Fig. 4-12(a) shows the result of the stability map for $b_c = 0.915\,\mathrm{mm}$. The origin represents the CSS process. The SSSV with $R_A = 4.051\%$ and $R_F = 14.718\%$ was still in a state of chatter in spite of the large negative energy balance, as seen in Fig. 4-11. This is because of the low RV factor which could not stabilize the process under a cutting width of

Table 4-2 Design candidates where $f_{cn} = 1500$ Hz, $S_n = 1393$ min^{-1}, and $N_r = 1$ ($k_{cn} = 64, \varepsilon_{cn} = 219°$)

#	1	2	3	4	5	6	7
m_f [–]	3.832	10.173	16.471	22.760	29.047	35.332	41.617
R_A [%]	0.944	2.504	4.051	5.589	7.119	8.639	10.146
Phase stability	HS	HS	HS	HS	MS	MS	US
$f_{s(max)}$ [Hz]	4.076	4.070	4.055	4.032	4.000	3.962	3.918
$f_{s(min)}$ [Hz]	8.438	4.474	3.417	2.803	2.335	2.088	2.002
$R_{F(min)}$ ($\tau_n f_{s(min)}$) [%]	36.347	19.270	14.718	12.073	10.057	8.995	8.625
RV [%]	0.343	0.483	0.596	0.675	0.716	0.777	0.875
Priority	N/A	N/A	10	9	8	7	6
#	8	9	10	11	12	13	14
m_f [–]	47.901	54.186	60.469	66.753	73.037	79.320	85.604
R_A [%]	11.640	13.118	14.579	16.022	17.444	18.846	20.225
Phase stability	US	HS	MS	US	HS	MS	MS
$f_{s(max)}$ [Hz]	3.867	3.812	3.753	3.690	3.624	3.556	3.486
$f_{s(min)}$ [Hz]	1.183	2.167	1.752	1.397	2.136	1.688	1.066
$R_{F(min)}$ ($\tau_n f_{s(min)}$) [%]	5.094	9.334	7.546	6.017	9.202	7.270	4.589
RV [%]	0.593	1.224	1.100	0.964	1.605	1.370	0.9282
Priority	11	3	4	5	1	2	N/A

0.915 mm; hence, it is recommended to select a combination of parameters with the highest RV possible. Here, the case of $R_A = 11.640\%$ with $R_F = 5.094\%$ was defined as a stable process in spite of having almost the same RV as #3. This is because the RVA had a much more stabilizing effect on the chatter, in general. However, a larger beat vibration emerged in the case of #8 than in the other conditions (Fig. 4-12(b)), as the RVF is alternatively low. However, excessively high RVF values must be avoided for securing the expected SSSV effect (Fig. 4-12(c)). In the case of $R_A = 5.589\%$, the chatter occurred again under a high RVF of 30.151% ($f_s = 7.000$ Hz), whereas the process was stable under an RVF of 12.073% ($f_s = 2.803$ Hz). In summary, it is important to set an upper bound constraint on the RVF.

Based on the RV factor, the highest priority candidate was #12. Next, the candidates of #13 and #9 were recommended in that order. In fact, these candidates had either HS or MS phase stability and relatively good energy balance. Note that the lower limit value of the SSSV frequency tended to become more secure, especially, in the HS condition. Consequently, the priority of HS candidates became relatively high. As already mentioned, there is a correlation between the phase stability and energy balance in the SSSV cycle. Therefore, the proper candidates actually having good energy balance are automatically sorted, based on the RV factor.

Fig. 4-13(a) shows the result of the stability map for a larger cutting width of $b_c = 1.525$ mm (2.5 times the asymptotic stability limit). The design candidates, #12 and #13 were stable because of their high RV. However, a large beat vibration was observed at some time portion in the case of #13, as shown in Fig. 4-13(b). Therefore, #12 could be regarded as the most stable candidate.

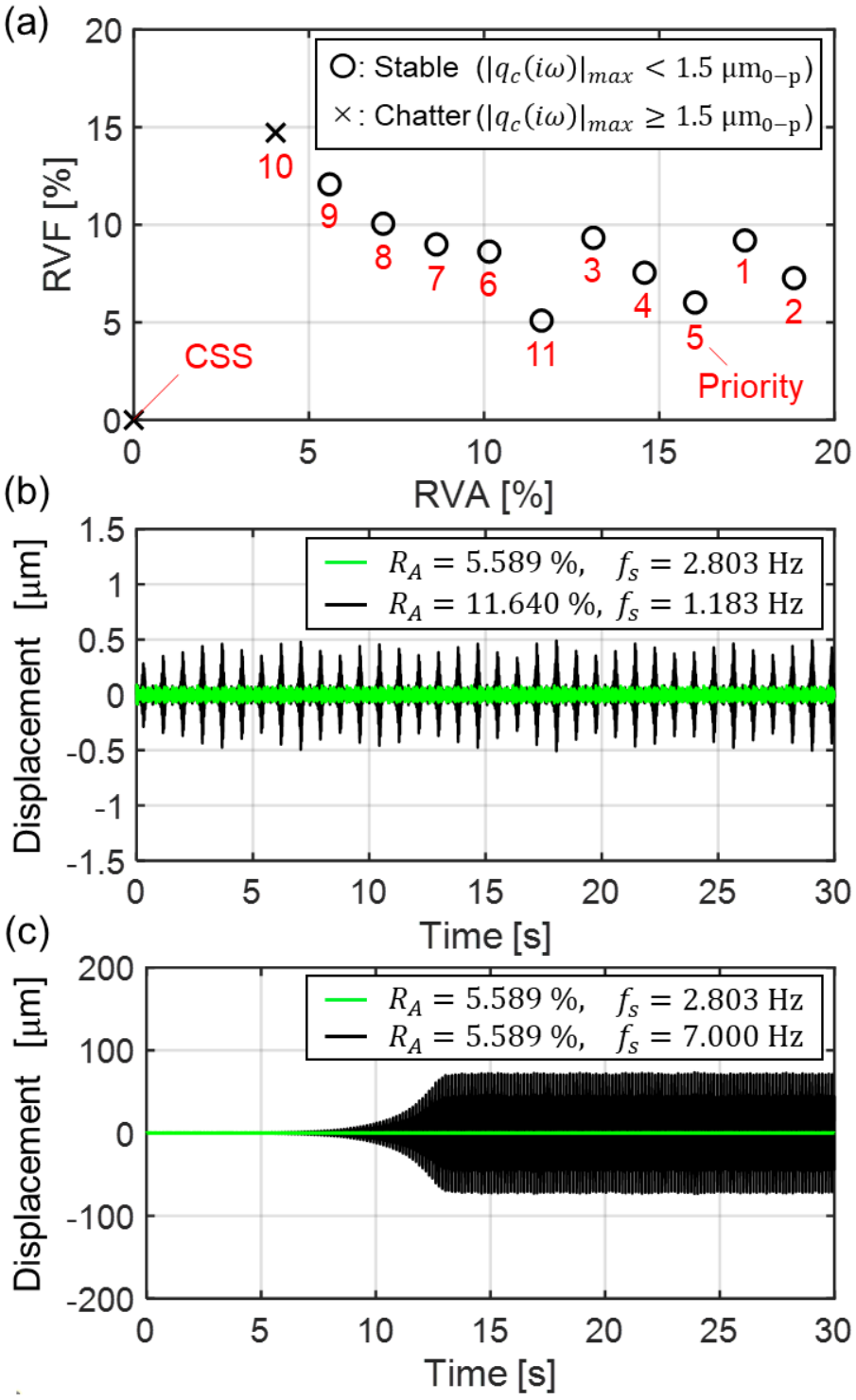

Fig. 4-12 Results for $b_c = 0.915$ mm: (a) stability map for each design candidate in Table 4-2; (b) comparison of design candidates, #4 and #8; (c) excessive RVF value in the candidate of #4

Note that as the vibration appeared to be small at some time instances and its frequency spectra were distributed, the determination of the process stability was difficult in the time-domain simulation [151]. In such a case, it is necessary to be careful, as it may not be possible to sufficiently improve the machined surface quality.

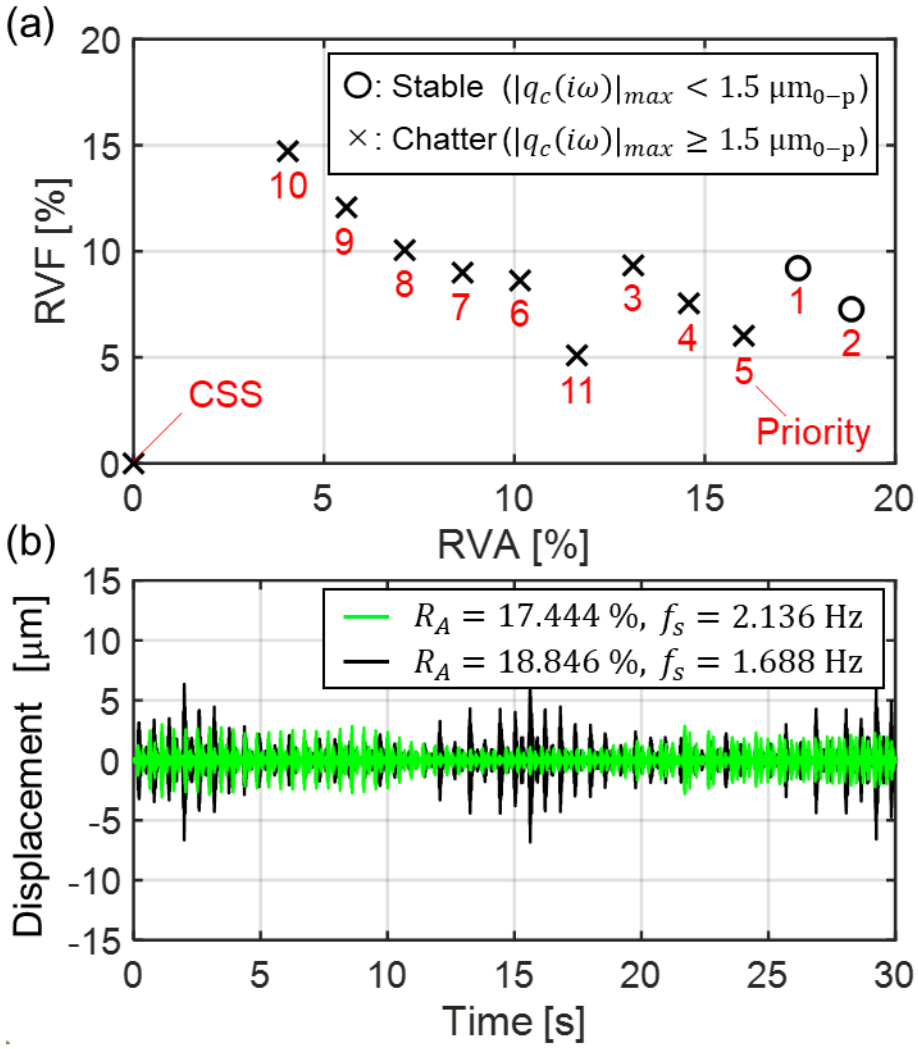

Fig. 4-13 Results for b_c = 1.525 mm: (a) stability map for each design candidate in Table 4-2; (b) time waveform in the candidates, #12 and #13

The RVA and/or RV factor in #12 and #13 may be relatively large for practical use, and the next proper candidate, namely #9 could be a reasonable solution. In fact, the process became stable for this candidate (i.e., $R_A = 13.118\%$ and $R_F = 9.334\%$) in the case of b_d = 1.495 mm (i.e., 2.45 times the asymptotic stability limit), as shown in Fig. 4-14.

Here, an additional simulation was performed for each RVA value, while changing the SSSV frequency so that the same RV of 1.224% was maintained. Its stability map is shown in Fig. 4-15(a). With a smaller RVA value, the process could not be stabilized even for the same RV value. This also substantiates that the RVA affected the chatter stability more significantly. The process was considered stable at the four RVA values, indicated by P1 – P4. However, as can be clearly seen in Fig. 4-15(b), the chatter vibration was most effectively suppressed at P1 and P3, whose RVA values were 13.118% and 17.444%, respectively. This result demonstrates the good correlation with the energy behavior in Fig. 4-11.

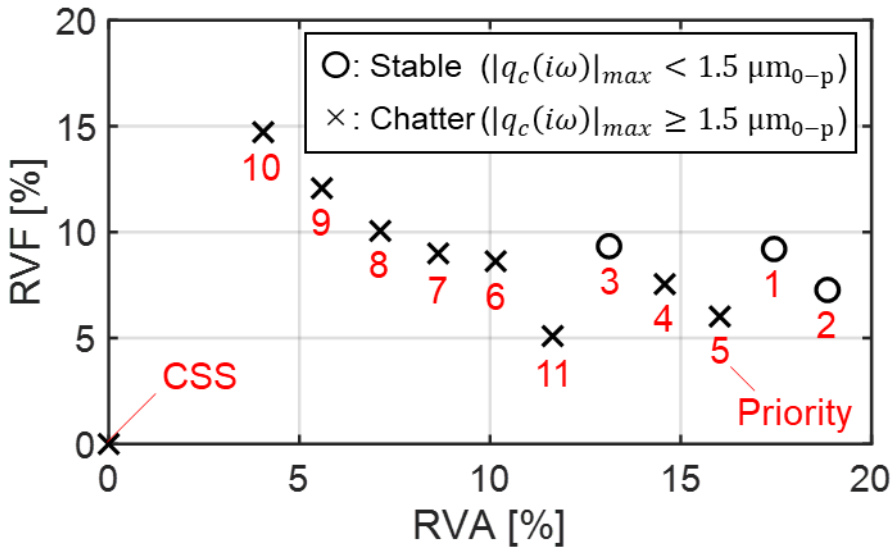

Fig. 4-14 Stability map of each design candidate in Table 4-2 for $b_c = 1.495$ mm

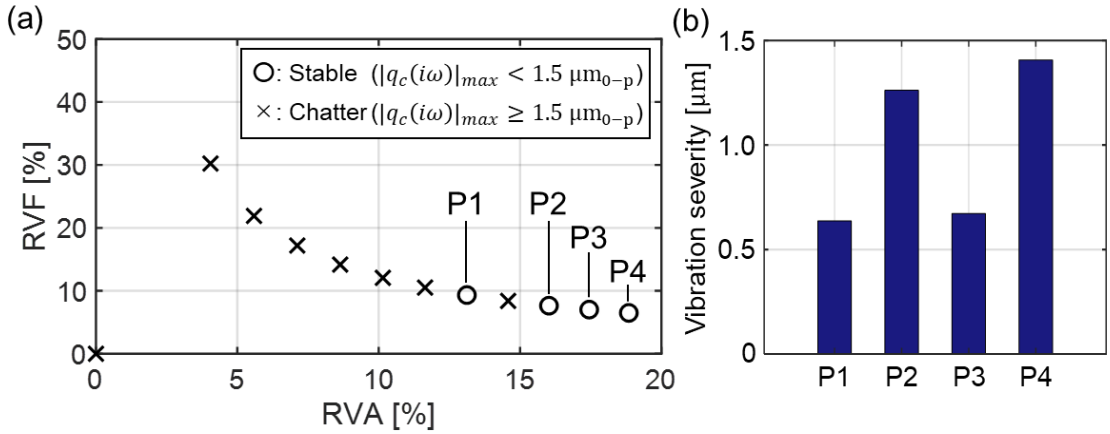

Fig. 4-15 Results for $b_c = 1.495$ mm at each RVA with a constant RV of 1.224%: (a) stability map; (b) vibration severity represented by standard deviation at stable conditions

Fig. 4-16 shows some additional results of stability map with a lower cutting width. The degree of stability improvement of the design candidates matched well with the priority based on the RV factor.

From the simulation results, it can be stated that the SSSV could be optimally designed with only the chatter frequency by the proposed design method, while considering the machine constraints. In particular, the candidates with good energy balance and high RV factor had the potential to robustly suppress the chatter vibration with less beat vibration. The actual behavior of the energy balance for the design candidates could be discriminated based on the phase shift stability at the extrema of the spindle speed. Note that good energy balance was also observed at some RVA values corresponding to local maxima of $J_0(m_f)$ (e.g., 9.4% and 15.4% in Fig. 4-11). Those points can be utilized by expanding the design candidates of Table 4-1 to include the local maxima of $J_0(m_f)$.

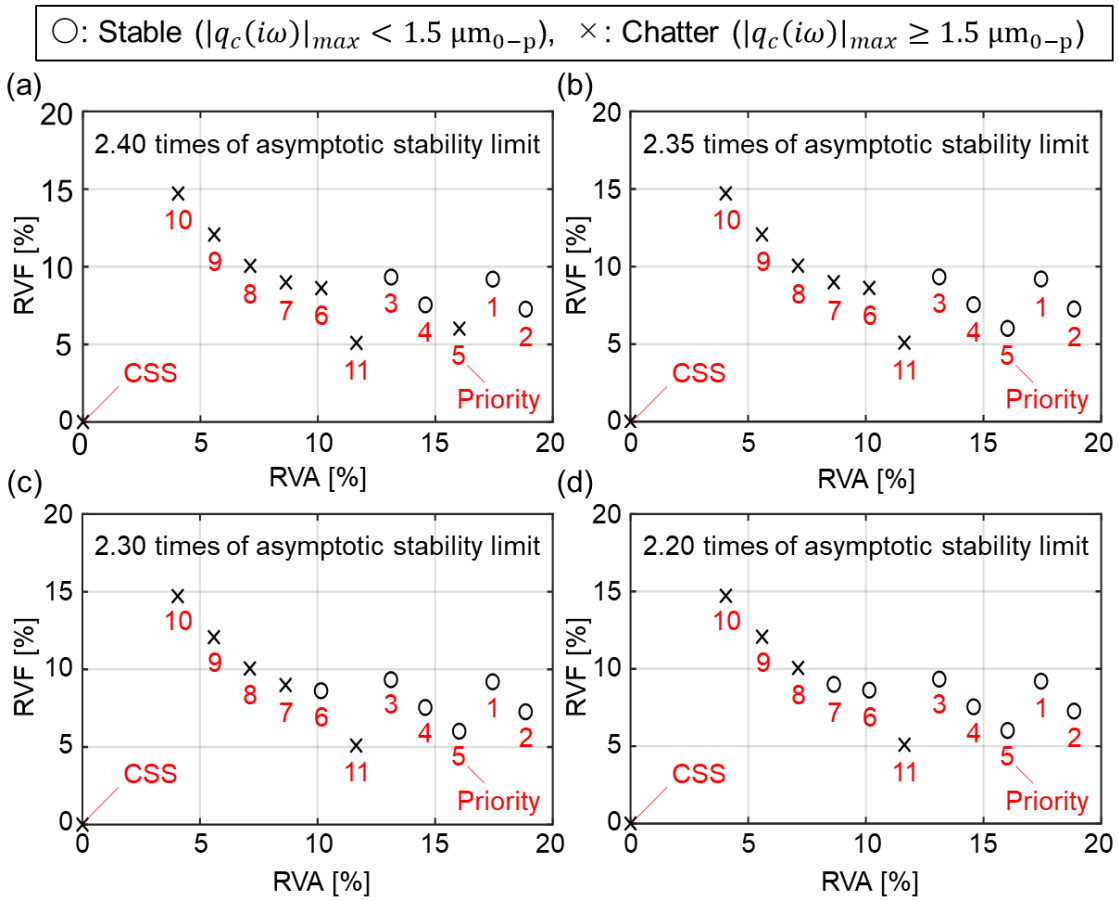

Fig. 4-16 Stability map for each design candidate in Table 4-2 for cutting widths of 1.342–1.464 mm: (a) b_c = 1.464 mm; (b) b_c = 1.434 mm; (c) b_c = 1.403 mm; (d) b_c = 1.342 mm

4.5. Experimental verification

4.5.1. Experimental setup

A series of boring tests were carried out for verification. Note that the cutting mechanics of the boring process are essentially the same as those of a general turning process [285].

Fig. 4-17 shows a large-scale double-column machining center (MPF-2614FS; Shibaura Machine Co., Ltd), having full-closed ball-screw-driven stages in XYZ-axes. The boring bar, having a single point cutter was fed in the Z-direction with rotation and then the inside of hole was machined. The common conditions of the boring tests are summarized in Table 4-3.

In most cases of the boring process, chatter is induced from a flexible boring bar. Using preliminary tap tests and modal analysis, the most flexibility was confirmed at the first bending mode of the boring bar at approximately 1480 Hz. The 3-axes accelerometers were attached on the non-rotational parts of both the spindle and workpiece, although only the acceleration results at the workpiece side are shown, as the vibration was clearly observed without the non-process vibration induced by spindle rotation. Note that MEDOB was implemented on all stages, and it was confirmed that chatter frequency can sensitively

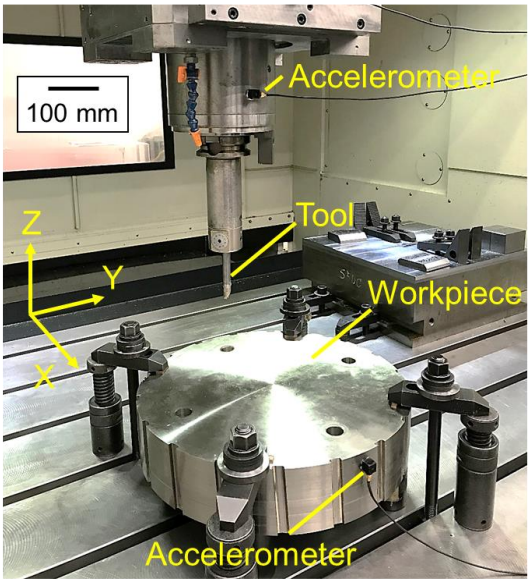

Fig. 4-17 Experimental setup for boring tests

Table 4-3 Common experimental conditions

Nominal spindle speed [min^{-1}]	1393
Length of boring bar [mm]	99
Diameter of boring bar [mm]	16
Insert nose radius [mm]	0.4
Workpiece material	S55C
Radial depth of cut [mm]	0.1
Feed rate [mm/rev]	0.08
Data sampling frequency [kHz]	10

extracted without additional sensors even in this large-scale machine tool.

4.5.2. Experimental results and discussion

Fig. 4-18(a) and (b) show the measured vibration and its FFT analysis of the CSS boring, respectively. Only the X-axis vibration is shown as a representative result because a similar trend was confirmed along the other axes. In the CSS process, the chatter vibration was clearly observed at approximately 1500 Hz (near the first bending mode of the boring bar), whereas two dominant chatter frequencies appeared to be excited (at 1503 and 1549 Hz). The chatter originated from the rotating boring part and was measured by an accelerometer at a stationary place. In this case, it was known that the vibration spectrum split into two peaks, which were located at $\pm n_m \times (S_0/60)$ from the actual frequency [173]. Here, n_m is the number of waves in the vibration mode, and it equaled 1 for the first bending mode; hence, the actual chatter frequency should be 1526 Hz. The chatter onset could be observed form the machined surface of Fig. 4-18(c).

The typical results of the SSSV process with $R_A = 16.0\%$ and $f_s = 1.0$ Hz ($R_F = 4.3\%$ and $RV = 0.69\%$), which were empirically defined by the operator, are also shown in Fig. 4-18(a) and (b). The beat vibration corresponding to the SSSV cycle was obviously observed in the time waveform. On the contrary, no noticeable spectral peaks were observed in the FFT result, unlike in a stable process because of the spectrum energy distribution by the FM, as discussed in Fig. 4-10(c). However, the machined surface appeared like a striped pattern, with alternating stable surfaces and chatter marks owing to the beat vibration (see Fig. 4-18(d)). Note that it was confirmed that the frequency distribution was wider than that suggested by Eq. (4-12) (i.e., $f_{cn} \pm f_s m_f$), which is discussed in **Appendix C** with the corresponding spectrogram of the unstable SSSV.

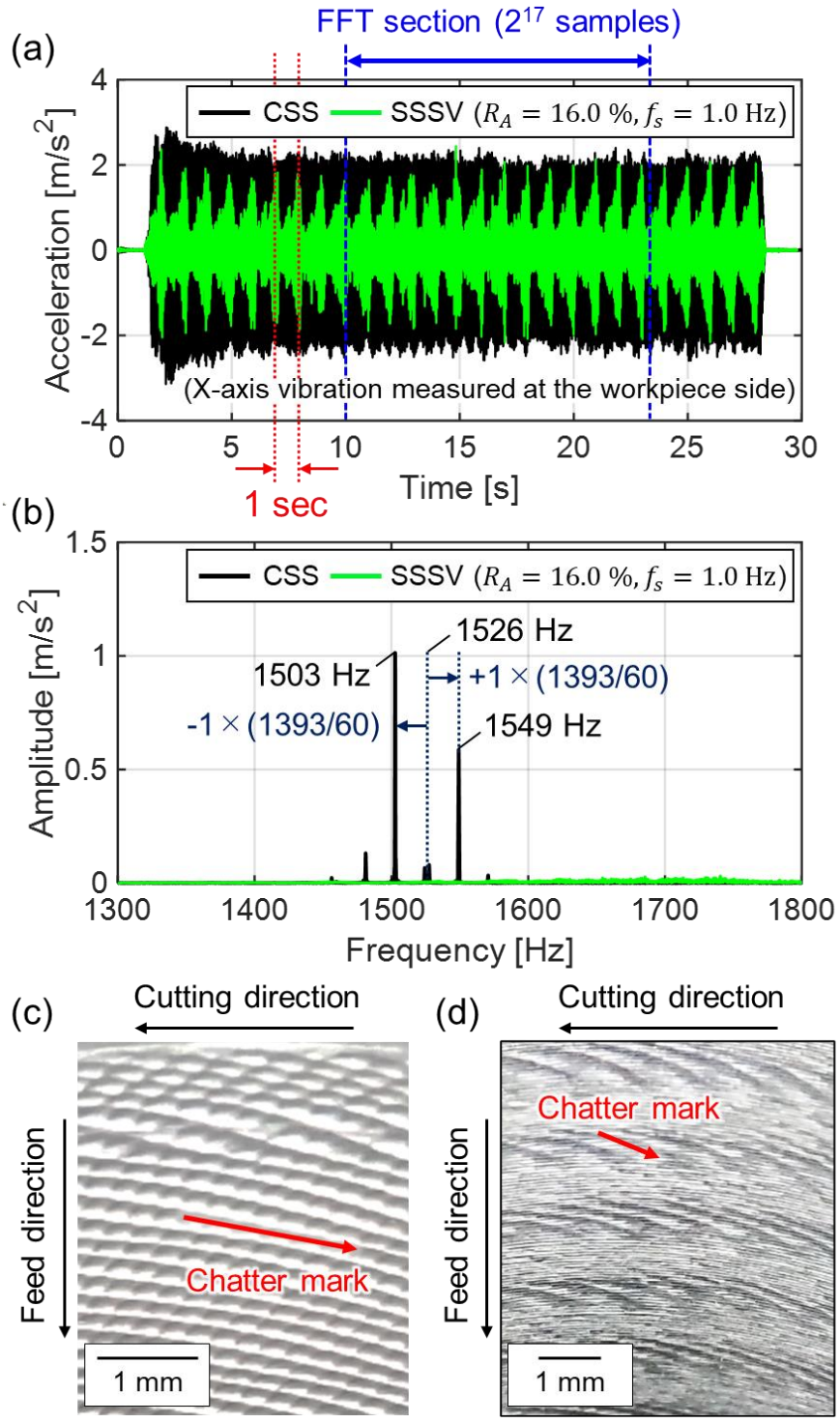

Fig. 4-18 Experimental results from CSS boring and typical SSSV (R_A = 16.0% and f_s = 1.0 Hz): (a) measured acceleration; (b) FFT analysis; (c) and (d) appearance of the machined surface in the CSS and the typical SSSV process, respectively

Based on the measured chatter frequency, the SSSV was designed by the proposed design procedure. As the chatter frequency and the commanded spindle speed were 1526 Hz and 1393 min^{-1}, respectively, the nominal chatter lobe number and the phase shift were

Table 4-4 Design candidates for the optimal SSSV in the experiment

Priority	7	5	3	4	1	2	6
m_f [–]	29.05	35.33	54.19	60.47	73.04	79.32	85.60
R_A [%]	7.0	8.5	12.9	14.3	17.2	18.5	19.9
Phase stability	MS	MS	HS	MS	HS	MS	MS
$f_{s(max)}$ [Hz]	4.00	3.97	3.82	3.76	3.64	3.57	3.50
$f_{s(min)}$ [Hz]	2.35	2.19	2.03	1.60	2.03	1.57	0.89
$R_{F(min)}$ [%]	10.11	9.45	8.75	6.90	8.74	6.75	3.84
RV [%]	0.71	0.80	1.13	0.99	1.50	1.25	0.76

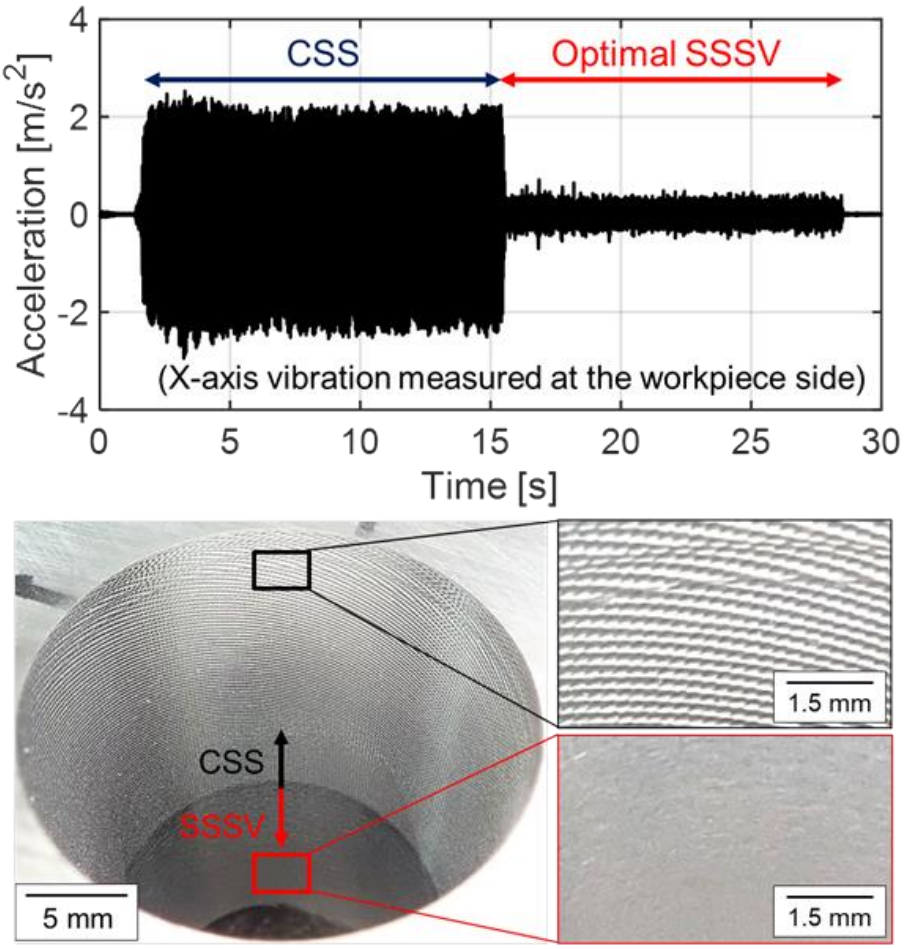

Fig. 4-19 Optimal SSSV designed by the proposed methodology ($R_A = 12.9\%$ and $f_s = 2.2$ Hz)

65 and 262°. Table 4-4 shows the seven design candidates with the highest priority. Note that $N_r = N_c = 1$ for calculating the lower limit SSSV frequency and only the candidates in Table 4-1 were considered. In addition, Eq. (4-44) (i.e., 95% limit curve) was used to calculate the upper limit frequency.

In this experimental verification, the candidate with $R_A = 12.9\%$ was applied as a reasonably optimal solution, considering the machine and process limitations. This

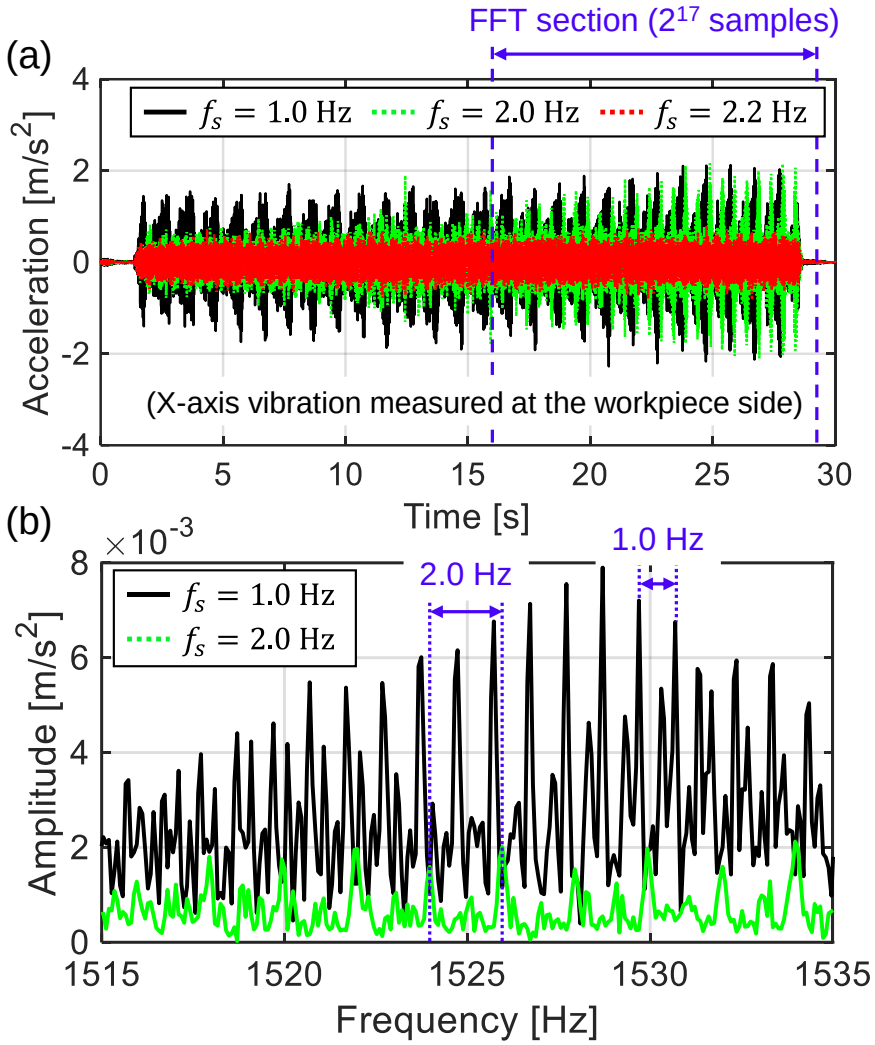

Fig. 4-20 Verification of lower limit criterion of the SSSV frequency under an optimal RVA of 12.9% for S_n = 1393 min^{-1}: (a) time waveform; (b) enlarged view of the FFT results (f_s = 1.0 and 2.0 Hz)

corresponded to the nineth local minimum point of $J_0(m_f)$ and $m_f = 54.186$. In addition, it possessed the HS phase stability. In fact, it had a large negative energy balance, which was confirmed by a numerical energy calculation. The SSSV frequency was set to 2.2 Hz for satisfying the lower limit criterion of 2.03 Hz.

Fig. 4-19 shows the experimental results for the optimal SSSV under $R_A = 12.9\%$ and $f_s = 2.2$ Hz. As can be seen clearly in Fig. 4-19, the chatter vibration was completely diminished without the large beat vibration after the SSSV was applied. As a result, the surface quality of machined surface was significantly improved. Note that the optimal RVA in accordance with Eq. (4-32) proposed by Al-Regib et al. [68] was 1.1%, which was close to the first local minimum point of $J_0(m_f)$. Furthermore, the corresponding lower limit value for the SSSV frequency, based on the existing criterion of Eq. (4-34) was 1.17 Hz. However, it was also confirmed that the chatter was not at all suppressed by the SSSV designed by existing method, as the values of the RVA and SSSV frequency were very small in this case.

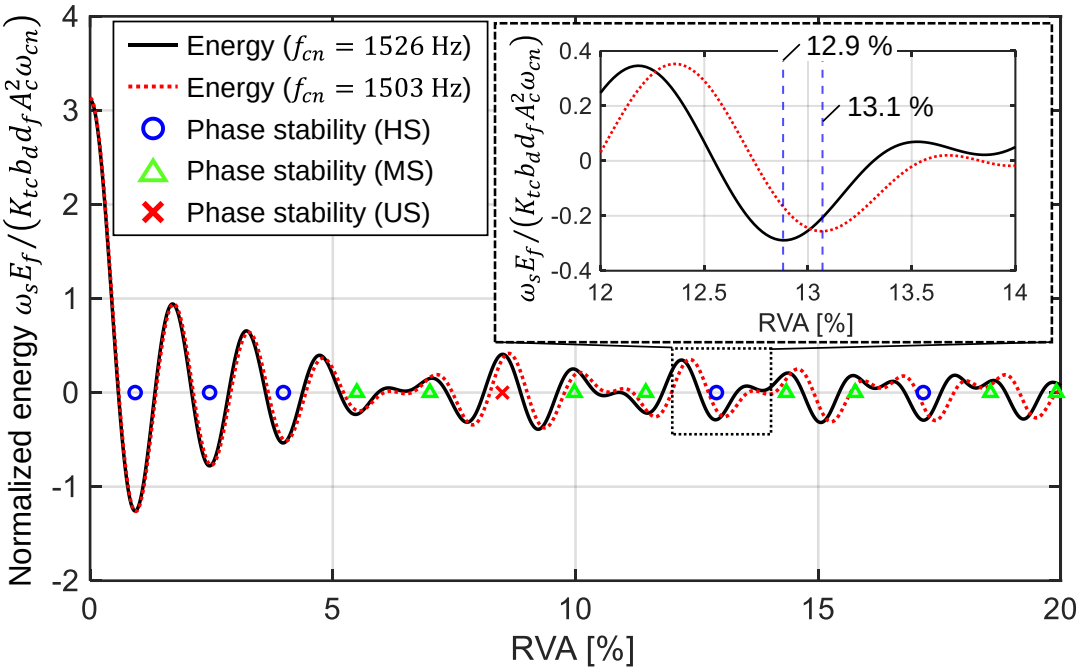

Fig. 4-21 Variation in the energy balance in the SSSV process owing to the identification error of the chatter frequency (1526 vs 1503 Hz; the energy was numerically calculated with the non-closed form model and the phase stability for f_{cn} = 1526 Hz was also depicted)

To verify its optimality, additional boring tests were also carried out. Fig. 4-20(a) shows the experimental results obtained by varying the SSSV frequency under an RVA of 12.9%. For f_s = 1.0 Hz, which was significantly smaller than the lower limit value, a vigorous beat vibration occurred immediately after the boring process was started, as in the case of the typical SSSV; this is depicted in Fig. 4-18(a). For f_s = 2.0 Hz, which was slightly smaller than the lower limit value, the chatter vibration was suppressed in the first half of the process, whereas the large beat vibration began to emerge in the latter half. It can be stated that the proposed lower limit criterion for the SSSV frequency was reasonable.

Additionally, the FFT results for f_s = 1.0 2.0 Hz are shown in Fig. 4-20(b), which was enlarged at approximately 1526 Hz. The side-band frequencies at intervals of SSSV frequency could be also observed in the experiment. Note that the corresponding results of the time-frequency analysis are also included in **Appendix C** to discuss the chatter frequency shift during the SSSV process.

Here, the proposed design method was directly affected by the measurement error of the chatter frequency. Assuming a simple strategy for chatter detection during the process (e.g., the maximum spectrum peak was regarded as the chatter frequency [103]), an online system would detect the chatter frequency as 1503 Hz in Fig. 4-18(b) (i.e., $k_{cn} = 64$ and $\varepsilon_{cn} = 266°$). Fig. 4-21 depicts the variation in the energy balance owing to the chatter identification error (i.e., 1526 vs 1503 Hz). As k_{cn} was one less in f_{cn} = 1503 Hz, the same modulation index computed a larger RVA than for f_{cn} = 1526 Hz. Focusing on m_f = 54.19,

the corresponding RVA value became 13.1% for $f_{cn} = 1503$ Hz. In addition, $f_{s(min)}$ was calculated as 2.00 Hz. These were not large deviations from the case of $f_c = 1526$ Hz; hence, this identification error would not cause any issues in this case (i.e., a high lobe number). However, it could cause a relatively large deviation of the design values in a low lobe-number case.

Finally, Fig. 4-22 shows an additional comparison of three different RVAs (7.0%, 12.9%, and 14.3%, which are respectively, the third, fourth, and seventh priority candidates in Table 4-4). To sufficiently satisfy $f_{s(min)}$ for each RVA, the frequency was set to 2.5, 2.2, and 2.0 Hz (corresponding to RV values of 0.75, 1.22%, and 1.23%, respectively). As seen in Fig. 4-22(a), the chatter was suppressed without an excessive beat vibration for all the combinations of the design parameters in the 0.1-mm radial depth of cut. However, the performance of chatter reduction was slightly different according to the design parameters. From Fig. 4-22(b) and (c), the slight beating vibration in accordance with the SSSV period and its harmonics remained, which was inevitable even in the stable SSV process. The reduction rates of the vibration severity over the chatter condition in the CSS were 79.2%, 82.0%, and 76.7% for RVA values of 7.0%, 12.9%, and 14.3%, respectively.

This shows a good correlation with the process energy behavior in the SSSV cycle, as the normalized energy balance at these RVA values were 0.15, −0.29, and 0.21, respectively (see Fig. 4-21). In fact, the RVA candidate of 12.9% had HS phase stability; hence the best performance of the chatter suppression was observed at this condition. Note that it was observed that the repeatability fluctuated at the RVA of 7.0% with $f_s = 2.5$ Hz (i.e., reproduced tests sometimes became unstable), whereas a high repeatability was confirmed in the other conditions. This might be because the candidate with the seventh priority was close to the stability boundary and consequently not robust.

Here, in the case of $R_A = 12.9\%$ and $f_s = 2.0$ Hz (i.e., $RV = 1.11\%$), the process became unstable in spite of a much higher RV value than that employed in the case of $R_A = 7.0\%$ and $f_s = 2.5$ Hz (i.e., $RV = 0.75\%$). This was contrary to the trend observed in the simulation depicted in Fig. 4-15(b), in which the same RV value with a larger RVA tended to be still stable (i.e., $R_A = 12.9\%$ and $f_s = 1.35$ Hz is expected to be stable). It suggests that the lower limit criterion for the SSSV frequency significantly impacted the process stabilization in this experiment. As pointed out in [151,239], many times, the expected process improvement cannot be achieved in the real experimental system of an SSV, owing to the large influence of the beat vibration. In such cases, it may be essential to conform with the lower limit criterion of the SSSV frequency for each RVA value. Nevertheless, the chatter can be properly suppressed by following the proposed design methodology, as demonstrated by both the simulations and experimental results. Especially, candidates with larger RV values and stable energy balance (i.e., HS phase stability) have the potential to effectively suppress the chatter vibration.

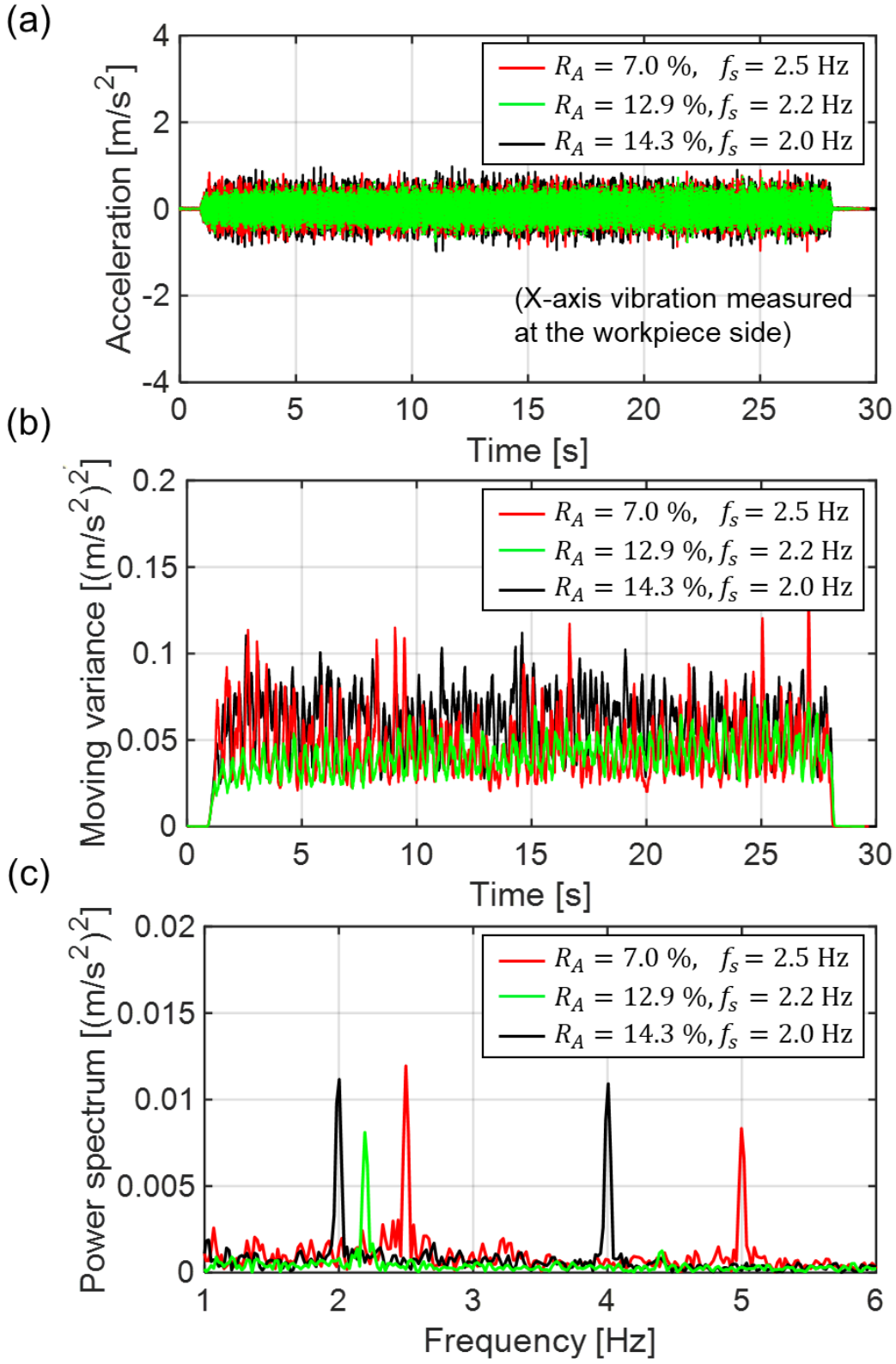

Fig. 4-22 Experimental results in three different combinations of proper design parameters (#3, #4, and #6 in Table 4-4): (a) time waveform; (b) moving variance (the window length was set to 0.1024 s, i.e., 2^{10} samples); (c) FFT of the moving variance

4.6. Summary

This chapter has proposed a novel programmable optimal design for the sinusoidal spindle speed variation (SSSV). The contents of this chapter can be summarized as follows:

1. Based on a technological analogy between frequency modulation (FM) and SSSV, a modulation index was introduced into the SSSV process as a novel design index. The optimum SSSV design candidates for the relative variation amplitude (RVA) were selected, so that the modulation index coincided with the extreme points of the 0-th order Bessel function of the first kind. In particular, the candidates having a stable phase stability at the maximum and minimum spindle speeds secured a large negative energy balance in the SSSV cycle.

2. Considering that the beat vibration tended to develop around the extrema of the spindle speed, a novel lower limit criterion for the SSSV frequency according to the RVA was proposed. In addition, an upper limit criterion for the relative frequency of the spindle speed variation (RVF) according to the RVA was also proposed for achieving the expected SSSV effect.

3. A series of time-domain simulations and boring tests were carried out to verify the proposed design methodology. It was confirmed that the design candidates with a good energy balance and a high RV (= RVA×RVF) value, identified through the proposed design procedure, could robustly dissipate the chatter vibration with a small beat vibration.

4. The requirement of the proposed design methodology is only the measurement of the chatter frequency, as in the case of discrete spindle speed tuning; hence it can contribute to autonomous chatter suppression integrated with chatter monitoring for the SOMS. Additionally, it is possible to incorporate the machine constraints into the design procedure in a flexible manner. As a result, a practical design of an SSSV becomes feasible on an actual shop floor.

Even though SSV is specifically effective in high lobe number scenarios, the proposed design procedure should be, in principle, applicable to low/middle lobe number scenarios as well. It is important that the proposed design method be applied to many real industrial applications and subjected to more verification for further development. Additionally, establishing a simple optimal design procedure for more general periodic spindle variation manner, where high-order multiple sinusoidal harmonics are superposed, is a research challenge, since special periodic shapes involving multiple harmonics inherently have potential to further improve the process stability [152,237,286].

5. Chatter suppression in parallel turning assisted with tool swing motion

5.1. Assumptions and concepts

This chapter proposes a novel concept for chatter suppression assisted with tool swing motion (TSM) in parallel turning [287,288]. To verify the proposed TSM process, it is assumed that rigid tools having the same insert geometries cut a flexible workpiece while sharing the machined surface with the same depth of cut. For chatter suppression under the same assumption, an effective methodology, known as unequal-pitch turning, has been proposed, where the optimal pitch angle is deduced based on the chatter frequency with a similar design methodology as VPCs [227,228]. As the pitch difference is given by turret position control, the unequal-pitch turning can flexibly respond to changes in the cutting state. However, the unequal pitch turning can cause the eccentricity of a flexible workpiece due to the unbalanced cutting forces (see Fig. 1-15). Therefore, the chatter stabilization performance and workpiece runout in the TSM process are experimentally evaluated and compared with conventional equal and unequal pitch turning.

In the TSM process, the two tools are swung in the circumferential direction of the workpiece sinusoidally while maintaining an equal pitch, as shown in Fig. 5-1; hence, the imbalance of the force vector is not caused ideally. The delay term between two consecutive cuts varies with time by applying TSM, as in the case of SSV. Based on the analogy between TSM and SSSV, the design procedure for SSSV discussed in Chapter 4 is extended for the TSM process. Consequently, TSM can be appropriately designed based solely on the chatter frequency. Similar to unequal pitch turning, TSM is also flexibly provided by the feed-drive system with turret position control. As the bandwidth of the position-control system is

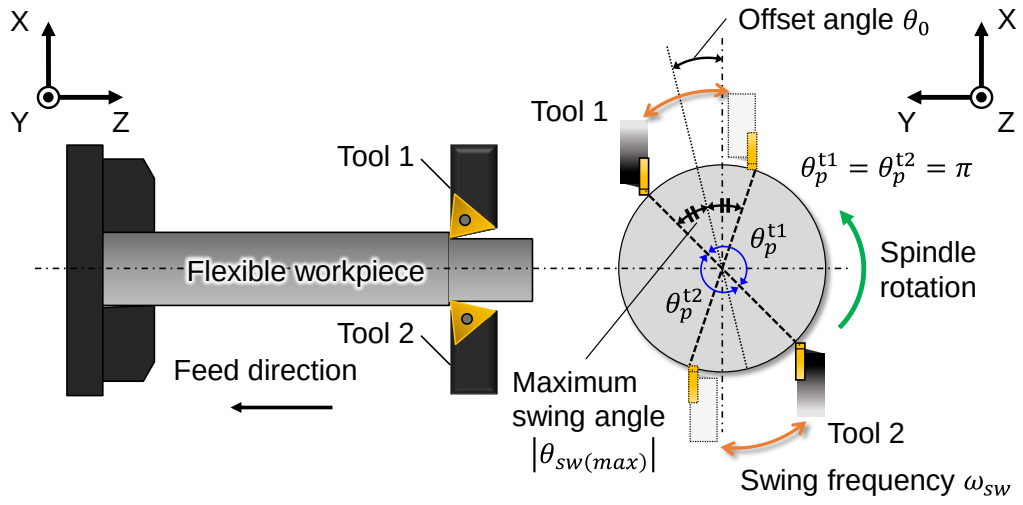

Fig. 5-1 Schematic of tool swing process in parallel turning

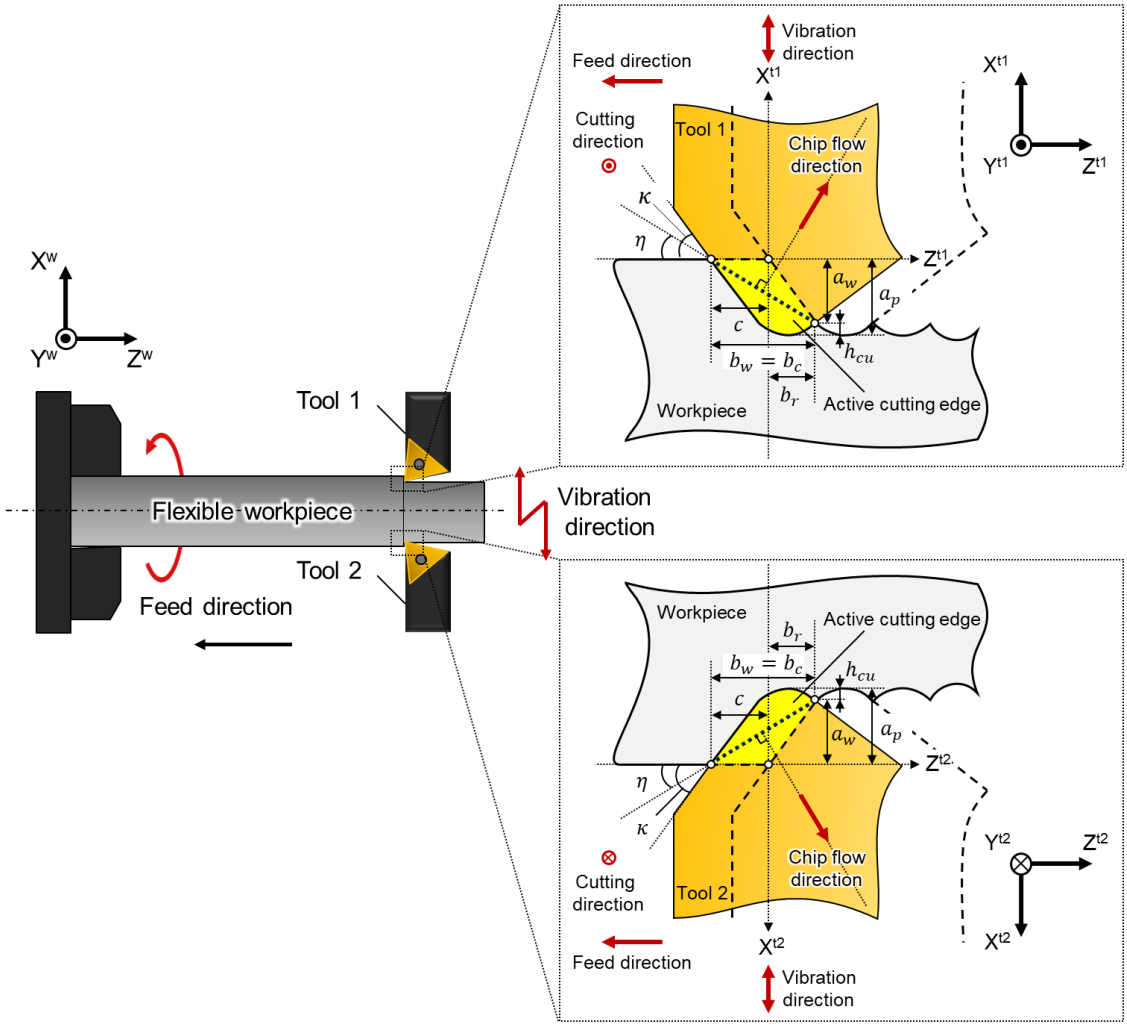

Fig. 5-2 Schematic of shared-surface parallel turning with flexible workpiece

generally much higher than that of the spindle system, the high-frequency modulation, which cannot be realized by the spindle system, is feasible. For instance, the bandwidth of the position control loop in the feed drive system is usually on the order of 25–30 Hz, even for a typical CNC machine [2,289]. This is an advantage for the TSM process, as the limitation of the SSV process often results from the machine, such as the bandwidth of the spindle system [240,242].

5.2. Process modeling of shared-surface parallel turning

First, the process model for shared-surface parallel turning with a flexible workpiece is developed to understand, in detail, the process dynamics and mechanism of unequal pitch turning and TSM process for chatter suppression.

Fig. 5-2 shows a schematic of shared-surface parallel turning with a slender workpiece. The local Cartesian coordinate system XYZ is defined in each tool and workpiece. It is

assumed that the vibration direction of the workpiece coincides with the X-direction for the intuitiveness, although the slender workpiece should also be flexible in the Y-direction (i.e., 2DoF system in XY-plane). In particular, the workpiece will elliptically vibrate in the XY-plane and the vibration direction can be defined as the long axis of the ellipse [290].

The general turning process model has already been shown in Chapter 4 (see Fig. 4-1). The parallel tuning model will be established by expanding the aforementioned process model of general single turning. Assuming the complete shared surface with the same tool geometries and depth of cut, the cutting force vector, $\boldsymbol{F_c}$, at each tool in its own coordinate system can be defined similarly to the single turning process, as follows:

$$\boldsymbol{F}_{\boldsymbol{c}}^{tp}(t) = A_s^{tp}(t) \cdot \mathbf{K_c} \tag{5-1}$$

where A_s [m^2] is the dynamic cutting area, $(\quad)^{tp}$ indicates value for p-th tool.

Here, the specific cutting force vector, $\mathbf{K_c}$, is defined with Colwell's empirical chip flow rule as follows:

$$\mathbf{K_c} = \{\mu_f K_{tc}\cos\eta \quad K_{tc} \quad \mu_f K_{tc}\sin\eta\}^{\mathrm{T}} = K_{tc}\{\mu_f\cos\eta \quad 1 \quad \mu_f\sin\eta\}^{\mathrm{T}} \tag{5-2}$$

where K_{tc} [N/m^2] is the specific principal force, μ_f [-] is the constant ratio of the force in chip flow direction to the principal force, and η [rad] is the chip-flow angle.

Additionally, the cutting width vector, $\mathbf{b_c}$ and regenerative width vector, $\mathbf{r_c}$ which constitute the dynamic cutting area, are defined as follows:

$$\mathbf{b_c} = \{b_w \quad 0 \quad a_w\}^{\mathrm{T}}, \tag{5-3}$$

$$\mathbf{r_c} = \{b_w - c \quad 0 \quad a_w\}^{\mathrm{T}} \tag{5-4}$$

where b_w [m], a_w [m] (i.e., cutting chord length projected onto Z- and X-axis, respectively), and η in Fig. 5-2 are geometrically calculated from the insert geometries (i.e., nose radius, r_ε [m] and approach angle, κ [rad]) and feed rate, c [m/tooth] as follows [159]:

$$b_w = \begin{cases} \dfrac{c}{2} + \dfrac{a_p - r_\varepsilon(1-\cos\kappa)}{\tan\kappa} + r_\varepsilon\sin\kappa & a_p > r_\varepsilon(1-\cos\kappa) \\ \dfrac{c}{2} + \sqrt{{r_\varepsilon}^2 - \left(r_\varepsilon - a_p\right)^2} & a_p \le r_\varepsilon(1-\cos\kappa) \end{cases} \tag{5-5}$$

$$h_{cu} = r_\varepsilon - \sqrt{{r_\varepsilon}^2 - \left(\frac{c}{2}\right)^2} \approx \frac{c^2}{8r_\varepsilon}\left(\frac{c}{r_\varepsilon} \ll 1\right) \rightarrow a_w = a_p - h_{cu} \tag{5-6}$$

$$\eta = \tan^{-1}(a_w / b_w) \tag{5-7}$$

where a_p [m] is a depth of cut as a cutting condition, and h_{cu} [m] is a geometric surface roughness (e.g., cusp height).

The dynamic cutting area is calculated by the inner product of the vibration vector and each width vector. Here, considering that the coordinate system for tool 2 is rotated by 180° around the Z-axis with respect to the workpiece coordinate system, the unit vibration vector, $\mathbf{e_x}$, at each CWS is defined as follows:

$$\mathbf{e}_{\mathbf{x}}^{\mathrm{t1}} = \begin{Bmatrix} 1 \\ 0 \\ 0 \end{Bmatrix}, \qquad \mathbf{e}_{\mathbf{x}}^{\mathrm{t2}} = \begin{bmatrix} \cos\pi & -\sin\pi & 0 \\ \sin\pi & \cos\pi & 0 \\ 0 & 0 & 1 \end{bmatrix} \begin{Bmatrix} 1 \\ 0 \\ 0 \end{Bmatrix} = \begin{Bmatrix} -1 \\ 0 \\ 0 \end{Bmatrix} \tag{5-8}$$

where only the workpiece vibration in the X-direction (i.e., $x^{\mathrm{w}}(t)$ [m]) is considered.

Assuming that the surface machined by tool 1 is regenerated at tool 2, and vice versa, the dynamic cutting area at each CWS can be defined as follows:

$$\begin{aligned} A_s^{\mathrm{t1}}(t) &= \mathbf{b_c} \cdot x^{\mathrm{w}}(t)\mathbf{e}_{\mathbf{x}}^{\mathrm{t1}} - \mathbf{r_c} \cdot x^{\mathrm{w}}(t-\tau^{\mathrm{t1}})\mathbf{e}_{\mathbf{x}}^{\mathrm{t2}} = b_c[x^{\mathrm{w}}(t) + \mu_c x^{\mathrm{w}}(t-\tau^{\mathrm{t1}})] \\ A_s^{\mathrm{t2}}(t) &= \mathbf{b_c} \cdot x^{\mathrm{w}}(t)\mathbf{e}_{\mathbf{x}}^{\mathrm{t2}} - \mathbf{r_c} \cdot x^{\mathrm{w}}(t-\tau^{\mathrm{t2}})\mathbf{e}_{\mathbf{x}}^{\mathrm{t1}} = -b_c[x^{\mathrm{w}}(t) + \mu_c x^{\mathrm{w}}(t-\tau^{\mathrm{t2}})] \end{aligned} \tag{5-9}$$

where $\left|\mathbf{b_c} \cdot \mathbf{e}_{\mathbf{x}}^{tp}\right| = b_w = b_c$, $\left|\mathbf{r_c} \cdot \mathbf{e}_{\mathbf{x}}^{tp}\right| = b_w - c = b_r$, and $\mu_c = b_r/b_c$ $(0 \le \mu_c \le 1)$. Here, b_c [m] and b_r [m] are the cutting and regenerative width in the vibration direction, respectively, and μ_c [−] is known as overlap factor. $(\ )^{\mathrm{w}}$ indicates value for workpiece.

The time delay, τ [s], in each CWS depends on not only the spindle speed, S [min^{-1}] but also the pitch angle, θ_p [rad], as follows:

$$\tau^{\mathrm{t1}} = \frac{60\theta_p^{\mathrm{t1}}}{2\pi S}, \qquad \tau^{\mathrm{t2}} = \frac{60\theta_p^{\mathrm{t2}}}{2\pi S} \tag{5-10}$$

As a result, considering the law of action and reaction in the workpiece coordinate system, the cutting force acting on the workpiece can be derived as follows:

$$\begin{aligned} \boldsymbol{F}_{\boldsymbol{c}}^{\mathrm{w}}(t) &= \begin{Bmatrix} F_x^{\mathrm{w}} \\ F_y^{\mathrm{w}} \\ F_z^{\mathrm{w}} \end{Bmatrix} = \begin{bmatrix} -1 & 0 & 0 \\ 0 & -1 & 0 \\ 0 & 0 & -1 \end{bmatrix} A_s^{\mathrm{t1}}(t) \cdot \mathbf{K_c} + \begin{bmatrix} 1 & 0 & 0 \\ 0 & 1 & 0 \\ 0 & 0 & -1 \end{bmatrix} A_s^{\mathrm{t2}}(t) \cdot \mathbf{K_c} \\ &= -K_{tc} b_c [x^{\mathrm{w}}(t) + \mu_c x^{\mathrm{w}}(t-\tau^{\mathrm{t1}})] \begin{Bmatrix} \mu_f \cos\eta \\ 1 \\ \mu_f \sin\eta \end{Bmatrix} - K_{tc} b_c [x^{\mathrm{w}}(t) + \mu_c x^{\mathrm{w}}(t-\tau^{\mathrm{t2}})] \begin{Bmatrix} \mu_f \cos\eta \\ 1 \\ -\mu_f \sin\eta \end{Bmatrix} \end{aligned} \tag{5-11}$$

where F_x [N], F_y [N], and F_z [N] are the cutting force in X-, Y-, and Z-direction, respectively.

The dynamic cutting force acting on the workpiece will excite the workpiece and produce vibration in the X-direction again. Therefore, considering $F_y^{\mathrm{w}} = F_x^{\mathrm{w}}/(\mu_f \cos\eta)$, the workpiece vibration in the X-direction can be described with the workpiece FRF as

$$\begin{aligned} x^{\mathrm{w}}(i\omega_c) &= \Phi_{xx}^{\mathrm{w}}(i\omega_c)F_x^{\mathrm{w}}(i\omega_c) + \Phi_{xy}^{\mathrm{w}}(i\omega_c)F_y^{\mathrm{w}}(i\omega_c) \\ &= \left[\Phi_{xx}^{\mathrm{w}}(i\omega_c) + \frac{\Phi_{xy}^{\mathrm{w}}(i\omega_c)}{\mu_f \cos\eta}\right] F_x^{\mathrm{w}}(i\omega_c) = \Phi_{xx}^{\mathrm{w(eq)}}(i\omega_c)F_x^{\mathrm{w}}(i\omega_c) \end{aligned} \tag{5-12}$$

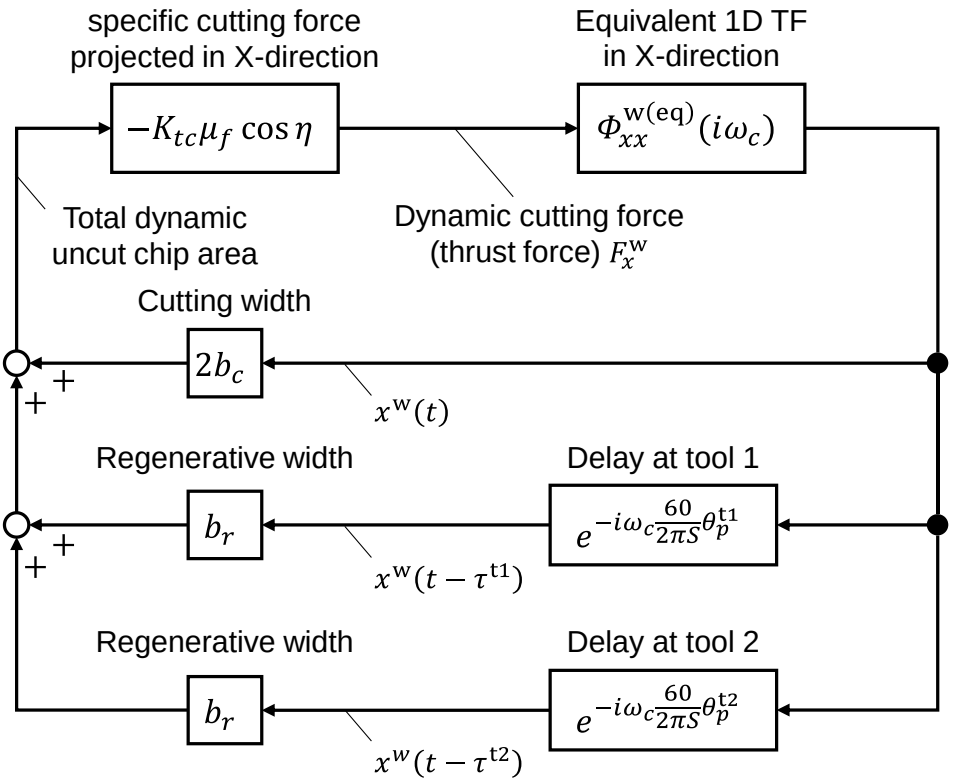

Fig. 5-3 Block diagram of shared-surface parallel turning with flexible workpiece

where $\Phi_{xx}^{\mathrm{w(eq)}}$ [m/N] is the 1D equivalent TF [171,285] of the workpiece for the X-directional cutting force to the X-directional vibration. Because $x^{\mathrm{w}}(t-\tau^{tp})$ is represented as $e^{-i\omega_c\tau^{tp}}x^{\mathrm{w}}(i\omega_c)$ at a certain chatter frequency, ω_c [rad/s], in the frequency domain, by substituting Eqs. (5-10) and (5-12) into Eq. (5-11), the characteristic force equation can be derived as follows:

$$\begin{aligned} F_x^{\mathrm{w}}(i\omega_c) &= -K_{tc}b_c\mu_f\cos\eta\left(2+\mu_c e^{-i\omega_c\tau^{\mathrm{t1}}}+\mu_c e^{-i\omega_c\tau^{\mathrm{t2}}}\right)x^{\mathrm{w}}(i\omega_c) \\ &= -K_{tc}b_c\mu_f\cos\eta\left(2+\mu_c e^{-i\frac{60\omega_c}{2\pi S}\theta_p^{\mathrm{t1}}}+\mu_c e^{-i\frac{60\omega_c}{2\pi S}\theta_p^{\mathrm{t2}}}\right)\Phi_{xx}^{\mathrm{w(eq)}}(i\omega_c)F_x^{\mathrm{w}}(i\omega_c) \end{aligned} \tag{5-13}$$

The block diagram of the shared-surface parallel turning process with a flexible workpiece, represented as Eq. (5-13), is shown in Fig. 5-3. In equal pitch turning (i.e., $\theta_p^{\mathrm{t1}}=\theta_p^{\mathrm{t2}}=\pi$), Eq. (5-13) can be further simplified as follows:

$$F_x^{\mathrm{w}}(i\omega_c) = -2K_{tc}b_c\mu_f\cos\eta\left(1+\mu_c e^{-i\frac{60\omega_c}{2S}}\right)\Phi_{xx}^{\mathrm{w(eq)}}(i\omega_c)F_x^{\mathrm{w}}(i\omega_c) \tag{5-14}$$

Here, in the conventional single parallel turning process, the characteristic force equation is derived as follows:

$$A_s^{\mathrm{t1}}(t) = \mathbf{b_c}\cdot x^{\mathrm{w}}(t)\mathbf{e_x^{t1}} - \mathbf{r_c}\cdot x^{\mathrm{w}}(t-\tau^{\mathrm{t1}})\mathbf{e_x^{t1}} = b_c[x^{\mathrm{w}}(t)-\mu_c x^{\mathrm{w}}(t-\tau^{\mathrm{t1}})] \tag{5-15}$$

$$\boldsymbol{F}_c^{\mathrm{w}}(t)=\begin{bmatrix}-1 & 0 & 0\\ 0 & -1 & 0\\ 0 & 0 & -1\end{bmatrix}A_s^{\mathrm{t1}}(t)\cdot\mathbf{K_c}=-K_{tc}b_c[x^{\mathrm{w}}(t)-\mu_c x^{\mathrm{w}}(t-\tau^{\mathrm{t1}})]\begin{Bmatrix}\mu_f\cos\eta\\ 1\\ \mu_f\sin\eta\end{Bmatrix} \tag{5-16}$$

$$\therefore\ F_x^{\mathrm{w}}(i\omega_c)=-K_{tc}b_c\mu_f\cos\eta\left(1-\mu_c e^{-i\frac{60\omega_c}{S}}\right)\Phi_{xx}^{\mathrm{w(eq)}}(i\omega_c)F_x^{\mathrm{w}}(i\omega_c) \tag{5-17}$$

Comparing Eqs. (5-14) and (5-17), the regenerative effect is found to work with twice the gain in the parallel turning process. In summary, the chatter vibration is more likely to occur in the shared-surface parallel turning process than the conventional single turning; hence, chatter suppression techniques are more important for maximizing the productivity advantage of the simultaneous process. Note that the "static" cutting forces in the XY-direction can be cancelled out in parallel turning; hence, the workpiece deformation caused by the cutting forces (i.e., deterioration of shape accuracy) can be suppressed.

The sign of the delay term is opposite in Eqs. (5-14) and (5-17), which suggests that the range of the chatter phase shift, ε_c [rad], is shifted in the shared-surface parallel turning process. In conventional single turning, represented as Eq. (5-17), the following relationship holds between the chatter phase shift and the phase angle of the compliance TF [25]:

$$\varepsilon_c=3\pi+2\tan^{-1}\left(\frac{\mathrm{Im}\left[\Phi_{xx}^{\mathrm{w(ep)}}(i\omega_c)\right]}{\mathrm{Re}\left[\Phi_{xx}^{\mathrm{w(ep)}}(i\omega_c)\right]}\right),\qquad \omega_c\tau=2\pi k_c+\varepsilon_c \tag{5-18}$$

where k_c [-] is the chatter lobe number. A similar expression has already been shown in Eq. (3-17). Eq. (5-18) means that, when the maximum negative real part of an equivalent 1D TF exists in the third quadrant in the complex plane (i.e., ranging from $-\pi/2$ to $-\pi$), the chatter vibration will occur in the following phase shift range:

$$3\pi+2\times(-\pi)<\varepsilon_c<3\pi+2\times\left(-\frac{\pi}{2}\right)\ \rightarrow\ \pi<\varepsilon_c<2\pi \tag{5-19}$$

Eq. (5-19) is also described intuitively in Fig. 1-6. Here, the delay term in Eq. (5-14) can be rearranged as follows:

$$e^{-i\frac{60\omega_c}{2S}}=-e^{-i\pi}e^{-i\frac{60\omega_c}{2S}}=-e^{-i\omega_c\left(\frac{60}{2S}+\frac{\pi}{\omega_c}\right)}\equiv-e^{-i\omega_c\tau'} \tag{5-20}$$

From the above, it can be deduced that the chatter phase shift against the tooth-passing period in Eq. (5-14) ranges from 0 to π:

$$\omega_{cn}\tau'=\frac{60\omega_c}{2S}+\pi=2\pi k_c+\varepsilon_c'\ \rightarrow\ \frac{60\omega_c}{2S}=2\pi k_c+\varepsilon_c'-\pi=2\pi k_c+\varepsilon_c \tag{5-21}$$
$$(\pi<\varepsilon_c'<2\pi\ \rightarrow\ 0<\varepsilon_c<\pi)$$

This point including the model of Fig. 5-3 was first suggested by this study. The validity of Eq. (5-21) is confirmed in the after-mentioned experimental results.

5.3. Chatter suppression in unequal pitch parallel turning

In this section, the existing unequal pitch turning, including its design methodology, is outlined based on the described parallel turning model. The performance of unequal pitch turning is compared to that of the TSM process in the later section.

Fig. 5-4 shows a schematic of shared-surface unequal pitch turning with a slender workpiece. The regenerative effect can be eliminated by setting an appropriate shifted pitch angle (i.e., $\Delta\theta_p/2$). When this angle is zero, it results in pitch parallel turning. The design method for unequal parallel turning is inspired from VPCs, where the pitch angle is designed such that the regeneration factor (RF) is zero [215]. RF is a quantitative index representing the regenerative effect in processes, and can be defined as

$$RF = \frac{1}{N_c}\sum_{j=1}^{N_c} e^{-i\omega_c \tau_j} = \frac{1}{N_c}\sum_{j=1}^{N_c} e^{-i\varepsilon_{c\,j}} \tag{5-22}$$

where τ_j [s] and $\varepsilon_{c\,j}$ [rad] are the delay and the phase shift left on the machined surface, at tooth j, respectively, and N_c [−] is the number of teeth.

In Eq. (5-13), the regeneration factor in shared-surface parallel turning can be defined similarly as $e^{-i\omega_c \tau^{t1}} + e^{-i\omega_c \tau^{t2}}$ if the regenerative width is the same on both sides. This is because the dynamic cutting area by tool 1 is entirely influenced by the surface pre-machined by tool 2, and vice versa, similar to the two-flute cutter. Consequently, if the difference in the phase shift $\Delta\varepsilon_c$ [rad] between tools 1 and 2 is set as

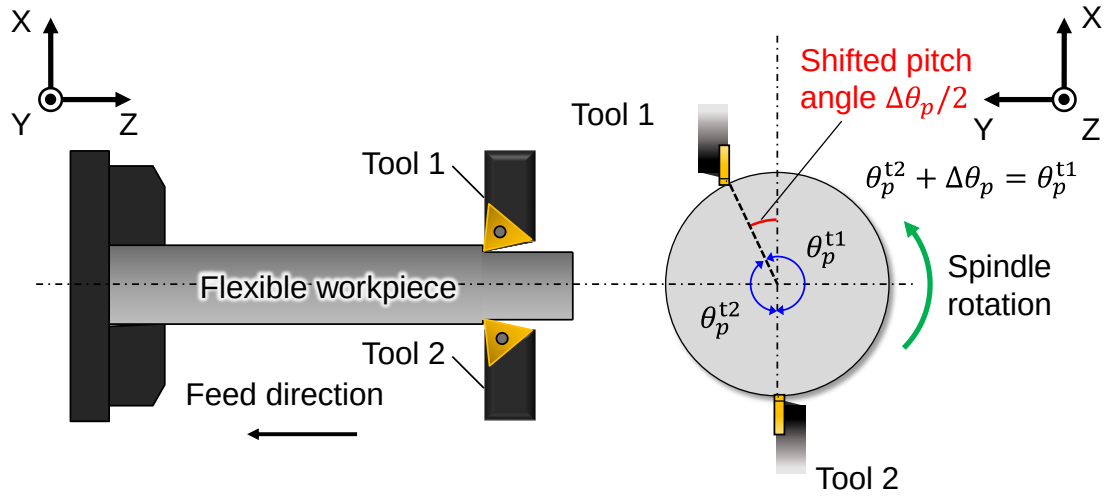

Fig. 5-4 Schematic of unequal pitch turning

$$\Delta\varepsilon_c = \varepsilon_c^{t1} - \varepsilon_c^{t2} = \pi(2m_p + 1), m_p \in \mathbb{Z} \;\rightarrow\; e^{-i\Delta\varepsilon_c} = e^{-i\pi(2m_p+1)} = -1, \tag{5-23}$$

the regenerative effect in the parallel turning process can be canceled out as follows:

$$e^{-i\omega_c\tau^{t1}} + e^{-i\omega_c\tau^{t2}} = e^{-i\varepsilon_c^{t1}} + e^{-i\varepsilon_c^{t2}} = +e^{-i\varepsilon_c^{t2}}e^{-i\Delta\varepsilon_c} + e^{-i\varepsilon_c^{t2}} = 0 \tag{5-24}$$

where m_p is an arbitrary integer number. In an equal pitch cutter, the absolute value of the regenerative factor $|RF|$ is equal to 1 because of $\Delta\varepsilon_c = 0$, i.e., the process is completely affected by the regenerative effect. In contrast, $|RF|$ in the equal pitch parallel turning becomes 2, and the regeneration affects the process with twice the gain, as mentioned above.

Here, the total chatter wavelength left within a certain pitch angle θ_p^{tp} can be expressed as follows:

$$2\pi k_c^{tp} + \varepsilon_c^{tp} = \frac{60\omega_c}{2\pi S}\theta_p^{tp} = \frac{60f_c}{S}\theta_p^{tp} \tag{5-25}$$

From Eqs. (5-23) and (5-25) , the following equation can be derived:

$$2\pi(k_c^{t1} - k_c^{t2}) + 2\pi\left(m_p + \frac{1}{2}\right) = \frac{60f_c}{S}\left(\theta_p^{t1} - \theta_p^{t2}\right) \tag{5-26}$$

The number of chatter marks k_c^{t1} and k_c^{t2} are integers that can be included in m_p. As a result, the pitch angle difference $\Delta\theta_p$ [rad] $\left(= \theta_p^{t1} - \theta_p^{t2}\right)$ between two tools should satisfy the following equation to cancel out the regenerative effect:

$$\Delta\theta_p = 2\pi\left(m_p + \frac{1}{2}\right) \cdot \frac{S}{60f_c} \tag{5-27}$$

which can be calculated from only the chatter frequency at a certain spindle speed. Eq. (5-27) is exactly the same as the design principle for alternating the pitch variation, which is a type of VPC. As the spindle speed and chatter frequency are involved in the optimal pitch design, it is necessary to know the cutting conditions and the vibration frequency in advance before creating VPCs. In the parallel turning process, however, as the pitch angle is adjusted by the turret position control, it can flexibly respond to changes in spindle speed and/or chatter frequency [228].

Note that Eq. (5-27) is valid only under the assumption of a flexible workpiece (i.e., chatter originates from the workpiece) in the parallel turning process. In case of tool-side chatter, the corresponding forces act on different bodies; hence, the phase shift neither has any effect nor is principally responsible for the process stability [226]. In this case, coupled or detuned dynamics of the two tools can substantially influence the process stability, although dynamic coupling is sensitive to the radial angle (i.e., pitch angle) between tools [206,226].

Furthermore, only a small pitch angle variation for unequal pitch turning is valid, because the dynamic forces contributing to chatter acting on the cutting edge are not exactly tangent and radial to the perimeter of the slender workpiece (Fig. 1-15). In summary, the sum of the force vectors cannot cancel out each other in unequal pitch turning, which may have a negative effect on process stability and workpiece eccentricity in shared-surface parallel turning for a flexible workpiece [163]. Additionally, the shifted pitch angle is provided without tool rotation in the radial direction due to mechanical limitation; hence, changes in apparent insert geometries, such as the rake angle and clearance angle, also help or impede process stabilization [163].

In addition, the vibration direction of the workpiece observed from tool 1, which is related to regenerative width, may change according to the shifted pitch angle:

$$\mathbf{e}_{\mathbf{x}}^{\mathrm{t1}} = \begin{bmatrix} \cos(\Delta\theta_p/2) & -\sin(\Delta\theta_p/2) & 0 \\ \sin(\Delta\theta_p/2) & \cos(\Delta\theta_p/2) & 0 \\ 0 & 0 & 1 \end{bmatrix} \begin{Bmatrix} 1 \\ 0 \\ 0 \end{Bmatrix} \rightarrow b_r^{\mathrm{t2}} = \mathbf{r_c} \cdot \mathbf{e}_{\mathbf{x}}^{\mathrm{t1}} \tag{5-28}$$

At a different regenerative width at each side, the regenerative effect cannot be ideally cancelled out in the parallel turning process.

If a relatively small pitch angle variation can be assumed, the above influences will be minimized. Therefore, the difference in the phase shift should be kept close to π (i.e., $m_p = 0$) to prevent a large pitch variation; that is, Eq. (5-27) can be explicitly rewritten as follows:

$$\Delta\theta_p = \frac{\pi S}{60 f_c} \tag{5-29}$$

Since the chatter lobe number is usually large in the turning process, the chatter vibration can be sufficiently suppressed with a small pitch angle difference.

5.4. Chatter suppression in tool swing parallel turning

The TSM process comprises the following three design parameters: the swing frequency, ω_{sw} [rad/s], maximum swing angle, $|\theta_{sw(max)}|$ [rad], and offset angle, θ_0 [rad] (Fig. 5-1). Here, TSM is applied sinusoidally like SSSV, as follows:

$$\theta_{sw}(t) = |\theta_{sw(max)}| \cos(\omega_{sw} t) + \theta_0 \tag{5-30}$$

The spindle speed is constant (i.e., S_n [min^{-1}]) in swing machining. However, the "relative" spindle speed of CWS incurs time variation due to TSM:

$$S_r(t) = S_n - \frac{60}{2\pi}\dot{\theta}_{sw}(t) = S_n\left(1 + \frac{60\omega_{sw}|\theta_{sw(max)}|}{2\pi S_n}\sin(\omega_{sw} t)\right) \tag{5-31}$$

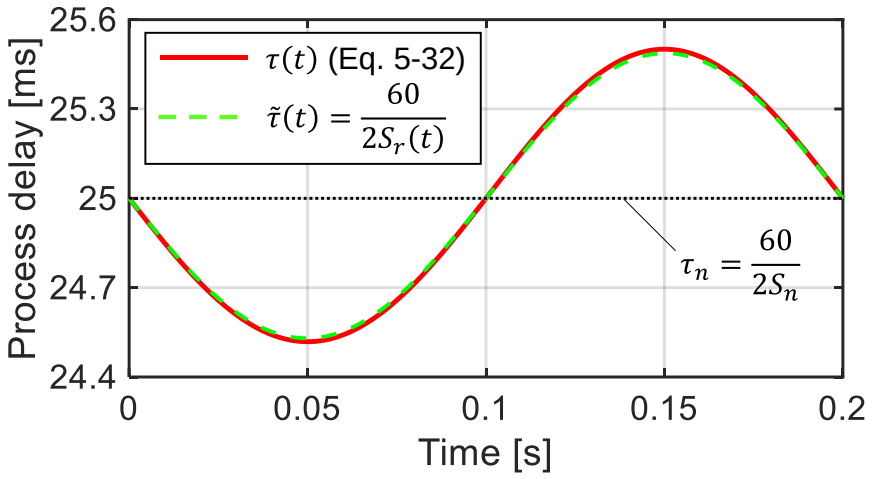

Fig. 5-5 Time-varying delay in shared-surface parallel turning with TSM ($|\theta_{sw(max)}| = 4.5°$, $f_{sw} = 5$ Hz, and $S_n = 1200$ min^{-1})

Consequently, the delay term representing the regenerative effect varies with time similar to the SSSV process. Fig. 5-5 indeed shows the time variation of the delay term. In shared-surface parallel turning, the following equation holds in terms of $\tau(t)$:

$$\int_{t-\tau(t)}^{t} \frac{2\pi S_n}{60} dt = \pi + |\theta_{sw(max)}| \cos(\omega_{sw} t) - |\theta_{sw(max)}| \cos\left(\omega_{sw}(t - \tau(t))\right) \tag{5-32}$$

By solving Eq. (5-32) with the set profile of tool swing motion, the exact time-varying delay can be obtained. For comparison, the non-closed form of approximated delay term, i.e., $\tilde{\tau}(t) = 60/(2S_r(t))$ is also shown in Fig. 5-5. The delay term can be represented with time-varying "relative" spindle speed. Note that the approximated delay term will deviate from the exact value as RVF increases, similar to the SSV discussed in Fig. 4-8 and Fig. 4-9. Similar to Eq. (4-8), RVF can also be defined in parallel turning as follows:

$$R_F = \frac{60 f_{sw}}{N_c S_n} \tag{5-33}$$

To sum up, the chatter vibration is suppressed by disrupting the regenerative effect with time-varying delay even in the TSM process. The sinusoidal TSM and SSSV process can be interpreted in a unified manner; hence, the RVA in the TSM process can be defined based on the similarity between Eq. (4-6) and Eq. (5-31) as follows:

$$R_A = \frac{60 \omega_{sw} |\theta_{sw(max)}|}{2\pi S_n} \tag{5-34}$$

An appropriate selection of the RVA value can be achieved by the criterion proposed in Chapter 4 (i.e., Eq. (4-31)). The chatter will occur in the range $0 < \varepsilon_{cn} < \pi$ in shared-surface parallel turning, as discussed in Section 5.2, although the unstable range is usually

$\pi < \varepsilon_{cn} < 2\pi$ in the conventional turning process. Nonetheless, the local minimum points of the 0th order Bessel function of the first kind are suitable options as the sign of energy balance is also reversed. Therefore, Eq. (4-31) can be directly used even for the parallel turning process. A more detailed discussion about the energy balance is shown in **Appendix E**. Note that only the 1st minimum point of the Bessel function (i.e., $J_0(3.832)$) is considered for a small swing angle, as the tool posture cannot be changed by synchronizing TSM. Consequently, the optimal design criterion for TSM can be derived as follows:

$$\left(\omega_{sw}\left|\theta_{sw(max)}\right|\right)_{opt} = \frac{2\pi S_n}{60} R_{A(opt)} \tag{5-35}$$

where

$$R_{A(opt)} = \frac{-(2\pi k_{cn} + \varepsilon_{cn}) + \sqrt{(2\pi k_{cn} + \varepsilon_{cn})^2 + 4m_f^2}}{2m_f}, m_f = 3.832 \tag{5-36}$$

To design the TSM based on Eq. (5-35), either the maximum swing angle or the frequency must be set first to determine the other parameter. In Chapter 4, the lower limit criteria for SSSV frequency are also proposed (e.g., Eq. (4-38)). However, as the unstable phase shift becomes $0 < \varepsilon_{cn} < \pi$, Eq. (4-38) is slightly modified to secure a robust lower limit criterion:

$$\omega_{sw(min)} = \frac{N_c S_{r(max)}}{60 N_r} \cos^{-1}\left(\frac{2\pi k_{cn} + \varepsilon_{cn}}{R_A\left(2\pi k_c^{S_{max}} + \varepsilon_c^{S_{max}} + \varepsilon_{cn}\right)} - \frac{1}{R_A}\right) \tag{5-37}$$

where

$$k_c^{S_{max}} = \mathrm{Int}\left(\frac{60 f_{cn}}{N_c S_{r(max)}}\right), \varepsilon_c^{S_{max}} = 2\pi \cdot \mathrm{Frac}\left(\frac{60 f_{cn}}{N_c S_{r(max)}}\right) \tag{5-38}$$

Eq. (5-37) indicates that the instantaneous chatter phase is shifted by ε_{cn} within N_r teeth passes from the maximum relative spindle speed to pass through the unstable region around it before the momentary chatter (i.e., beat vibration) grows significantly.

In terms of the upper limit criterion for the swing frequency, Eq. (4-44) representing a 95% upper limit curve could be observed even in the TSM simulation with Eqs. (5-32)–(5-34); hence, Eq. (4-44) can be employed directly, as follows:

$$R_{F(max)} = -0.5243 R_A^4 + 1.2404 R_A^3 - 0.9219 R_A^2 + 0.0147 R_A + 0.1755 \tag{5-39}$$

Since the criteria for the frequency can be calculated once the RVA value is extracted from Eq.(5-36), the TSM frequency, f_{sw} [Hz] ($= \omega_{sw}/(2\pi)$) is determined first to satisfy the following relationship:

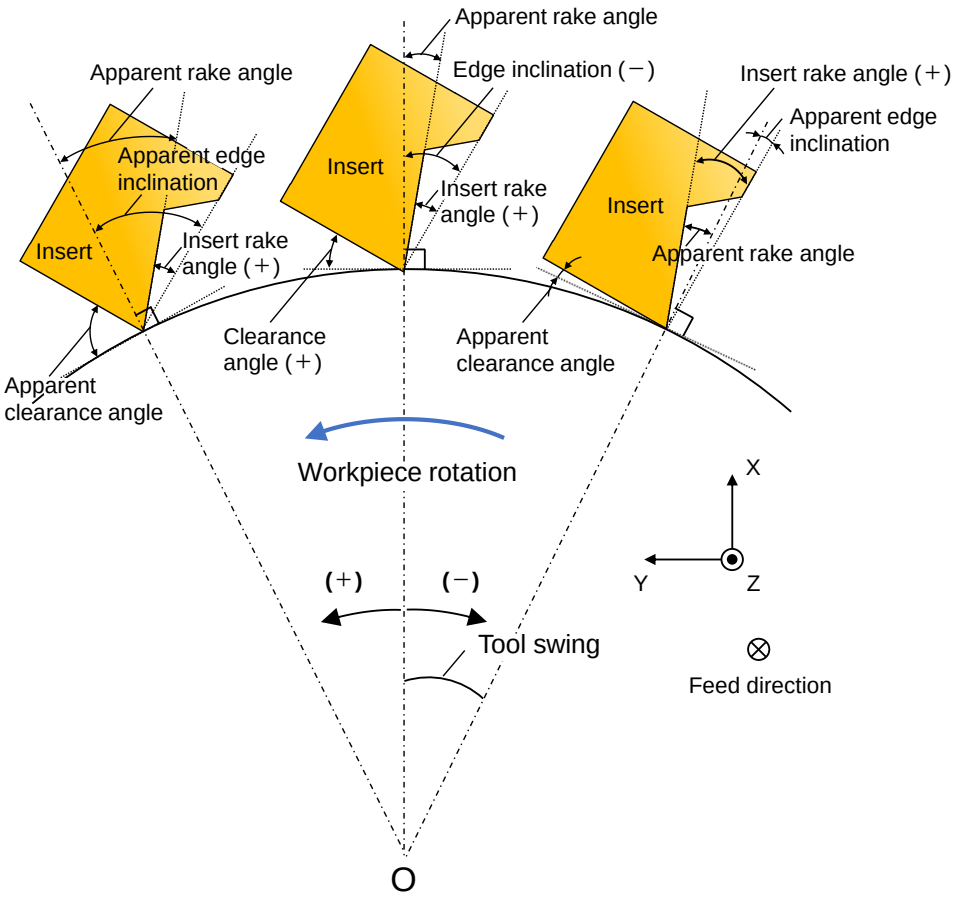

Fig. 5-6 Variation in apparent tool geometries according to TSM

$$R_{F(min)} \leq \frac{60 f_{sw}}{N_c S_n} \leq R_{F(max)} \rightarrow \frac{N_c S_n}{60} R_{F(min)} \leq f_{sw} \leq \frac{N_c S_n}{60} R_{F(max)} \tag{5-40}$$

Then, the optimal combination of maximum swing angle is determined from Eq. (5-35). In addition, the apparent tool geometry changes according to the TSM, as the machine tool is usually incapable of rotating the tool posture to synchronize with the TSM. Consequently, the offset angle must be set to avoid excessive contact of the tools and workpiece at the flank face when the swing angle exceeds the clearance angle (Fig. 5-6).

Finally, the design procedure is summarized in Fig. 5-7. The requirements for conducting the proposed design procedure are only the commanded nominal spindle speed (i.e., cutting conditions) and the chatter frequency at that time. If the relative relationship between the nominal lobe number and phase shift is the same, the normalized design criteria for RVA and RVF are the same even under different cutting conditions. Consequently, the same TSM is recommended. Note that the workpiece diameter must be known when the TSM path is generated, although the TSM design can be achieved regardless of the workpiece diameter. Practically, the current information about the workpiece diameter can be obtained by interlocking with upstream CAM systems.

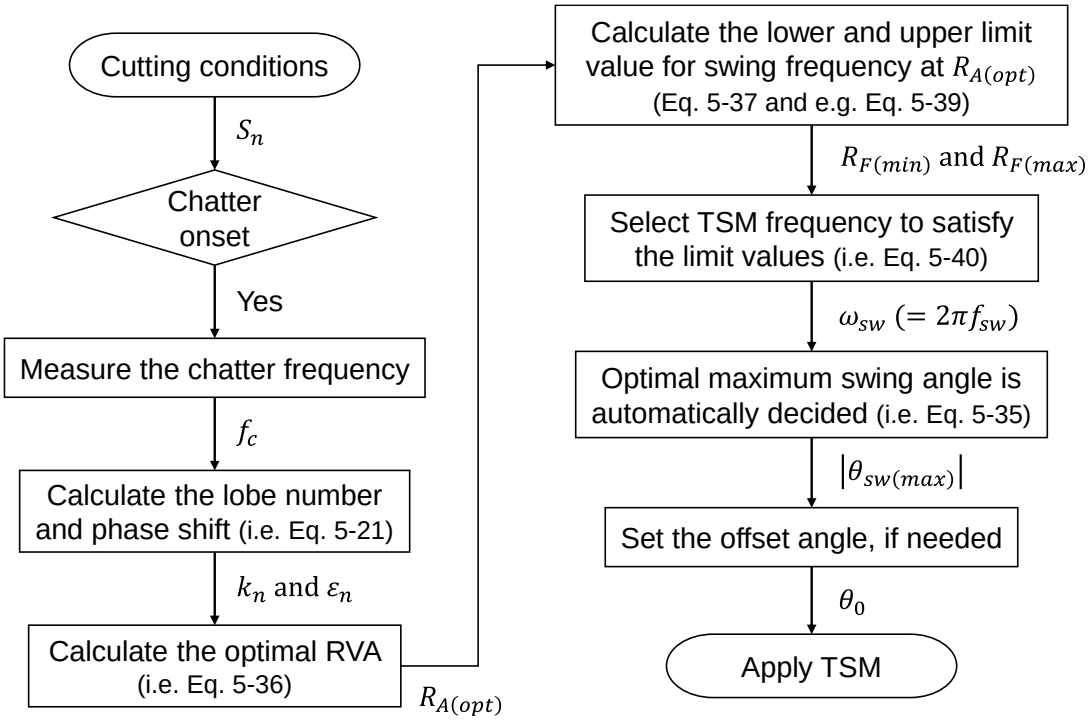

Fig. 5-7 Design procedure for the proposed TSM process based on analogy with SSSV

5.5. Experimental verification

5.5.1. Experimental setup

Fig. 5-8 shows a prototype multi-tasking machine tool (Super NTY3, Nakamura-Tome Precision Industry Co., Ltd., Japan), which was modified to be flexibly controlled by an industrial motion controller (Power PMAC, OMRON Corporation, Japan) (Fig. 5-8(a)). It comprises three turrets and two work spindles. The cutting tools for parallel turning were attached to turrets 1 and 2, each of which can move in three translational directions of XYZ-axes. A slender cylindrical workpiece (Fig. 5-9) was chucked on a left-side work spindle. Then, the workpiece was machined simultaneously from both sides by two tools attached on the left-side upper and lower turrets, respectively (Fig. 5-8(b)). The type of driven system and encoder specification in the left-side upper and lower turrets and work spindle are summarized in Table 5-1. More detailed specifications are summarized in **Appendix A**.

Fig. 5-10 shows the system configuration for parallel turning tests. The control signals were generated by the motion controller (i.e., power PMAC) at a sampling frequency of 9000 Hz (i.e., 111 μs). An optimal linear encoder was attached to only the X1- and Y1-axes of turret 1, where the fully closed control could be applied. The MEDOB (i.e., Eq. (2-22)) was also implemented in X1- and Y1-axes for cutting force estimation. The estimated cutting force was employed to evaluate the chatter vibration (i.e., vibration frequency and severity). It has been confirmed that the MEDOB can monitor the high-frequency chatter state at the

Fig. 5-8 Prototype multi-tasking machine tool: (a) external appearance (b) workspace view

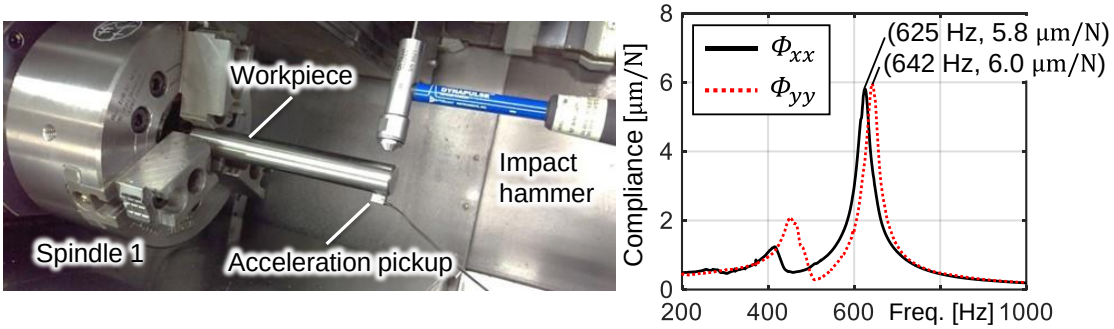

Fig. 5-9 FRFs of flexible workpiece obtained by tap test

cutting point even in a high-damping guideway, such as the sliding type (e.g., Y1-axis), by integrating the high-resolution linear encoder information [273]. Although the estimated cutting force is calculated in each servo cycle of 111 μs inside the machine tool, the data for the analysis can be gathered only every 333 μs (i.e., 3 kHz).

The tool positions are given by the feed drive systems in the translational axes of turret 1 and/or 2. Therefore, the shifted pitch angle and swing angle can be changed flexibly. The swing frequency can be enhanced up to the bandwidth of position control, which is much larger than that of the spindle-drive system, regardless of the workpiece mass unlike the SSV technique. It was experimentally confirmed that the position response in turrets 1 and

Table 5-1 Specification of driven system of left-side upper and lower turret and work spindle

	Unit	X1	Y1	Z1	X2	Y2	Z2	C1
Type of guideway	-	Rolling	Sliding	Rolling	Rolling	Sliding	Rolling	-
Lead length	mm	8	6	12	8	6	12	-
Drive system	-	BS + coupling	BS + coupling	BS + coupling	BS + belt	BS + belt	BS + coupling	Belt
Reduction ratio	-	1	1	1	1	1	1	14/13
Encoder resolution								
Linear encoder	nm	1	1	-	-	-	-	-
Rotary encoder	count/rev	120000	160000	80000	120000	160000	80000	262144
	nm	66.7	37.5	150	66.7	37.5	150	-
Ring encoder	count/rev	-	-	-	-	-	-	19660800

* BS: Ball-screw

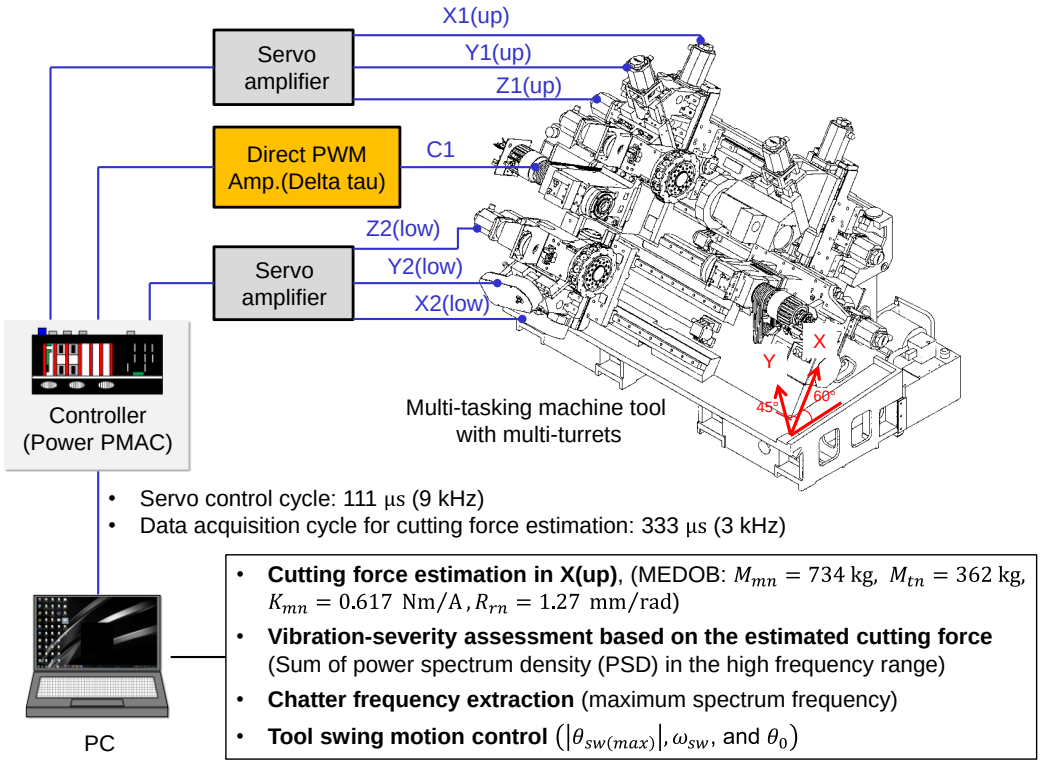

Fig. 5-10 System configuration for parallel turning tests

2 can be controlled within ±1 dB against the command value of up to 20 Hz at least.

Note that the actual machine axes of each turret are not mutually perpendicular (i.e., Y'-axis). The angle between X1- and Y'1-axes is 45°, as is the angle between the X2- and Y'2-axes. Turret1/turret2 actually moves in X1/X2 and Y'1/Y'2 directions to provide the desired displacement in X1Y1/X2Y2 plane (Fig. 5-11). The tool cannot rotate in the radial direction owing to the mechanical limitation; hence, the tool posture did not change according to the shifted pitch angle or swing angle.

The positions of the two tools were identical with the same feed speed, so that the rigid tools would share the same surface of the slender workpiece. The most flexible mode was

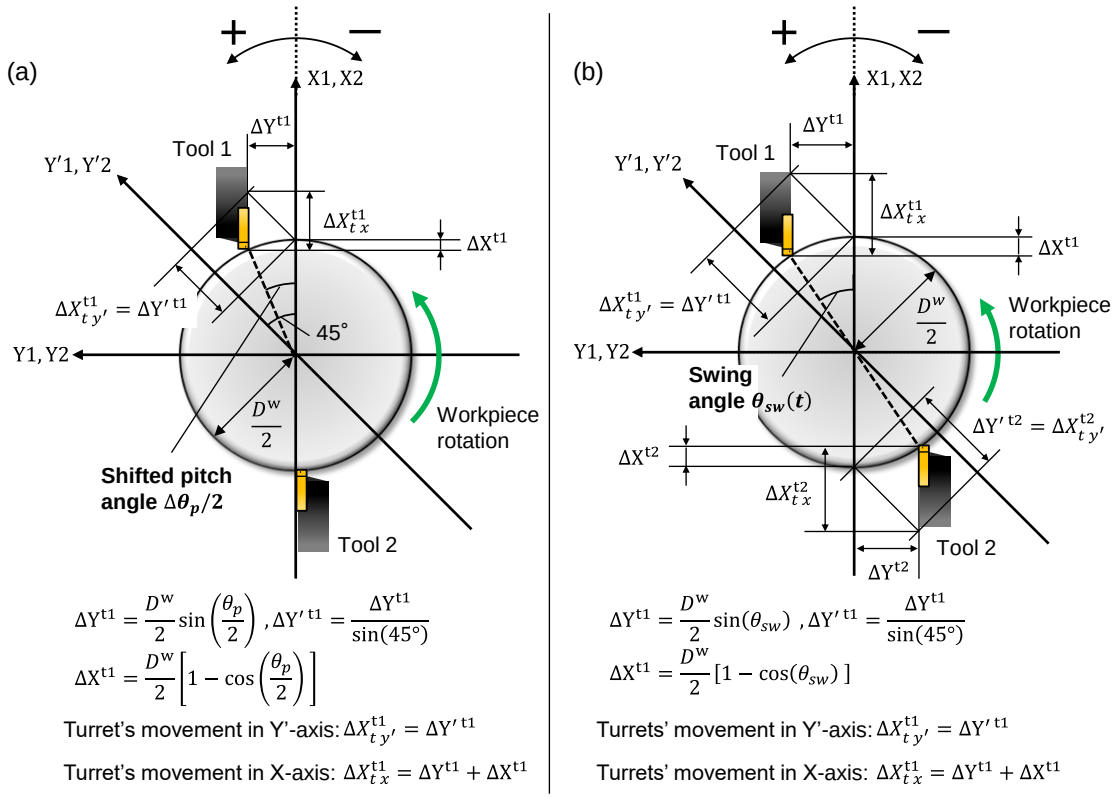

Fig. 5-11 Angle generation by turret's movement: (a) unequal pitch process, (b) TSM process

Table 5-2 Common cutting conditions in parallel milling tests and system conditions for MEDOB

Cutting conditions			
Spindle speed [min^{-1}]	1200	Nose radius, r_ε [mm]	0.79
Depth of cut in each tool, a_p [mm]	0.2	Insert rake angle [°]	15
Feed speed [mm /s] (Feed rate, c [mm/tooth])	3.0 (0.075)	Side/Front clearance angle [°] (made by edge inclination)	6
Material of workpiece	SUS303	Side cutting edge angle [°]	5
Diameter of workpiece, D^w [mm]	25	(Approach angle, κ [°])	(85)
Projection length [mm]	130	Cutting edge inclination [°]	-6
System conditions for MEDOB (X1-axis)			
Equivalent rotating mass, M_{mn} [kg]	734	Conversion factor, R_{rn} [m/rad]	1.27×10^{-3}
Movable mass, M_{tn} [kg]	362	Sampling frequency [Hz]	3000
Torque coefficient, K_{mn} [Nm/A]	0.617	Cutoff frequency of LPF [Hz]	1000

confirmed around 625–645 Hz (Fig. 5-9), which is a local first bending mode of the workpiece. Based on the conclusion in [163], the same depth of cut was set on both sides to obtain high process stability. The common cutting conditions and system conditions for MEDOB are summarized in Table 5-2.

The nominal masses for MEDOB were simply set to the design values. Since only the high-frequency chatter component was focused, the static/quasistatic friction compensation for MEDOB was not performed. In addition, the estimated force on the X1-axis was used

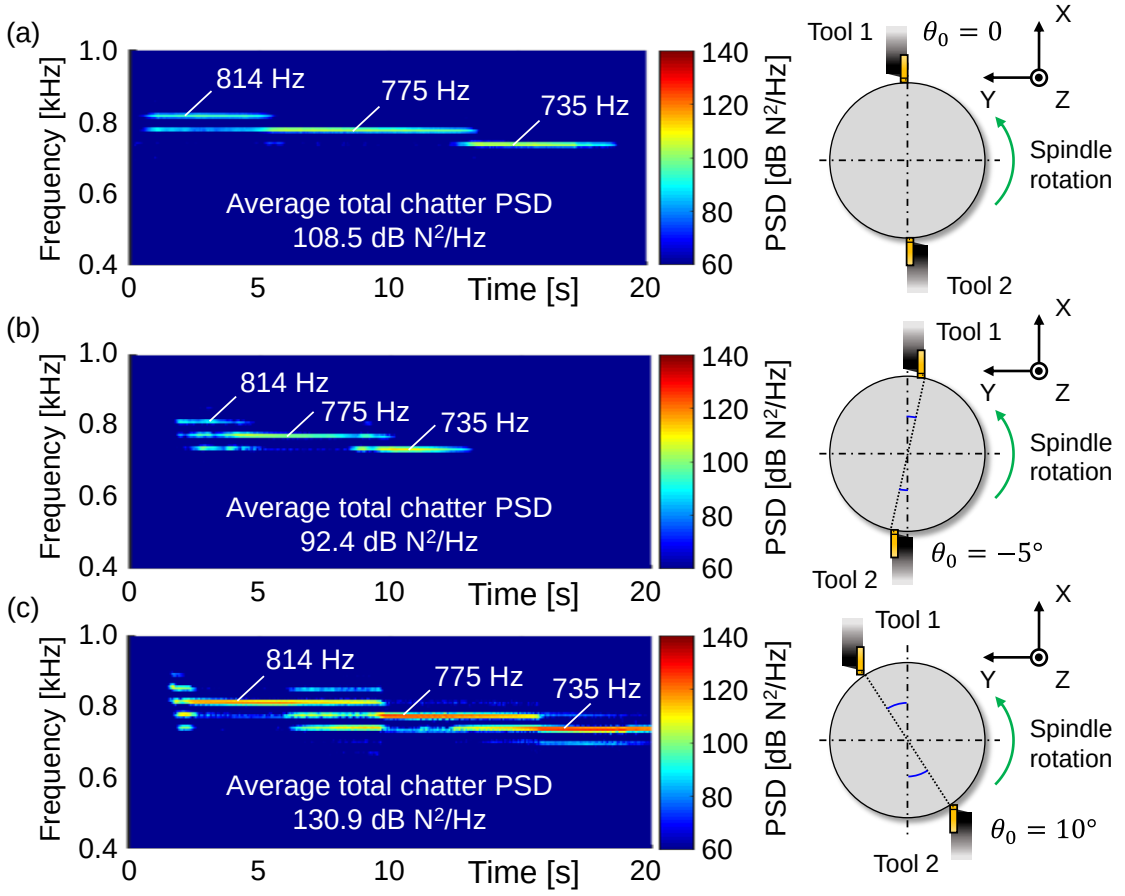

Fig. 5-12 Spectrogram of the cutting force in X1-axis estimated by MEDOB in equal pitch parallel turning with several offset angles: (a) $\theta_0 = 0°$, (b) $\theta_0 = -5°$, (c) $\theta_0 = 10°$

for chatter evaluation because of the low-damping rolling guideway, although the results did not change substantially even if the Y'1-axis was analyzed. When evaluating the chatter severity, HPF with 400 Hz cutoff was additionally applied.

5.5.2. Results of conventional equal pitch parallel turning process

First, the conventional parallel turning tests were conducted. Owing to mechanical limitations, the tool postures cannot be changed, and the apparent tool geometries are varied due to TSM, as shown in Fig. 5-6. This implies that the variation in apparent tool geometries can help or impede the chatter suppression effect caused by TSM. In addition, the equal pitch turning tests at several offset angles are performed to correctly evaluate the chatter suppression effect in unequal pitch and TSM process.

Fig. 5-12 shows the STFT results for the cutting force estimated by MEDOB on the X1-axis. In Fig. 5-12(a), the chatter is clearly observed. The maximum PSD components regarded as dominant chatter frequency change with time from 813 to 734 Hz at an interval of ~40 Hz (i.e., tooth-pass frequency) due to changes in the cutting point along the axial direction of the workpiece. In Fig. 5-12(b), the chatter seems to be slightly mitigated,

especially in the latter half of the process. In contrast, violent chatter vibration is clearly observed in Fig. 5-12(c). This may be because of the variation in apparent tool geometries. The negative offset angle yields a small apparent clearance angle and a large apparent rake angle. In contrast, the large apparent clearance angle and small apparent rake angle result from the positive offset angle.

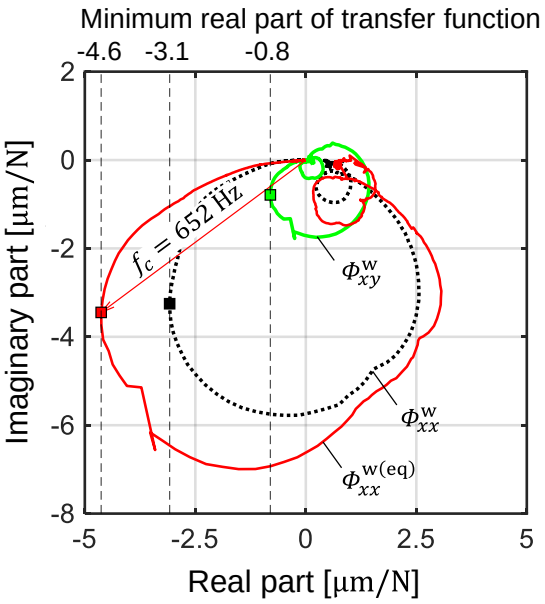

Fig. 5-13 Vector diagram of equivalent 1D TF ($\kappa = 85°, r_\varepsilon = 0.79$ mm, $c = 0.075$ mm, $a_p = 0.2$ mm, and μ_f is assumed as $K_{rc}/K_{tc} = 0.393$ in **Appendix D** → $b_w = 0.56$ mm, $b_r = 0.49$ mm, $h_{cu} = 0.89$ μm, and $\eta = 19.5°$)

Generally, the low clearance angle yields a high process damping effect and increases the chatter stability [160,223,291,292]. In [160,291], the monotonic increases in stability were analytically indicated as the clearance angle decreases. Liu et al. [292] experimentally observed the high process stability by utilizing a low-clearance-angle insert. Similar results were obtained in [223], where cutting-edge chamfers were fabricated to decrease the apparent clearance angle. Additionally, a larger rake angle tends to enhance the process stability [292], whereas a lower rake angle makes chatter more likely because a larger thrust force is induced. In [293], it was found that a smaller rake angle leads to a larger thrust force, and consequently, induces a larger chatter amplitude. For a shared-surface parallel turning process with a flexible workpiece, Azvar and Budak [163] suggested that tool geometries that induce a large thrust force will shrink the stability region of SLD. Nevertheless, the chatter is not completely mitigated in Fig. 5-12(b) despite the small apparent clearance angle and large apparent rake angle, which are expect to have a positive effect on process stability.

Here, the observed chatter frequencies seem to be high, considering that the regenerative chatter often occurs near the negative peak of the real part of the frequency response function [25,245] (e.g., 652 Hz in $\Phi_{xx}^{w(eq)}$; Fig. 5-13). This indicates that the loop/contact stiffness of the total system increases due to the double-side cutting. Although a stationary tap test identifies the resonance in the cantilever-beam state (Fig. 5-9), the real system may behave like a double-supported beam in shared-surface parallel turning and be sensitive to the boundary condition of CWS as well as the cutting position.

Note that the phase shift (i.e., Eq. (5-21)) corresponding to the chatter frequencies of 814, 775, and 735 Hz were 126°, 135°, and 135°, respectively, all of which range within $0 < \varepsilon_c < \pi$. The chatter within $0 < \varepsilon_c < \pi$ can also occur depending on the characteristic of

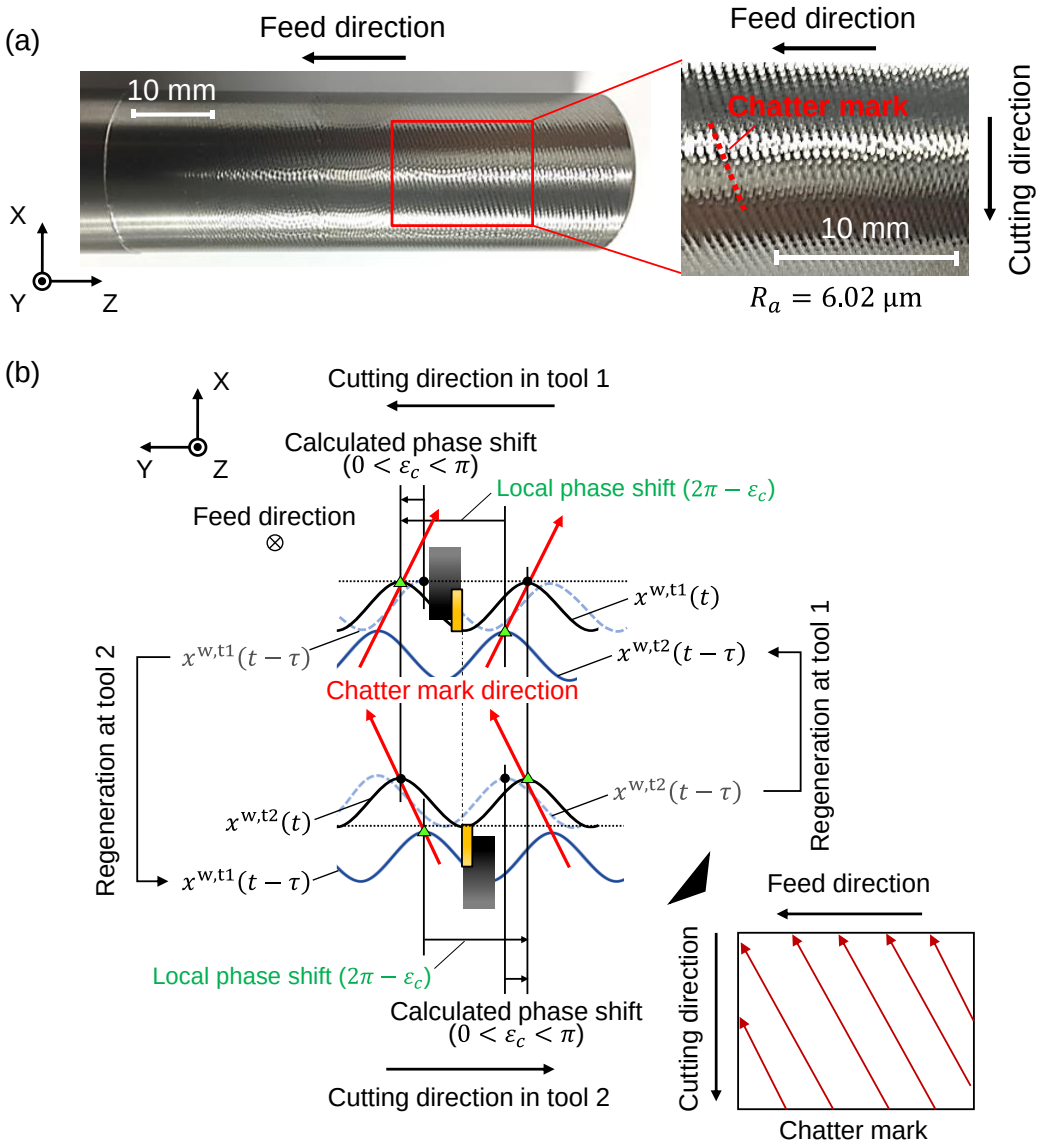

Fig. 5-14 Appearance of machined surface in equal pitch shared-surface parallel turning ($\theta_0 = 0°$): (a) surface picture, (b) consideration of the relationship between phase shift and chatter mark

$\Phi_{xx}^{w(eq)}$ even in the conventional turning process. The maximum negative real part of $\Phi_{xx}^{w(eq)}$ can be sometimes in the second quadrant in the complex plane, ranging from $-\pi$ to $-3\pi/2$. Consequently, the phase shift becomes $0 < \varepsilon_c < \pi$ in Eq. (5-19). This phenomenon can be treated in the framework of the directional factor. Considering Fig. 5-13, however, the results shown in Fig. 5-12 (i.e., $0 < \varepsilon_c < \pi$) are attributable to the inherent process–machine interaction of the parallel turning model, as shown in Fig. 5-3.

Fig. 5-14(a) shows the observed machined surface for $\theta_0 = 0°$. The machined surface has deteriorated due to the chatter vibration. The surface roughness was measured by the stylus profiling (Flex-50A form Tokyo Seimitsu Co., Ltd.), and became a value of 6.02 μm. Here, observing the chatter marks in detail, the tilt of the chatter marks appears to increase to the left. This is a well-known chatter-surface topography corresponding to the phase shift

of $\pi < \varepsilon_c < 2\pi$ and appears to contradict the experimental results of $0 < \varepsilon_c < \pi$.

This phenomenon can probably be understood as shown in Fig. 5-14(b). In parallel turning, the previous vibration at the opposite tool is regenerated; hence, the resultant phase shift between the previous vibration at the opposite side (i.e., dash wave of $x^{\mathrm{w,tp}}(t-\tau)$) and the present vibration (i.e., solid wave of $x^{\mathrm{w,tp}}(t)$) appears to range $0 < \varepsilon_c < \pi$, which is directly calculated by Eq. (5-21). However, the phase shift observed from the local view of the CWS system (i.e., between solid waves of $x^{\mathrm{w,tp}}(t)$ and $x^{\mathrm{w,tp}}(t-\tau)$) may be $2\pi - \varepsilon_c$ in range of $\pi < \varepsilon_c < 2\pi$. Thus, the resultant chatter marks appear to rise to the left. Furthermore, as the actual local phase shift in each CWS ranges from π to 2π, similar to that shown in Fig. 1-6(d), the energy flows into the workpiece from both sides. In summary, the accumulated net inflow energy becomes double, which is consistent with the double regeneration gain.

5.5.3. Results of parallel turning assisted with tool swing motion

Based on the observed dominant vibration frequencies, the TSM design and verification tests were demonstrated.

Table 5-3 shows the results of design criteria for TSM at three dominant chatter frequencies obtained by the proposed design procedure in Fig. 5-7. As $N_r = 1$ may be too restrictive, $N_r = N_c = 2$ (i.e., one spindle rotation) was set for Eq. (5-37).

To discuss the validity of TSM design criteria, a series of tool swing parallel turning were conducted while varying the TSM design parameters. First, the RVA was changed by varying the tool swing angle at a certain swing frequency. The swing frequency was set as 5 Hz (i.e., RVF was set as 12.5%) to fully satisfy the lower-limit criterion at all chatter frequencies. Note that the offset angle was set when the swing angle exceeded the nominal clearance angle of 6° to avoid excessive contact between the flank face and workpiece. An apparent minimum clearance angle of 1° was ensured. The experimental conditions are shown in Table 5-4, and the results are summarized in Fig. 5-15.

Fig. 5-15(a) shows some of the spectrograms (STFT, $N_w = 2^9$ samples) of the estimated cutting force on the X1-aixs. The chatter was clearly suppressed from $|\theta_{sw(max)}| = 4.0°$ ($R_A = 1.75$ %). As the chatter vibration is not completely damped out in Fig. 5-12(b), the chatter suppression effect is yielded by TSM. Fig. 5-15(b) shows the average chatter

Table 5-3 Criteria for TSM designed by the proposed procedure in Fig. 5-7

Chatter frequency, f_{cn} [Hz]	814	775	735
Nominal lobe number, k_{cn}	20	19	18
Nominal phase shift, ε_{cn} [°]	117	135	135
Optimal RVA, $R_{A(opt)}$ [%]	2.99	3.14	3.32
Upper limit frequency, $f_{sw(max)}$ [Hz]	7.01	7.00	7.00
Lower limit frequency, $f_{sw(max)}^{95\%}$ [Hz]	3.80	3.96	3.97

Table 5-4 TSM conditions for experimental tests while varying maximum swing angle at $f_{sw} = 5.0$ Hz

Swing frequency, f_{sw} [Hz]					5.0				
Corresponding RVF, R_F [%]					12.5				
Swing angle, $\lvert\theta_{sw(max)}\rvert$ [°]	2.0	3.0	4.0	4.5	5.0	6.0	7.0	8.0	9.0
Corresponding RVA, R_A [%]	0.87	1.31	1.75	1.96	2.18	2.61	3.05	3.49	3.93
RV factor, $RV = R_A \cdot R_F$ [%]	0.11	0.16	0.22	0.25	0.27	0.33	0.38	0.44	0.49
Offset angle, θ_0 [°]	0.0	0.0	0.0	0.0	0.0	1.0	2.0	3.0	4.0
Movement in Y'-axis, $X_{t\,y'}$ [mm]	0.62	0.93	1.2	1.4	1.5	1.8	2.2	2.5	2.8
Movement in X-axis, $X_{t\,x}$ [mm]	0.44	0.67	0.90	1.0	1.1	1.4	1.6	1.9	2.1

* Turrets' movement in Y'-axis, $X_{t\,y'}$, and X-axis, $X_{t\,x}$, are calculated based on $\lvert\theta_{sw(max)}\rvert$.

reduction rate, compared to the normal equal pitch turning in Fig. 5-12(a). Spectrum peaks corresponding to the swing frequency were observed in the residual signal of the estimated cutting force; hence, Fig. 5-15(c) also summarizes the reduction rates calculated after applying a comb filter with the basic frequency of 5 Hz. Although the optimal RVA was approximately $\lvert\theta_{sw(max)}\rvert = 7.0°$ ($R_A = 3.05$ %), no significant differences could be observed. However, the chatter was robustly suppressed in a large swing angle with the offset angle, where a large thrust force might be induced by a small apparent rake angle. This suggests that the design range of the swing angle can be secured.

The chatter was sufficiently suppressed from $R_A = 1.75$ %, which was relatively small compared to the predicted optimal value. This may be because $R_A = 1.75$ % with $R_F = 12.5\%$ (i.e., $RV = 0.22$ %) was enough to suppress the chatter at a cutting depth of 0.2 mm. Here, considering the region of negative energy balance around $m_f = 3.832$ ranging $2.405 < m_f < 5.502$ (see Fig. 4-4), the RVA is 1.97% at $m_f = 2.405$ (i.e., the first Bessel null point) for $f_c = 775$ Hz. This is close to $\lvert\theta_{sw(max)}\rvert = 4.5°$, where the process starts stabilizing.

Observing the results of SLD studies for the SSV process [151,152,230], it seems that the stability starts to improve after a certain RVA value, and then, the stability limit increases or decreases according to the RVA and RVF. Similarly, in the net inflow energy behavior of SSV governed by $J_0(m_f)$, the energy is extremely high at a very low RVA before $m_f = 2.405$, and then increases and decreases according to m_f; however, its local maximum point is small compared to that in the CSS process. Therefore, the boundary for stability improvement may exist around $m_f = 2.405$, although $R_A = 3.05\%$ is expected to be robust in a larger depth of cut (i.e., stronger chatter condition).

If the RVA design criterion proposed by Al-Regib et al. (Eq. (4-32): $R_{A(opt)} = \varepsilon_{cn}/(2\pi k_{cn})$) is employed, the RVA is also 1.97 % for $f_c = 775$ Hz and the corresponding lower limit value of the swing frequency in Eq. (5-37) becomes 5.1 Hz. This seems reasonable for the experimental results. As discussed in Fig. 4-5 and Fig. 4-6, however, Eq. (4-32) is very sensitive to the phase shift, because it eventually has the same formula as DSST. For example, if the chatter frequency is observed at 771 Hz (deviates by only 4 Hz from 775 Hz), the phase shift becomes 99° and the resultant optimal RVA value is 1.45%, which is close

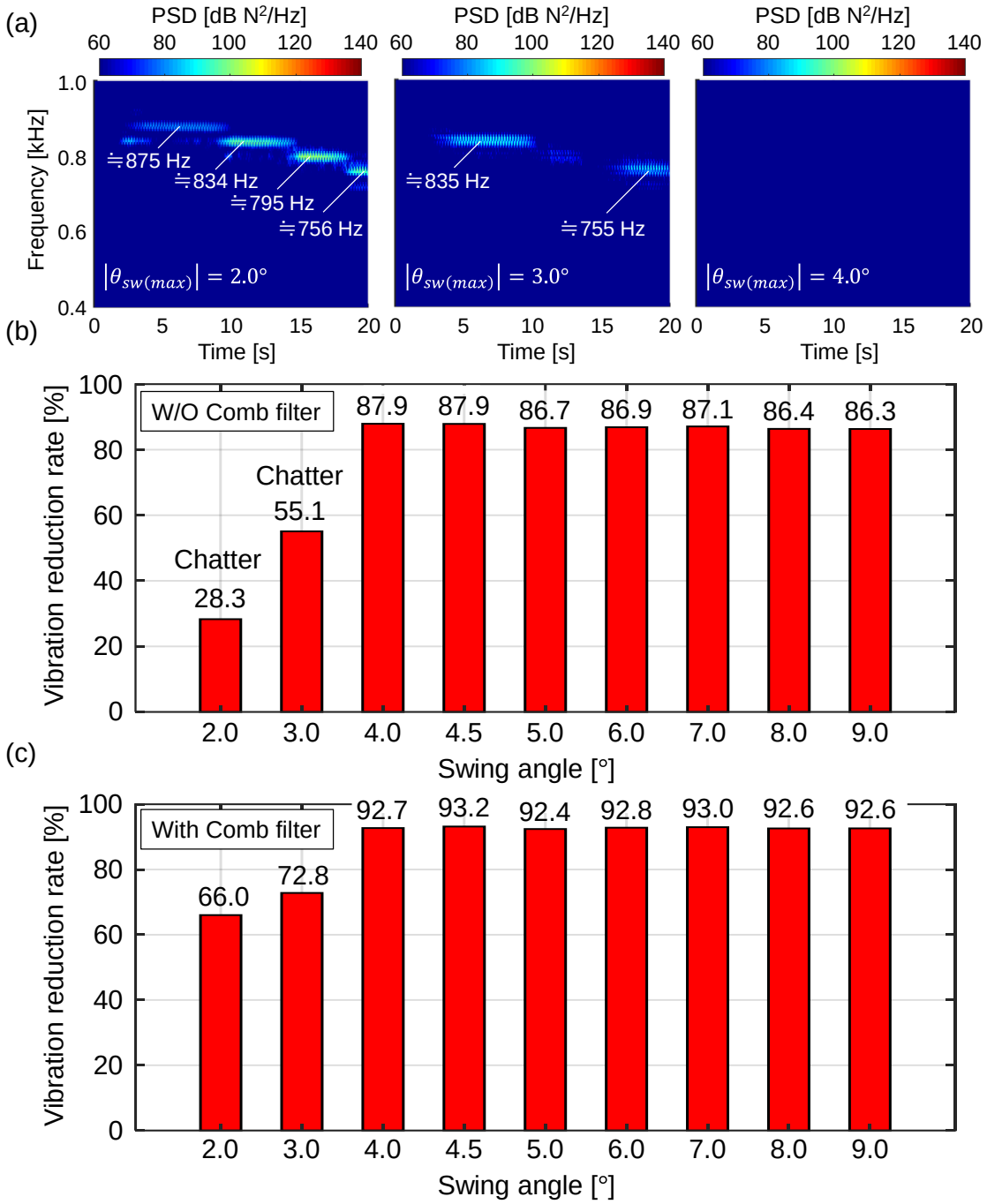

Fig. 5-15 Summary of experiments while varying the maximum swing angle at f_{sw} = 5.0 Hz: (a) part of STFT results of the estimated cutting force on X-axis ($|\theta_{sw(max)}| = 2.0°, 3.0°,$ and $4.0°$), (b) chatter reduction rate, (c) chatter reduction rate eliminating swing-frequency-induced spectrum

to $|\theta_{sw(max)}| = 3.0°$, where chatter occurs. As a phase shift close to 0° is regarded as a stability pocket in DSST, the RVA value is calculated to be small (see Fig. 4-6).

Here, Fig. 5-16 shows the results when no offset angle is applied at $|\theta_{sw(max)}| = 9.0°$. A large vibration occurs because of the excessive impact on the flank face in every swing period, rather than the regenerative effect. In fact, the frequency range of the vibration was obviously different from that shown in Fig. 5-15(a) and closer to the workpiece resonant

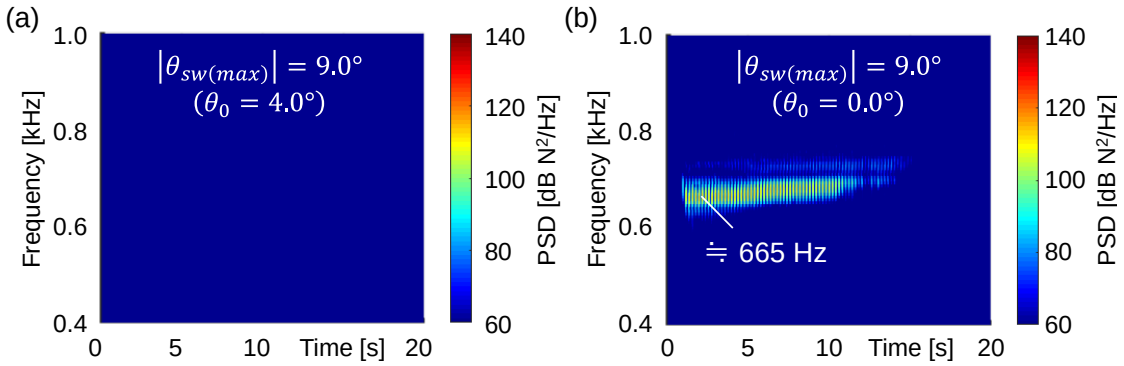

Fig. 5-16 Comparison result with or without angle offset in $|\theta_{sw(max)}| = 9.0°$: (a) $\theta_0 = 4.0°$, (b) $\theta_0 = 0.0°$

Table 5-5 TSM conditions for experimental tests while varying swing frequency at $|\theta_{sw(max)}| = 5.0°$

Swing frequency, f_{sw} [Hz]	2.0	3.0	4.0	4.5	5.0	6.0	7.0	8.0	9.0
Corresponding RVF, R_F [%]	5.00	7.50	10.0	11.3	12.5	15.0	17.5	20.0	22.5
Swing angle, $|\theta_{sw(max)}|$ [°]					5.0				
Corresponding RVA, R_A [%]	0.87	1.31	1.75	1.96	2.18	2.61	3.05	3.49	3.93
RV factor, $RV = R_A \cdot R_F$ [%]	0.043	0.098	0.17	0.22	0.27	0.39	0.53	0.70	0.88
Offset angle, θ_0 [°]					0.0				
Movement in Y'-axis, $X_{t\,y'}$ [mm]					1.5				
Movement in X-axis, $X_{t\,x}$ [mm]					1.1				

* Turrets' movement in Y'-axis, $X_{t\,y'}$, and X-axis, $X_{t\,x}$, are calculated based on $|\theta_{sw(max)}|$

frequency. As the flank face is scraped off around the contact area as the machining progresses, the vibration might have gradually disappeared. The excessive progress of the flank wear was observed after machining. Thus, it is important to set the offset angle properly for a safe process.

In addition, a series of experimental tests were conducted while changing the swing frequency at $|\theta_{sw(max)}| = 5.0°$. The experimental conditions are shown in Table 5-5, and the results are summarized in Fig. 5-17. In short, the results were similar to those shown in Fig. 5-15, although RV factor was different in the same RVA. This suggests that the RVA tends to affect the chatter stability more substantially than the RVF, similar to the SSV process. In addition, the RVA in the TSM process can be controlled by not only the swing angle but also the swing frequency, as predicted in Eq. (5-35), although no significant differences for the optimal RVA value are observed in these experiments.

Fig. 5-18 also shows the results of the experimental tests conducted at different swing frequencies ($f_{sw} = 3.0$ Hz, $f_{sw} = 4.5$ Hz, $f_{sw} = 20$ Hz) under a fixed RVA value (i.e., swing angle is also changed). An RVA of 1.96% was employed to avoid an excessively large swing angle. In Fig. 5-18(a), the estimated cutting force in each test is shown. Note that the frequency components synchronizing the swing frequency were eliminated by the comb filter. In addition, Fig. 5-18(b) shows the swing angle response calculated from the turret position responses in case of $f_{sw} = 3.0$ Hz. The relative spindle speed calculated from the

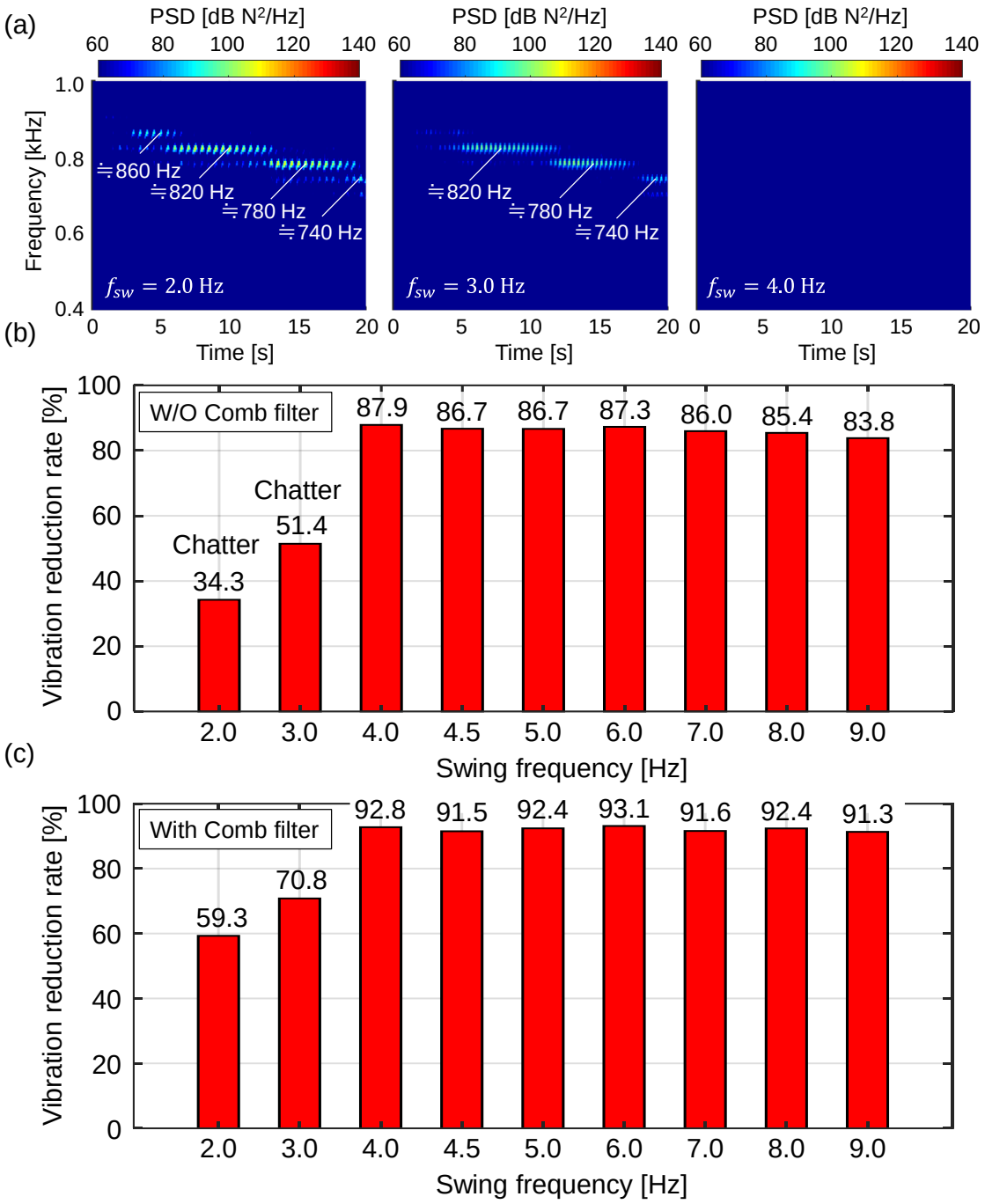

Fig. 5-17 Summary of experiments while varying maximum swing angle at $|\theta_{sw(max)}| = 5.0°$: (a) part of STFT results of the estimated cutting force in X-axis ($f_{sw} = 2.0°, 3.0°,$ and $4.0°$), (b) Chatter reduction rate, (c) Chatter reduction rate with eliminating swing-frequency-induced spectrum

swing angle response is also shown on the right-side vertical axis. At $f_{sw} = 3.0$ Hz, the beat vibration was clearly observed around the maximum relative spindle speed similar to the SSV process, because of the insufficient swing frequency, whereas the chatter was suppressed at $f_{sw} = 4.5$ Hz.

However, the suppression performance was deteriorated again at $f_{sw} = 20$ Hz ($R_F = 50$ %). As already discussed in Fig. 4-9, an excessively high RVF can reduce the efficiency

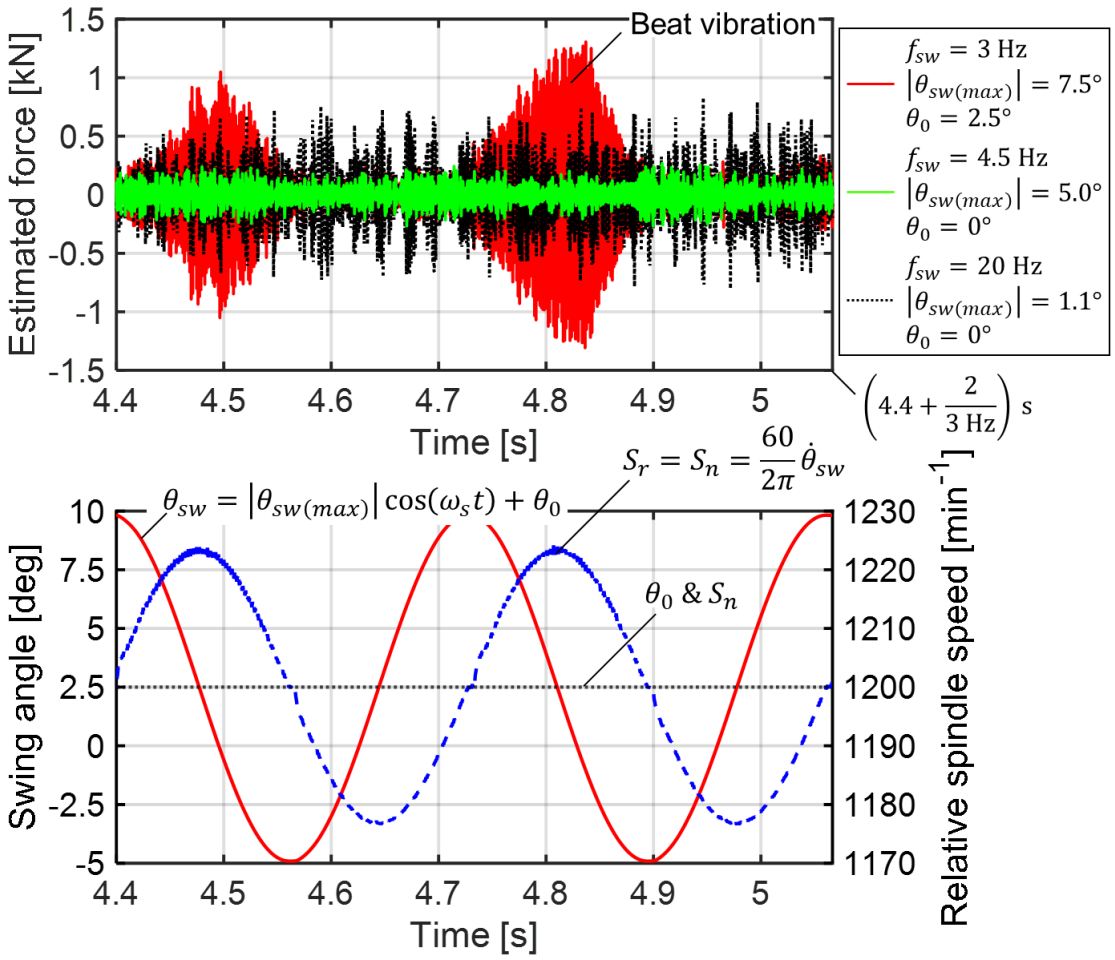

Fig. 5-18 Experimental results obtained with various swing frequency at R_A = 1.96 %: (a) enlarged view of estimated cutting force in each test, (b) time-varying swing angle and relative spindle speed calculated from the actual turret position response at f_{sw} = 3.0 Hz, $|\theta_{sw(max)}|$ = 7.5°, and θ_0 = 2.5°

of the SSV/TSM effect. At R_F = 50 % with R_A = 1.96%, it is confirmed that the amplitude ratio of the delay terms representing the efficiency (i.e., Eq. (4-43)) has already dropped by 64%. In short, the delay variation appears as the case of R_A = 1.25% even at R_A = 1.96%. The chatter reduction rate with the comb filter at f_{sw} = 20 Hz is 68.3%.

From the above results, the swing frequency of ~4 Hz seems to be necessary to sufficiently suppress the chatter vibration. Here, a high variation frequency, such as 4 Hz, is generally severe for the spindle drive system. Several studies have indicated the practical difficulty of a fast SSV due to machine limitations, such as spindle-motor bandwidth and power [240,242]. These limitations are attributed to the machine and workpiece specification [280]. To maintain a low variation frequency, the RVA is alternatively set to be high in the SSV process by allowing a large variation in the cutting speed. However, this large variation will reduce the tool life [294]. The machinability limitation originates from the tool insert and workpiece material. Nevertheless, the tool life will be substantially extended when the process is stabilized from the chatter condition [295].

In contrast, the bandwidth of the position control loop in the feed drive system is usually on the order of 25–30 Hz even for typical CNC machines [2,289]; hence, the constraint of the frequency bandwidth will not be a big problem for realization. As a result, there is a good possibility of using a low RVA (i.e., local minimum point of $J_0(m_f)$ with low modulation index), especially in the turning process. However, the swing angle can become relatively large even at a low RVA value. As the tool posture cannot be changed, a large swing angle and offset angle will accelerate the tool wear because of the large thermo-mechanical load [294] in the positive-swing-angle region (i.e., small apparent rake angle) or a long contact length on the flank face [224] in the negative-swing-angle region (i.e., small apparent clearance angle). To minimize such adverse effect of TSM and maintain little turret movement, it is preferable to set the swing frequency as large as possible for the same RVA to minimize the maximum swing angle. In this case, the upper-frequency-limit curve (e.g., Eq. (5-39)) can be directly used to determine the swing frequency, as the recommended RVA value is determined first. If this is still not enough for the acceptable maximum swing angle, $m_f = 2.405$, which is the boundary for the negative energy balance around $J_0(3.832)$, may be an alternative.

5.5.4. Comparison of chatter stabilizing performance

In this subsection, the chatter stabilizing performance is compared with the unequal pitch turning. The pitch angle difference, θ_p, was designed as 4.6° with Eq. (5-29) based on $f_c = 775$ Hz as a representative value. The corresponding amounts of turret movement on the Y- and X-axes are 0.72 and 0.52 mm, respectively. In tool swing parallel turning, $|\theta_{sw(max)}| = 4.5°, f_{sw} = 5.0$ Hz, and $\theta_0 = 0.0°$ were employed since this combination of TSM parameters has been confirmed to sufficiently suppress the chatter.

Fig. 5-19 shows the results of the moving average (MV) of the estimated cutting force in the high-frequency range (i.e., 400–1000 Hz). Note that for a fair comparison, the comb filter was not applied to signals in the TSM process. The window length for MV is set to 2^9

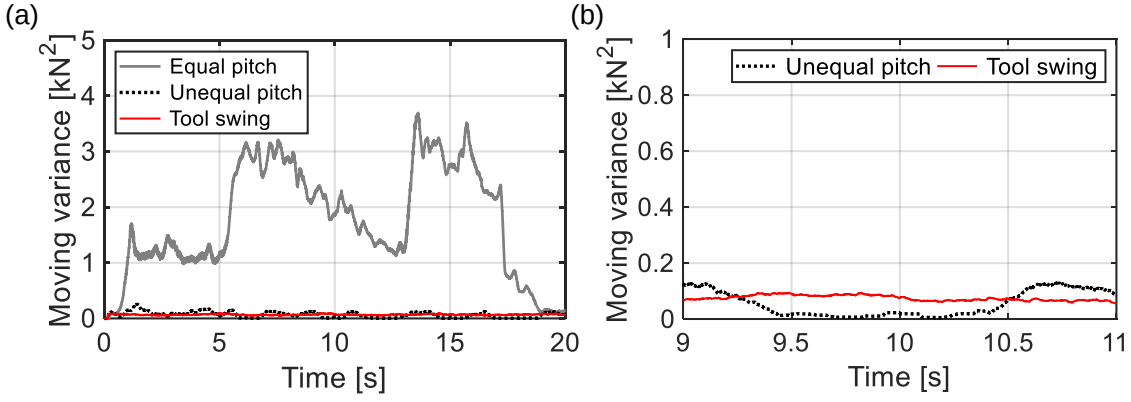

Fig. 5-19 Results of moving variance of the estimated cutting force in each process: (a) Overview, (b) enlarged view

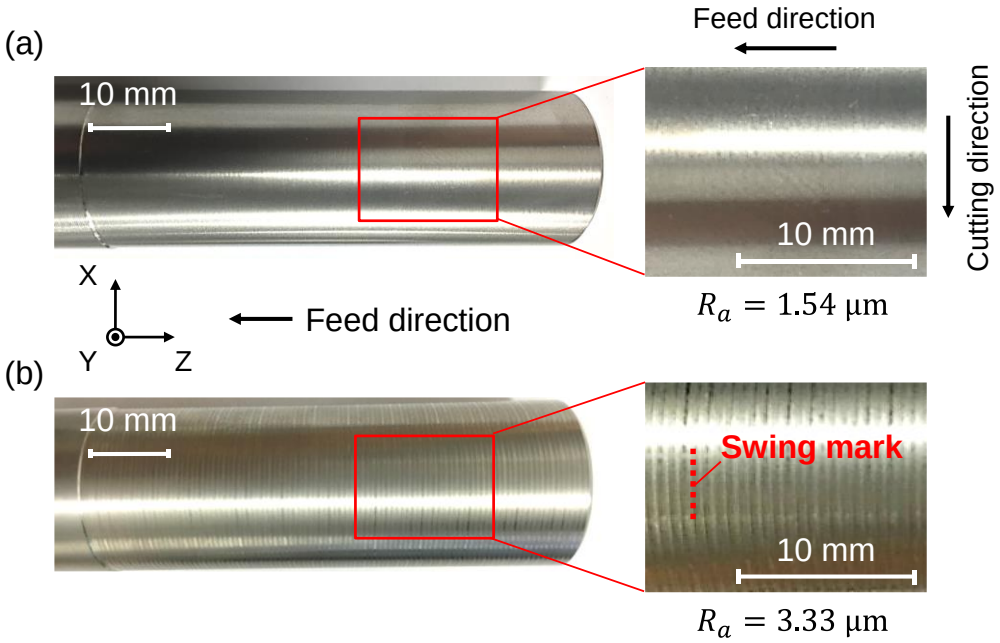

Fig. 5-20 Machine surface: (a) unequal pitch parallel turning, (b) tool swing parallel turning

samples, as in STFT in the previous analysis. Because the variance represents the total power spectrum of the whole frequency band, except the DC component, MV shows a temporal change in the total power spectrum.

In the overview of Fig. 5-19(a), on one hand, a high MV is clearly observed in equal pitch turning because of the large power spectrum of the chatter vibration. On the other hand, a very small MV is confirmed for the unequal pitch and tool swing parallel turning. This means that the chatter vibrations were completely suppressed in these processes. As can be seen in the enlarged view of Fig. 5-19(b), the MV of the chatter vibration in the TSM process is as small as that in the case of unequal pitch turning. In summary, the proposed tool swing parallel turning exhibits the same level of chatter stabilizing performance as the unequal pitch, and thus, is remarkably effective for chatter suppression.

However, TSM-induced marks were observed on the machined surface, as shown in Fig. 5-20. The chatter surface in the conventional equal pitch turning has already been shown in Fig. 5-14(a). In the unequal pitch turning of Fig. 5-20(a), the surface quality is considerably improved because of chatter suppression. In the TSM process of Fig. 5-20(c), periodic vertical marks can be observed, although there are no chatter marks. They are marks generated by the tool swing process, as evidenced by the period of the marks coinciding with the swing period. A possible reason causing the swing marks is a follow-up error of the turret position during TSM.

Fig. 5-21 shows an exemplary result of the position responses in the XY-plane of the upper and lower turrets in air cutting with TSM. The position trajectories deviated from the ideal circumferential locus of the workpiece. This may be because of a tracking error of

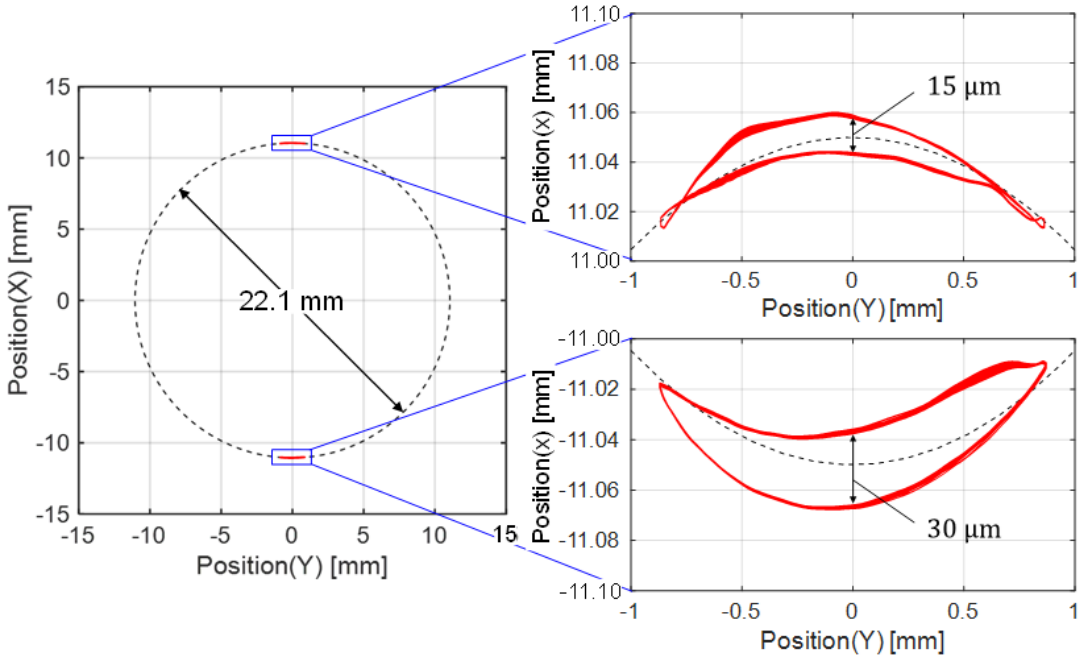

Fig. 5-21 Follow-up error of turret position control during tool swing motion ($D^{w} = 22.1$ mm, $f_{sw} = 5.0$ Hz, $|\theta_{sw(max)}| = 4.5°$, and $\theta_0 = 0.0°$)

the position control system in the prototype machine tool controlled by an open CNC controller. As shown in Fig. 5-11, since the actual machine-tool axes of Y'1 and Y'2 are tilted (i.e., oblique coordinate system), positions in both X- and Y-axes are changed at the same time when a turret moves in Y'-direction; hence, the position responses in XY'-axes of machine tool should be synchronized elaborately to obtain the desired displacement in XY-plane. Therefore, the swing marks would be eliminated by tuning the position responsiveness of machine tool axes through changing controller gains or inputting compensation signals. Although there were swing marks, because they were not unstable, the surface quality was still enhanced compared to the chatter condition. Note that the apparent tool geometries also change continuously according to the TSM. This may also affect the surface quality of the machined workpiece; hence, it is important to design the swing angle as small by increasing the swing frequency from the viewpoint of not only tool wear but also surface integrity. As the lobe number is usually large in the turning process, there is a high possibility that the maximum swing angle is small.

5.5.5. Comparison in workpiece runout

As mentioned in the first section, one of motivations for tool swing parallel turning is the concern that unequal pitch turning would cause the eccentricity of a flexible workpiece due to unbalanced cutting forces (see Fig. 1-15).

Fig. 5-22 shows the experimental setup for measuring the workpiece runout during the machining process. A special jig equipped with three eddy current displacement sensors (EX-305, from KEYENCE) was fixed to the upper-right turret of the machine tool. The

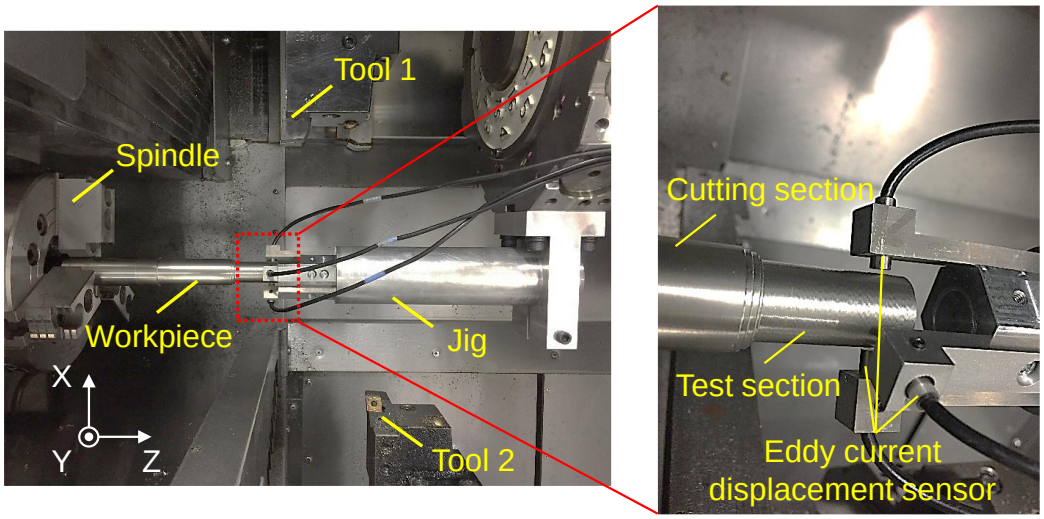

Fig. 5-22 Experimental setup for measuring workpiece runout

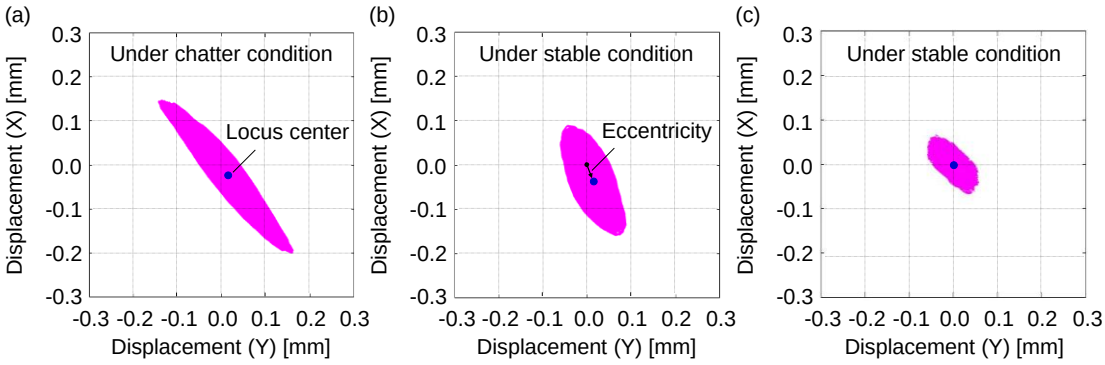

Fig. 5-23 Vibration locus of the workpiece center: (a) equal pitch turning, (b) unequal pitch parallel turning, (c) tool swing parallel turning

vibration displacement at the test section of the workpiece was measured during process. To visualize the vibration trajectory of the workpiece center, the output obtained from the three eddy current displacement sensors was reconstructed to illustrate the displacement in the XY-plane by using the three-point method.

Fig. 5-23 shows the vibration locus of the workpiece center in the XY-plane. In the equal pitch turning shown in Fig. 5-23(a), the trajectory exhibited a large variation because of the chatter onset. Under the stable conditions shown in Fig. 5-23(b) and (c), the variation reduced as the chatter was suppressed. However, in the unequal pitch turning shown in Fig. 5-23(b), the deviation of the locus center from the coordinate center was large despite the stable condition. This would be because the static-force vectors cannot cancel each other out, as illustrated in Fig. 1-15. The eccentricity of the workpiece in unequal pitch turning may increase either when a longer workpiece is machined or when the shifted pitch angle is larger. In contrast, Fig. 5-23(c) shows that tool swing parallel turning could suppress the chatter vibration without eccentricity of the workpiece.

5.6. Summary

This chapter proposed a chatter suppression technique in parallel turning using the TSM provided by a feed drive system of CNC machine tools under the assumption: rigid tools under the same cutting conditions machine the shared surface of the flexible workpiece. In the TSM process, two tools are swung in the circumferential direction of the workpiece sinusoidally while maintaining equal pitch. The contents are summarized as follows:

1. The essential mechanism for chatter suppression in the TSM process could be interpreted in the same way as the SSV process; hence, the systematic monitoring-based (i.e., chatter frequency basis) design procedure for TSM in a sinusoidal manner was also considered based on the analogy with SSSV shown in Chapter 4. As TSM is provided by only the feed drive system, not only the design parameters can be flexibly adjusted similar to SSV but also there may be a good chance to fulfill the frequency threshold for effective chatter suppression due to the bandwidth advantage.

2. In the TSM process, RVA could be controlled by not only the swing angle but also the swing frequency. When the tool posture cannot be changed by synchronizing TSM, the combination with a larger swing frequency and a smaller swing angle should be better considering the side-effects, such as tool wear. Similar to SSV, however, a too high RVF led to a decrease in the efficiency of the TSM effect, and chatter could reoccur. This phenomenon can be avoided by introducing the RVF limit boundary, as also discussed in subsection 4.3.3. Considering the inevitable side-effects, such as promoting motor-energy consumption and tool wear, the TSM process should be applied only when the chatter onset is confirmed. In that case, the system integration with real-time chatter detection/monitoring and automatic in-situ design must be achieved.

3. The chatter stabilization performance in the TSM process was experimentally evaluated and compared with the conventional equal pitch and unequal pitch turning. The TSM process exhibited an effective chatter suppression performance at the same level as the unequal pitch turning. Instead of the chatter marks, however, swing marks were observed on the machined surface. This could be mainly attributed to the follow-up error of the turret position depending on the tool swing motion in the prototype machine tool.

4. The eccentricity of the workpiece during the TSM process was also compared with the conventional equal pitch and unequal pitch turning. In the TSM process, the chatter vibration was suppressed without the eccentricity of the workpiece, whereas the workpiece runout from the coordinate center was observed in unequal pitch turning. This may be because the unbalanced force vectors are not induced in the TSM process.

6. Chatter suppression in parallel milling with adaptive spindle speed control

6.1. Assumptions and concepts

With regard to parallel milling process, Shamoto et al. [244,245] proposed a simple strategy, in which regenerative effect is canceled out comprehensively by a plurality of cutters rotating at different speeds. This technique is called the speed difference method (SDM). In the SDM, the optimal speed difference is also provided only from the chatter frequency based on a design principle similar to that of a VPC tool. Some of the previous studies presented the SDM for a flexible thin plate, machined by a double-sided face milling machine rotating in the "same" direction, where an SDoF vibration in a 1D space perpendicular to the machining surface (i.e., thickness direction of the thin-plate workpiece) can be assumed. Considering only the regenerative effect in the thickness direction, the effectiveness of the SDM was clarified analytically and experimentally (Fig. 1-11).

However, if the workpiece is flexible on a plane perpendicular to the tool axis direction, two tools should be rotated in opposite directions to avoid the torsional deformation of the workpiece by balancing the cutting forces, as shown in Fig. 6-1. Additionally, the dynamic variations of the cutting width will dominantly occur on this plane (i.e., ZY-plane, shown in Fig. 6-1), and not along the thickness direction (i.e., X-direction); hence, the process–machine interaction/dynamics on the ZY-plane must be considered.

In this chapter, the SDM for a flexible workpiece, machined simultaneously by two tools rotating in opposite directions is analyzed by developing a process model that focuses on the regenerative effect on a plane perpendicular to the tool axis direction. Because the effectiveness of the SDM has not been elucidated for this scenario, it is discussed with a series of developed process simulations in time- as well as frequency- domains, in addition to a set of experiments. Furthermore, an automatic chatter suppression system oriented towards an SOMS is also presented in this chapter. By adaptively optimizing the difference in the spindle speeds during the process (i.e., an adaptive SDM), the chatter can be suppressed more robustly. The adaptive SDM system is achieved by real-time tracking of the chatter frequency from the observer-based estimated cutting force.

6.2. Modeling of double-sided parallel milling process

6.2.1. Time-domain modeling

Fig. 6-1 shows a schematic of the double-sided parallel end milling process. A local Cartesian coordinate system XYZ and a rotating coordinate UV are defined for each tool.

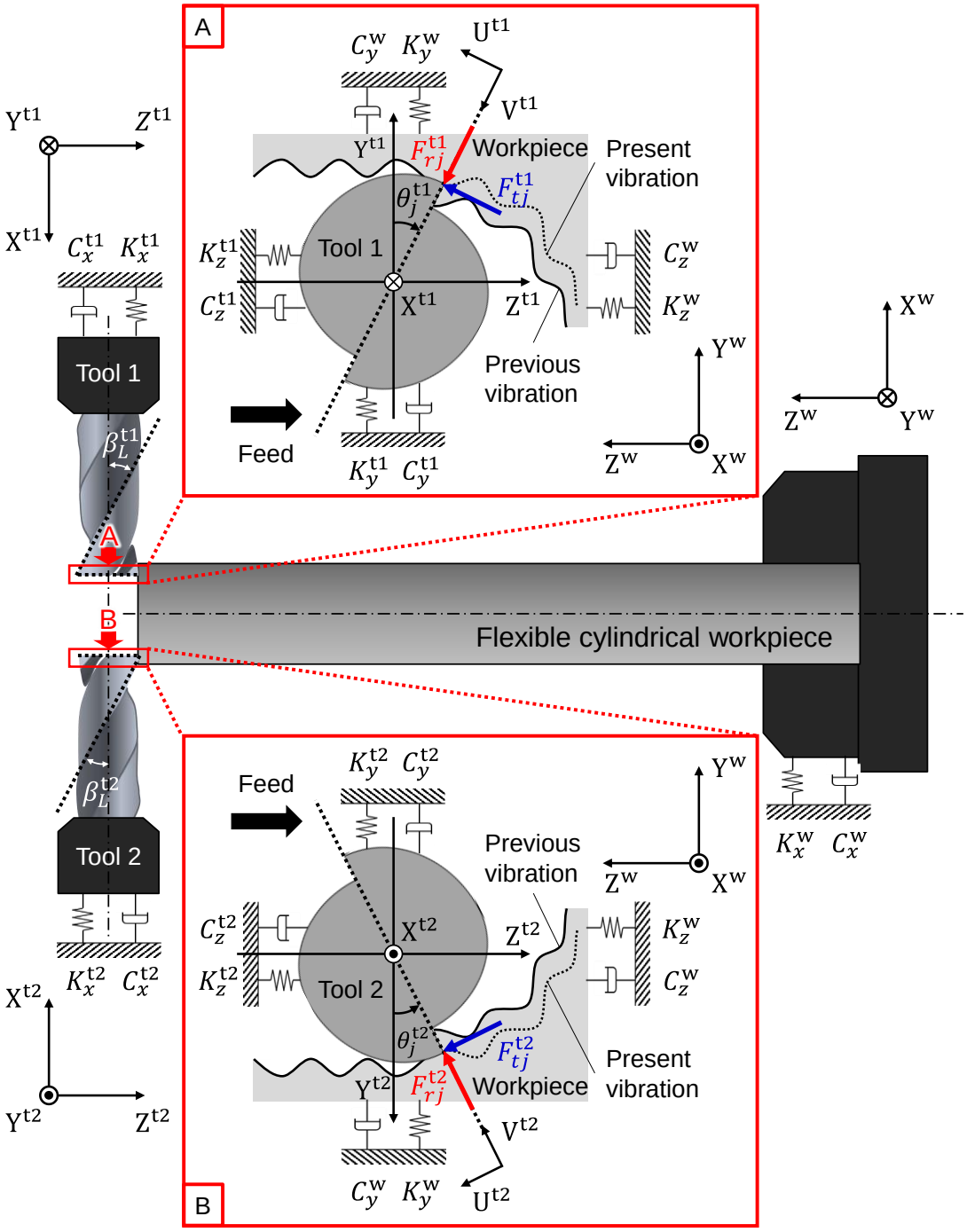

Fig. 6-1 Schematic diagram of a double-sided parallel end milling process

The workpiece coordinate system $X^wY^wZ^w$ coincides with the global coordinate system of the machine (refer to the experimental setup of Fig. 6-10). In the time-domain simulation, the minute cutting forces are calculated in all the discrete minute disk elements, which are the divisions along the tool axial direction, with $\Delta a_p = a_p/N_L$, where a_p [m] is an axial depth of cut, N_L [−] is the number of minute disk elements, and therefore Δa_p [m] is the thickness of each minute disk element.

Subsequently, the total cutting force is derived by summing up all the directional minute cutting forces. Assuming that each minute cutting force acts on a corresponding cutting edge, the minute cutting forces in the tangential, radial, and axial directions at tooth j ($i = 1,2,\dots,N_c^{tp}$) in disk h ($h = 1,2,\dots,N_L^{tp}$) of tool p ($p = 1,2$) can be calculated as follows:

$$\begin{aligned} dF_{t\,j,h}^{tp}(\theta_{j,h}^{tp}) &= \left[K_{tc}^{tp} h_{c\,j,h}^{tp}(\theta_{j,h}^{tp}) + K_{te}^{tp}\right]\delta(\theta_{j,h}^{tp})\Delta a_p^{tp} \\ dF_{r\,j,h}^{tp}(\theta_{j,h}^{tp}) &= \left[K_{rc}^{tp} h_{c\,j,h}^{tp}(\theta_{j,h}^{tp}) + K_{re}^{tp}\right]\delta(\theta_{j,h}^{tp})\Delta a_p^{tp} \\ dF_{a\,j,h}^{tp}(\theta_{j,h}^{tp}) &= \left[K_{ac}^{tp} h_{c\,j,h}^{tp}(\theta_{j,h}^{tp}) + K_{ae}^{tp}\right]\delta(\theta_{j,h}^{tp})\Delta a_p^{tp} \end{aligned} \tag{6-1}$$

where dF_t [N], dF_r [N], and dF_a [N] are the minute tangential, radial, and axial cutting forces, respectively, and K_{tc} [N/m^2], K_{rc} [N/m^2], K_{ac} [N/m^2], K_{te} [N/m], K_{re} [N/m], and K_{ae} [N/m] are the cutting/edge force coefficients in each corresponding direction. Note that $(\ \ )^{tp}$ indicates values for tool p ($p = 1,2$).

Here, $\theta_{j,h}^{tp}$ [rad] are a rotation angle at j-th tooth in h-th disk of p-th tool, and $\delta(\theta_{j,h}^{tp})$ is a unit step function to discriminate whether the corresponding cutting edge is in or out of cut, which are defined as follows:

$$\theta_{j,h}^{tp} = \theta_{1,1}^{tp} + (j-1)\theta_p^{tp} - \frac{2(h-1)\tan\beta_L^{tp}}{D^{tp}}\Delta a_p^{tp} \tag{6-2}$$

$$\delta(\theta_{j,h}^{tp}) = \begin{cases} 1 & \leftarrow \theta_{st}^{tp} \le \theta_{j,h}^{tp} \le \theta_{ex}^{tp} \\ 0 & \leftarrow \theta_{j,h}^{tp} < \theta_{st}^{tp} \text{ or } \theta_{j,h}^{tp} > \theta_{ex}^{tp} \end{cases} \tag{6-3}$$

where θ_p [rad], β_L [rad], and D^{t} [m] are the pitch angle, helix angle, and diameter of tool, respectively. In addition, the start angle, θ_{st} [rad], and the exit angle, θ_{ex} [rad], can be basically calculated based on the relationship between the tool diameter and the radial depth of the cut, a_e [m], as follows:

$$\begin{aligned} \theta_{st}^{tp} &= \begin{cases} 0 & , \quad \text{for an up cut} \\ \cos^{-1}\left(\dfrac{2a_e^{tp} - D^{tp}}{D^{tp}}\right), & \text{for a down cut} \end{cases} \\ \theta_{ex}^{tp} &= \begin{cases} \cos^{-1}\left(\dfrac{D^{tp} - 2a_e}{D^{tp}}\right), & \text{for an up cut} \\ \pi & , \quad \text{for a down cut} \end{cases} \end{aligned} \tag{6-4}$$

Note that when a cylindrical workpiece is machined as shown in Fig. 6-1, the starting and exit angles for the engagement also depend on the height in the tool axis direction; hence the engagement angle must be modified at each of the minute disk elements. However, Eq. (6-4) is simply used in the simulation to capture the process stability tendency.

The uncut chip thicknesses, $h_{c\,j,h}^{t1}(\theta_{j,h}^{t1})$ [m] and $h_{c\,j,h}^{t2}(\theta_{j,h}^{t2})$ [m], can be derived by considering the dynamic vibration of the CWS due to the present and previous vibration

(i.e., $q(t)$ and $q(t-\tau)$; $q: y, z$), as follows:

$$\begin{aligned} h_{c\,j,h}^{\mathrm{t}1}\left(\theta_{j,h}^{\mathrm{t}1}\right) &= c^{\mathrm{t}1}\sin\theta_{j,h}^{\mathrm{t}1} + (\Delta z^{\mathrm{t}1} + \Delta z^{\mathrm{w,t}1})\sin\theta_{j,h}^{\mathrm{t}1} + (\Delta y^{\mathrm{t}1} - \Delta y^{\mathrm{w,t}1})\cos\theta_{j,h}^{\mathrm{t}1} \\ h_{c\,j,h}^{\mathrm{t}2}\left(\theta_{j,h}^{\mathrm{t}2}\right) &= c^{\mathrm{t}2}\sin\theta_{j,h}^{\mathrm{t}2} + (\Delta z^{\mathrm{t}2} + \Delta z^{\mathrm{w,t}2})\sin\theta_{j,h}^{\mathrm{t}2} + (\Delta y^{\mathrm{t}2} + \Delta y^{\mathrm{w,t}2})\cos\theta_{j,h}^{\mathrm{t}2} \end{aligned} \tag{6-5}$$

where

$$\Delta q^{tp} = q^{tp}(t) - q^{tp}(t-\tau^{tp});\ \ \Delta q^{\mathrm{w},tp} = q^{\mathrm{w}}(t) - q^{\mathrm{w}}(t-\tau^{tp});\ \ q: y, z \tag{6-6}$$

Note that $(\ \ )^{\mathrm{w}}$ indicates values for the workpiece.

Next, the minute cutting force in Eq. (6-1) can be converted to a cutting force in the Cartesian tool coordinate system (i.e., dF_x [N], dF_y [N], and dF_z [N]) as follows:

$$\begin{aligned} dF_{x\,j,h}^{tp}\left(\theta_{j,h}^{tp}\right) &= -dF_{a\,j,h}^{tp} \\ dF_{y\,j,h}^{tp}\left(\theta_{j,h}^{tp}\right) &= +dF_{t\,j,h}^{tp}\sin\theta_{j,h}^{tp} - dF_{r\,j,h}^{tp}\cos\theta_{j,h}^{tp} \\ dF_{z\,j,h}^{tp}\left(\theta_{j,h}^{tp}\right) &= -dF_{t\,j,h}^{tp}\cos\theta_{j,h}^{tp} - dF_{r\,j,h}^{tp}\sin\theta_{j,h}^{tp} \end{aligned} \tag{6-7}$$

Subsequently, the total cutting forces of the p-th tool in the XYZ-direction, F_q [N] ($q: x, y, z$) are obtained by summing Eq. (6-7),as follows:

$$F_q^{tp}(\theta^{tp}) = \sum_{j=1}^{N_c^{tp}}\sum_{h=1}^{N_L^{tp}} dF_{q\,j,h}^{tp}\left(\theta_{j,h}^{tp}\right), \qquad q: x, y, z \tag{6-8}$$

Finally, the cutting forces acting on the workpiece are defined based on the directional cutting forces of each tool by considering the law of action and reaction, as follows:

$$\begin{aligned} F_x^{\mathrm{w}}(\theta^{\mathrm{t}1}, \theta^{\mathrm{t}2}) &= +F_x^{\mathrm{t}1}(\theta^{\mathrm{t}1}) - F_x^{\mathrm{t}2}(\theta^{\mathrm{t}2}) \\ F_y^{\mathrm{w}}(\theta^{\mathrm{t}1}, \theta^{\mathrm{t}2}) &= -F_y^{\mathrm{t}1}(\theta^{\mathrm{t}1}) + F_y^{\mathrm{t}2}(\theta^{\mathrm{t}2}) \\ F_z^{\mathrm{w}}(\theta^{\mathrm{t}1}, \theta^{\mathrm{t}2}) &= +F_z^{\mathrm{t}1}(\theta^{\mathrm{t}1}) + F_z^{\mathrm{t}2}(\theta^{\mathrm{t}2}) \end{aligned} \tag{6-9}$$

A time-domain chatter simulation can be performed using a coupled calculation of the cutting force, the vibration responses of the tools and workpiece based on equations above and the modeled machine FRFs. Next, the frequency-domain model is described to discuss the stability behavior.

6.2.2. Frequency-domain modeling

Fig. 6-2 shows a general block diagram representing the dynamic variation of the double-sided parallel end milling process in the ZY-plane, which can be derived from the developed process model represented by Eqs. (6-1)–(6-9). Note that the helix angle is not considered in Fig. 6-2 and the time-varying directional matrix of the milling process force composed of $\alpha_{qq'}$ is the same as that in a conventional milling process [24,25,125], which is represented as follows:

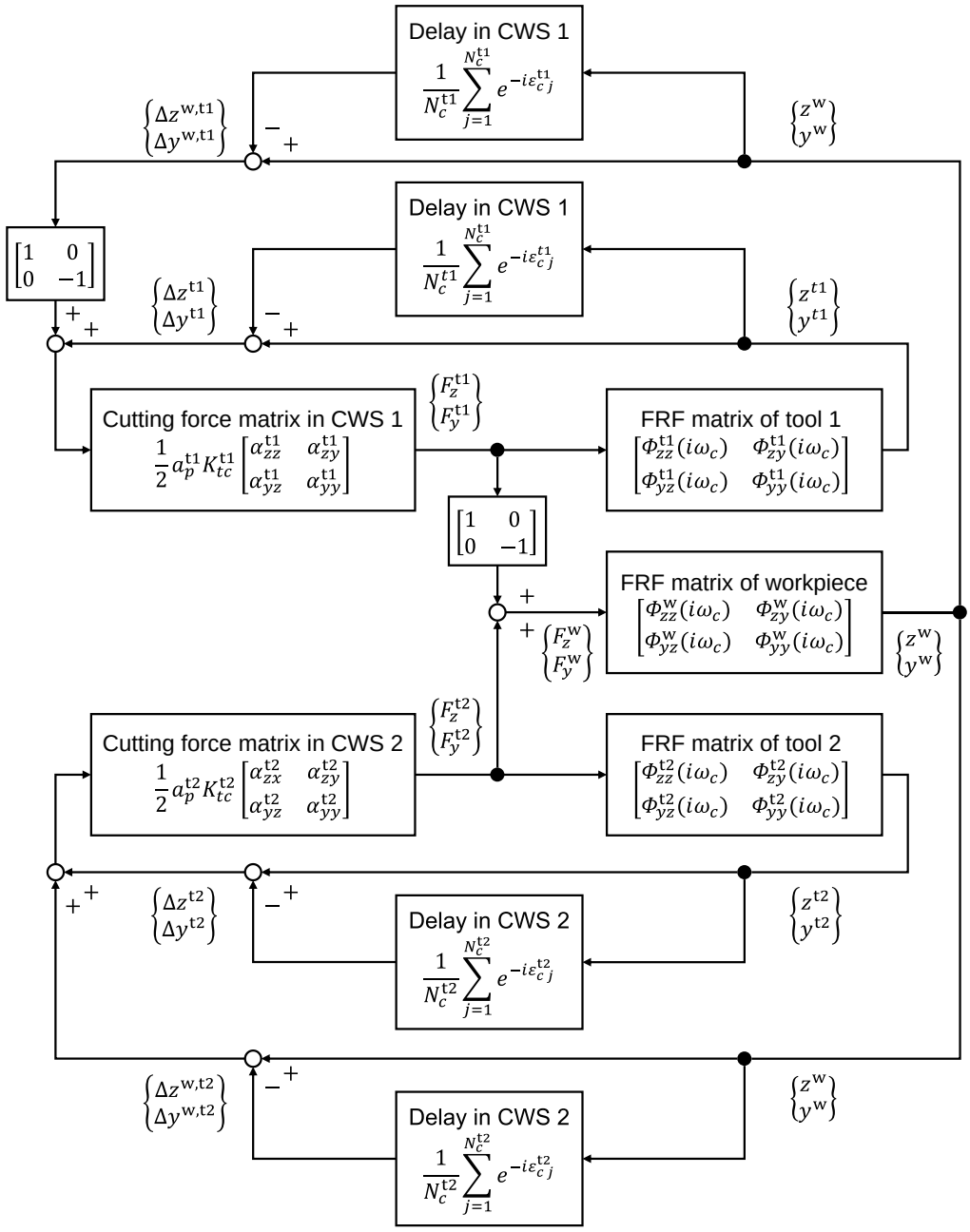

Fig. 6-2 Block diagram of double-sided parallel end milling process

$$\begin{aligned}
\alpha_{zz}^{tp} &= \sum_{j=1}^{N_c^{tp}} -\delta\left(\theta_j^{tp}\right)\left[\sin\left(2\theta_j^{tp}\right) + k_r^{tp}\left(1-\cos\left(2\theta_j^{tp}\right)\right)\right]\\
\alpha_{zy}^{tp} &= \sum_{j=1}^{N_c^{tp}} -\delta\left(\theta_j^{tp}\right)\left[\left(1+\cos\left(2\theta_j^{tp}\right)\right) + k_r^{tp}\sin\left(2\theta_j^{tp}\right)\right]\\
\alpha_{zz}^{tp} &= \sum_{j=1}^{N_c^{tp}} -\delta\left(\theta_j^{tp}\right)\left[\sin\left(2\theta_j^{tp}\right) + k_r^{tp}\left(1-\cos\left(2\theta_j^{tp}\right)\right)\right]\\
\alpha_{zy}^{tp} &= \sum_{j=1}^{N_c^{tp}} -\delta\left(\theta_j^{tp}\right)\left[\left(1+\cos\left(2\theta_j^{tp}\right)\right) + k_r^{tp}\sin\left(2\theta_j^{tp}\right)\right]
\end{aligned} \tag{6-10}$$

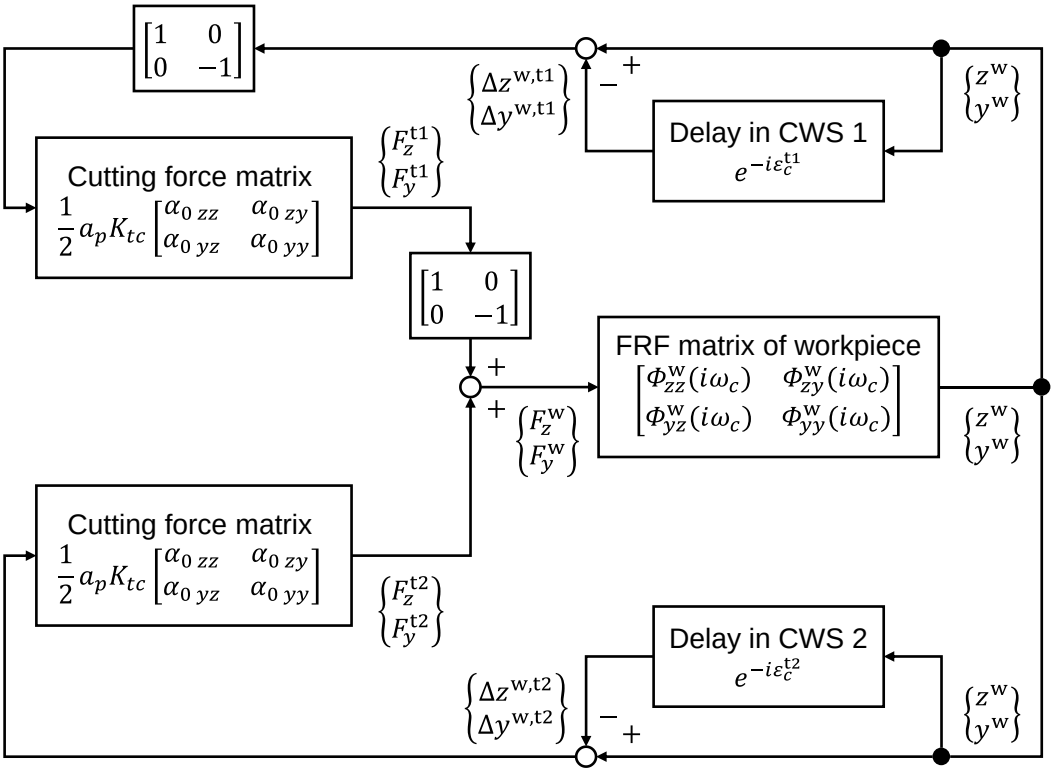

Fig. 6-3 Block diagram with ZOA of double-side parallel milling with a flexible workpiece (identical rigid tool with the same pitch and cutting conditions is assumed, except for the spindle).

where k_r [−] is the ratio of radial to tangential cutting force: $k_r = K_{rc}/K_{tc}$.

Here, the tool vibration can be neglected, as a flexible workpiece is assumed in this dissertation. Additionally, the same cutting conditions on both sides with identical equal-pitch tools are assumed except for the spindle speed (i.e., $a_p^{t1} = a_p^{t2}$, $K_{tc}^{t1} = K_{tc}^{t2}$, $\alpha_{qq'}^{t1} = \alpha_{qq'}^{t2}$, and $\varepsilon_{c\,j}^{t1} = \varepsilon_{c\,j}^{t2}$). Consequently, Fig. 6-2 is simplified to Fig. 6-3, where the zeroth order approximation (ZOA) (i.e., $\alpha_{qq'}$ becomes time-invariant average directional dynamic milling force coefficient of $\alpha_{0\,qq'}$) [125] is also assumed.

Based on Fig. 6-3, the characteristic force equation to analyze the process stability can be obtained as follows:

$$\begin{Bmatrix} F_z^{\mathrm{w}} \\ F_y^{\mathrm{w}} \end{Bmatrix} = \frac{1}{2} a_p K_{tc} \left(\begin{bmatrix} 2\alpha_{0\,zz} & 0 \\ 0 & 2\alpha_{0\,yy} \end{bmatrix} - e^{-i\varepsilon_c^{t1}} \begin{bmatrix} \alpha_{0\,zz} & -\alpha_{0\,zy} \\ -\alpha_{0\,yz} & \alpha_{0\,yy} \end{bmatrix} - e^{-i\varepsilon_c^{t2}} \begin{bmatrix} \alpha_{0\,zz} & \alpha_{0\,zy} \\ \alpha_{0\,yz} & \alpha_{0\,yy} \end{bmatrix} \right) \begin{bmatrix} \Phi_{zz}^{\mathrm{w}} & \Phi_{zy}^{\mathrm{w}} \\ \Phi_{yz}^{\mathrm{w}} & \Phi_{yy}^{\mathrm{w}} \end{bmatrix} \begin{Bmatrix} F_z^{\mathrm{w}} \\ F_y^{\mathrm{w}} \end{Bmatrix} \tag{6-11}$$

where

$$\begin{aligned} \alpha_{0\,zz} &= N_c/(4\pi)\,[\cos(2\theta) - 2k_r\theta + k_r \sin(2\theta)]_{\theta_{st}}^{\theta_{ex}} \\ \alpha_{0\,zy} &= N_c/(4\pi)\,[-\sin(2\theta) - 2\theta + k_r \cos(2\theta)]_{\theta_{st}}^{\theta_{ex}} \\ \alpha_{0\,yz} &= N_c/(4\pi)\,[-\sin(2\theta) + 2\theta + k_r \cos(2\theta)]_{\theta_{st}}^{\theta_{ex}} \\ \alpha_{0\,yy} &= N_c/(4\pi)\,[-\cos(2\theta) - 2k_r\theta - k_r \sin(2\theta)]_{\theta_{st}}^{\theta_{ex}} \end{aligned} \tag{6-12}$$

Here, it is assumed that the phase difference between tools 1 and 2, $\Delta\varepsilon_c$ [rad] can be controlled by changing the spindle speed as follows:

$$\varepsilon_c^{t2} = \varepsilon_c^{t1} + \Delta\varepsilon_c \;\rightarrow\; e^{-i\varepsilon_c^{t2}} = e^{-i\Delta\varepsilon_c} e^{-i\varepsilon_c^{t1}} \tag{6-13}$$

Therefore, Eq. (6-11) can be rearranged as follows:

$$\begin{Bmatrix} F_z^w \\ F_y^w \end{Bmatrix} = \frac{1}{2} a_p K_{tc} \left\{ [\boldsymbol{A_0}] - e^{-i\varepsilon_c^{t1}} [\boldsymbol{DM_\Delta}] \right\} [\boldsymbol{TF}] \begin{Bmatrix} F_z^w \\ F_y^w \end{Bmatrix} \tag{6-14}$$

$$[\boldsymbol{A_0}] = \begin{bmatrix} 2\alpha_{0\,zz} & 0 \\ 0 & 2\alpha_{0\,yy} \end{bmatrix} \tag{6-15}$$

$$[\boldsymbol{DM_\delta}] = \begin{bmatrix} \left(+1 + e^{-i\Delta\varepsilon_c}\right)\alpha_{0\,zz} & \left(-1 + e^{-i\Delta\varepsilon_c}\right)\alpha_{0\,zy} \\ \left(-1 + e^{-i\Delta\varepsilon_c}\right)\alpha_{0\,yz} & \left(+1 + e^{-i\Delta\varepsilon_c}\right)\alpha_{0\,yy} \end{bmatrix} \tag{6-16}$$

$$[\boldsymbol{TF}] = \begin{bmatrix} \Phi_{zz}^w & \Phi_{zy}^w \\ \Phi_{yz}^w & \Phi_{yy}^w \end{bmatrix} \tag{6-17}$$

Note that the helix angle is assumed to be zero when the block diagrams of Fig. 6-2 and Fig. 6-3 are derived. Nonetheless, the helix angle does not affect the average milling force coefficients in the ZOA, represented by Eq. (6-12); hence, the characteristic force equation of Eq. (6-11)/(6-14) (i.e., Fig. 6-3) will be valid for any arbitrary helix angle. The influence of the helix angle on the stability may be analyzed by modifying the characteristic equation to include the helix angle, as developed in [296].

Here, a slender cylindrical workpiece is evidently flexible in the X-direction also, and can cause chatter as observed in [244,245]. However, the regenerative gain (i.e., the dynamic variation of cutting width and resultant dynamic cutting force) should be significantly smaller than that in the Y-direction in the case of Fig. 6-1. Therefore, the vibration on the ZY-plane (especially in the Y- direction) will become the dominant factor for the chatter onset. The corresponding critical axial depth of cut in various conditions can be obtained by applying a numerical search, so that Eq. (6-14) is satisfied.

6.3. Proper control strategy for spindle speed

6.3.1. Principle of SDM for chatter suppression

In [244,245], the SDM for chatter suppression was used in double-sided face milling of flexible thin plates. In the current scenario, the delay term of the total CWS at the workpiece is simply expressed as $e^{-i\varepsilon_c^{t1}} + e^{-i\varepsilon_c^{t2}}$, if the regenerative widths are almost the

same on both the sides. Subsequently, by setting $\Delta\varepsilon_c$ as

$$\Delta\varepsilon_c = \pi(2m_p + 1), \qquad m_p \in \mathbb{Z} \tag{6-18}$$

the total delay term ideally becomes zero (i.e., the regenerative effect generally diminishes) as follows:

$$e^{-i\varepsilon_c^{t1}} + e^{-i\varepsilon_c^{t2}} = e^{-i\varepsilon_c^{t1}} + e^{-i\Delta\varepsilon_c}e^{-i\varepsilon^{t1}} \rightarrow e^{-i\varepsilon_c^{t1}}\left(1 + e^{-i(\pi+2\pi m_p)}\right) = 0 \tag{6-19}$$

As also described in the unequal pitch turning in Section 5.3 of Chapter 5, this is same as the design principle for VPC tools. Here, Eq. (6-19) is equivalent to setting the difference between the tooth-pass periods of the two tools, $\Delta\tau$ [s] as follows:

$$\Delta\tau = \frac{\Delta\varepsilon_c}{\omega_c} = \left(\frac{1}{2} + m_p\right)\frac{1}{f_c} \tag{6-20}$$

where ω_c [rad/s] or f_c [Hz] is a chatter frequency.

This is the principle of the SDM for chatter suppression, which is inspired from VPCs. However, the effectiveness of the SDM has not been elucidated in the process model of Fig. 6-3. Therefore, it is discussed through both frequency-domain stability analysis and time-domain process simulations. In the simulations, the cutting conditions (e.g., tool geometries, feed speed, and radial depth of cut) have been unified to the experimental ones shown later (see Table 6-1). In addition, the experimentally identified values are used for the force coefficients and dynamics of the flexible workpiece, which are summarized in **Appendix D**.

6.3.2. Stability analysis in the frequency-domain

Fig. 6-4 shows the SLDs of conventional and parallel milling processes for the same spindle speed on both the sides. In this study, the asymptotic axial depth in each tool ($a_p^{t1} = a_p^{t2}$) was 0.23 mm for the parallel milling with the same spindle speed, whereas a more= than twice asymptotic borderline of 0.64 mm was predicted for the conventional milling process. This shows that parallel milling affected the regenerative effect more significantly than the conventional process, and the total material removable rate (MRR) could not be increased in this case. However, the process stability could be enhanced by providing an appropriate phase difference, via controlling the spindle speed.

Fig. 6-5 shows the SLDs with some phase shift differences. The stability limit increased when different phase shifts were applied by controlling the spindle speed; the maximum stability was observed at $\Delta\varepsilon = \pi$, which was similar to the observations made in some previous studies [244,245]. This is because the dominant flexibility existed only in the Y-direction, where the process could be regarded as an SDoF system. Based on Eq. (6-16), the diagonal terms of the delay matrix were cancelled out. However, the nondiagonal terms remained, as the average directional force coefficients in the simulated conditions were

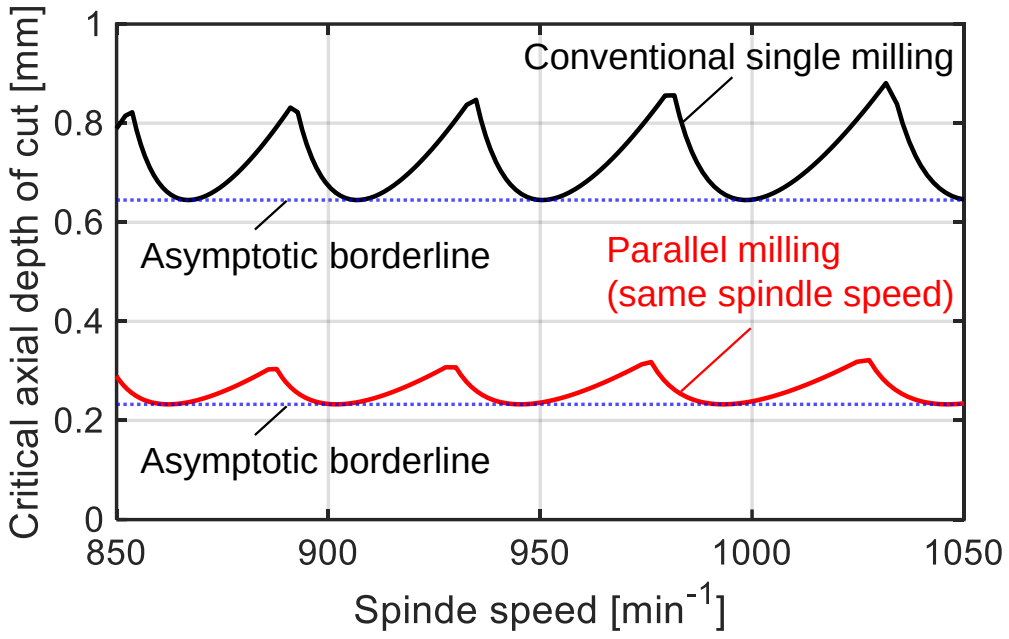

Fig. 6-4 SLDs of conventional and parallel milling with the same spindle speed on both the sides

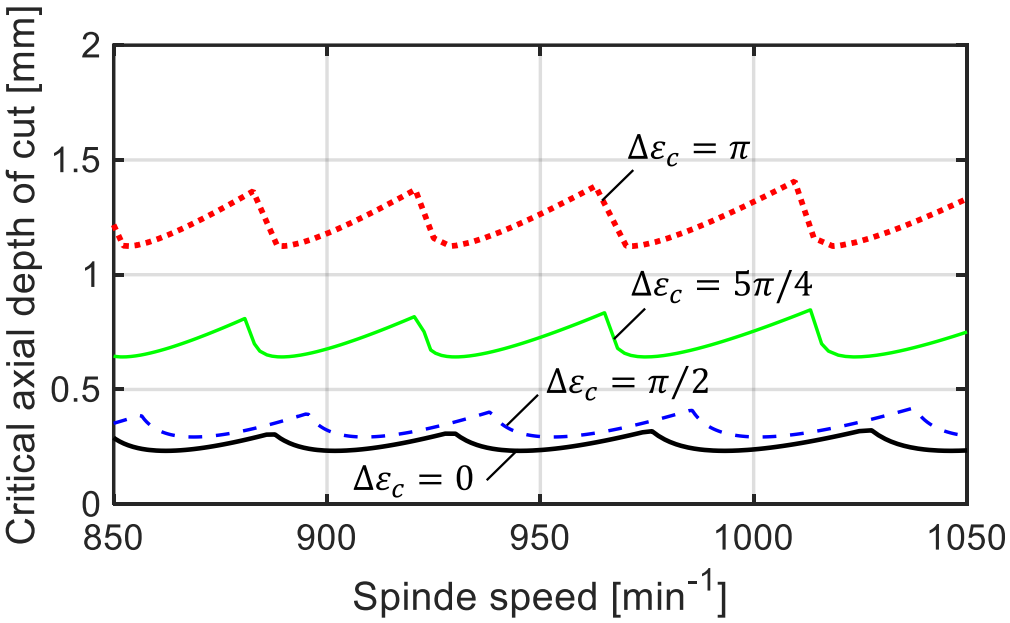

Fig. 6-5 SLDs of conventional and parallel milling with a phase shift difference

$\alpha_{0\,zz} = -0.39$; $\alpha_{0\,zy} = -1.00$; $\alpha_{0\,yz} = 1.00$; and $\alpha_{0\,yy} = -0.39$.

Fig. 6-6 summarizes the behavior of the average directional force coefficients corresponding to various conditions, such as cutting types (i.e., up/down cut), engagement angles (i.e., θ_{st}, θ_{ex}), and component force ratio (i.e., K_{rc}/K_{tc}). As shown in Fig. 6-6, the diagonal terms of the delay matrix, $\alpha_{0\,zz}$ and $\alpha_{0\,yy}$, could not both become zero at the same time in either the up cut or the down cut. Similarly, the nondiagonal terms of the delay matrix, $\alpha_{0\,zy}$ and $\alpha_{0\,yz}$, could not become zero at the same time.

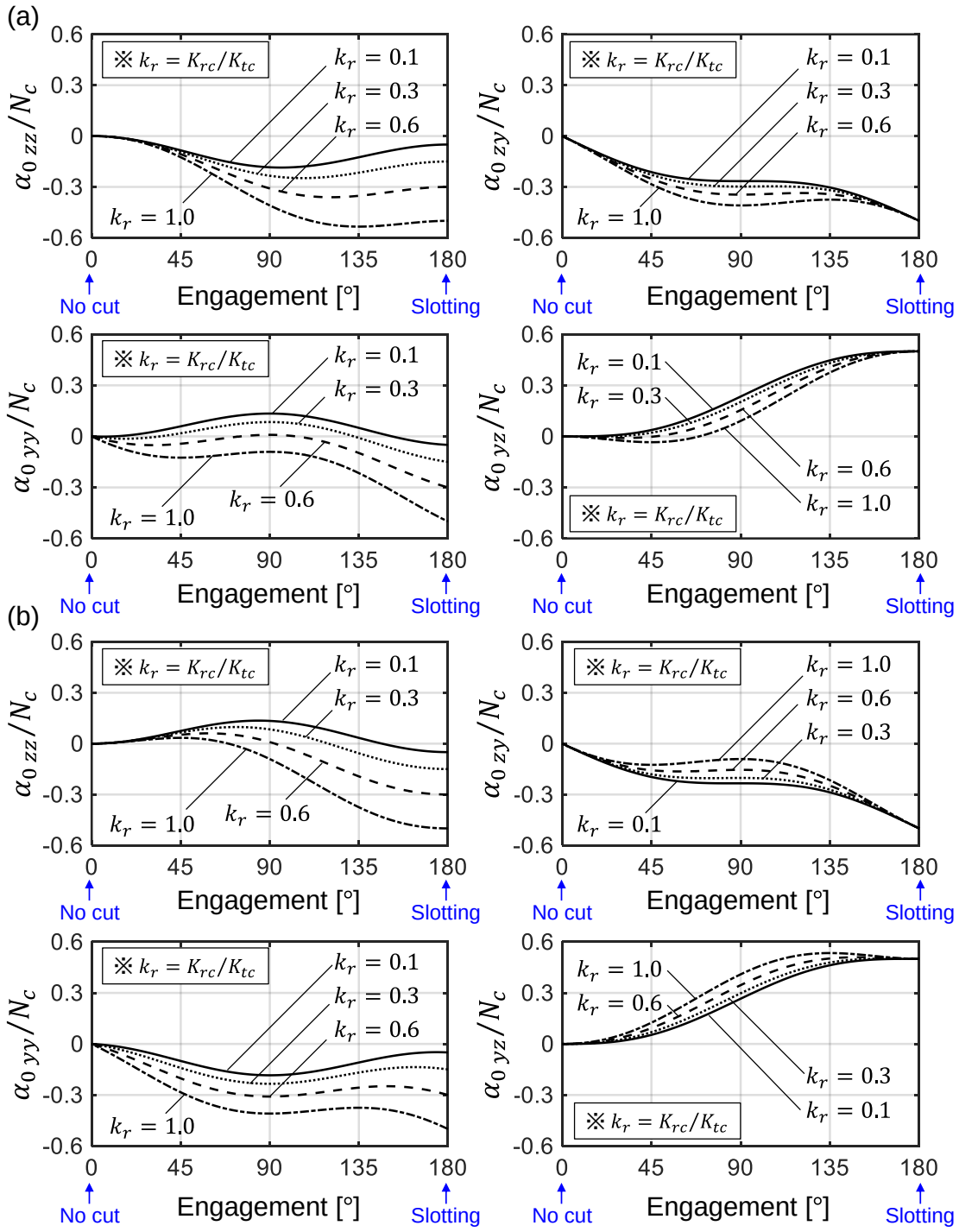

Fig. 6-6 Behavior of average directional force coefficients according to the engagement angle ($\theta_{ex} - \theta_{st}$) under various force component ratios and cutting types: (a) up cut ($\theta_{st} = 0$); (b) down cut ($\theta_{ex} = \pi$)

In summary, it is inherently impossible to completely cancel out the regenerative effect as was the case with the previous studies. When the SDM was applied, the regenerative effect in the Y-direction was transferred to the Z-direction, and vice versa, owing to the nondiagonal regenerative terms. Nevertheless, the stability could be improved, as can be observed from Fig. 6-5, as the workpiece in the Z-direction was very rigid in the model case.

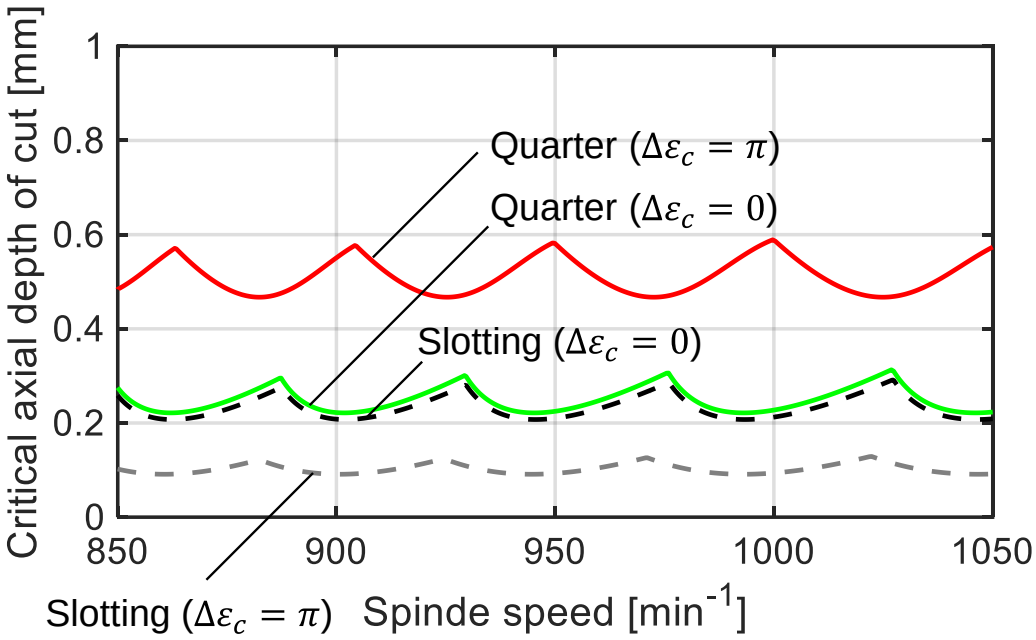

Fig. 6-7 SLDs of parallel milling process having symmetric dynamics ($\Phi_{zz}^{w} = \Phi_{yy}^{w}$)

Generally, the mode coupling chatter is inevitable even in the SDM. Especially, the remaining nondiagonal terms may encourage the mode coupling effect. Fig. 6-7 shows the SLDs in cases involving symmetric dynamics (i.e., $\Phi_{zz}^{w} = \Phi_{yy}^{w}$) under slotting and quarter-immersion down cut. Other process conditions were the same as those depicted in Fig. 6-5.

Fig. 6-7 shows that $\Delta\varepsilon_c = \pi$ decreased the stability in the slotting case. This is because the nondiagonal terms of the delay matrix were amplified by the SDM, thus producing a large mode-coupling effect. A simple method to eliminate the mode-coupling was through regulating the radial depth of the cut [220]. The stability improvement with $\Delta\varepsilon = \pi$ could, in fact, be observed in a quarter immersion down cut, where $\alpha_{0\,zz} = 0.16$, $\alpha_{0\,zy} = -0.38$, $\alpha_{0\,yz} = 0.29$, and $\alpha_{0\,yy} = -0.42$. Thus, the SDM must be carefully applied if the process has a 2-DoF system with a mode coupling effect.

6.3.3. Time-domain process simulation

Fig. 6-8 shows the simulation results of parallel milling using the same spindle speed of 960 min^{-1} (i.e., $\Delta\varepsilon_c = 0$), wherein the axial depth of cut in each tool was 0.4 mm. As shown in Fig. 6-4, this simulation should be unstable. In the time-domain simulation, the vibration responses were calculated by solving the modeled differential equation at each sampling period of 100 μs (i.e., 10 kHz) using the fourth order Runge–Kutta method. Nonlinearities [283], such as the jumping effect of the CWS were considered (i.e., the cutting forces became zero, when the negative uncut chip thickness was calculated), whereas the multiple regenerative effect [284] was not considered. Additionally, the forced vibration components

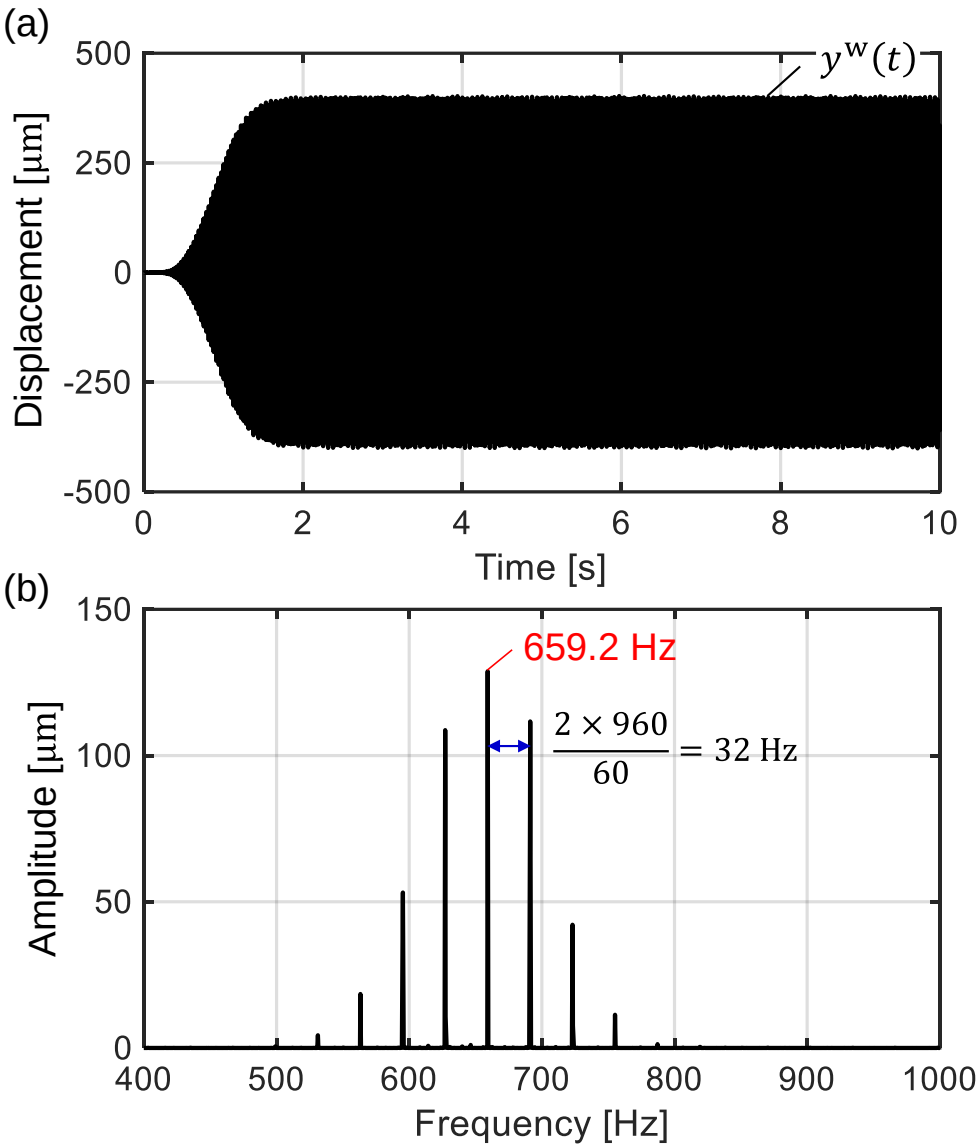

Fig. 6-8 Time-domain simulation of parallel milling process with the same spindle speed ($S^{t1} = S^{t2} = 960$ min^{-1} and $a_p = 0.4$ mm): (a) time waveform; (b) its FFT

yielded by the tooth-pass and its harmonic cutting forces were eliminated by using a comb filter [53]; thus, only the chatter components are displayed.

In Fig. 6-8, chatter vibration is clearly observed, as predicted from Fig. 6-4. Note that the ATO (i.e., the offset angle of spindle rotation between the two tools) was set to zero. In this case, the chatter would not ideally occur because the cutting force in the Y-direction was completely canceled out at both the sides. However, the cross FRFs began to destabilize the process because the cutting force in the Z-direction could not be canceled out simultaneously. As soon as a slight vibration occurred in the Y-direction, the process would be significantly affected by the regenerative effect. Here, it is noteworthy that multiple vibration frequencies were excited even in the slotting test, with one dominant mode considered. These frequencies were in the neighborhood of the most dominant resonant

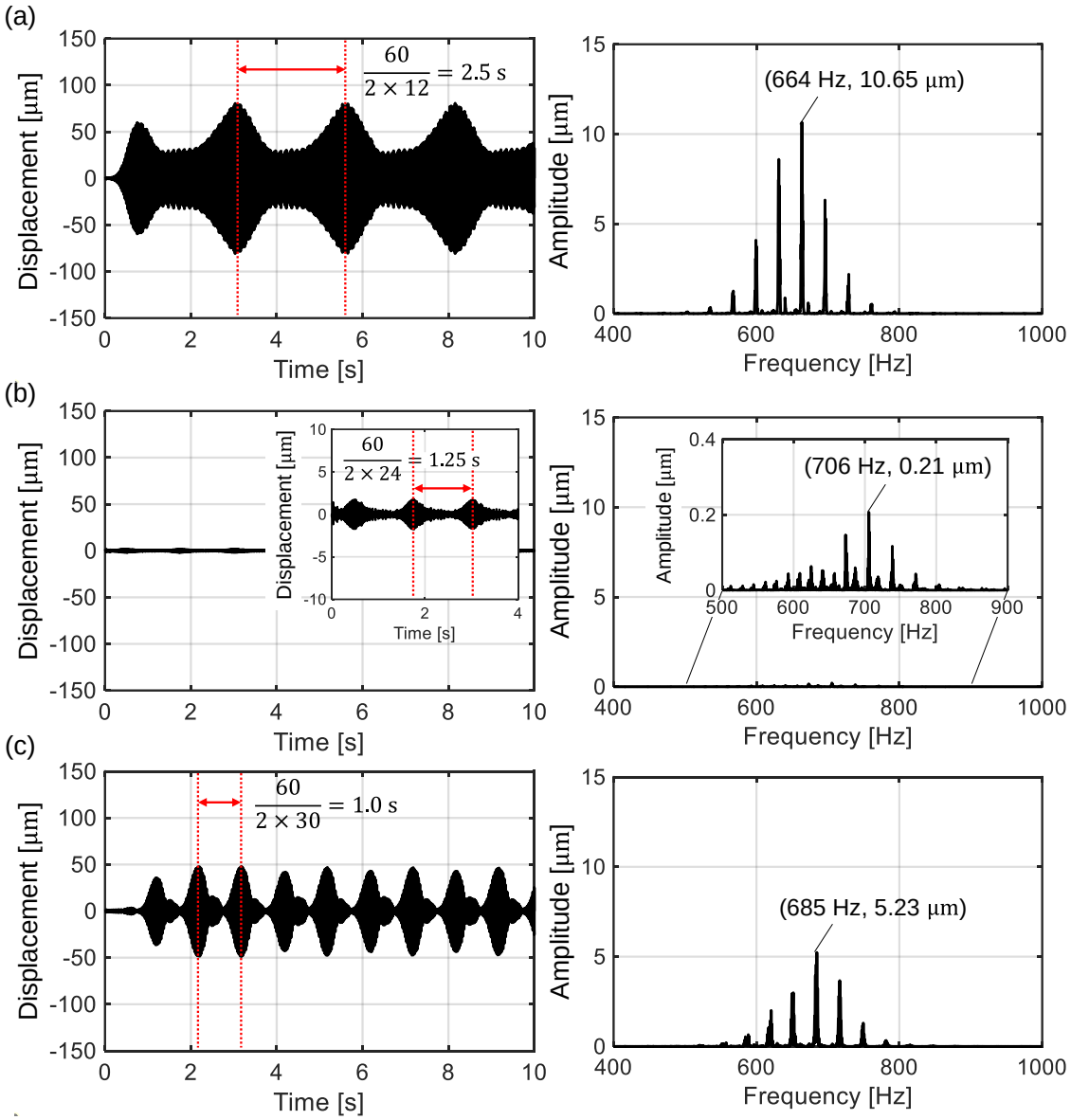

Fig. 6-9 Results of the simulated parallel milling with speed difference ($S^{t2} = 960$ min^{-1} and $a_p = 0.4$ mm): (a) $\Delta\varepsilon_c = \pi/2$ ($S^{t1} = 972$ min^{-1}); (b) $\Delta\varepsilon_c = \pi$ ($S^{t1} = 984$ min^{-1}); (c) $\Delta\varepsilon_c = 5\pi/4$ ($S^{t1} = 990$ min^{-1})

frequency (i.e., 642 Hz in Φ_{yy}), with a frequency spacing of 32 Hz corresponding to the tooth-pass frequency. This indicates that the ZOA, which assumed a single dominant chatter frequency, might not be suitable for accurately analyzing the SLDs, although the process stability tendency could be captured. Therefore, the maximum frequency spectrum component was simply regarded as the chatter frequency (i.e., 659.2 Hz).

Fig. 6-9 shows the results of applying the SDM with $\Delta\varepsilon_c = \pi/2$ ($S^{t1} = 972$ min^{-1}); $\Delta\varepsilon_c = \pi$ ($S^{t1} = 984$ min^{-1}); and $\Delta\varepsilon_c = 5\pi/4$ ($S^{t1} = 990$ min^{-1}). The other conditions were the same as those depicted in Fig. 6-8. Note that the ATO did not affect the process when different spindle speeds were assigned for tools 1 and 2, because the rotational angle between the tools varied continuously [164]. As shown in Fig. 6-9, the chatter was attenuated in all the

results, with the most effective chatter suppression being observed at $\Delta\varepsilon_c = \pi$. These results were consistent with the stability behavior presented in Fig. 6-5.

However, it is noteworthy that the vibration increased and decreased periodically according to the difference in the tooth-pass frequencies of the two tools. A similar beat vibration was often observed in the spindle speed variation process, as discussed in Chapter 4 (e.g., Fig. 4-18). Generally, this nonlinear beat vibration cannot be analyzed by a frequency-domain stability analysis [151]. Consequently, the beat vibration complicated the process stability interpretation. For instance, the vibration level was sufficiently low at some time points in the case of $\Delta\varepsilon_c = 5\pi/4$, where the corresponding stability limit was higher than the applied depth of cut (see Fig. 6-5). However, the vibration was amplified at other time points. This beat vibration would pose a problem if the SDM was applied in the parallel end milling process; hence, it should be avoided to the extent possible. In a high lobe number zone, such as the currently simulated case ($k_c = \mathrm{Floor}(60 \times 659.2/(2 \times 960)) = 20$), the beat vibration could be very sensitive to a slight difference in the spindle speed (e.g., only a 6 min^{-1} difference between Fig. 6-9(b) and (c)). Therefore, it is crucial to select the spindle speed, based on an accurate tracking of the chatter frequency in actual conditions during the process.

6.4. Experimental observation of beat vibration in the SDM

6.4.1. Experimental setup

The effectiveness of the SDM in parallel end milling was verified through experiments as well. Fig. 6-10 shows the schematic diagram of the experimental setup and procedure for the parallel milling tests. The same multi-tasking machine tool and workpiece as in the parallel turning process were used here as well; hence a more detailed system configuration and specification could be also obtained in Subsection 5.5.1 of Chapter 5 and **Appendix A**. The same cutting force estimation system as used with the MEDOB was implemented along the X1-axis of the upper turret (see Table 5-2), and utilized to evaluate the chatter state in the parallel milling tests.

A slender cylindrical workpiece chucked on the left-side work spindle was machined simultaneously from both the sides using tool 1 (upper) and tool 2 (lower). The axial and radial depths of the cut were set to be the same at both the sides. In addition, the tool positions of the two tools along the Z-direction were identical; hence, the feed speed was fixed even if the spindle speed of either of the tools changed. The tools rotated in opposite directions when viewed from the same direction to balance the cutting force in the X- and Y-directions. The cutting conditions are summarized in Table 6-1.

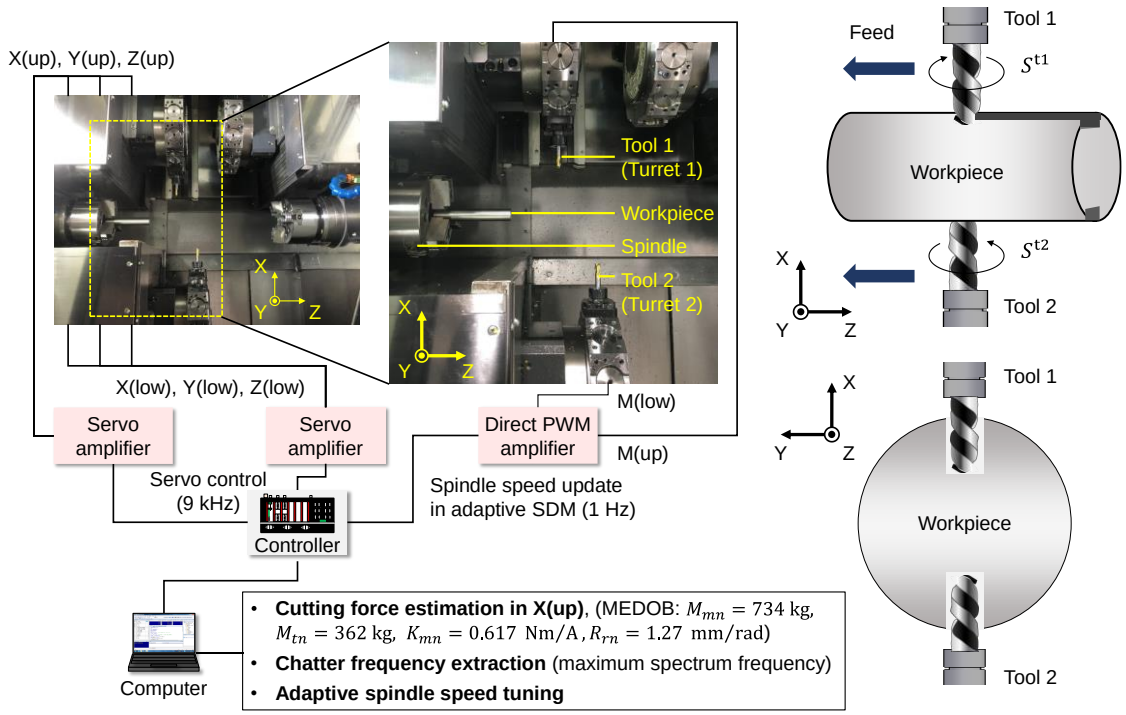

Fig. 6-10 Experimental setup for the parallel milling process

Table 6-1 Common cutting conditions and system conditions for the MEDOB

Cutting tools	HSS square end mill
Tool geometries	$D^{tp} = 10$ mm, $N_c^{tp} = 2$ and $\beta_L^{tp} = 30°$
Projection length of tools [mm]	30
Material of workpiece	SUS303
Diameter of workpiece [mm]	25
Projection length of workpiece [mm]	130
Reference spindle speed (Tool 2) [min^{-1}]	960
Axial depth of cut (Tools 1 and 2) [mm]	2
Radial depth of cut (Tools 1 and 2) [mm]	10 (slotting)
Feed speed (Tools 1 and 2) [mm/min]	60

Note that it was confirmed that the dominant local modes of the tools existed at approximately 2 kHz, which was much higher than in the workpiece mode. Additionally, the corresponding compliance gains of the tools were significantly smaller than those of the workpiece; hence the regenerative chatter should be predominantly induced by the dynamics of the flexible workpiece.

6.4.2. Experimental results

Fig. 6-11(a) shows the experimental results in the parallel milling with the same spindle speed on both the sides (i.e., $S^{t1} = S^{t2} = 960\,\mathrm{min}^{-1}$). Note that the cutting force was overestimated, particularly, in the high-frequency region, owing to modeling errors and

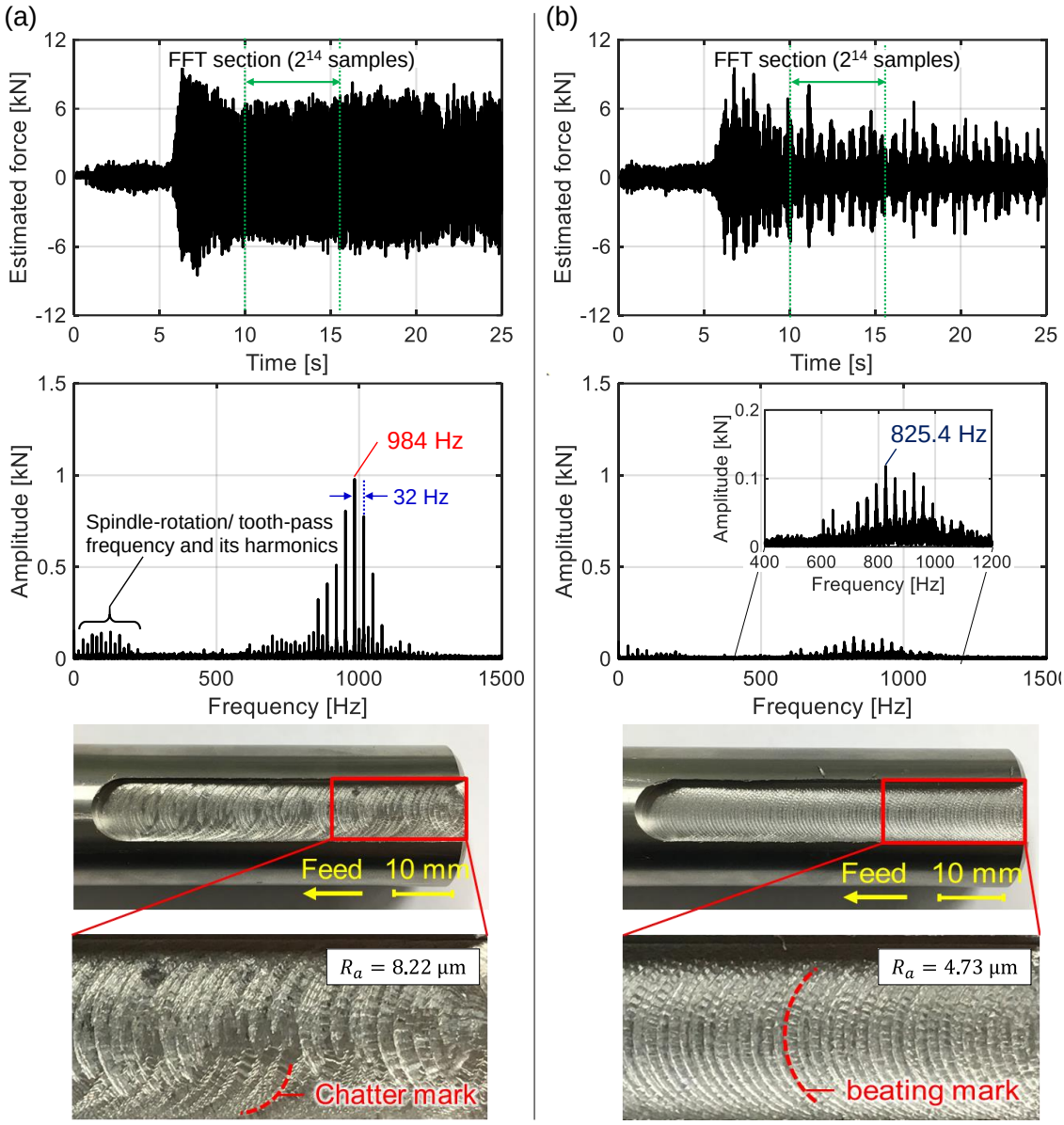

Fig. 6-11 Experimental results of parallel milling tests (top: time waveform of the estimated cutting force; middle: Its FFT; bottom: machined surface): (a) same spindle speed (S^{t1} = 960 min^{-1} and S^{t2} = 960 min^{-1}); (b) SDM designed offline (S^{t1} = 1009 min^{-1} and S^{t2} = 960 min^{-1})

numerical differentiation. Nevertheless, the estimated cutting force sensitively reflected the vibrational state, including the high-frequency chatter and low-frequency forced vibration components, as can be seen in the FFT result. As discussed in the simulation result of Fig. 6-8, multiple chatter frequencies were clearly observed in the tooth-pass frequency interval (i.e., 32 Hz). In fact, the chatter marks and consequently a deteriorated surface roughness of 8.22 μm (measured using Surfcom Flex-50A; Tokyo Seimitsu Co., Ltd) were observed.

Here, the axial depth of cut for the chatter state in the experiment (i.e., a_p = 2 mm) was significantly larger than the analyzed stability limit in the simulation. One possible reason

was a decrease in the engagement angle along the tool axial direction owing to the cylindrical shape of the workpiece, which was not considered to be so in the simulation. Additionally, the loop stiffness of the CWS probably increased under actual cutting conditions. Because the double-side slotting test was performed at the same position along the Z-direction, the system might be assumed to behave similar to a double-supported beam. In fact, the measured chatter frequency was significantly higher than the resonant frequency obtained by the tap test under the cantilever-beam state. This suggests the difficulty of accurate process prediction and importance of automatic and adaptive chatter suppression system by tracking the chatter frequency during the actual process conditions.

Based on Fig. 6-11(a), the maximum spectrum frequency of 984 Hz was regarded as the chatter frequency, and the SDM was designed by using Eq. (6-19) with $m_p = 1$. As a result, the spindle speed of tool 1 (S^{t1}) was changed to $1009\ \mathrm{min}^{-1}$. The spindle speed of tool 2 remained the same (i.e., $S^{t2} = 960\ \mathrm{min}^{-1}$). The results are shown in Fig. 6-11(b). The chatter vibration was clearly suppressed by the SDM, and the surface roughness was reduced to 4.73 μm. However, a beat vibration in the time waveform and beat marks on the machined surface were observed. Based on the observation of the machined surface, there were five beat marks, one after every 3 mm, corresponding to an interval of approximately 1.67 /s, considering the feed speed of 60 mm/min. This was approximately the same as the difference between the tooth-pass frequencies of the two tools (i.e.,$(2 \times 49)/60 = 1.63$ Hz), as suggested in the simulation section as well.

6.5. Adaptive SDM system for reliable chatter suppression

6.5.1. Methodology with online chatter-frequency extraction

One of the possible reasons for the large beat vibration in Fig. 6-11(b) was the variation in the phase difference from the optimal value. Particularly, it changed sensitively in the high-lobe number zone ($k_c = \mathrm{Floor}(60 \times 984/(2 \times 960)) = 30$) with a slight difference in the spindle speed. In a real system, the chatter frequency might vary according to the cutting position, material removed, and/or slight variation of the experimental setup (e.g., the projection length of the workpiece). Therefore, an automatic chatter suppression system with the adaptive SDM based on an in-process monitoring of the chatter state was developed.

To automatically track the chatter frequency in real time during the process, the moving Fourier transform (MFT) [55], which is a type of the SDFT [116], was applied to the estimated cutting force. In the MFT, the power spectrum at a certain frequency, ω_{ext} [rad/s] could be calculated with a low computational cost, while sliding the window, N_w [−], in a similar manner as in the MA algorithm as follows:

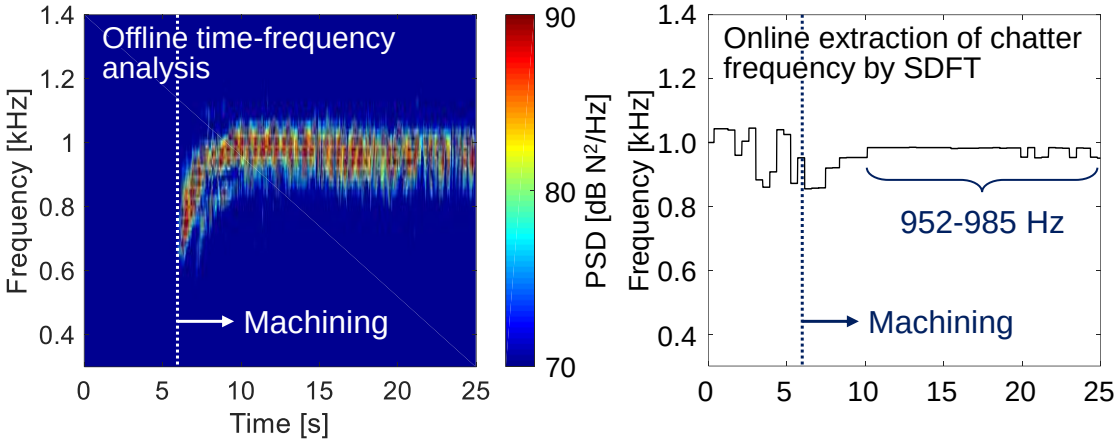

Fig. 6-12 Online extraction of chatter frequency by MFT applied to the estimated cutting force

$$MFT[k] = MFT[k-1] + \frac{2u[k]}{N_w} e^{i\omega_{ext} T_s k} - \frac{2u[k-N_w]}{N_w} e^{i\omega_{ext} T_s (k-N_w)} \tag{6-21}$$

where $u[k]$ and $MFT[k]$ are the analyzed signal and its MFT value, at the k-th sample data under the sampling frequency of T_s [s], respectively.

By applying the MFT to multiple frequencies at an arbitrary frequency interval (resolution) within an arbitrary frequency range, the most excited frequency component can be determined, which is simply regarded as the chatter frequency [103].

Fig. 6-12 shows an example result of the in-process chatter frequency extraction from the cutting force, estimated in the same-speed parallel milling shown in Fig. 6-11(a). The frequency resolution and window length for the MFT were set to 1 Hz and 4000 samples (i.e., 444 ms under a 9-kHz servo cycle), respectively. The chatter frequency was updated when all the data in the calculation window were updated (i.e., after every 444 ms), as the chatter frequency did not change suddenly with each sampling period. Here, as the computational power of the PC used in the experiment was not adequate to analyze the entire frequency range, the measurement range of the chatter frequency was limited (e.g., 850–1050 Hz) as a case study. The spindle speed difference was adaptively tuned based on the identified chatter frequency in real time.

6.5.2. Experimental results of the adaptive SDM

Fig. 6-13 summarizes the results of the adaptive SDM. The spindle control system was switched on from 10 s, although it could be automatically started using a chatter detection technique. Note that the spindle speed of tool 1 was altered after every 1.0 s. The experimental results clearly show that the developed system suppressed the chatter vibration by adaptively controlling the spindle speed during the process, based on the chatter frequency that was automatically extracted from the estimated cutting force in real

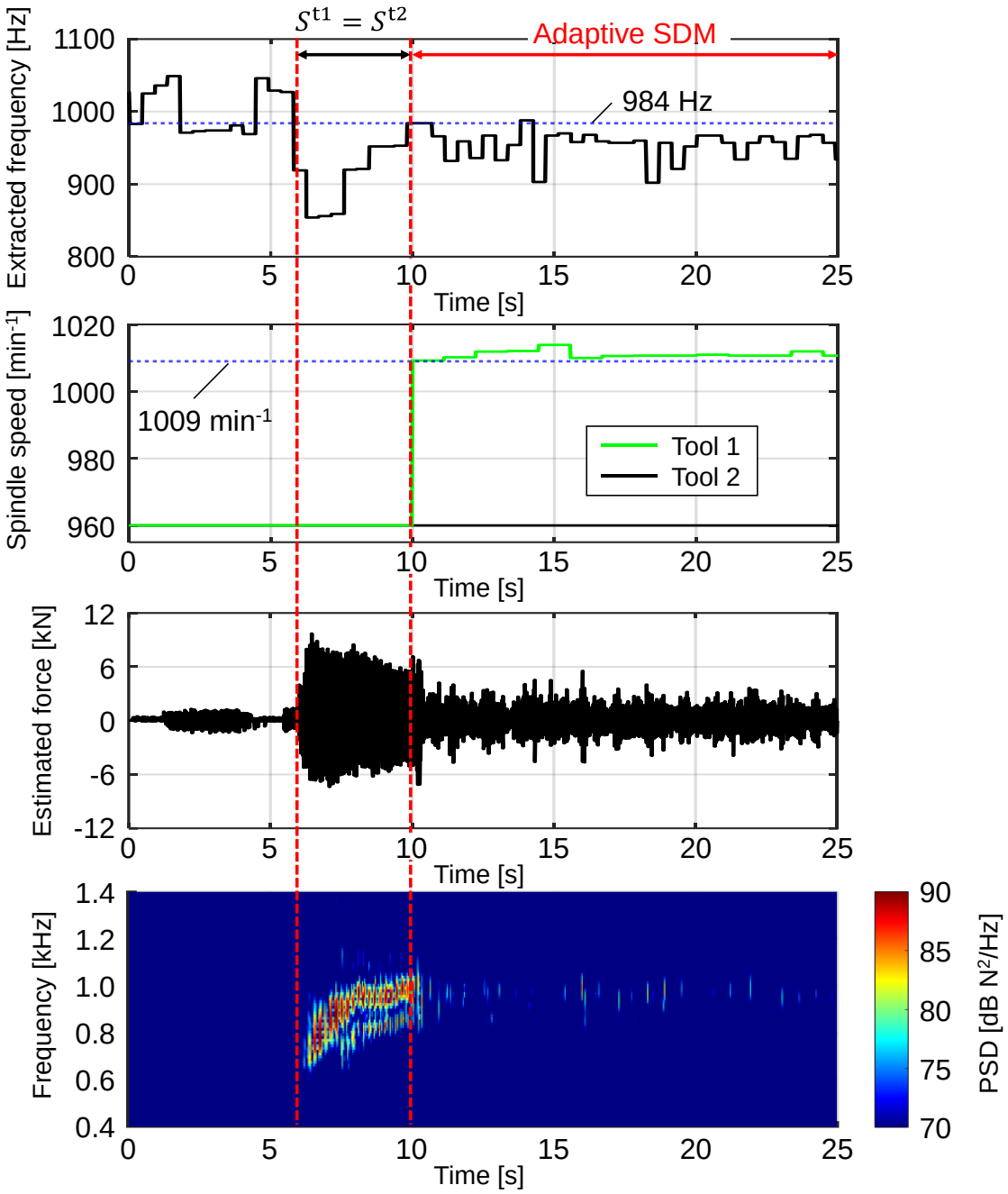

Fig. 6-13 Experimental results of the adaptive SDM: (a) extracted chatter frequency; (b) spindle speed; (c) estimated cutting force; (d) spectrogram (STFT)

time. Because only the servo information and spindle control system were used for chatter monitoring and suppression, this system required no additional equipment or sensors. Therefore, it would benefit the next-generation machine tools that integrate the SOMS.

Fig. 6-14(a) shows the moving variance representing the temporal power spectrum of the entire frequency range except for the DC component during each process. The experimental data of the conventional parallel milling with the same spindle speed and SDM was the same as that depicted in Fig. 6-11. In the SDM designed offline, on one hand,

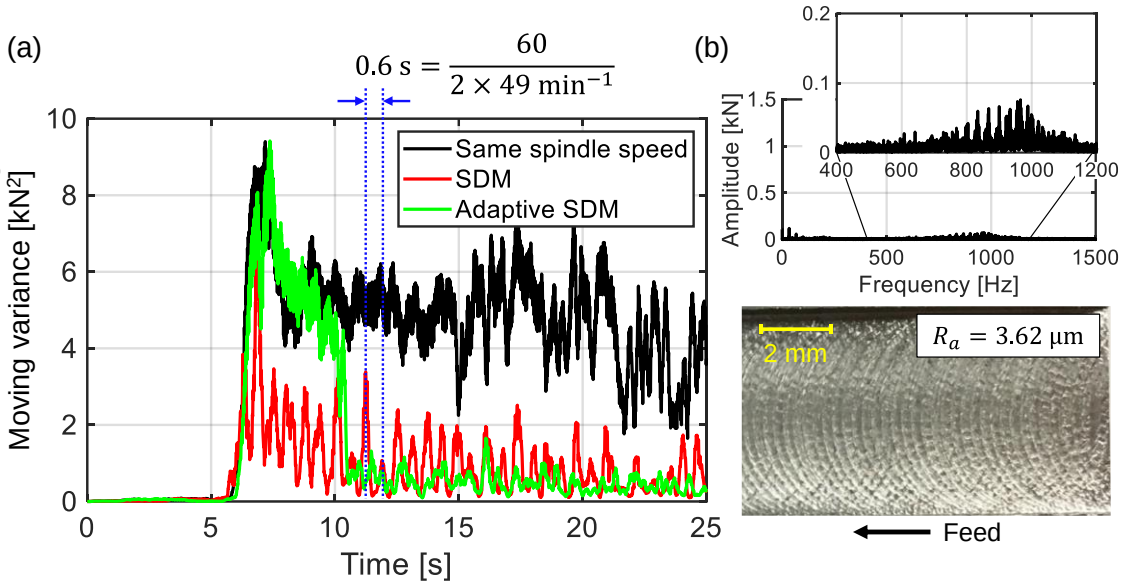

Fig. 6-14 Comparison of processes: (a) Moving variance of the estimated cutting force; (b) FFT of the estimated cutting force and machined surface in the adaptive SDM (compared to Fig. 6-11)

the beat vibration according to the difference between the tooth-pass frequencies could be clearly observed, although the chatter was reduced. On the other hand, the adaptive SDM system reduced the chatter vibration more effectively, including the beat vibration, and consequently the surface roughness was reduced to 3.17 µm, as seen in Fig. 6-14(b). This could be because the speed difference approached the optimal value in the current real condition. The experimental results suggested that the adaptive system was highly promising in achieving a more effective chatter suppression.

Note that the slight beat marks remained even in the adaptive SDM system. However, the SDM is not suitable for finishing processes because of the forced vibration. In finishing processes with a low cutting depth, which is sufficient to avoid the chatter, the forced vibration should be cancelled out by perfectly synchronizing the tool rotation angles and direction on both the sides [246].

6.6. Summary

In this chapter, the effectiveness of the SDM for the parallel end milling process was discussed. It was assumed that a slender and flexible workpiece on a plane perpendicular to the tool axis direction, was machined simultaneously by two end mills rotating in opposite directions. Based on the obtained findings through the developed process simulation, a monitoring-based real-time spindle speed control system (i.e., an adaptive SDM) for robust chatter suppression was developed. The contents of this chapter can be summarized as follows:

1. The SDM with $\Delta\varepsilon_c = \pi(2\pi m_p + 1)$; $m_p \in \mathbb{Z}$ could improve the process stability if the mode-coupling effect did not exist. However, in a process with mode-coupling, the SDM might exhibit a contrary effect.

2. When the SDM was applied, the beat vibration occurred according to the difference between the tooth-pass frequencies of the two tools, which was also transcribed on the machine surface; hence, it is necessary to avoid the beat vibration to the extent possible. In cases involving large chatter lobe numbers, the beat vibration would be very sensitive to even a slight difference from the optimal value of the spindle speed.

3. By using the adaptive SDM system with an observer-based chatter state extraction in real time, the chatter could be suppressed more effectively with less beat vibration. The developed automatic chatter suppression system required no additional equipment or sensors.

In this study, the spindle speed of one side was fixed during process. However, further improvement of the stability may be achieved by adaptively optimizing not only the difference of tooth-pass period between tools but also the reference speed. Furthermore, applying SSV techniques to parallel milling process and/or combination of SSV and SDM can also be considered. More comprehensive strategies for adaptive optimal spindle speed control for simultaneous milling processes should be further studied in the future.

7. Conclusions

This dissertation proposed novel enabling technologies for SOMS, where the machine tool can self-actively suppress the chatter vibration according to the monitored chatter state. In the chatter vibration, the “phase shift” is a key factor. All methodologies for chatter detection and suppression proposed in this dissertation are interpreted from the perspective of phase-shift control and monitoring. Additionally, only the internal servo information and motors of the machine tool are utilized to monitor and suppress the chatter.

In Chapter 1, an overview of SOMS functionalities is provided. SOMS is a novel intelligent concept to address the recent high-level manufacturing issues, such as energy/labor-saving, flexibility, traceability, and reliability. The machining chatter problem is a main concern even in SOMS, as it remains a major impediment to productivity. The basic categorization and mechanism of machining chatter are also given, followed by the state-of-the-art enabling technologies for SOMS in the chatter issue. Based on the problems of existing chatter monitoring and suppression techniques, the research direction and concrete objective/applications in this dissertation are explicitly defined.

In Chapter 2, the existing sensorless cutting force estimation techniques using the internal servo information of the machine tool are derived with in-depth description of their characteristics through a series of exemplary simulations and experiments. On one hand, the conventional DOB is useful in the linear-motor-driven stage, where a single-inertia model can be assumed. On the other hand, the expanded DOB techniques, such as MEDOB, LDOB, and VMDOB, should be used in the ball-screw-driven system. These techniques can be applied to machine tools with fully closed ball-screw-driven stages, which have become recent mainstream. In case that the ball-screw-driven system can be regarded as a dual-inertial model, MEDOB, LDOB, and VMDOB can accurately estimate the cutting force with a sufficiently reliable bandwidth. Interestingly, although these three techniques should produce the same estimation results in ideal cases, their behavior is strongly characterized by the internal component forces, contributing to the estimated cutting force. In addition, the limitations of the sensorless cutting force estimation system are mentioned. Especially, the essential limitation is attributed to the complex structural dynamics that make the dual-inertia model ambiguous. To overcome this limitation, the pre-compensation concept with a cutting-data-driven self-optimized compensation digital filter is proposed. If the proposed compensation techniques can be applied successfully, the accuracy of the sensorless cutting force estimation system can be substantially enhanced with sufficient bandwidth. Note that the estimated cutting force can capture a very high-frequency chatter by integrating linear encoder information (i.e., high sensitivity can be maintained),

although the estimation accuracy of the spectrum amplitude depends on the modeling error. In this dissertation, the estimated cutting force is consistently used for chatter monitoring.

In Chapter 3, an online chatter detection method is proposed based on the novel concept of phase shift monitoring by using MPF and MEF, which are proposed anew as indices for chatter detection, inspired from the power factor in the AC circuit. The MPF and MEF during the machining process represent the phase differences between the cutting force and tool velocity/displacement, and can be utilized to detect the forced vibration and self-excited (regenerative) chatter, respectively. In addition, a concrete algorithm for type-assorted online fast chatter detection by MPF/MEF with low computational cost is described. Additionally, the system integration with a sensorless cutting estimation technique is proposed. Note that, in principle, the chatter detection with MPF/MEF can be applied to the sensor-based system with a dynamometer and displacement/acceleration sensor. If MEF/MPF can be calculated ideally, on one hand, the MEF becomes rapidly negative when the regenerative chatter occurs. On the other hand, the MPF become fairly close to 1 during only forced vibration (i.e., resonance). The experimental verification is performed in the prototype precision lathe with linear-motor-driven stage, where the SDoF system can be ideally assumed and a highly accurate cutting force estimation can be attained. However, it is believed that further improvements of the proposed method must be studied systemically for ball-screw-driven stage, other machining processes with or without MDoF system, and/or local chatter of tool/workpiece/spindle. System Integration to a spindle axis and/or adaptronic intelligent machine components is also interesting. Because the thresholds for phase-shift monitoring with MEF/MPF are determined from the chatter mechanism, it is expected that the chatter can be detected independent of the workpiece materials and cutting conditions. If this can be achieved, the adaptability of chatter monitoring function to SOMS addressing mass customization will be significantly enhanced. It is also thought that the reliability of the system can be improved using MPF/MEF together with the existing chatter detection techniques.

The simple, practical, and optimal design of the SSV process has been an open issue for both industry and academia for a long time. Chapter 4 attempted integrating the SSSV process in the framework of FM technology and constructing a systematic and comprehensive design methodology, which can be online or integrable in CNC machine tools. The proposed method stands on the minimization of the net inflow energy in the CWS during the SSSV cycle. In the process of deriving the design methodology, the technological analogy between the SSSV and PM/FM used in the radio communication engineering is found and focused on. This allows the MI to be defined as a novel design index for SSSV. As a result, the net inflow energy model can be expressed with the Bessel function having MI as an argument. It provides design candidates for selecting the optimal amplitude of SSSV,

which will effectively dissipate the chatter energy. Additionally, several limit criteria for SSSV frequency according to the variation amplitude are proposed from the viewpoints of SSSV efficiency and beat vibration. Note that the requirement of the proposed design methodology is to only measure the chatter frequency, similar to DSST; hence, it can contribute to self-acting chatter suppression integrated with a chatter monitoring system. Additionally, it is possible to flexibly take the machine constraints into the design procedure as several recommend design candidates are presented. As a result, the practical design of SSSV is feasible on the actual shop floor; hence, it is important that the proposed design method be applied to many real industrial applications and subjected to more verification for further development. The future SOMS will need to include an effective and flexible chatter avoidance system with autonomous spindle control that achieves the appropriate use and in-situ optimal design of DSST and CSSV according to the observed chatter lobe number, chatter origin, and machining process information.

In Chapter 5, a novel chatter stabilizing machining method employing TSM was proposed in the parallel turning process under the following assumptions: two identical rigid tools machine a flexible workpiece sharing the surface with the same depth of cut. In the TSM process, the two tools are swung in the circumferential direction of the workpiece sinusoidally while maintaining an equal pitch. An appropriate practical design procedure for TSM is also discussed considering the technological analogy with the SSSV process and the side-effects in the TSM process. In a prototype multi-tasking machine tool modified to be flexibly controlled, the chatter stabilization performance and workpiece runout in the TSM process are experimentally evaluated and compared with conventional equal and unequal pitch turning. The results show that the TSM process can perform an effective chatter suppression without the eccentricity of the workpiece, which may be induced by the unbalanced cutting forces, although the swing marks due to the follow-up error of the turret position are observed. The main advantage of the TSM process compared to the SSV process is the bandwidth of the feed drive system, which is independent of the workpiece mass and generally much greater than the spindle drive system; hence, the TSM process can provide a sufficient variation frequency for effective chatter suppression. There is also a possibility that the design range can be further expanded in combination with SSV techniques in the future. As TSM is provided by only the feed drive system and the design parameters can be flexibly adjusted, as in the case of SSV, the proposed TSM has potential to be a practical enabling technology for SOMS addressing the machining chatter issue.

In Chapter 6, the effectiveness of SDM for the parallel end-milling process was discussed. It is assumed that two end mills rotating in opposite directions simultaneously machine a slender workpiece having flexibility on a plane perpendicular to the tool axis direction. In SDM, the spindle speed difference between two tools is just given to suppress

the chatter. In addition, the speed difference is designed based on only chatter frequency; hence, SDM is a promising enabling technology for SOMS. Although the concept of SDM has already been proposed for the double-sided face milling of an SDoF thin plate where tools rotate in the same direction [244,245], the effectiveness of SDM has not been elucidated for the scenario mentioned in this dissertation. Therefore, the process model is developed first. Based on an analysis with the developed time- and frequency-domain simulations, the SDM corresponding to $\Delta\varepsilon_c = \pi + 2\pi m_p$ can improve the process stability, if the mode coupling effect does not exist. However, the SDM may decrease the process stability with mode coupling because of non-diagonal regenerative terms that cannot be erased. In addition, the beat vibration according to the difference in the tooth-pass frequency between two tools is observed in both simulation and experiment when the SDM is applied. As it is clearly observed that the beat vibration is transcribed on the machine surface, the beat vibration should be avoided to the maximum possible extent. Nonetheless, the beat vibration changes sensitively with slight differences from the optimal speed difference value, especially in a high-lobe-number scenario. To address this issue, a real-time adaptive system is a potential solution. By developing an adaptive SDM system with the observer-based chatter-frequency extraction in real time, chatter can be suppressed more robustly with less beat vibration. In this study, however, the spindle speed of one side was fixed during process. Further improvement of the stability may be achieved by adaptively optimizing not only the difference of tooth-pass period between tools but also the reference speed in the future.

None of the proposed systems require additional equipment, such as actuators and sensors; hence, they can be implemented on machine tools as an add-on and contribute the 8th and 9th functions for SOMS (Fig. 1-1). Especially, these functionalities (i.e., control-integrated monitoring and process control) are the fundamental SOMS functions inherently possessed by the machine tool. Furthermore, as these two functions exhibit high affinity, a highly intelligent cooperation between the two is expected. To achieve this expectation, this dissertation is believed to provide valuable enabling techniques and essential information for the process interpretation and control. Note that interpretation of process-machine interaction with a simple model is essential for adaptive process control in SOMS. It is very important to systematically organize the process control strategies involving simple models. Particularly, there are no studies of autonomous process control for complex turn-milling processes. If further process interpretation with a simpler and essential model progresses also in turn-milling process, it is considered that elaborated cooperative process-control strategies between a work spindle and single- or multiple milling spindles, involving DSST, SSV, and/or SDM techniques, will be established.

Not to mention, further research for advanced cooperation and interaction between other functionalities is also important. For instance, robustness and reliability of process and condition monitoring for a harsh and changeable real machining environment would be enhanced by integrating and refurbishing various external and internal sensors through a modeling filter with digital simulations and/or machine learning. The hybrid strategies with simultaneous adaptive control of several process parameters, in addition to an additional adaptronic actuator, would be necessary while considering the process characteristics and predicted surface quality. The feedforward process planning based on the simulated process results, including the machined surface, is also essential for the dual safety system while considering all characteristics of the process, machine, and controller. Furthermore, the research on how to incorporate human know-how into SOMS (i.e., human–machine interaction) is an interesting new direction for SOMS.

Appendices

A) Specifications of the experimental setup

Table A-1. Major specifications in the 3-axes double-column-type prototype machine tool

Ball screw (BSS1505-3E from NSK Ltd.)			
Lead length [mm]	5		
Diameter [mm]	15		
Stroke [mm]	200 (X- and Y-axes); 100 (Z-axis)		
Support type	Double anchor		
Preload type	Oversized ball		
Guideway type	Rolling		
Synchronous AC servomotor (TSM3204N2305E200 from Tamagawa Seiki Co., Ltd.)			
Pole number	10		
Slot number	12		
Torque constant [Nm/A]	0.37		
Rated torque [Nm]	1.27		
Bandwidth of current control loop [rad/s]	5000		
Motor-side rotary encoder (in the AC servo motor)			
Measurement type	Absolute method		
Resolution [bit]	23		
Equivalent resolution in translational motion [nm]	0.60		
Signal period [count/rev]	512 (= 2^9)		
Interpolation times	16384 (= 2^{14})		
Counter-motor-side rotary encoder (TS5667N701 from Tamagawa Seiki Co., Ltd.)			
Measurement type	Incremental method		
Resolution [bit]	17		
Equivalent resolution in translational motion [nm]	38		
Signal period [count/rev]	512 (= 2^9)		
Interpolation times	256 (= 2^8)		
Linear encoder (LIF481, from HEIDENHAIN Co., Ltd.)			
Measurement type	Incremental method		
Signal type	Sine wave		
Resolution [nm]	0.24		
Grating period [μm]	8		
Signal period after interpolation at scanning head [μm]	4		
Spindle (BMS-4020RA from Nakanishi Co., Ltd.)			
Rotation deflection accuracy [μm]	< 1μm		
Maximum spindle speed [min^{-1}]	20000		
Maximum torque [Nm]	1.0		
Controller (Power PMAC from Delta Tau Data Systems, Inc.)			
Interface board	ACC-24E3-2		
Servo cycle [μs]	100 (10 kHz)		
Phase cycle [μs]	100 (10 kHz)		
Servo amplifier (VLASX-012P2-SXM from Toshiba machine Co., Ltd)			
Resolution of A/D conversion [bit]	12		
Piezoelectric dynamometer (Type 9129AA from Kistler Instrumente AG)			
	F_x	F_y	F_y
Dynamic resolution [N]	< 0.01	< 0.01	< 0.01
Sensitivity [pC/N]	8	4.1	8
Natural frequency [kHz]	≈ 3.5	≈ 4.5	≈ 3.5
Linearity, all ranges [%FSO]	< ±0.3	< ±0.3	< ±0.3

Table A-2. Major specifications in the prototype linear motor-driven high-precision lathe

	X stage	Z stage
Linear motor	(S160T from GMC Hillstone)	(S160Q from GMC Hillstone)
Maximum thrust force [N]	58	78
Thrust-force coefficient [N/A]	18.5	20.5
Linear encoder	(LIF401R from HEIDENHAIN)	(LIP401R from HEIDENHAIN)
Scale pitch [μm]	4	2
Resolution [nm]	0.244	0.122
Linear guide	(LSP20100 from THK)	(LSP1390 from THK)
Type	Ball slide guide	Ball slide guide
Maximum stroke [mm]	75	50
Servo amplifier	(SVFM2-H3-DSP from Servoland)	(SVFM2-H3-DSP from Servoland)
Rated current [A]	5.5 (max) / 3.9 (rms)	5.5 (max) / 3.9 (rms)
PWM cycle [μs]	62.5 (16 kHz)	62.5 (16 kHz)
Work spindle (ϕ70 mm × 220 mm, steel) with aerostatic bearing		
Flameless motor (B09-13 from SinMaywa Industries)		
Max. rotational speed [min^{-1}]	4400	
Torque coefficient [N・m/A]	0.43	
Max. torque [N・m]	0.83	
Rotor inertia [kg・m^2]	0.000060	
Rotary encoder (ERM280 from HEIDENHAIN Co., Ltd.)		
Scale pitch [pulse/rev]	512	
Resolution [pulse/rev]	8388608	
Servo amplifier (S30TA-2-345 from SinMaywa Industries)		
Rated current [A]	13.0 (max) / 9.2 (rms)	
PWM cycle [μs]	62.5 (16 kHz)	
Motion controller (Power PMAC from Delta Tau Data System), common to all axes		
Interface card	ACC-24E3	
Servo cycle [μs]	80 (12.5 kHz)	
Phase cycle [μs]	20 (50.0 kHz)	
Sampling time of position/angle data [μs]	0.32 (3.125 MHz)	
Position data size [bit]	34	
Command current data size [bit]	16	

Table A-3. Major specifications of the experimental setup in the prototype multi-tasking machine tool

Work spindle C1(left)-axis	
Mechanical specification ([spindle-side, motor-side])	
Inertia of rotating element [kg・m^2]	[0.09003, 0.01758]
Diameter of belt pulley [mm]	[140, 130]
Conversion factor of spindle and motor side	0.9288
Servo motor/driver specification (motor: HG-JR903 from Mitsubishi Electric Co., Ltd.; driver: GPL301 from Delta Tau Co., Ltd.)	
Rated current [A]	41.0
Rated torque [Nm]	28.6
Torque constant [Nm/A]	0.6976
Maximum current [A]	134
Encoder feedback [cts/rev]	262144
Encoder resolution [deg]	0.00137
Specification of ring encoder at the spindle side (AK ERM 280 from HEIDENHAIN Co., Ltd.)	
Encoder feedback [cts/rev]	19660800
Encoder resolution [deg]	0.00018

Rotary axis of upper and lower milling ([M1(up)-axis, M2(low)-axis])	
Mechanical specification	
Inertia of rotating element [kg・m²]	[0.00132, 0.00132]
Servo motor/driver specification (motor: [HG-JR353, HG-JR353] from Mitsubishi Electric Co., Ltd.; driver: [GPL301, GPL301] from Delta Tau Co., Ltd.)	
Rated current [A]	[17.0, 17.0]
Rated torque [Nm]	[10.5, 10.5]
Torque constant [Nm/A]	[0.6176, 0.6176]
Maximum current [A]	[51, 51]
Encoder feedback [cts/rev]	[40000, 40000]
Encoder resolution [deg]	[0.009, 0.009]
Upper left turret ([X1(up)-axis, Y1(up)-axis, Z1(up)-axis])	
Mechanical specification	
Mass of driven body [kg]	[362.24, 233.53, 595.74]
Diameter [mm]	[32, 32, 32]
Ball screw lead length [mm]	[8, 6, 12]
Stroke [mm]	[600, 398, 786]
Reduction ratio	[1:1, 1:1, 1:1]
Motion conversion factor [m/rad]	[0.0080/(2×π), 0.0060/(2×π), 0.0120/(2×π)]
Inertia of rotating element [kg・m²]	[0.001189987, 0.002119255, 0.001228125]
Equivalent mass of rotating element [kg]	[734.04, 2324.02, 336.70]
Servo motor/driver specification (motor: [HG-JR353B, HG-SR152B, HG-JR353] from Mitsubishi Electric Co., Ltd.; driver: [MR-J4-350A, MR-J4-200A, MR-J4-350A] from Mitsubishi Electric Co., Ltd.)	
Rated current [A]	[18.0, 9.4, 17.0]
Rated torque [Nm]	[11.1, 7.2, 15.0]
Torque constant [Nm/A]	[0.6167, 0.7660, 0.6176]
Maximum current [A]	[71, 29, 51]
Rotary encoder resolution [count/rev]	[120000, 160000, 80000]
Linear encoder specification ([LC415-Endat2.2, LC415-Endat2.2, N/A] from HEIDENHAIN Co., Ltd.)	
Accuracy grade [μm]	[±3, ±3]
Resolution [nm]	[1, 1]
Measurement length [mm]	[220, 220]
Lower left turret ([X2(low)-axis, Y2(low)-axis, Z2(low)-axis])	
Mass of driven body [kg]	[364.13, 228.13, 639.74]
Diameter [mm]	[32, 32, 32]
Ball screw lead length [mm]	[8, 6, 12]
Stroke [mm]	[600, 398, 1129]
Reduction ratio	[1:1, 1:1, 1:1]
Motion conversion factor [m/rad]	[0.0080/(2×π), 0.0060/(2×π), 0.012/(2×π)]
Inertia of rotating element [kg・m²]	[0.001189987, 0.002119255, 0.001228125]
Equivalent mass of rotating element [kg]	[734.04, 2324.02, 336.70]
Servo motor/driver specification (motor: [HG-JR353B, HG-SR152B, HG-JR353] from Mitsubishi Electric Co., Ltd.; driver: [MR-J4-350A, MR-J4-200A, MR-J4-350A] from Mitsubishi Electric Co., Ltd.)	
Rated current [A]	[18.0, 9.4, 17.0]
Rated torque [Nm]	[11.1, 7.2, 15.0]
Torque constant [Nm/A]	[0.6167, 0.7660, 0.6176]
Maximum current [A]	[71, 29, 51]
Rotary encoder resolution [count/rev]	[120000, 160000, 80000]

B) Training results from the pre-compensation step

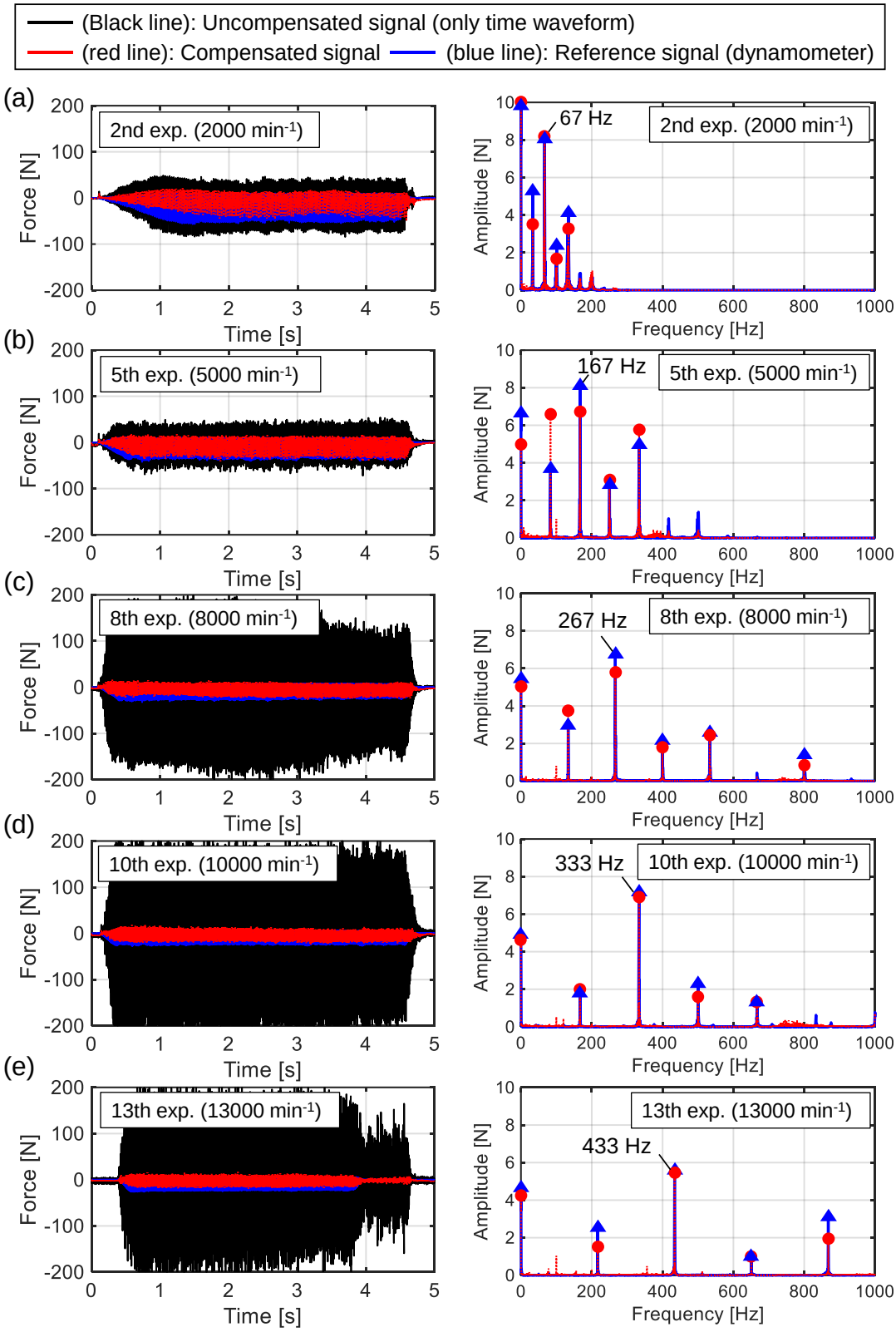

Fig. B-1 Representative learning results from the pre-compensation step (i.e., confirmation of the fitting for the training data): (a) $S = 2000\ \mathrm{min}^{-1}$; (b) $S = 5000\ \mathrm{min}^{-1}$; (c) $S = 8000\ \mathrm{min}^{-1}$; (d) $S = 10000\ \mathrm{min}^{-1}$; (e) $S = 13000\ \mathrm{min}^{-1}$

C) Chatter frequency shift in SSSV

Nam et al. [232] empirically found that the chatter in SSV generally grows at a constant spatial frequency and represented the time shift of the chatter frequency as follows:

$$\omega_c(t) = \big(1 + r_a(t)\big)\omega_c\big(t - \tau(t)\big), \qquad \text{where } r_a(t) = \frac{S(t)}{S\big(t - \tau(t)\big)} - 1 \tag{C-1}$$

where r_a is the acceleration rate, as defined by Nam et al. Here, denoting the initial chatter frequency in CSS and the modulated frequency in Eq. (4-12) as $\omega_{c(0)}$ and $\omega_{c(1)}$, Eq. (4-12) can be rearranged as follows:

$$\begin{gathered} \omega_{c(1)}(t) = \omega_{c(0)} + \omega_s m_f \cos(\omega_s t) \\ \rightarrow \omega_{c(1)}(t) = \omega_{c(0)} + \omega_s \frac{R_A \omega_{c(0)} \tau_n}{1 - R_A^2} \cos(\omega_s t) = \left(1 + \frac{2\pi RV}{1 - R_A^2} \cos(\omega_s t)\right) \omega_{c(0)} \end{gathered} \tag{C-2}$$

By comparing Eqs. (C-1) and (C-2), it can be deduced that Eq. (4-12) represents the 1-st modulation frequency. Therefore, the corresponding vibration models are redefined as: $q_{c(0)} \equiv q_c(t)$ in Eq. (4-3) and $q_{c(1)} \equiv q_{c(0)}\big(t - \tau(t)\big)$ in Eq. (4-10). Additionally, an approximated acceleration rate $\tilde{r}_a(t)$ and its maximum value $\big|r_{a(max)}\big|$ in the SSSV process can be deduced as follows (see Fig. C-1):

$$\tilde{r}_a(t) = \big|r_{a(max)}\big| \cos(\omega_s t) \text{ where } \big|r_{a(max)}\big| = \frac{2\pi RV}{1 - R_A^2} = \frac{R_A \omega_s \tau_n}{1 - R_A^2} = \frac{m_f \omega_s}{\omega_{c(0)}} \tag{C-3}$$

Note that the average acceleration rate in the SSV period, which was used in [232] as the stability index, is always zero in Eq. (C-3), as $\tilde{r}_a(t)$ is simply expressed by a cosine function based on the approximation used for deriving Eq. (4-12). A similar relationship holds good in the next modulation (i.e., $q_{c(2)} \equiv q_{c(1)}\big(t - \tilde{\tau}(t)\big)$) as follows:

$$\begin{aligned} & q_{c(2)} \equiv q_{c(1)}\big(t - \tilde{\tau}(t)\big) \\ & \quad = A_c \cos\big(\omega_{c(0)} t - 2\varepsilon_{cn} + m_f \sin(\omega_s t) + m_f \sin\big(\omega_s t - \omega_s \tau_n + \big|r_{a(max)}\big| \sin(\omega_s t)\big) + \psi_c\big) \\ & \rightarrow \omega_{c(2)}(t) = \omega_{c(0)} + m_f \omega_s \cos(\omega_s t) \\ & \qquad\qquad + m_f \big\{\omega_s + \big|r_{a(max)}\big| \omega_s \cos(\omega_s t)\big\} \cos\big(\omega_s t - \omega_s \tau_n + \big|r_{a(max)}\big| \sin(\omega_s t)\big) \\ & \quad = \left(1 + \frac{m_f \omega_s}{\omega_{c(0)}} \cos(\omega_s t)\right) \big\{1 + \big|r_{a(max)}\big| \cos\big(\omega_s t - \omega_s \tau_n + \big|r_{a(max)}\big| \sin(\omega_s t)\big)\big\} \omega_{c(0)} \\ & \quad = \big(1 + \tilde{r}_a(t)\big) \omega_{c(1)}\big(t - \tilde{\tau}(t)\big) \end{aligned} \tag{C-4}$$

where

$$\omega_s \tilde{\tau}(t) = \omega_s \tau_n \left(1 - \frac{R_A}{1 - R_A^2} \sin(\omega_s t)\right) = \omega_s \tau_n - \big|r_{a(max)}\big| \sin(\omega_s t) \tag{C-5}$$

In summary, the modulation in the previous vibration may emerge as the present vibration according to the spindle rotation, via excitation by the cutting force, including the regeneration. Consequently, the range of frequency shift becomes broader than that given by Eq. (4-12), and appears to approximately range from $(1 \pm R_A)f_{cn}$, as implied in [232] (also see Fig. C-3). Although the analytical vibration model and its net energy inflow in that case should be further investigated, it is worth noting that the energy balance of the SSV cycle with different combinations of the modulation waves does not change, as shown in Fig. C-2. In short, the following relationship holds good in Eq. (4-26) as:

$$\frac{E_f}{\mu_c K_{tc} b_c d_f} = \int_0^{\frac{1}{f_s}} q_{c(l+1)}(t)\dot{q}_{c(l)}(t)\,dt = \int_0^{\frac{1}{f_s}} q_{c(l'+1)}\dot{q}_{c(l')}(t)\,dt, \qquad l, l' \in \mathbb{N}_0 \tag{C-6}$$

To show the typical behavior of the frequency shift during SSSV, the spectrograms (i.e., STFT) of the unstable SSSV tests described in Section 4.5 are summarized in Fig. C-3.

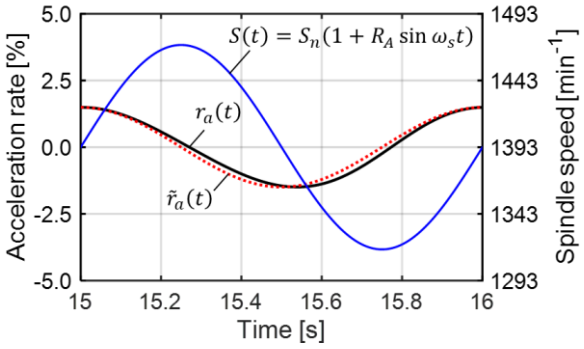

Fig. C-1 Approximated acceleration rate (analysis conditions are same as those shown in Fig. 4-10)

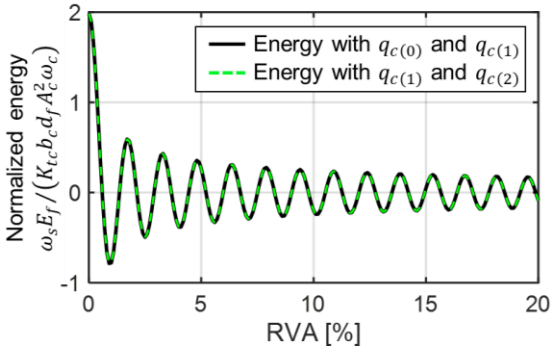

Fig. C-2 Energy behavior calculated with high order modulated waves (Analysis conditions are the same as Fig. 4-11)

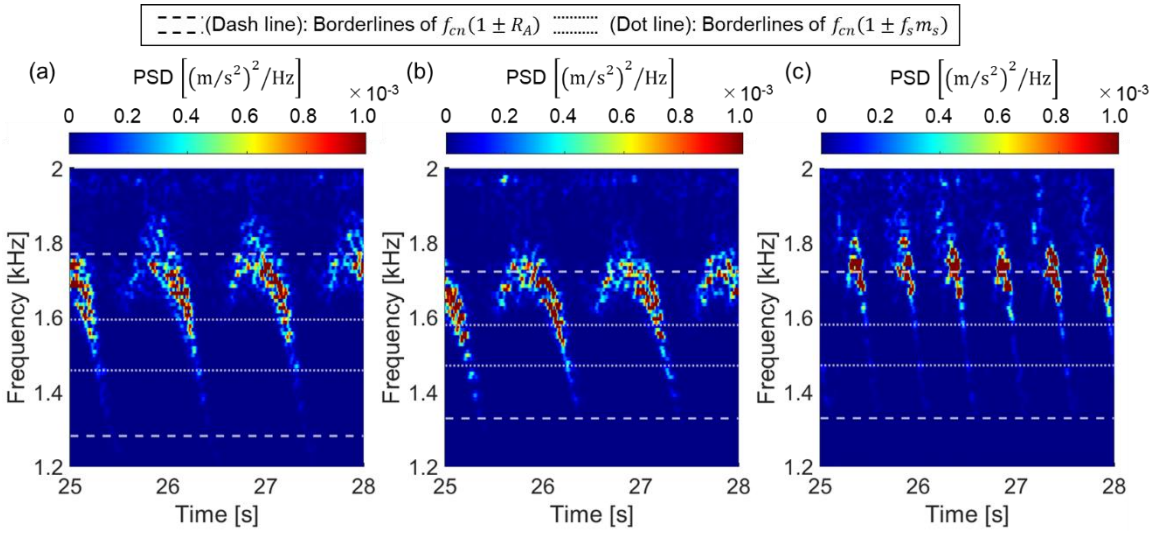

Fig. C-3 Spectrograms of unstable SSSV in the experiment (the common experimental conditions are those shown in Table 4-3 and f_{cn} = 1526 Hz. The data samples of the analysis sliding window and its overlap were set to 1024 and 1009 samples, respectively): (a) R_A = 16.0%, f_s = 1.0 Hz (i.e., Fig. 4-18); (b) R_A = 12.9%, f_s = 1.0 Hz (i.e., Fig. 4-20); (c) R_A = 12.9%, f_s = 2.0 Hz (i.e., Fig. 4-20)

D) Dynamics of the slender workpiece and specific cutting-force coefficients in the parallel turning/milling process

Fig. D-1 and Table D-1 summarize the experimental FRFs and identified modal parameters of the flexible workpiece used in the experimental setup for the parallel turning and milling processes.

Table D-1 Identified modal parameters of the flexible workpice

FRF	Φ_{xx}		Φ_{xy}		Φ_{yy}		Φ_{yz}		Φ_{zz}		Φ_{zy}	
Mode #	1	2	1	2	1	2	1	2	1	2	1	2
M [kg]	1.51	0.236	3.73	1.45	0.749	0.254	16.2	2.20	129	11.2	6.05	1.15
C [Ns/m]	451	45.4	755	143	186	41.6	3.89e3	412	3.69e4	1.95e3	1.49e3	185
K [N/μm]	10.5	3.63	31.9	23.8	6.41	4.12	142	36.1	1.13e3	182	51.2	18.4

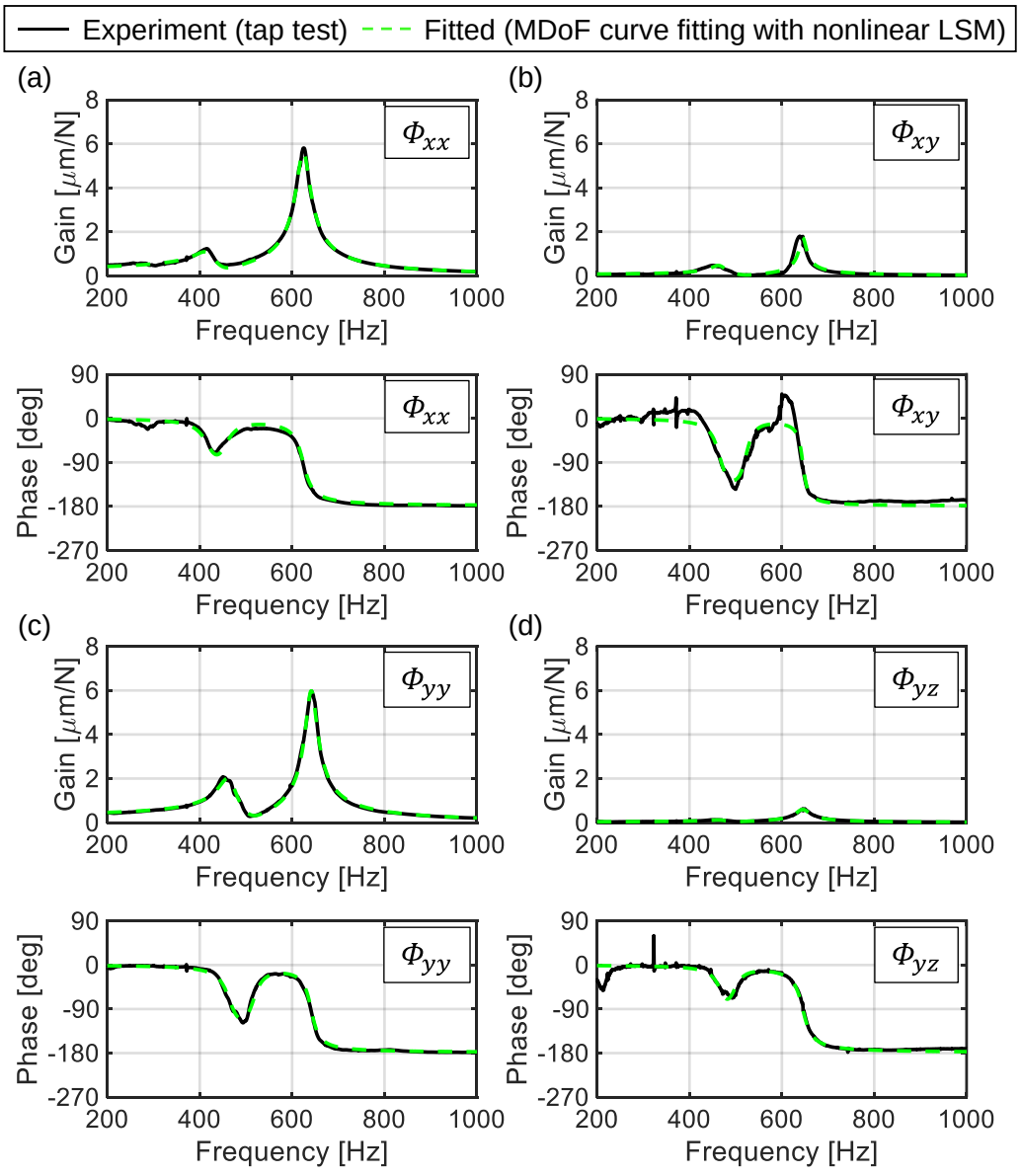

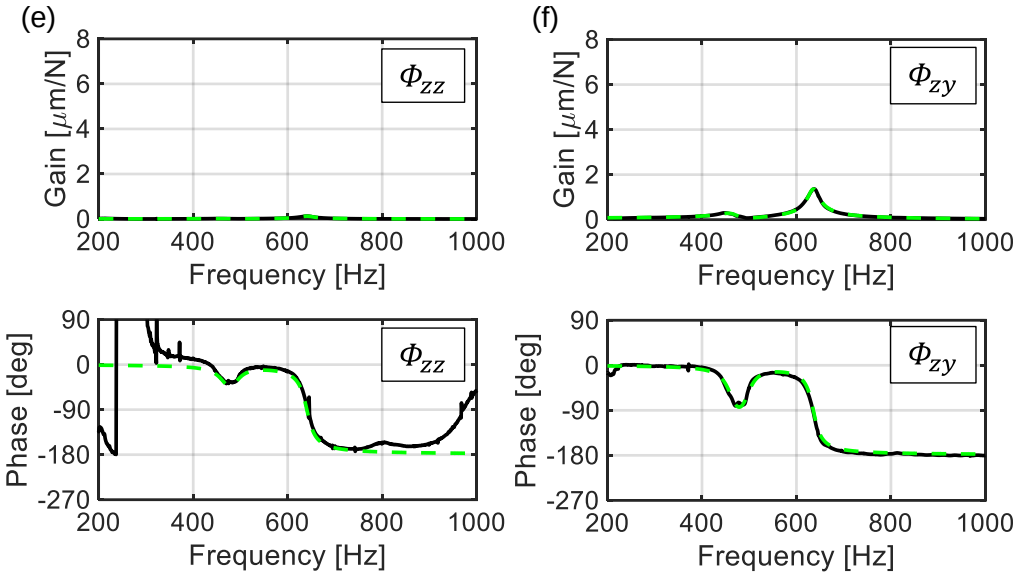

Fig. D-1 Experimental and fitted FRFs of the flexible workpiece in the prototype multi-tasking machine tool: (a) $\Phi_{xx}(i\omega)$; (b) $\Phi_{xy}(i\omega)$; (c) $\Phi_{yy}(i\omega)$; (d) $\Phi_{yz}(i\omega)$; (e) $\Phi_{zz}(i\omega)$; (f) $\Phi_{zy}(i\omega)$

Additionally, a series of ordinal single milling tests (stable slotting) using an SUS303 plate and a similar tool, used for parallel milling, were performed on a three-axis milling center. The specific cutting forces and edge-force coefficients were identified using the average cutting force method [297]. The results are summarized in Fig. D-2 and Table D-2.

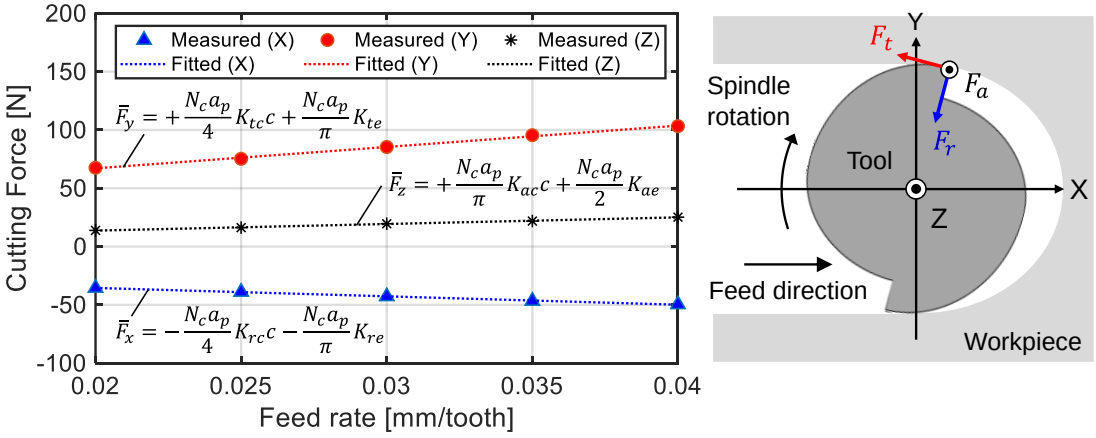

Fig. D-2 Results of the stable slotting tests with SUS303 with various feed rates c ($N_c = 2$, $a_p = 2.0$ mm, and $S = 1000$ min^{-1}. The cutting force was measured by a Kistler type 9257B piezoelectric table dynamometer.)

Table D-2 Identified cutting force coeffcients in the SUS303 plate

Direction	Tangential (K_{tc}, K_{te})	Radial (K_{rc}, K_{re})	Axial (K_{ac}, K_{ae})
Specific cutting force [MPa]	1831	720	446
Edge force [N/mm]	24	17	1.2

E) Net inflow of energy in the tool swing parallel turning

As the vibration direction was assumed to coincide with the X-direction, only the net inflow of energy owing to the cutting force in the X-direction was considered. From Eq. (5-11), the cutting force in the X-direction at the workpiece can be written as follows:

$$F_x^{\mathrm{w}}(t) = -2K_{tc}b_c d_f[x^{\mathrm{w}}(t) + \mu_c x^{\mathrm{w}}(t-\tau)], \qquad \text{where } d_f = \mu_f \cos\eta \tag{E-1}$$

Note that an equal pitch was assumed (i.e., $\tau^{\mathrm{t1}} = \tau^{\mathrm{t2}} = \tau = 60/(N_c S_n)$; $N_c = 2$). Similar to Eqs. (4-3) and (4-4), the workpiece vibration is defined as follows:

$$x^{\mathrm{w}}(t) = A_c \cos(\omega_c t + \psi_c) \;\rightarrow\; x^{\mathrm{w}}(t-\tau) = A_c \cos(\omega_c t - \omega_c \tau + \psi_c) \tag{E-2}$$

As the TSM with a sinusoidal manner is inherently the same as SSSV, the previous vibration with time-varying delay can be expressed as follows, similar to Eq. (4-16):

$$x^{\mathrm{w}}\big(t-\tau(t)\big) \approx A_c \sum_{l=-\infty}^{\infty} J_l(m_f) \cos\big((\omega_{cn} + l\omega_{sw})t - \varepsilon_{cn} + \psi_c\big) \tag{E-3}$$

Here, in the TSM process, even the MI is defined in the same way. Consequently, focusing only on the terms related to the regeneration, the process energy balance is defined as follows:

$$\begin{aligned} E_f &= \int_{t_b}^{t_e} F_x^{\mathrm{w}}(t)\cdot \dot{x}^{\mathrm{w}}(t)dt \approx \int_{t_b}^{t_e} -2\mu_c K_{tc} b_c d_f x^{\mathrm{w}}\big(t-\tau(t)\big)\dot{x}^{\mathrm{w}}(t)\,dt \\ &\approx \mu_c K_{tc} b_c d_f A_c^2 \omega_{cn} \times \sum_{l=-\infty}^{\infty} J_l(m_f) \left\{ \begin{array}{c} \displaystyle\int_{t_b}^{t_e} \sin\big((2\omega_{cn} + l\omega_{sw})t - \varepsilon_{cn} + 2\psi_c\big)\,dt \\ \displaystyle -\int_{t_b}^{t_e} \sin(l\omega_{sw}t - \varepsilon_{cn})\,dt \end{array} \right\} \end{aligned} \tag{E-4}$$

By comparing Eqs. (4-26) and (E-4), the process energy balance in the TSM cycle (i.e., $[t_b, t_e] = [0, 2\pi/\omega_{sw}]$) can be easily deduced as follows:

$$E_f \rightarrow \frac{2\pi\mu_c K_{tc} b_c d_f A_c^2 \omega_{cn} J_0(m_f)}{\omega_{sw}} \sin\varepsilon_{cn} \tag{E-5}$$

From the above, Eq. (E-5) become positive in the CSS process (i.e., $J_0(0) = 1$) under $0 < \varepsilon_{cn} < \pi$ (Eq. (5-21)), as the other coefficients are generally positive. Therefore, it can be interpreted that chatter would occur within $0 < \varepsilon_{cn} < \pi$ in equal pitch parallel turning. Additionally, the accumulated net inflow of energy becomes double in the CSS condition, which corresponds to a double regeneration gain.

References

[1] Brecher C, Jeschke S, Schuh G, Aghassi S, Arnoscht J, Bauhoff F, et al. Integrative Production Technology for High-wage Countries. Integr. Prod. Technol. High-Wage Ctries., Berlin, Heidelberg: Springer Berlin Heidelberg; 2012, p. 17–76. https://doi.org/10.1007/978-3-642-21067-9_2.

[2] Altintas Y, Verl A, Brecher C, Uriarte L, Pritschow G. Machine tool feed drives. CIRP Ann 2011;60(2):779–96. https://doi.org/10.1016/j.cirp.2011.05.010.

[3] Moriwaki T. Multi-functional machine tool. CIRP Ann 2008;57(2):736–49. https://doi.org/10.1016/j.cirp.2008.09.004.

[4] Nakamoto K, Takeuchi Y. Recent Advances in multiaxis control and multitasking machining. Int J Autom Technol 2017;11(2):140–54. https://doi.org/10.20965/ijat.2017.p0140.

[5] Nakanishi K, Sawada M, Sakamoto J. A newly developed multi-axis controlled turning machine equipped with a swing type turret head. Int J Autom Technol 2015;9(6):707–13. https://doi.org/10.20965/ijat.2015.p0707.

[6] Lauwers B, Klocke F, Klink A, Tekkaya AE, Neugebauer R, Mcintosh D. Hybrid processes in manufacturing. CIRP Ann 2014;63(2):561–83. https://doi.org/10.1016/j.cirp.2014.05.003.

[7] Yamazaki T. Development of a hybrid multi-tasking machine tool: integration of additive manufacturing technology with CNC machining. Procedia CIRP 2016;42:81–6. https://doi.org/10.1016/j.procir.2016.02.193.

[8] Morimura S, Sugiura H, Iguchi K, Yoshimura T, Shibata T. Development of a fully integrated machine tool with built-in robot. J Japan Soc Precis Eng 2020;86(2):136–9 (in Japanese). https://doi.org/10.2493/jjspe.86.136.

[9] Gao RX, Wang L, Helu M, Teti R. Big data analytics for smart factories of the future. CIRP Ann 2020;69(2):668–92. https://doi.org/10.1016/j.cirp.2020.05.002.

[10] Möhring H-C, Wiederkehr P, Erkorkmaz K, Kakinuma Y. Self-optimizing machining systems. CIRP Ann 2020;69(2):740–63. https://doi.org/10.1016/j.cirp.2020.05.007.

[11] Monostori L, Kádár B, Bauernhansl T, Kondoh S, Kumara S, Reinhart G, et al. Cyber-physical systems in manufacturing. CIRP Ann 2016;65(2):621–41. https://doi.org/10.1016/j.cirp.2016.06.005.

[12] Liu C, Xu X. Cyber-physical machine tool – the era of machine tool 4.0. Procedia CIRP 2017;63:70–5. https://doi.org/10.1016/j.procir.2017.03.078.

[13] Qiao Q, Wang J, Ye L, Gao RX. Digital twin for machining tool condition prediction. Procedia CIRP 2019;81:1388–93. https://doi.org/10.1016/j.procir.2019.04.049.

[14] Tseng GWG, Chen CQG, Erkorkmaz K, Engin S. Digital shadow identification from feed drive structures for virtual process planning. CIRP J Manuf Sci Technol 2019;24:55–65. https://doi.org/10.1016/j.cirpj.2018.11.002.

[15] Sudo M, Aoyama H. Basic development of data sharing CNC system (case study on high accuracy machining of characteristic lines). J Adv Mech Des Syst Manuf 2020;14(1):JAMDSM0003. https://doi.org/10.1299/jamdsm.2020jamdsm0003.

[16] Sencer B, Tajima S. Frequency optimal feed motion planning in computer numerical

controlled machine tools for vibration avoidance. J Manuf Sci Eng 2017;139(1):011006. https://doi.org/10.1115/1.4034140.

[17] Sencer B, Dumanli A, Yamada Y. Spline interpolation with optimal frequency spectrum for vibration avoidance. CIRP Ann 2018;67(1):377–80. https://doi.org/10.1016/j.cirp.2018.03.002.

[18] Dumanli A, Sencer B. Robust trajectory generation for multi-axis vibration avoidance. IEEE/ASME Trans Mechatronics 2020;25(6):2938–49. https://doi.org/10.1109/TMECH.2020.2999743.

[19] Sencer B, Kakinuma Y, Yamada Y. Linear Interpolation of machining tool-paths with robust vibration avoidance and contouring error control. Precis Eng 2020;66:269–81. https://doi.org/10.1016/j.precisioneng.2020.04.007.

[20] Dumanli A, Sencer B. Pre-compensation of servo tracking errors through data-based reference trajectory modification. CIRP Ann 2019;68(1):397–400. https://doi.org/10.1016/j.cirp.2019.03.017.

[21] Dumanli A, Sencer B. Data-driven iterative trajectory shaping for precision control of flexible feed drives. IEEE/ASME Trans Mechatronics 2020 (in press). https://doi.org/10.1109/TMECH.2020.3045444.

[22] Altintas Y, Kersting P, Biermann D, Budak E, Denkena B, Lazoglu I. Virtual process systems for part machining operations. CIRP Ann 2014;63(2):585–605. https://doi.org/10.1016/j.cirp.2014.05.007.

[23] Wiederkehr P, Siebrecht T. Virtual machining: capabilities and challenges of process simulations in the aerospace industry. Procedia Manuf 2016;6:80–7. https://doi.org/10.1016/j.promfg.2016.11.011.

[24] Altintas Y, Stepan G, Budak E, Schmitz T, Kilic ZM. Chatter stability of machining operations. J Manuf Sci Eng 2020;142(11):110801. https://doi.org/10.1115/1.4047391.

[25] Altintas Y, Weck M. Chatter stability of metal cutting and grinding. CIRP Ann 2004;53(2):619–42. https://doi.org/10.1016/S0007-8506(07)60032-8.

[26] Biermann D, Kersting P, Surmann T. A general approach to simulating workpiece vibrations during five-axis milling of turbine blades. CIRP Ann 2010;59(1):125–8. https://doi.org/10.1016/j.cirp.2010.03.057.

[27] Tieng H, Yang H-C, Hung M-H, Cheng F-T. A novel virtual metrology scheme for predicting machining precision of machine tools. 2013 IEEE Int. Conf. Robot. Autom., Karlsruhe, Germany: IEEE; 2013, pp. 264–9. https://doi.org/10.1109/ICRA.2013.6630586.

[28] Brecher C, Eckel H-M, Motschke T, Fey M, Epple A. Estimation of the virtual workpiece quality by the use of a spindle-integrated process force measurement. CIRP Ann 2019;68(1):381–4. https://doi.org/10.1016/j.cirp.2019.04.020.

[29] Krüger M, Denkena B. A model-based approach for monitoring of shape deviations in peripheral milling. Int J Adv Manuf Technol 2013;67:2537–50. https://doi.org/10.1007/s00170-012-4672-4.

[30] Fujishima M, Ohno K, Nishikawa S, Nishimura K, Sakamoto M, Kawai K. Study of sensing technologies for machine tools. CIRP J Manuf Sci Technol 2016;14:71–5. https://doi.org/10.1016/j.cirpj.2016.05.005.

[31] Möhring H-C, Litwinski KM, Gümmer O. Process monitoring with sensory machine tool components. CIRP Ann 2010;59(1):383–6.

https://doi.org/10.1016/j.cirp.2010.03.087.

[32] Möhring H-C, Bertram O. Integrated autonomous monitoring of ball screw drives. CIRP Ann 2012;61(1):355–8. https://doi.org/10.1016/j.cirp.2012.03.138.

[33] Zaeh MF, Kleinwort R, Fagerer P, Altintas Y. Automatic tuning of active vibration control systems using inertial actuators. CIRP Ann 2017;66(1):365–8. https://doi.org/10.1016/j.cirp.2017.04.051.

[34] Kleinwort R, Platz J, Zaeh MF. Adaptive active vibration control for machine tools with highly position-dependent dynamics. Int J Autom Technol 2018;12(5):631–41. https://doi.org/10.20965/ijat.2018.p0631.

[35] Matsubara A, Maeda M, Yamaji I. Vibration suppression of boring bar by piezoelectric actuators and LR circuit. CIRP Ann 2014;63(1):373–6. https://doi.org/10.1016/j.cirp.2014.03.132.

[36] Cao H, Zhang X, Chen X. The concept and progress of intelligent spindles: a review. Int J Mach Tools Manuf 2017;112:21–52. https://doi.org/10.1016/j.ijmachtools.2016.10.005.

[37] Abele E, Altintas Y, Brecher C. Machine tool spindle units. CIRP Ann 2010;59(2):781–802. https://doi.org/10.1016/j.cirp.2010.05.002.

[38] Neugebauer R, Denkena B, Wegener K. Mechatronic systems for machine tools. CIRP Ann 2007;56(2):657–86. https://doi.org/10.1016/j.cirp.2007.10.007.

[39] Denkena B, Koeller M. Simulation based parameterization for process monitoring of machining operations. Procedia CIRP 2013;12:79–84. https://doi.org/10.1016/j.procir.2013.09.015.

[40] Altintas Y, Aslan D. Integration of virtual and on-line machining process control and monitoring. CIRP Ann 2017;66(1):349–52. https://doi.org/10.1016/j.cirp.2017.04.047.

[41] Nouri M, Fussell BK, Ziniti BL, Linder E. Real-time tool wear monitoring in milling using a cutting condition independent method. Int J Mach Tools Manuf 2015;89:1–13. https://doi.org/10.1016/j.ijmachtools.2014.10.011.

[42] Putz M, Frieß U, Wabner M, Friedrich A, Zander A, Schlegel H. State-based and self-adapting algorithm for condition monitoring. Procedia CIRP 2017;62:311–6. https://doi.org/10.1016/j.procir.2016.06.073.

[43] Altintas Y, Brecher C, Week M, Witt S. Virtual machine tool. CIRP Ann 2005;54(2):115–38. https://doi.org/10.1016/s0007-8506(07)60022-5.

[44] Kadir AA, Xu X, Hämmerle E. Virtual machine tools and virtual machining — a technological review. Robot Comput Integr Manuf 2011;27(3):494–508. https://doi.org/10.1016/j.rcim.2010.10.003.

[45] Noguchi S, Sato R, Nishida I, Shirase K. Coupled simulation between machine tool behavior and cutting force using voxel simulator. Proc. Int. Conf. Lead. Edge Manuf. 21st century: LEM21 2017;2017.9:044. https://doi.org/10.1299/jsmelem.2017.9.044.

[46] Koike R, Kakinuma Y, Aoyama T, Ohnishi K. Development of sensor-less wear monitoring method by means of servo information based on disturbance observer theory. Proc Int Conf Lead Edge Manuf 21st century: LEM21 2013;2013.7:457–62. https://doi.org/10.1299/jsmelem.2013.7.457.

[47] Corne R, Nath C, El Mansori M, Kurfess T. Study of spindle power data with neural

network for predicting real-time tool wear/breakage during inconel drilling. J Manuf Syst 2017;43(2):287–95. https://doi.org/10.1016/j.jmsy.2017.01.004.

[48] Rivero A, López de Lacalle LN, Luz Penalva M. Tool wear detection in dry high-speed milling based upon the analysis of machine internal signals. Mechatronics 2008;18(10):627–33. https://doi.org/10.1016/j.mechatronics.2008.06.008.

[49] Pejryd L, Repo J, Beno T. Machine tool internal encoders as sensors for the detection of tool wear. Procedia CIRP 2012;4:46–51. https://doi.org/10.1016/j.procir.2012.10.009.

[50] Lee JM, Choi DK, Kim J, Chu CN. Real-time tool breakage monitoring for NC milling process. CIRP Ann 1995;44(1):59–62. https://doi.org/10.1016/S0007-8506(07)62275-6.

[51] Koike R, Kakinuma Y, Aoyama T. Drill fracture detection by integrating disturbance observer and rotational digital filter. CIRP J Manuf Sci Technol 2014;7(3):177–84. https://doi.org/10.1016/j.cirpj.2014.04.001.

[52] Koike R, Ohnishi K, Aoyama T. A sensorless approach for tool fracture detection in milling by integrating multi-axial servo information. CIRP Ann 2016;65(1):385–8. https://doi.org/10.1016/j.cirp.2016.04.101.

[53] Aslan D, Altintas Y. On-line chatter detection in milling using drive motor current commands extracted from CNC. Int J Mach Tools Manuf 2018;132:64–80. https://doi.org/10.1016/j.ijmachtools.2018.04.007.

[54] Kakinuma Y, Sudo Y, Aoyama T. Detection of chatter vibration in end milling applying disturbance observer. CIRP Ann 2011;60(1):109–12. https://doi.org/10.1016/j.cirp.2011.03.080.

[55] Koike R, Kakinuma Y, Aoyama T, Ohnishi K. Development of chatter vibration detection utilizing disturbance observer (2nd report). J Japan Soc Precis Eng 2015;81(7):692–8 (in Japanese). https://doi.org/10.2493/jjspe.81.692.

[56] Bergmann B, Witt M. Feeling machine for material-specific machining. CIRP Ann 2020;69(1):353–6. https://doi.org/10.1016/j.cirp.2020.04.102.

[57] Nishida I, Tsuyama R, Shirase K, Onishi M, Koarashi K. Development of innovative intelligent machine tool based on CAM-CNC integration concept − adaptive control based on predicted cutting force −. Int J Autom Technol 2019;13(3):373–81. https://doi.org/10.20965/ijat.2019.p0373.

[58] Hasegawa T, Sato R, Shirase K. Cutting force simulation referring workpiece voxel model for end-milling operation and adaptive control based on predicted cutting force. J Japan Soc Precis Eng 2016;82(5):467–72 (in Japanese). https://doi.org/10.2493/jjspe.82.467.

[59] Denkena B, Boujnah H. Feeling machines for online detection and compensation of tool deflection in milling. CIRP Ann 2018;67(1):423–6. https://doi.org/10.1016/j.cirp.2018.04.110.

[60] Shamoto E, Fujimaki S, Sencer B, Suzuki N, Kato T, Hino R. A novel tool path/posture optimization concept to avoid chatter vibration in machining – proposed concept and its verification in turning. CIRP Ann 2012;61(1):331–4. https://doi.org/10.1016/j.cirp.2012.03.133.

[61] Soliman E, Ismail F. A control system for chatter avoidance by ramping the spindle speed. J Manuf Sci Eng 1998;120(4):674–83. https://doi.org/10.1115/1.2830206.

[62] Gao W, Haitjema H, Fang FZ, Leach RK, Cheung CF, Savio E, et al. On-machine and in-process surface metrology for precision manufacturing. CIRP Ann 2019;68(2):843–66.

https://doi.org/10.1016/j.cirp.2019.05.005.

[63] Quintana G, Ciurana J. Chatter in machining processes: a review. Int J Mach Tools Manuf 2011;51(5):363–76. https://doi.org/10.1016/j.ijmachtools.2011.01.001.

[64] Munoa J, Beudaert X, Dombovari Z, Altintas Y, Budak E, Brecher C, et al. Chatter suppression techniques in metal cutting. CIRP Ann 2016;65(2):785–808. https://doi.org/10.1016/j.cirp.2016.06.004.

[65] Zhu L, Liu C. Recent progress of chatter prediction, detection and suppression in milling. Mech Syst Signal Process 2020;143:106840. https://doi.org/10.1016/j.ymssp.2020.106840.

[66] Shamoto E. Mechanism and suppression of chatter vibrations in cutting. DENKI SEIKO 2011;82:143–55 (in Japanese).

[67] Suzuki N. Chatter vibration in cutting, Part 1. J Japan Soc Precis Eng 2010;76(3):280–4 (in Japanese). https://doi.org/10.2493/jjspe.76.280.

[68] Al-Regib E, Ni J, Lee S-H. Programming spindle speed variation for machine tool chatter suppression. Int J Mach Tools Manuf 2003;43(12):1229–40. https://doi.org/10.1016/S0890-6955(03)00126-3.

[69] Hajikolaei KH, Moradi H, Vossoughi G, Movahhedy MR. Spindle speed variation and adaptive force regulation to suppress regenerative chatter in the turning process. J Manuf Process 2010;12(2):106–15. https://doi.org/10.1016/j.jmapro.2010.08.002.

[70] Zhang H, Ni J. Internal energy based analysis on mechanism of spindle speed variation for regenerative chatter control. J Vib Control 2010;16(2):281–301. https://doi.org/10.1177/1077546309103562.

[71] Ding L, Sun Y, Xiong Z. Online chatter suppression in turning by adaptive amplitude modulation of spindle speed variation. J Manuf Sci Eng 2018;140(12):121003. https://doi.org/10.1115/1.4041248.

[72] Ma C, Ma J, Shamoto E, Moriwaki T. Analysis of regenerative chatter suppression with adding the ultrasonic elliptical vibration on the cutting tool. Precis Eng 2011;35(2):329–38. https://doi.org/10.1016/j.precisioneng.2010.12.004.

[73] Takemura T, Kitamura T, Hoshi T. Active suppression of chatter by programed variation of spindle speed. CIRP Ann 1974;23(1):121–2.

[74] Suzuki N, Ikada T, Hino R, Shamoto E. Comprehensive study on milling conditions to avoid forced / self-excited chatter vibrations. J Japan Soc Precis Eng 2009;75(7):908–14 (in Japanese). https://doi.org/10.2493/jjspe.75.908.

[75] Zhu K, Wong YS, Hong GS. Wavelet analysis of sensor signals for tool condition monitoring: a review and some new results. Int J Mach Tools Manuf 2009;49(7–8):537–53. https://doi.org/10.1016/j.ijmachtools.2009.02.003.

[76] Kurada S, Bradley C. A review of machine vision sensors for tool condition monitoring. Comput Ind 1997;34(1):55–72. https://doi.org/10.1016/S0166-3615(96)00075-9.

[77] Dutta S, Pal SK, Mukhopadhyay S, Sen R. Application of digital image processing in tool condition monitoring: a review. CIRP J Manuf Sci Technol 2013;6(3):212–32. https://doi.org/10.1016/j.cirpj.2013.02.005.

[78] Dai Y, Zhu K. A machine vision system for micro-milling tool condition monitoring. Precis Eng 2018;52:183–91. https://doi.org/10.1016/j.precisioneng.2017.12.006.

[79] Lei N, Soshi M. Vision-based system for chatter identification and process optimization

in high-speed milling. Int J Adv Manuf Technol 2017;89:2757–69. https://doi.org/10.1007/s00170-016-9770-2.

[80] Eppel A, Enikov ET, Insperger T, Gabor S. Feasibility study of optical detection of chatter vibration during milling. Int J Optomechatronics 2010;4(2):195–214. https://doi.org/10.1080/15599612.2010.484520.

[81] Shimana K, Kondo E, Karashima H, Kawagoishi N. Fast detection of chatter in end-milling using pseudo auto-correlation function. Int J Autom Technol 2012;6(6):728–35. https://doi.org/10.20965/ijat.2012.p0728.

[82] Abellan-Nebot JV, Romero Subirón F. A review of machining monitoring systems based on artificial intelligence process models. Int J Adv Manuf Technol 2010;47:237–57. https://doi.org/10.1007/s00170-009-2191-8.

[83] Lauro CH, Brandão LC, Baldo D, Reis RA, Davim JP. Monitoring and processing signal applied in machining processes – a review. Meas J Int Meas Confed 2014;58:73–86. https://doi.org/10.1016/j.measurement.2014.08.035.

[84] Li X, Dong S, Yuan Z. Discrete wavelet transform for tool breakage monitoring. Int J Mach Tools Manuf 1999;39(12):1935–44. https://doi.org/10.1016/S0890-6955(99)00021-8.

[85] Jemielniak K, Arrazola PJ. Application of AE and cutting force signals in tool condition monitoring in micro-milling. CIRP J Manuf Sci Technol 2008;1(2):97–102. https://doi.org/10.1016/j.cirpj.2008.09.007.

[86] Chiou RY, Liang SY. Analysis of acoustic emission in chatter vibration with tool wear effect in turning. Int J Mach Tools Manuf 2000;40(7):927–41. https://doi.org/10.1016/S0890-6955(99)00093-0.

[87] Delio T, Tlusty J, Smith S. Use of audio signals for chatter detection and control. J Eng Ind 1992;114(2):146–57. https://doi.org/10.1115/1.2899767.

[88] Li XQ, Wong YS, Nee AYC. Tool wear and chatter detection using the coherence function of two crossed accelerations. Int J Mach Tools Manuf 1997;37(4):425–35. https://doi.org//10.1016/S0890-6955(96)00030-2.

[89] Lamraoui M, Thomas M, El Badaoui M. Cyclostationarity approach for monitoring chatter and tool wear in high speed milling. Mech Syst Signal Process 2014;44(1–2):177–98. https://doi.org/10.1016/j.ymssp.2013.05.001.

[90] Ricardo Castro L, Viéville P, Lipinski P. Correction of dynamic effects on force measurements made with piezoelectric dynamometers. Int J Mach Tools Manuf 2006;46(14):1707–15. https://doi.org/10.1016/j.ijmachtools.2005.12.006.

[91] Tlusty J, Andrews GC. A critical review of sensors for unmanned machining. CIRP Ann 1983;32(2):563–72. https://doi.org/10.1016/S0007-8506(07)60184-X.

[92] Kuljanic E, Sortino M, Totis G. Multisensor approaches for chatter detection in milling. J Sound Vib 2008;312(4–5):672–93. https://doi.org/10.1016/j.jsv.2007.11.006.

[93] Jun MB, Burak Ozdoganlar O, DeVor RE, Kapoor SG, Kirchheim A, Schaffner G. Evaluation of a spindle-based force sensor for monitoring and fault diagnosis of machining operations. Int J Mach Tools Manuf 2002;42(6):741–51. https://doi.org/10.1016/S0890-6955(01)00156-0.

[94] Altintas Y, Park SS. Dynamic compensation of spindle-integrated force sensors. CIRP Ann 2004;53(1):305–8. https://doi.org/10.1016/S0007-8506(07)60703-3.

[95] Park SS, Altintas Y. Dynamic compensation of spindle integrated force sensors with Kalman filter. J Dyn Syst Meas Control 2004;126(3):443–52. https://doi.org/10.1115/1.1789531.

[96] Klocke F, Adams O, Auerbach T, Gierlings S, Kamps S, Rekers S, et al. New concepts of force measurement systems for specific machining processes in aeronautic industry. CIRP J Manuf Sci Technol 2015;9:31–8. https://doi.org/10.1016/j.cirpj.2015.01.006.

[97] van Dijk NJM, Doppenberg EJJ, Faassen RPH, van de Wouw N, Oosterling JAJ, Nijmeijer H. Automatic in-process chatter avoidance in the high-speed milling process. J Dyn Syst Meas Control 2010;132(3):031006. https://doi.org/10.1115/1.4000821.

[98] Soliman E, Ismail F. Chatter detection by monitoring spindle drive current. Int J Adv Manuf Technol 1997;13:27–34. https://doi.org/10.1007/BF01179227.

[99] Ohnishi K, Shibata M, Murakami T. Motion control for advanced mechatronics. IEEE/ASME Trans Mechatronics 1996;1(1):56–67. https://doi.org/10.1109/3516.491410.

[100] Yao Z, Mei D, Chen Z. On-line chatter detection and identification based on wavelet and support vector machine. J Mater Process Technol 2010;210(5):713–9. https://doi.org/10.1016/j.jmatprotec.2009.11.007.

[101] Lamraoui M, Barakat M, Thomas M, Badaoui M El. Chatter detection in milling machines by neural network classification and feature selection. J Vib Control 2015;21(7):1251–66. https://doi.org/10.1177/1077546313493919.

[102] Yesilli MC, Khasawneh FA, Otto A. On transfer learning for chatter detection in turning using wavelet packet transform and ensemble empirical mode decomposition. CIRP J Manuf Sci Technol 2020;28:118–35. https://doi.org/10.1016/j.cirpj.2019.11.003.

[103] Altintas Y, Chan PK. In-process detection and suppression of chatter in milling. Int J Mach Tools Manuf 1992;32(3):329–47. https://doi.org/10.1016/0890-6955(92)90006-3.

[104] Yeh L-J, Lai G-J. A study of the monitoring and suppression system for turning slender workpieces. Proc Inst Mech Eng Part B J Eng Manuf 1995;209(3):227–36. https://doi.org/10.1243/PIME_PROC_1995_209_077_02.

[105] Yoon MC, Chin DH. Cutting force monitoring in the endmilling operation for chatter detection. Proc Inst Mech Eng Part B J Eng Manuf 2005;219(6):455–65. https://doi.org/10.1243/095440505X32292.

[106] Berger BS, Minis I, Harley J, Rokni M, Papadopoulos M. Wavelet based cutting state identification. J Sound Vib 1998;213(5):813–27. https://doi.org/10.1006/jsvi.1997.1495.

[107] Mei Y, Mo R, Sun H, Bu K. Chatter detection in milling based on singular spectrum analysis. Int J Adv Manuf Technol 2018;95:3475–86. https://doi.org/10.1007/s00170-017-1366-y.

[108] Caliskan H, Kilic ZM, Altintas Y. On-line energy-based milling chatter detection. J Manuf Sci Eng 2018;140(11):111012. https://doi.org/10.1115/1.4040617.

[109] Yang K, Wang G, Dong Y, Zhang Q, Sang L. Early chatter identification based on an optimized variational mode decomposition. Mech Syst Signal Process 2019;115:238–54. https://doi.org/10.1016/j.ymssp.2018.05.052.

[110] Tao J, Qin C, Liu C. A synchroextracting-based method for early chatter identification of robotic drilling process. Int J Adv Manuf Technol 2019;100:273–85. https://doi.org/10.1007/s00170-018-2739-6.

[111] Liu C, Zhu L, Ni C. Chatter detection in milling process based on VMD and energy entropy. Mech Syst Signal Process 2018;105:169–82. https://doi.org/10.1016/j.ymssp.2017.11.046.

[112] Zhang Z, Li H, Meng G, Tu X, Cheng C. Chatter detection in milling process based on the energy entropy of VMD and WPD. Int J Mach Tools Manuf 2016;108:106–12. https://doi.org/10.1016/j.ijmachtools.2016.06.002.

[113] Cao H, Zhou K, Chen X. Chatter identification in end milling process based on EEMD and nonlinear dimensionless indicators. Int J Mach Tools Manuf 2015;92:52–9. https://doi.org/10.1016/j.ijmachtools.2015.03.002.

[114] Xi S, Cao H, Zhang X, Chen X. Zoom synchrosqueezing transform-based chatter identification in the milling process. Int J Adv Manuf Technol 2019;101:1197–213. https://doi.org/10.1007/s00170-018-3002-x.

[115] Chen Y, Li H, Hou L, Bu X. Feature extraction using dominant frequency bands and time-frequency image analysis for chatter detection in milling. Precis Eng 2019;56:235–45. https://doi.org/10.1016/j.precisioneng.2018.12.004.

[116] Jacobsen E, Lyons R. The sliding DFT. IEEE Signal Process Mag 2003;20(2):74–80. https://doi.org/10.1109/MSP.2003.1184347.

[117] Ota H, Kawai T, Yoshino T, Ye J. Monitoring of cutting conditions by means of vibration analysis. (1st report: monitoring of chatter). Trans Japan Soc Mech Eng Ser C 1991;57(540):2752–7 (in Japanese). https://doi.org/10.1299/kikaic.57.2752.

[118] Siddhpura M, Paurobally R. A review of chatter vibration research in turning. Int J Mach Tools Manuf 2012;61:27–47. https://doi.org/10.1016/j.ijmachtools.2012.05.007.

[119] Kuljanic E, Totis G, Sortino M. Development of an intelligent multisensor chatter detection system in milling. Mech Syst Signal Process 2009;23(5):1704–18. https://doi.org/10.1016/j.ymssp.2009.01.003.

[120] Duro JA, Padget JA, Bowen CR, Kim HA, Nassehi A. Multi-sensor data fusion framework for CNC machining monitoring. Mech Syst Signal Process 2016;66–67:505–20. https://doi.org/10.1016/j.ymssp.2015.04.019.

[121] Liang SY, Hecker RL, Landers RG. Machining process monitoring and control: the state-of-the-art. J Manuf Sci Eng 2004;126(2):297–310. https://doi.org/10.1115/1.1707035.

[122] Teti R, Jemielniak K, O'Donnell G, Dornfeld D. Advanced monitoring of machining operations. CIRP Ann 2010;59(2):717–39. https://doi.org/10.1016/j.cirp.2010.05.010.

[123] Tobias J, Fishwick W. Theory of regenerative machine tool chatter. Engineer 1958;205:199–203.

[124] Tlusty J, Polacek M. The stability of machine tools against self excited vibrations in machining. Proc. ASME Int. Res. Prod. Eng., ASME; 1963, pp. 465–474.

[125] Altintaş Y, Budak E. Analytical prediction of stability lobes in milling. CIRP Ann 1995;44(1):357–62. https://doi.org/10.1016/S0007-8506(07)62342-7.

[126] Budak E, Altintas¸ Y. Analytical prediction of chatter stability in milling—part I: general formulation. J Dyn Syst Meas Control 1998;120(1):22–30. https://doi.org/10.1115/1.2801317.

[127] Davies MA, Pratt JR, Dutterer BS, Burns TJ. The stability of low radial immersion milling. CIRP Ann 2000;49(1):37–40. https://doi.org/10.1016/S0007-8506(07)62891-1.

[128] Merdol SD, Altintas Y. Multi frequency solution of chatter stability for low immersion milling. J Manuf Sci Eng 2004;126(3):459–66. https://doi.org/10.1115/1.1765139.

[129] Insperger T, Stépán G. Semi-discretization method for delayed systems. Int J Numer Methods Eng 2002;55(5):503–18. https://doi.org/10.1002/nme.505.

[130] Insperger T, Stépán G. Updated semi-discretization method for periodic delay-differential equations with discrete delay. Int J Numer Methods Eng 2004;61(1):117–41. https://doi.org/10.1002/nme.1061.

[131] Jiang S, Sun Y, Yuan X, Liu W. A second-order semi-discretization method for the efficient and accurate stability prediction of milling process. Int J Adv Manuf Technol 2017;92:583–95. https://doi.org/10.1007/s00170-017-0171-y.

[132] Sastry S, Kapoor SG, DeVor RE. Floquet theory based approach for stability analysis of the variable speed face-milling process. J Manuf Sci Eng 2002;124(1):10–7. https://doi.org/10.1115/1.1418695.

[133] Ding Y, Zhu L, Zhang X, Ding H. A full-discretization method for prediction of milling stability. Int J Mach Tools Manuf 2010;50(5):502–9. https://doi.org/10.1016/j.ijmachtools.2010.01.003.

[134] Ozoegwu CG, Omenyi SN, Ofochebe SM. Hyper-third order full-discretization methods in milling stability prediction. Int J Mach Tools Manuf 2015;92:1–9. https://doi.org/10.1016/j.ijmachtools.2015.02.007.

[135] Shamoto E, Akazawa K. Analytical prediction of chatter stability in ball end milling with tool inclination. CIRP Ann 2009;58(1):351–4. https://doi.org/10.1016/j.cirp.2009.03.087.

[136] Dombovari Z, Altintas Y, Stepan G. The effect of serration on mechanics and stability of milling cutters. Int J Mach Tools Manuf 2010;50(6):511–20. https://doi.org/10.1016/j.ijmachtools.2010.03.006.

[137] Turner S, Merdol D, Altintas Y, Ridgway K. Modelling of the stability of variable helix end mills. Int J Mach Tools Manuf 2007;47(9):1410–6. https://doi.org/10.1016/j.ijmachtools.2006.08.028.

[138] Dombovari Z, Stepan G. The effect of helix angle variation on milling stability. J Manuf Sci Eng 2012;134(5):051015. https://doi.org/10.1115/1.4007466.

[139] Otto A, Radons G. Frequency domain stability analysis of milling processes with variable helix tools. Nineth Int Conf High Speed Mach., San Sebastian, Spain: 2012. https://doi.org/10.13140/2.1.1253.8882.

[140] Altıntas¸ Y, Engin S, Budak E. Analytical stability prediction and design of variable pitch cutters. J Manuf Sci Eng 1999;121(2):173–8. https://doi.org/10.1115/1.2831201.

[141] Olgac N, Sipahi R. Dynamics and stability of variable-pitch milling. J Vib Control 2007;13(7):1031–43. https://doi.org/10.1177/1077546307078754.

[142] Sellmeier V, Denkena B. Stable islands in the stability chart of milling processes due to unequal tooth pitch. Int J Mach Tools Manuf 2011;51(2):152–64. https://doi.org/10.1016/j.ijmachtools.2010.09.007.

[143] Zatarain M, Dombovari Z. Stability analysis of milling with irregular pitch tools by the implicit subspace iteration method. Int J Dyn Control 2014;2:26–34. https://doi.org/10.1007/s40435-013-0052-7.

[144] Iglesias A, Dombovari Z, Gonzalez G, Munoa J, Stepan G. Optimum selection of variable

pitch for chatter suppression in face milling operations. Materials 2018;12(1):112. https://doi.org/10.3390/ma12010112.

[145] Kurata Y, Suzuki N, Hino R, Shamoto E. Chatter stability limits in end milling with anisotropic flexible tools. J Japan Soc Precis Eng 2011;77(1):97–104 (in Japanese). https://doi.org/10.2493/jjspe.77.97.

[146] Comak A, Ozsahin O, Altintas Y. Stability of milling operations with asymmetric cutter dynamics in rotating coordinates. J Manuf Sci Eng 2016;138(8):081004. https://doi.org/10.1115/1.4032585.

[147] Altintas Y, Ko JH. Chatter stability of plunge milling. CIRP Ann 2006;55(1):361–4. https://doi.org/10.1016/S0007-8506(07)60435-1.

[148] Sexton JS, Milne RD, Stone BJ. A stability analysis of single-point machining with varying spindle speed. Appl Math Model 1977;1(6):310–8. https://doi.org/10.1016/0307-904X(77)90062-2.

[149] Otto A, Kehl G, Mayer M, Radons G. Stability analysis of machining with spindle speed variation. Adv Mater Res 2011;223:600–9. https://doi.org/10.4028/www.scientific.net/AMR.223.600.

[150] Insperger T, Stepan G. Stability analysis of turning with periodic spindle speed modulation via semidiscretization. J Vib Control 2004;10(12):1835–55. https://doi.org/10.1177/1077546304044891.

[151] Zatarain M, Bediaga I, Muñoa J, Lizarralde R. Stability of milling processes with continuous spindle speed variation: Analysis in the frequency and time domains, and experimental correlation. CIRP Ann 2008;57(1):379–84. https://doi.org/10.1016/j.cirp.2008.03.067.

[152] Niu J, Ding Y, Zhu L, Ding H. Stability Analysis of milling processes with periodic spindle speed variation via the variable-step numerical integration method. J Manuf Sci Eng 2016;138(11):114501. https://doi.org/10.1115/1.4033043.

[153] Insperger T, Schmitz TL, Burns TJ, Stépán G. Comparison of analytical and numerical simulations for variable spindle speed turning. ASME 2003 Int. Mech. Eng. Congr. Expo., Washington, DC, USA: ASME; 2003, p. 41–7. https://doi.org/10.1115/IMECE2003-41809.

[154] Stépán G. Modelling nonlinear regenerative effects in metal cutting. Philos Trans R Soc A 2001;359(1781):739–57. https://doi.org/10.1098/rsta.2000.0753.

[155] Bayly PV, Halley JE, Mann BP, Davies MA. Stability of interrupted cutting by temporal finite element analysis. J Manuf Sci Eng 2003;125(2):220–5. https://doi.org/10.1115/1.1556860.

[156] Szalai R, Stépán G. Lobes and lenses in the stability chart of interrupted turning. J Comput Nonlinear Dynam 2006;1(3):205–11. https://doi.org/10.1115/1.2198216.

[157] Landers RG, Ulsoy AG. Nonlinear feed effect in machining chatter analysis. J Manuf Sci Eng 2008;130(1):011017. https://doi.org/10.1115/1.2783276.

[158] Hayasaka T, Jung H, Azuma K, Shamoto E. Consolidated chatter stability prediction model considering material removing and ploughing processes. Precis Eng 2019;59:120–33. https://doi.org/10.1016/j.precisioneng.2019.06.006.

[159] Eynian M, Altintas Y. Chatter stability of general turning operations with process damping. J Manuf Sci Eng 2009;131(4):041005. https://doi.org/10.1115/1.3159047.

[160] Ahmadi K, Ismail F. Analytical stability lobes including nonlinear process damping effect on machining chatter. Int J Mach Tools Manuf 2011;51(4):296–308. https://doi.org/10.1016/j.ijmachtools.2010.12.008.

[161] Feng J, Wan M, Gao TQ, Zhang WH. Mechanism of process damping in milling of thin-walled workpiece. Int J Mach Tools Manuf 2018;134:1–19. https://doi.org/10.1016/j.ijmachtools.2018.06.001.

[162] Budak E, Ozturk E. Dynamics and stability of parallel turning operations. CIRP Ann 2011;60(1):383–6. https://doi.org/10.1016/j.cirp.2011.03.028.

[163] Azvar M, Budak E. Multi-dimensional chatter stability for enhanced productivity in different parallel turning strategies. Int J Mach Tools Manuf 2017;123:116–28. https://doi.org/10.1016/j.ijmachtools.2017.08.005.

[164] Budak E, Comak A, Ozturk E. Stability and high performance machining conditions in simultaneous milling. CIRP Ann 2013;62(1):403–6. https://doi.org/10.1016/j.cirp.2013.03.141.

[165] Brecher C, Trofimov Y, Bäumler S. Holistic modelling of process machine interactions in parallel milling. CIRP Ann 2011;60(1):387–90. https://doi.org/10.1016/j.cirp.2011.03.025.

[166] Comak A, Altintas Y. Dynamics and stability of turn-milling operations with varying time delay in discrete time domain. J Manuf Sci Eng 2018;140(10):101013. https://doi.org/10.1115/1.4040726.

[167] Sun T, Qin L, Fu Y, Hou J. Chatter stability of orthogonal turn-milling analyzed by complete discretization method. Precis Eng 2019;56:87–95. https://doi.org/10.1016/j.precisioneng.2018.10.012.

[168] Cordes M, Hintze W, Altintas Y. Chatter stability in robotic milling. Robot Comput Integr Manuf 2019;55(Part A):11–8. https://doi.org/10.1016/j.rcim.2018.07.004.

[169] Urbikain G, Olvera D, López de Lacalle LN, Beranoagirre A, Elías-Zuñiga A. Prediction methods and experimental techniques for chatter avoidance in turning systems: A review. Appl Sci 2019;9(21):4718. https://doi.org/10.3390/app9214718.

[170] Munoa J, Beudaert X, Erkorkmaz K, Iglesias A, Barrios A, Zatarain M. Active suppression of structural chatter vibrations using machine drives and accelerometers. CIRP Ann 2015;64(1):385–8. https://doi.org/10.1016/j.cirp.2015.04.106.

[171] Suzuki N, Nishimura K, Shamoto E, Yoshino K. Effect of cross transfer function on chatter stability in plunge cutting. J Adv Mech Des Syst Manuf 2010;4(5):883–91. https://doi.org/10.1299/jamdsm.4.883.

[172] Altintas Y, Cao Y. Virtual design and optimization of machine tool spindles. CIRP Ann 2005;54(1):379–82. https://doi.org/10.1016/S0007-8506(07)60127-9.

[173] Hayasaka T, Xu Y, Jung H, Shamoto E, Xu L. Regenerative chatter by teeth allocated in the cutting direction with position-dependent modal displacement ratios. CIRP Ann 2019;68(1):409–12. https://doi.org/10.1016/j.cirp.2019.04.003.

[174] Tuysuz O, Altintas Y. Frequency domain updating of thin-walled workpiece dynamics using reduced order substructuring method in machining. J Manuf Sci Eng 2017;139(7):071013. https://doi.org/10.1115/1.4036124.

[175] Shi J, Song Q, Liu Z, Ai X. A novel stability prediction approach for thin-walled component milling considering material removing process. Chinese J Aeronaut 2017;30(5):1789–98. https://doi.org/10.1016/j.cja.2017.05.011.

[176] Suzuki N, Kurata Y, Kato T, Hino R, Shamoto E. Identification of transfer function by inverse analysis of self-excited chatter vibration in milling operations. Precis Eng 2012;36(4):568–75. https://doi.org/10.1016/j.precisioneng.2012.04.004.

[177] Eynian M. In-process identification of modal parameters using dimensionless relationships in milling chatter. Int J Mach Tools Manuf 2019;143:49–62. https://doi.org/10.1016/j.ijmachtools.2019.04.003.

[178] Bachrathy D, Kiss AK, Kossa A, Berezvai S, Hajdu D, Stepan G. In-process monitoring of changing dynamics of a thin-walled component during milling operation by ball shooter excitation. J Manuf Mater Process 2020;4(3):78. https://doi.org/10.3390/jmmp4030078.

[179] Löser M, Otto A, Ihlenfeldt S, Radons G. Chatter prediction for uncertain parameters. Adv Manuf 2018;6:319–33. https://doi.org/10.1007/s40436-018-0230-0.

[180] Totis G, Sortino M. Polynomial Chaos-Kriging approaches for an efficient probabilistic chatter prediction in milling. Int J Mach Tools Manuf 2020;157:103610. https://doi.org/10.1016/j.ijmachtools.2020.103610.

[181] Grossi N, Scippa A, Sallese L, Sato R, Campatelli G. Spindle speed ramp-up test: a novel experimental approach for chatter stability detection. Int J Mach Tools Manuf 2015;89:221–30. https://doi.org/10.1016/j.ijmachtools.2014.11.013.

[182] Koike R, Kakinuma Y, Aoyama T, Ohnishi K. Identification method for stable spindle rotations against chatter by means of servo information. Trans JSME 2015;81(830):15-00387 (in Japanese). https://doi.org/10.1299/transjsme.15-00387.

[183] Cherukuri H, Perez-Bernabeu E, Selles MA, Schmitz TL. A neural network approach for chatter prediction in turning. Procedia Manuf 2019;34:885–92. https://doi.org/10.1016/j.promfg.2019.06.159.

[184] Tunc LT, Ozsahin O. Use of inverse stability solutions for identification of uncertainties in the dynamics of machining processes. Adv Manuf 2018;6:308–18. https://doi.org/10.1007/s40436-018-0233-x.

[185] Brecher C, Chavan P, Epple A. Efficient determination of stability lobe diagrams by in-process varying of spindle speed and cutting depth. Adv Manuf 2018;6:272–9. https://doi.org/10.1007/s40436-018-0225-x.

[186] Mancisidor I, Beudaert X, Etxebarria A, Barcena R, Munoa J, Jugo J. Hardware-in-the-loop simulator for stability study in orthogonal cutting. Control Eng Pract 2015;44:31–44. https://doi.org/10.1016/j.conengprac.2015.07.006.

[187] Stepan G, Beri B, Miklos A, Wohlfart R, Bachrathy D, Porempovics G, et al. On stability of emulated turning processes in HIL environment. CIRP Ann 2019;68(1):405–8. https://doi.org/10.1016/j.cirp.2019.04.035.

[188] Muhammad BB, Wan M, Feng J, Zhang WH. Dynamic damping of machining vibration: a review. Int J Adv Manuf Technol 2017;89:2935–52. https://doi.org/10.1007/s00170-016-9862-z.

[189] Bandivadekar T, Jangid R. Optimization of multiple tuned mass dampers for vibration control of system under external excitation. J Vib Control 2013;19(12):1854–71. https://doi.org/10.1177/1077546312449849.

[190] Yang Y, Muñoa J, Altintas Y. Optimization of multiple tuned mass dampers to suppress machine tool chatter. Int J Mach Tools Manuf 2010;50(9):834–42. https://doi.org/10.1016/j.ijmachtools.2010.04.011.

[191] Wang M, Zan T, Yang Y, Fei R. Design and implementation of nonlinear TMD for chatter suppression: An application in turning processes. Int J Mach Tools Manuf 2010;50(5):474–9. https://doi.org/10.1016/j.ijmachtools.2010.01.004.

[192] Burtscher J, Fleischer J. Adaptive tuned mass damper with variable mass for chatter avoidance. CIRP Ann 2017;66(1):397–400. https://doi.org/10.1016/j.cirp.2017.04.059.

[193] Fei J, Lin B, Yan S, Ding M, Xiao J, Zhang J, et al. Chatter mitigation using moving damper. J Sound Vib 2017;410:49–63. https://doi.org/10.1016/j.jsv.2017.08.033.

[194] Fei J, Lin B, Xiao J, Ding M, Yan S, Zhang X, et al. Investigation of moving fixture on deformation suppression during milling process of thin-walled structures. J Manuf Process 2018;32:403–11. https://doi.org/10.1016/j.jmapro.2018.03.011.

[195] Ozturk E, Barrios A, Sun C, Rajabi S, Munoa J. Robotic assisted milling for increased productivity. CIRP Ann 2018;67(1):427–30. https://doi.org/10.1016/j.cirp.2018.04.031.

[196] Zhang Z, Li H, Meng G, Ren S. Milling chatter suppression in viscous fluid: a feasibility study. Int J Mach Tools Manuf 2017;120:20–6. https://doi.org/10.1016/j.ijmachtools.2017.02.005.

[197] Zhang Z, Li H, Liu X, Zhang W, Meng G. Chatter mitigation for the milling of thin-walled workpiece. Int J Mech Sci 2018;138–139:262–71. https://doi.org/10.1016/j.ijmecsci.2018.02.014.

[198] Munoa J, Sanz-Calle M, Dombovari Z, Iglesias A, Pena-Barrio J, Stepan G. Tuneable clamping table for chatter avoidance in thin-walled part milling. CIRP Ann 2020;69(1):313–6. https://doi.org/10.1016/j.cirp.2020.04.081.

[199] Möhring H-C, Brecher C, Abele E, Fleischer J, Bleicher F. Materials in machine tool structures. CIRP Ann 2015;64(2):725–48. https://doi.org/10.1016/j.cirp.2015.05.005.

[200] Shinagawa M, Shamoto E. Prediction of chatter stability of machine tool with consideration of friction damping in guide (development of basic model and investigation on effects of friction and stiffness). Trans JAPAN Soc Mech Eng Ser C 2012;78(787):1013–25 (in Japanese). https://doi.org/10.1299/kikaic.78.1013.

[201] Maeda O, Cao Y, Altintas Y. Expert spindle design system. Int J Mach Tools Manuf 2005;45(4–5):537–48. https://doi.org/10.1016/j.ijmachtools.2004.08.021.

[202] Mohammadi Y, Azvar M, Budak E. Suppressing vibration modes of spindle-holder-tool assembly through FRF modification for enhanced chatter stability. CIRP Ann 2018;67(1):397–400. https://doi.org/10.1016/j.cirp.2018.03.003.

[203] Gibbons TJ, Ozturk E, Xu L, Sims ND. Chatter avoidance via structural modification of tool-holder geometry. Int J Mach Tools Manuf 2020;150:103514. https://doi.org/10.1016/j.ijmachtools.2019.103514.

[204] Li D, Cao H, Liu J, Zhang X, Chen X. Milling chatter control based on asymmetric stiffness. Int J Mach Tools Manuf 2019;147:103458. https://doi.org/10.1016/j.ijmachtools.2019.103458.

[205] Ozturk E, Comak A, Budak E. Tuning of tool dynamics for increased stability of parallel (simultaneous) turning processes. J Sound Vib 2016;360:17–30. https://doi.org/10.1016/j.jsv.2015.09.009.

[206] Reith MJ, Bachrathy D, Stepan G. Optimal detuning of a parallel turning system—theory and experiments. J Dyn Syst Meas Control 2017;139(1):014503. https://doi.org/10.1115/1.4034497.

[207] Beudaert X, Erkorkmaz K, Munoa J. Portable damping system for chatter suppression on flexible workpieces. CIRP Ann 2019;68(1):423–6. https://doi.org/10.1016/j.cirp.2019.04.010.

[208] Kakinuma Y, Enomoto K, Hirano T, Ohnishi K. Active chatter suppression in turning by band-limited force control. CIRP Ann 2014;63(1):365–8. https://doi.org/10.1016/j.cirp.2014.03.136.

[209] Zatarain M, Bediaga I, Muñoa J, Insperger T. Analysis of directional factors in milling: importance of multi-frequency calculation and of the inclusion of the effect of the helix angle. Int J Adv Manuf Technol 2010;47:535–42. https://doi.org/10.1007/s00170-009-2230-5.

[210] Maulimov M, Sencer B. Effect of directional relations on milling chatter stability and development of a stability index. Procedia Manuf 2018;26:372–82. https://doi.org/10.1016/j.promfg.2018.07.045.

[211] Sun C, Altintas Y. Chatter free tool orientations in 5-axis ball-end milling. Int J Mach Tools Manuf 2016;106:89–97. https://doi.org/10.1016/j.ijmachtools.2016.04.007.

[212] Tunc LT, Stoddart D. Tool path pattern and feed direction selection in robotic milling for increased chatter-free material removal rate. Int J Adv Manuf Technol 2017;89:2907–18. https://doi.org/10.1007/s00170-016-9896-2.

[213] Verl A, Valente A, Melkote S, Brecher C, Ozturk E, Tunc LT. Robots in machining. CIRP Ann 2019;68(2):799–822. https://doi.org/10.1016/j.cirp.2019.05.009.

[214] Chen Y, Dong F. Robot machining: recent development and future research issues. Int J Adv Manuf Technol 2013;66:1489–97. https://doi.org/10.1007/s00170-012-4433-4.

[215] Suzuki N, Ishiguro R, Kojima T. Design of irregular pitch end mills to attain robust suppression of regenerative chatter. CIRP Ann 2016;65(1):129–32. https://doi.org/10.1016/j.cirp.2016.04.041.

[216] Comak A, Budak E. Modeling dynamics and stability of variable pitch and helix milling tools for development of a design method to maximize chatter stability. Precis Eng 2017;47:459–68. https://doi.org/10.1016/j.precisioneng.2016.09.021.

[217] Stepan G, Hajdu D, Iglesias A, Takacs D, Dombovari Z. Ultimate capability of variable pitch milling cutters. CIRP Ann 2018;67(1):373–6. https://doi.org/10.1016/j.cirp.2018.03.005.

[218] Budak E. An analytical design method for milling cutters with nonconstant pitch to increase stability, part 2: application. J Manuf Sci Eng 2003;125(1):35–8. https://doi.org/10.1115/1.1536656.

[219] Yusoff AR, Sims ND. Optimisation of variable helix tool geometry for regenerative chatter mitigation. Int J Mach Tools Manuf 2011;51(2):133–41. https://doi.org/10.1016/j.ijmachtools.2010.10.004.

[220] Hayasaka T, Ito A, Shamoto E. Generalized design method of highly-varied-helix end mills for suppression of regenerative chatter in peripheral milling. Precis Eng 2017;48:45–59. https://doi.org/10.1016/j.precisioneng.2016.11.004.

[221] Kojima T, Suzuki N, Hino R, Shamoto E. A novel design method of variable helix cutters to attain robust regeneration suppression. Procedia CIRP 2013;8:363–7. https://doi.org/10.1016/j.procir.2013.06.117.

[222] Koca R, Budak E. Optimization of serrated end mills for reduced cutting energy and higher stability. Procedia CIRP 2013;8:570–5.

https://doi.org/10.1016/j.procir.2013.06.152.

[223] Sellmeier V, Denkena B. High speed process damping in milling. CIRP J Manuf Sci Technol 2012;5(1):8–19. https://doi.org/10.1016/j.cirpj.2011.12.001.

[224] Suzuki N, Takahashi W, Igeta H, Nakanomiya T. Flank face texture design to suppress chatter vibration in cutting. CIRP Ann 2020;69(1):93–6. https://doi.org/10.1016/j.cirp.2020.04.037.

[225] Stepan G, Munoa J, Insperger T, Surico M, Bachrathy D, Dombovari Z. Cylindrical milling tools: Comparative real case study for process stability. CIRP Ann 2014;63(1):385–8. https://doi.org/10.1016/j.cirp.2014.03.137.

[226] Brecher C, Epple A, Neus S, Fey M. Optimal process parameters for parallel turning operations on shared cutting surfaces. Int J Mach Tools Manuf 2015;95:13–9. https://doi.org/10.1016/j.ijmachtools.2015.05.003.

[227] Sakata S, Kadota T, Yamada Y, Nakanishi K, Yoshioka H, Suzuki N, et al. Chatter avoidance in parallel turning with unequal pitch angle using observer-based cutting force estimation. J Manuf Sci Eng 2018;140(4):044501. https://doi.org/10.1115/1.4039111.

[228] Yamato S, Yamada Y, Nakanishi K, Suzuki N, Yoshioka H, Kakinuma Y. Integrated in-process chatter monitoring and automatic suppression with adaptive pitch control in parallel turning. Adv Manuf 2018;6:291–300. https://doi.org/10.1007/s40436-018-0222-0.

[229] Tarng YS, Lee EC. A critical investigation of the phase shift between the inner and outer modulation for the control of machine tool Chatter. Int J Mach Tools Manuf 1997;37(12):1661–72. https://doi.org/10.1016/S0890-6955(97)00035-7.

[230] Jayaram S, Kapoor SG, DeVor RE. Analytical stability analysis of variable spindle speed machining. J Manuf Sci Eng 2000;122(3):391–7. https://doi.org/10.1115/1.1285890.

[231] Seguy S, Insperger T, Arnaud L, Dessein G, Peigné G. On the stability of high-speed milling with spindle speed variation. Int J Adv Manuf Technol 2010;48:883–95. https://doi.org/10.1007/s00170-009-2336-9.

[232] Nam S, Hayasaka T, Jung H, Shamoto E. Proposal of novel chatter stability indices of spindle speed variation based on its chatter growth characteristics. Precis Eng 2020;62:121–33. https://doi.org/10.1016/j.precisioneng.2019.11.018.

[233] Sexton JS, Stone BJ. The stability of machining with continuously varying spindle speed. CIRP Ann 1978;27(1):321–26.

[234] Fansen K, Peng L, Xingang Z. Simulation and experimental research on chatter suppression using chaotic spindle speed variation. J Manuf Sci Eng 2011;133(1):014502. https://doi.org/10.1115/1.4003476.

[235] Yilmaz A, AL-Regib E, Ni J. Machine tool chatter suppression by multi-level random spindle speed variation. J Manuf Sci Eng 2002;124(2):208–16. https://doi.org/10.1115/1.1378794.

[236] Hayasaka T, Nam S, Jung H, Shamoto E, Saito K. Proposal of 'accelerative cutting' for suppression of regenerative chatter. CIRP Ann 2018;67(1):401–4. https://doi.org/10.1016/j.cirp.2018.04.030.

[237] Wang C, Zhang X, Yan R, Chen X, Cao H. Multi harmonic spindle speed variation for milling chatter suppression and parameters optimization. Precis Eng 2019;55:268–74.

https://doi.org/10.1016/j.precisioneng.2018.09.017.

[238] Lin SC, DeVor RE, Kapoor SG. The effects of variable speed cutting on vibration control in face milling. J Eng Ind 1990;112(1):1–11. https://doi.org/10.1115/1.2899290.

[239] Sexton JS, Stone BJ. An investigation of the transient effects during variable speed cutting. J Mech Eng Sci 1980;22(3):107–18. https://doi.org/10.1243/JMES_JOUR_1980_022_024_02.

[240] Otto A, Radons G. Application of spindle speed variation for chatter suppression in turning. CIRP J Manuf Sci Technol 2013;6(2):102–9. https://doi.org/10.1016/j.cirpj.2013.02.002.

[241] Fukagawa S, Fujimoto H, Terada Y, Ishii S. Experimental verification of chatter suppression in end milling process using cooperative control of spindle and stage motors. IECON 2015 - 41st Annu. Conf. IEEE Ind. Electron. Soc., Yokohama, Japan: IEEE; 2015, pp. 002794–9. https://doi.org/10.1109/IECON.2015.7392525.

[242] Urbikain G, Olvera D, de Lacalle LNL, Elías-Zúñiga A. Spindle speed variation technique in turning operations: modeling and real implementation. J Sound Vib 2016;383:384–96. https://doi.org/10.1016/j.jsv.2016.07.033.

[243] Ding L, Sun Y, Xiong Z. Active chatter suppression in turning by simultaneous adjustment of amplitude and frequency of spindle speed variation. J Manuf Sci Eng 2020;142:021004. https://doi.org/10.1115/1.4045618.

[244] Shamoto E, Mori T, Nishimura K, Hiramatsu T, Kurata Y. Suppression of regenerative chatter vibration in simultaneous double-sided milling of flexible plates by speed difference. CIRP Ann 2010;59(1):387–90. https://doi.org/10.1016/j.cirp.2010.03.028.

[245] Shamoto E, Mori T, Sencer B, Suzuki N, Hino R. Suppression of regenerative chatter vibration in multiple milling utilizing speed difference method – analysis of double-sided milling and its generalization to multiple milling operations. Precis Eng 2013;37(3):580–9. https://doi.org/10.1016/j.precisioneng.2013.01.003.

[246] Mori T, Hiramatsu T, Shamoto E. Simultaneous double-sided milling of flexible plates with high accuracy and high efficiency—suppression of forced chatter vibration with synchronized single-tooth cutters. Precis Eng 2011;35(3):416–23. https://doi.org/10.1016/j.precisioneng.2011.02.002.

[247] Bediaga I, Muñoa J, Hernández J, López de Lacalle LN. An automatic spindle speed selection strategy to obtain stability in high-speed milling. Int J Mach Tools Manuf 2009;49(5):384–94. https://doi.org/10.1016/j.ijmachtools.2008.12.003.

[248] Mizoguchi T, Nozaki T, Ohnishi K. The power factor in mechanical system. 2013 IEEE Int. Conf. Mechatronics (ICM), Vicenza, Italy: IEEE; 2013, pp. 576–81. https://doi.org/10.1109/ICMECH.2013.6519106.

[249] Mizoguchi T, Nozaki T, Ohnishi K. A method to derive on time mechanical power factor. 2014 IEEE Int. Conf. Ind. Technol. (ICIT), Busan, South Korea: IEEE; 2014, pp. 73–8. https://doi.org/10.1109/ICIT.2014.6894975.

[250] Yamato S, Sugiyama A, Suzuki N, Irino N, Imabeppu Y, Kakinuma Y. Enhancement of cutting force observer by identification of position and force-amplitude dependent model parameters. Int J Adv Manuf Technol 2019;104:3589–605. https://doi.org/10.1007/s00170-019-04080-8.

[251] Yamato S, Kakinuma Y. Precompensation of machine dynamics for cutting force estimation based on disturbance observer. CIRP Ann 2020;69(1):333–6.

https://doi.org/10.1016/j.cirp.2020.04.068.

[252] Fujita J, Hayama S, Hamamura M, Kakino Y, Matsubara A, Ohwaki S. The influence of the torsional vibration of ballscrew on the stability of NC servo drive system. J Japan Soc Precis Eng 1999;65(8):1190–4 (in Japanese). https://doi.org/10.2493/jjspe.65.1190.

[253] Kakino Y, Matsubara A, Li Z, Ueda D, Nakagawa H, Takeshita T, et al. A study on the total tuning of feed drive systems in NC machine tools (1st report). J Japan Soc Precis Eng 1994;60(8):1097–101 (in Japanese). https://doi.org/10.2493/jjspe.60.1097.

[254] Matsubara A, Ibaraki S, Kakino Y, Endo M, Umemoto M. Vibration control of feed drive in NC machine tools by dual actuation (1st report). J Japan Soc Precis Eng 2003;69(3):422–6 (in Japanese). https://doi.org/10.2493/jjspe.69.422.

[255] Sato R, Tsutsumi M. Mathematical model of feed drive systems consisting of AC servo motor and linear ball guide. J Japan Soc Precis Eng 2005;71(5):633–8 (in Japanese). https://doi.org/10.2493/jspe.71.633.

[256] Iwashita Y, Nakamura T, Ikai S, Takayama K. A study on low frequency vibration suppression control by two-mass system model for feed axes of NC machine tools. J Japan Soc Precis Eng 2016;82(8):745–50 (in Japanese). https://doi.org/10.2493/jjspe.82.745.

[257] Yamada Y, Kakinuma Y. Sensorless cutting force estimation for full-closed controlled ball-screw-driven stage. Int J Adv Manuf Technol 2016;87:3337–48. https://doi.org/10.1007/s00170-016-8710-5.

[258] Yamada Y, Kakinuma Y. Mode decoupled cutting force monitoring by applying multi encoder based disturbance observer. Procedia CIRP 2016;57:643–8. https://doi.org/10.1016/j.procir.2016.11.111.

[259] Yamada Y, Yamato S, Kakinuma Y. Mode decoupled and sensorless cutting force monitoring based on multi-encoder. Int J Adv Manuf Technol 2017;92:4081–93. https://doi.org/10.1007/s00170-017-0427-6.

[260] Katsura S, Suzuki J, Ohnishi K. Pushing operation by flexible manipulator taking environmental information into account. IEEE Trans Ind Electron 2006;53(5):1688–97. https://doi.org/10.1109/TIE.2006.881960.

[261] Mitsantisuk C, Nandayapa M, Ohishi K, Katsura S. Parameter estimation of flexible robot using multi-encoder based on disturbance observer. IECON 2012 - 38th Annu. Conf. IEEE Ind. Electron. Soc., Montreal, QC, Canada: IEEE; 2012, pp. 4424–9. https://doi.org/10.1109/IECON.2012.6389473.

[262] Mitsantisuk C, Nandayapa M, Ohishi K, Katsura S. Design for sensorless force control of flexible robot by using resonance ratio control based on coefficient diagram method. Automatika 2013;54(1):62–73. https://doi.org/10.7305/automatika.54-1.311.

[263] Henke B, Sawodny O, Neumann R. Distributed parameter modeling of flexible ball screw drives using ritz series discretization. IEEE/ASME Trans Mechatronics 2015;20(3):1226–35. https://doi.org/10.1109/TMECH.2014.2333775.

[264] Ewins DJ. Modal testing: theory, practice, and application. 2nd ed. Research Studies Press; 2000.

[265] Matsubara M, Tajiri D, Takehara S, Kawamura S. Linear fit method for modal parameter estimation using the real and imaginary parts of frequency response function (identification accuracy improvement based on weighted least square method). Trans

JSME 2019;85(873):18-00433 (in Japanese).
https://doi.org/10.1299/transjsme.18-00433.

[266] Yamada Y, Kakinuma Y. Influence of error factors in sensorless cutting force estimation. Trans JSME 2017;83(851):17-00098 (in Japanese).
https://doi.org/10.1299/transjsme.17-00098.

[267] Kim GD, Chu CN. Indirect cutting force measurement considering frictional behaviour in a machining centre using feed motor current. Int J Adv Manuf Technol 1999;15:478–84. https://doi.org/10.1007/s001700050092.

[268] Kono D, Matsubara A, Shirai T, Hoshide K, Miura T, Togashi T. Analysis of positional deviation caused by position-dependent disturbances in ball screw drive. J Japan Soc Precis Eng 2016;82(6):589–94. https://doi.org/10.2493/jjspe.82.589.

[269] Heydarzadeh MS, Rezaei SM, Azizi N, Kamali E A. Compensation of friction and force ripples in the estimation of cutting forces by neural networks. Measurement 2018;114:354–64. https://doi.org/10.1016/j.measurement.2017.09.032.

[270] Johanastrom K, Canudas-de-Wit C. Revisiting the LuGre friction model. IEEE Control Syst Mag 2008;28(6):101–14. https://doi.org/10.1109/MCS.2008.929425.

[271] Al-Bender F, Lampaert V, Swevers J. The generalized Maxwell-slip model: a novel model for friction Simulation and compensation. IEEE Trans Automat Contr 2005;50(11):1883–7. https://doi.org/10.1109/TAC.2005.858676.

[272] Sato R, Hasegawa M, Shirase K. Cutting force monitoring based on the frequency analysis of feed motor torques. J Soc Manuf Eng - Japan 2013;2:7–12.

[273] Yamada Y, Kadota T, Sakata S, Tachibana J, Nakanishi K, Sawada M, et al. Integrated chatter monitoring based on sensorless cutting force/torque estimation in parallel turning. Int J Autom Technol 2017;11(2):215–25.
https://doi.org/10.20965/ijat.2017.p0215.

[274] Aslan D, Altintas Y. Prediction of cutting forces in five-axis milling using feed drive current measurements. IEEE/ASME Trans Mechatronics 2018;23(2):833–44.
https://doi.org/10.1109/TMECH.2018.2804859.

[275] Sakai Y, Tanaka T, Yoshioka H, Zhu J, Tsutsumi M, Saito Y. Influence of nonlinear spring behavior of friction on dynamic characteristics of a rolling guideway. J Adv Mech Des Syst Manuf 2015;9(1):JAMDSM0004.
https://doi.org/10.1299/jamdsm.2015jamdsm0004.

[276] Futami S, Furutani A, Yoshida S. Nanometer positioning and its micro-dynamics. Nanotechnology 1990;1(1):31–7. https://doi.org/10.1088/0957-4484/1/1/006.

[277] Mizoguchi T, Nozaki T, Ohnishi K. Free motion mechanical power factor; comparison between robots in different structure and coordinate. 2014 Int. Power Electron. Conf. (IPEC-Hiroshima 2014 - ECCE ASIA), Hiroshima, Japan: IEEE; 2014, pp. 1660–4.
https://doi.org/10.1109/IPEC.2014.6869805.

[278] Mizoguchi T, Nozaki T, Ohnishi K. Power factor analyses in mechanical system focusing on trajectory and environment. 2013 IEEE Int. Symp. Ind. Electron., Taipei, Taiwan: IEEE; 2013, pp. 1–6. https://doi.org/10.1109/ISIE.2013.6563706.

[279] Yamato S, Ito T, Matsuzaki H, Fujita J, Kakinuma Y. Self-acting optimal design of spindle speed variation for regenerative chatter suppression based on novel analysis of internal process energy behavior. Int J Mach Tools Manuf 2020;159(Part A):103639.
https://doi.org/10.1016/j.ijmachtools.2020.103639.

[280] Albertelli P, Musletti S, Leonesio M, Bianchi G, Monno M. Spindle speed variation in turning: technological effectiveness and applicability to real industrial cases. Int J Adv Manuf Technol 2012;62:59–67. https://doi.org/10.1007/s00170-011-3790-8.

[281] Jemielniak K, Widota A. Suppression of self-excited vibration by the spindle speed variation method. Int J Mach Tool Des Res 1984;24(3):207–14. https://doi.org/10.1016/0020-7357(84)90005-2.

[282] Radulescu R, Kapoor SG, DeVor RE. An investigation of variable spindle speed face milling for tool-work structures with complex dynamics, part 2: physical explanation. J Manuf Sci Eng 1997;119(3):273–80. https://doi.org/10.1115/1.2831104.

[283] Tlusty J, Ismail F. Basic non-linearity in machining chatter. CIRP Ann 1981;30(1):299–304. https://doi.org/10.1016/S0007-8506(07)60946-9.

[284] Kondo Y, Kawano O, Sato H. Behavior of self-excited chatter due to multiple regenerative effect. J Eng Ind 1981;103(3):324–9. https://doi.org/10.1115/1.3184492.

[285] Suzuki N, Nishimura K, Watanabe R, Kato T, Shamoto E. Development of novel anisotropic boring tool for chatter suppression. Procedia CIRP 2012;1:56–9. https://doi.org/10.1016/j.procir.2012.04.008.

[286] Nam S, Hayasaka T, Jung H, Shamoto E. Proposal of novel spindle speed variation profile with constant acceleration rate for improvement of chatter stability. Precis Eng 2021;68:218–34. https://doi.org/10.1016/j.precisioneng.2020.12.008.

[287] Yamato S, Okuma T, Nakanishi K, Tachibana J, Suzuki N, Kakinuma Y. Chatter suppression in parallel turning assisted with tool swing motion provided by feed system. Int J Autom Technol 2019;13(1):80–91. https://doi.org/10.20965/ijat.2019.p0080.

[288] Yamato S, Nakanishi K, Suzuki N, Kakinuma Y. Experimental verification of design methodology for chatter suppression in tool swing–assisted parallel turning. Int J Adv Manuf Technol 2020;110:1759–71. https://doi.org/10.1007/s00170-020-05951-1.

[289] Hecker RL, Flores GM, Xie Q, Haran R. Servocontrol of machine-tools: a review. Lat Am Appl Res 2008;38:85–94.

[290] Wang JJ, Sung CF. Trajectories of forces and displacements in stable and unstable milling. Int J Adv Manuf Technol 2017;89:2803–19. https://doi.org/10.1007/s00170-016-9833-4.

[291] Tunç LT, Budak E. Effect of cutting conditions and tool geometry on process damping in machining. Int J Mach Tools Manuf 2012;57:10–9. https://doi.org/10.1016/j.ijmachtools.2012.01.009.

[292] Liu CR, Liu TM. Automated chatter suppression by tool geometry control. J Eng Ind 1985;107(2):95–8. https://doi.org/10.1115/1.3185989.

[293] Tarng YS, Young HT, Lee BY. An analytical model of chatter vibration in metal cutting. Int J Mach Tools Manuf 1994;34(2):183–97. https://doi.org/10.1016/0890-6955(94)90100-7.

[294] Albertelli P, Mussi V, Monno M. The analysis of tool life and wear mechanisms in spindle speed variation machining. Int J Adv Manuf Technol 2014;72:1051–61. https://doi.org/10.1007/s00170-014-5736-4.

[295] Kayhan M, Budak E. An experimental investigation of chatter effects on tool life. Proc Inst Mech Eng Part B J Eng Manuf 2009;223(11):1455–63. https://doi.org/10.1243/09544054JEM1506.

[296] Zatarain M, Muñoa J, Peigné G, Insperger T. Analysis of the influence of mill helix angle on chatter stability. CIRP Ann 2006;55(1):365–8. https://doi.org/10.1016/S0007-8506(07)60436-3.

[297] Budak E, Altintas¸ Y, Armarego EJA. Prediction of milling force coefficients from orthogonal cutting data. J Manuf Sci Eng 1996;118(2):216–24. https://doi.org/10.1115/1.2831014.

Acknowledgements

This dissertation is a summary of my research work carried out from 2016 to 2021 as a member of the Manufacturing Science laboratory in Keio University. Thanks to the endless guidance and support of numerous people, I could successfully complete my doctorial study.

Firstly, I would like to express my deepest gratitude to my supervisor, Professor Dr. Yasuhiro Kakinuma. He always enthusiastically supported and guided me during my PhD program. His advice has always played an important role in the progress of my research and helped me develop my philosophy as a researcher. He provided me with various opportunities, which are essential for an independent researcher, such as attending conferences, writing journal articles, preparing and applying for grants and proposals for new projects, and engaging in collaborative research with both academia and industry.

I would also like to express my gratitude to Professor Emeritus Dr. Tojiro Aoyama. His insightful comments during our research meetings were helpful to deepen my understanding. Additionally, I would like to thank Professor Dr. Hideki Aoyama, Professor Dr. Jiwang Yan, and Assistant Professor Dr. Ryo Koike of Keio University as well as Associate Professor Dr. Norikazu Suzuki of Nagoya University. They provided me with very beneficial comments and suggestions in developing this dissertation.

I received a great deal of technical support and advice from industry in carrying out my research. I would like to express my heartfelt gratitude to Takamichi Ito, Dr. Jun Fujita, Hirohiko Matsuzaki, and Yutaka Asanome from Shibaura Machine Co., Ltd.; Dr. Kenichi Nakanishi from Nakamura-Tome Precision Industry Co., Ltd.; Junji Tachibana, Takashi Ikeda, Naoki Kudoh, and Noriyuki Shiomi from OMRON Corporation; and Dr. Naruhiro Irino, Yasuhiro Imabeppu, and Kengo Kawai from DMG MORI Co., Ltd. Thanks to their assistance, I could carry out my experimental verifications. In addition, their frank comments helped me refine my research direction.

I appreciate the former and current students in the laboratory — Dr. Yuki Yamada, Dr. Yuta Mizumoto, Takayuki Hirano, Toshiki Okuma, Akihiro Sugiyama, Taiki Sato, and Keisuke Yamamoto. I am really grateful to Kana Igarashi and Michie Ishiwata for their continuous contributions to sustaining a favorable research environment. I would also like to acknowledge the financial support provided to me by the Grant-in-Aid for JSPS Research Fellowship from the Japan Society for the Promotion of Science, and the Keio University Doctoral Student Grant-in-Aid Program.

My sincere appreciation goes to my beloved wife Kayoko Yamato and her parents for their warm support. Finally, I would like to express my special thanks to my beloved parents for their endless support.

February 2021

Shuntaro Yamato